2019

PALAEOMAGNETIC AND STRUCTURAL ANALYSIS OF THE METAMORPHIC SOLE ROCKS OF THE MERSIN OPHIOLITE, SOUTHERN TURKEY

Cavdar, Bugra

http://hdl.handle.net/10026.1/15163

http://dx.doi.org/10.24382/717
University of Plymouth

UNIVERSITY OF
PLYMOUTH

PALAEOMAGNETIC AND STRUCTURAL ANALYSIS OF THE METAMORPHIC SOLE ROCKS OF THE MERSIN OPHIOLITE, SOUTHERN TURKEY

by

BUĞRA ÇAVDAR

A thesis submitted to the University of Plymouth in partial fulfilment for the degree of

RESEARCH MASTERS

School of Geography, Earth, and Environmental Sciences

March 2019

Copyright statement

BUĞRA ÇAVDAR

PALAEOMAGNETIC AND STRUCTURAL ANALYSIS OF THE METAMORPHIC SOLE ROCKS OF THE MERSIN OPHIOLITE, SOUTHERN TURKEY

Abstract

The Mersin ophiolite (Tauride Belt, southern Turkey) is a well-exposed Neo-Tethyan suprasubduction zone ophiolite that formed in the Late Cretaceous. It is underlain by metamorphic sole rocks (predominantly amphibolites) inferred to have formed at the top of the down-going plate during subduction. A recent model for exhumation of such rocks from peak metamorphic depths involves slab flattening caused by removal of material from the mantle wedge during fore-arc spreading, implying significant rotation of the sole after formation. Previous palaeomagnetic analysis of non-metamorphosed dykes cutting the Mersin sole rocks indicates a ~45° clockwise rotation of the sole and dykes around a NE-trending, shallowly plunging, ridge-parallel axis. This study aims to quantify any potential rotation of the Mersin sole rocks prior to dyke intrusion to test models of sole exhumation. The amphibolites carry a stable magnetization that is statistically different from that of the dykes, providing evidence for an earlier phase of rotation. However, tectonic interpretation of these data in the absence of paleohorizontal markers cannot be achieved by using standard palaeomagnetic tilt corrections. Therefore, a Monte Carlo approach was used to model potential net tectonic rotation axes after back-stripping the later rotation of sole-hosted dykes from the palaeomagnetic and structural data and by incorporating statistical uncertainties into the analysis. Results suggest that the sole acquired its remanence while the metamorphic foliation dipped moderately (~30-40°) to the ENE and then underwent an early phase of anticlockwise rotation around an inclined, NW plunging axis. This is consistent with a two-stage model involving an earlier phase of exhumation by slab flattening and rotation followed by a later spreading-related rotation around a ridge-parallel axis after accretion of the sole to the base of the lithosphere (and future ophiolite). These rotations around different axes are consistent with a tectonic setting similar to the modern Andaman Sea subduction zone system, where spreading in the suprasubduction zone environment occurs obliquely to the direction of subduction of the down-going plate.

Table of contents

List of figures

List of tables

ACKNOWLEDGEMENTS

I would first like to thank my supervisors Professor Antony Morris, Professor Mark Anderson, and Dr Luca Menegon for their endless support and patience throughout my research and writing up period. They have always been helpful and tried to create time for conservations about my project. Particularly, I am thankful and grateful for everything new I have learnt in terms of palaeomagnetism at University of Plymouth.

Besides my supervisors, I would like to thank the Ministry of National Education of Republic of Turkey for the scholarship and covering all the expenses. Also, apart from the financial issues, I appreciate that authorized personnel in London working for the Ministry always tried to help for other concerns too.

I would like to give my special thanks to Louise Koornneef who is PhD student at University of Plymouth for all her help during the palaeomagnetic analyses in the laboratory, and also I appreciate her helpful comments on results I obtained.

I also would like to thank to Drs Arjan Dijkstra and Colin Wilkins especially for their help for the conversations about mineralogy and geochemistry of my samples. Moreover, special thanks go to Professor Dr Osman Parlak from Çukurova University for help during the fieldwork in Mersin/Mezitli.

I am very thankful to Dr. Chuang Xuan who played a crucial role in my research by giving me a chance to use the 2G Enterprises Superconducting Rock Magnetometer at the University of Southampton, and also technicians there who helped me to use the equipment.

Last but not the least, I would like to thank to my beloved parents, sister, my niece Bilge and to my cousin Rabia and my friends: Kerim Yılmaz, Caner Tanrıverdi, Serhat Kağan Çalışkan, Akın Çil, Pelin Güngör, Deniz Cem Kaplan, Iliana Dekastrou for supporting me spiritually throughout doing my research, writing this thesis and my life in general. Special thanks also go to Elif Dilek Bilgin who finished her masters at Leeds University for her endless support literally every day.

"Our true mentor in life is science." ***Mustafa Kemal Atatürk (1881-1938)***

AUTHOR'S DECLARATION

At no time during the registration for the degree of Research Masters has the author been registered for any other University award without prior agreement of the Doctoral College Quality Sub-Committee.

Work submitted for this research degree at the University of Plymouth has not formed part of any other degree either at the University of Plymouth or at another establishment.

This study was financed with the aid of a scholarship from Ministry of National Education of Republic of Turkey.

A programme of advanced study was undertaken, which included GEOL5001 Geoscience Frontiers: Research and Communication, and GEOL5002 MGeol Advanced Fieldwork.

External institutions visited:

-University of Southampton, to use 2G Cryogenic Magnetometer for advanced analyses

Conference abstracts:

-Çavdar, B., Morris, A., Anderson, M., Menegon, L. and Parlak, O. (2019). Beyond the standard tilt correction: analysing the palaeomagnetism of metamorphic soles. *Geophysical Research Abstracts*, 21(EGU2019-15948).

Presentations:

-CRES Research Conference **oral presentation**, title: "Metamorphic sole rocks of Mersin ophiolite". University of Plymouth, November 2018.

Conferences attended:

-CRES Research Conference / University of Plymouth, November 2017

-Magnetic Interactions Annual Meeting / University of Oxford, 4 – 5 January. 2018.

Participation in field trips:

-Troodos Ophiolite/Cyprus field trip in the scope of the module GEOL5002.

Word count of main body of thesis: 20344 words

Signed:

Date: 27/03/2019

Chapter 1- Introduction

1.1 Aims and objectives

Most ophiolites have geological, geochemical and geophysical signatures that point to their formation by supra-subduction seafloor spreading and it is believed that they are generally underlain by the metamorphic sole rocks which have formed at the top of the undergoing plate and accreted below the supra-subduction zone lithosphere immediately following ophiolite formation.

The main aim of this Masters project is to research and study the metamorphic sole rocks of the Mersin ophiolite of southern Turkey by using palaeomagnetic, magnetic fabric, structural and petrographic data to address the following scientific objectives:

1- To establish the magnetic carriers and magnetic remanence characteristics of the metamorphic sole rocks, and explain how their magnetisation was acquired

2- To determine the nature and magnitude of any early phase of rotation experienced by the Mersin ophiolite metamorphic sole rocks prior to intrusion by dykes related to the overlying ophiolite, to test models for metamorphic sole exhumation

3- To determine the nature of microstructures in the sole rocks and interpret their structural evolution

4-To interpret the pressure-temperature conditions at the time when the sole rocks have formed

1.2 Ophiolites

Ophiolites are remnants of ancient oceanic crust and underlying mantle that have been uplifted and exposed above sea level. When complete, their crustal sequences consist of layered and isotropic gabbros at the base, overlain by upper crustal sections of sheeted dykes and extrusive igneous rocks (including pillow lavas) (Fig. 1.1). At the broadest level they may be subdivided into two types based on their geochemical compositional signatures: mid-oceanic ridge (MOR) type and supra-subduction zone (SSZ) type (Fig. 1.2). MOR-type ophiolites have mid-oceanic ridge basalts and lavas whereas SSZ type ophiolites have island arc tholeiites, forearc basalts, back-arc basin basalt and possibly boninites (Dilek and Furnes, 2014). Additionally, boninites can be observed in SSZ type ophiolites because of the ultra-depletion of the mantle wedge resulting from fluid assisted melting (Pagé et al., 2009; van Hinsbergen et al., 2015). The existence of the podiform chromite deposits and crystallisation of clinopyroxene before plagioclase are other features of SSZ type ophiolites (Dilek and Furnes, 2014; Pearce et al., 1984).

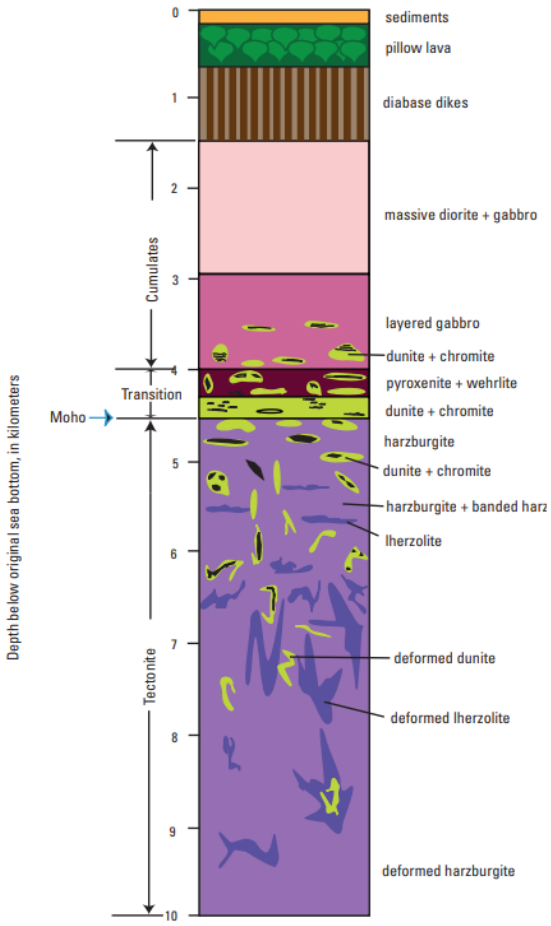

Figure 1.1. Generalized succession of the ophiolites (from Mosier et al., 2012)

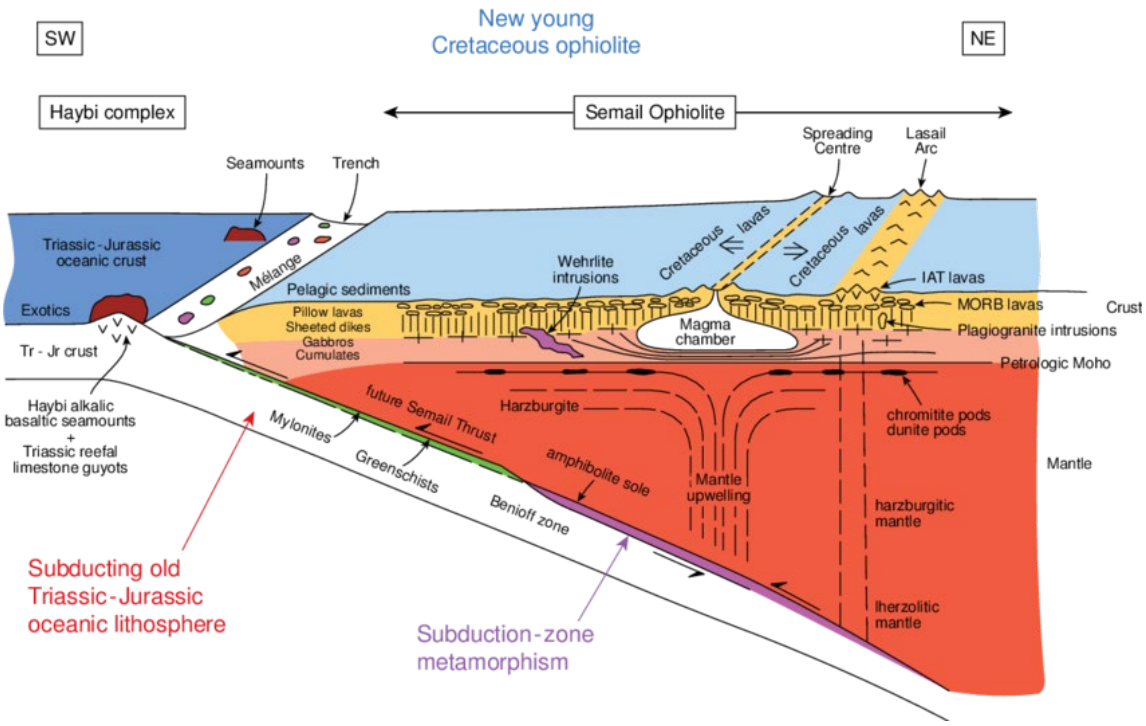

Figure 1.2. Illustration of the supra-subduction zone origin of ophiolites (in this case, for the Oman ophiolite) (from Searle, 2014)

The most known, best-exposed ophiolitic sequences are the Semail ophiolite (Oman), Troodos ophiolite (Cyprus), Bay of Islands ophiolite (Newfoundland), Yakuno, Horokanai, and Poroshiri ophiolites (Japan). Some of the units are missing for the other ophiolites observed in different locations as shown below (Fig. 1.3). The existence of cumulate complexes and/or sheeted dykes in the ophiolite determines the nature of the spreading centre regarding the chemistry or mineralogy.

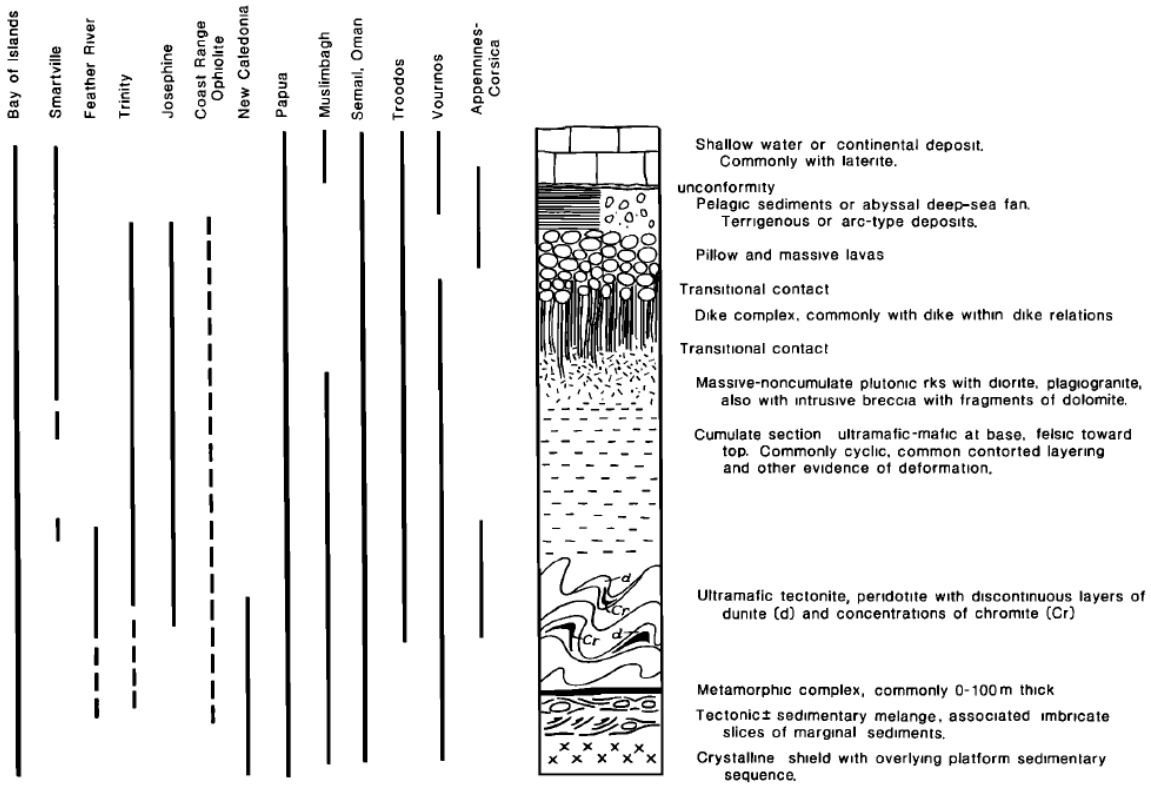

Figure 1.3. Comparison of some of the well-known ophiolites around the world and Penrose sequence (From Moores, 1982)

Recent studies (e.g. Stern et al., 2012) have suggested that formation of supra-subduction zone ophiolites takes place during phases of subduction initiation. Hence, as well as providing insights into processes of seafloor spreading, ophiolites also provide the best environment in which to understand this poorly understood component of the plate tectonic system. In this context, the metamorphic soles that are associated with many ophiolites are now considered to form at the top of the down-going plate in a newly initiated subduction zone and are then exhumed from peak metamorphic depths to be accreted to the base of ophiolites prior to final emplacement upon continental margins (van Hinsbergen et al., 2015). This thesis explores whether the palaeomagnetism of metamorphic sole rocks may be used to help constrain this tectonic process of exhumation.

Chapter 2- Scientific Background

2.1 General overview of Turkish terranes and suture zones

The tectonic blocks that comprise Turkey were located between the two stable and ancient continents of Laurasia in the north and Gondwana in the southern part, separated by the Tethys Ocean in the Paleozoic-Mesozoic and Early Tertiary. In this period, while Laurasia was the active continental margin, Gondwana was the passive margin. Some continental fragments separated from Gondwana and these fragments accreted to Laurasia during Paleozoic-Mesozoic time. Present-day Turkey is formed of six major lithospheric fragments or terranes which have separated from Gondwana and continent at different times: Sakarya zone, İstanbul zone, the Strandja zone, the Anatolide-Tauride Block, the Central Anatolian Crystalline Complex (Kırşehir Massif) and the Arabian platform (Bozkurt and Mittwede, 2001; Şengör and Yilmaz, 1981; Moix et al., 2008; Okay and Kelley, 1994; Okay, 1989; Okay and Whitney, 2010; Robertson, 1998; Robertson et al., 2012; Robertson et al., 2013). The last collision occurred between the Anatolian Plate and Arabian Plate during Late Tertiary time. The Sakarya, İstanbul, and Strandja zones are classified as the Pontides (Western), and they show the Laurasian features (Bozkurt and Mittwede, 2001; Okay and Whitney, 2010). The Pontides are separated from the Anatolide-Tauride block and the Kırşehir Massif by the İzmir-Ankara-Erzincan suture. The suture zone formed after the collision of Anatolian and Arabian platforms is called as Assyrian-Zagros suture. Also, the boundary between the Sakarya and İstanbul zones is represented as the Intra-Pontide suture (Fig. 2.1).

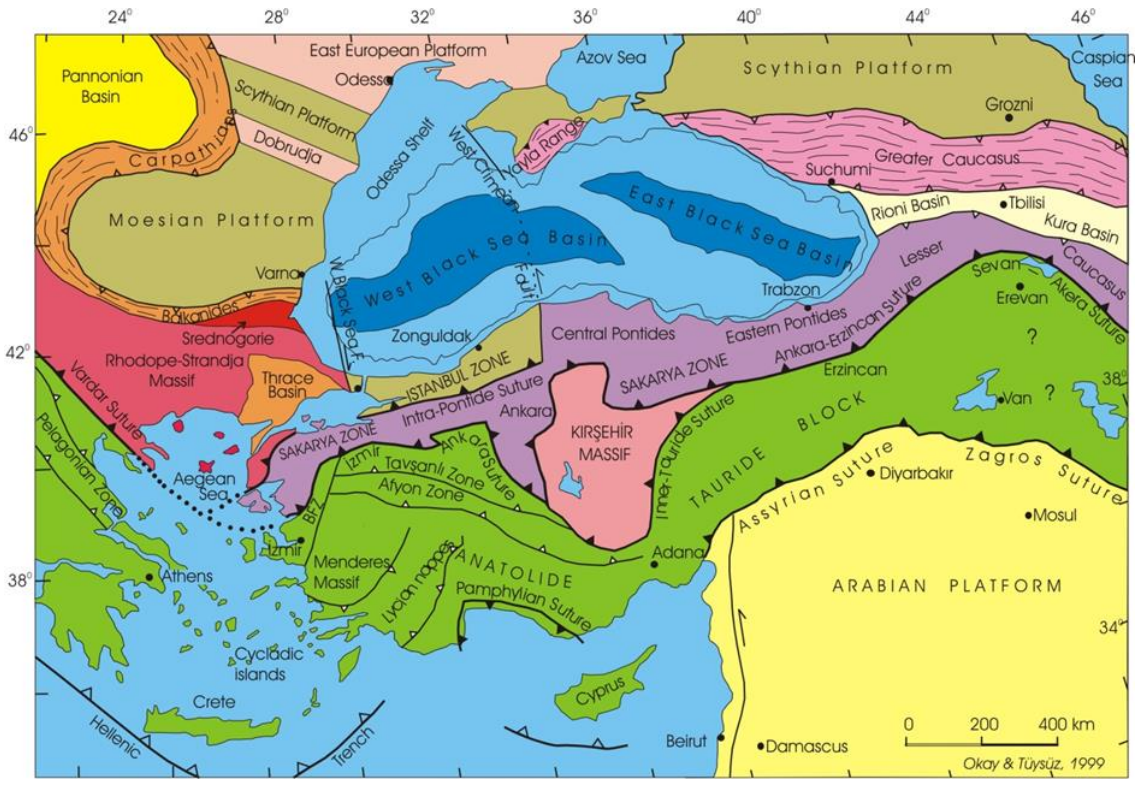

Figure 2.1. The suture zones located in Turkey with surrounding suture zones and main continental fragments (from Okay and Whitney, 2010)

The Anatolide-Tauride block represents the platform between İzmir-Ankara-Erzincan Ocean to the north and the southern branch of Neo-Tethys to the south. The Anatolides form the western part of the present Anatolide-Tauride block, and Taurides form the eastern part of the block. The Tauride Platform consists of generally non-metamorphosed nappes whereas the Anatolides consist of the Menderes Massif to the west and the Central Anatolian Crystalline Complex to the east representing the central metamorphic part and the Kütahya-Bolkardağ Belt representing the northern margin of the platform (Göncüoglu et al., 2010). However, the reason why they are classified as one block is that they share some common features, i.e. Pan-African crystalline basement, a discontinuous Cambrian to Devonian succession dominated by siliciclastic rocks, a Permian-Carboniferous sequence of intercalated limestones, shales and quartzites, and a thick Late Triassic to Late Cretaceous carbonate sequence (Okay and Tüysüz, 1999; Okay and Whitney, 2010).

The Kırşehir massif is also interpreted as a metamorphosed margin of Northern Anatolide-Tauride Block (Kaymakci et al., 2009; Yaliniz et al., 1996). This massif experienced multiple deformation stages during and after the closure of the surrounding oceans. (Cinku et al., 2016; Seymen, 1983). The Pontides form the northernmost part of present-day Turkey with its different zones and geologic complexities. They consist of an E-W trending orogenic belt that is divided into the western, central and eastern Pontides that show different stratigraphical and structural characteristics (Robinson, 1997; Ustaomer and Robertson, 1998)

The northern part of the Arabian Platform forms the south-eastern region of Turkey. This platform was separated from the Anatolide-Taurides as a southern branch of Neo-Tethys in the Mesozoic and Tertiary. In consequence of the collision in the Miocene between the Arabian and Anatolian platforms, all traces of the intact oceanic crust were gone (Robertson and Grasso, 1995; Şengör et al., 1985; Yilmaz, 1993). Eventually, the present shape of Turkey was constructed after this collision.

2.2 Ophiolites in Turkey

The Tethyan ophiolites of Turkey are divided into five main belts: Northern belt comprising Pontide ophiolites, Tauride ophiolite belt, Anatolian ophiolite belt, Southeast Anatolian ophiolite belt and the peri-Arabian ophiolite belt (Bağci et al., 2005; Rizaoğlu et al., 2006) (Fig. 2.2).

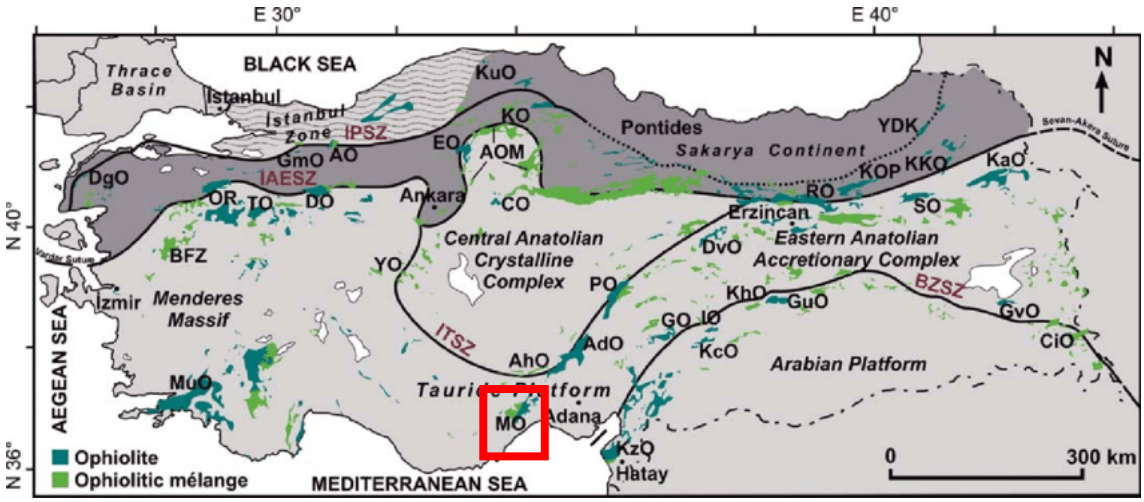

Figure 2.2. Distribution of the ophiolites located in Turkey and main suture zones , the Mersin ophiolite is shown in the red square; DgO—Denizgören ophiolite; GmO—Geyve meta-ophiolite; AO—Almacık ophiolite; KuO—Küre ophiolite; YDK—Yusufeli dike complex). IAESZ—İzmir-Ankara-Erzincan suture zone (BFZ—Bornova flysch zone; OR—Orhaneli ophiolite; TO—Tavşanlı ophiolite; DO—Dağküplü ophiolite; EO—Eldivan ophiolite; KO—Kargı ophiolite; CO— Çicekdağ ophiolite; AOM Ankara mélange; RO—Refahiye ophiolite; KOP—Kop ophiolite; SO—

Şahvelet ophiolite; KKO—Kırdağ-Karadağ ophiolite; KaO—Kağızman ophiolite; MuO—Muğla ophiolite). ITSZ—Inner-Tauride suture zone (YO—Yunak ophiolite; AhO Alihoca ophiolite; MO—Mersin ophiolite; AdO—Aladağ ophiolite; PO—Pınarbaşı ophiolite; DvO—Divriği ophiolite). BZSZ—Bitlis-Zagros suture zone (KzO—Kızıldağ ophiolite; GO—Göksun ophiolite; IO—Ispendere ophiolite; KhO Kömürhan ophiolite; GuO—Guleman ophiolite; KcO— Koçali ophiolite; GvO—Gevaş ophiolite; CiO—Cilo ophiolite (from Sarıfakıoğlu et al., 2017)

Most formed in a supra-subduction zone (SSZ) setting according to petrologic and geochemical evidence (Aktaş and Robertson, 1984; Al-Riyami et al., 2002; Collins and Robertson, 1998; Floyd et al., 2000; Lytwyn and Casey, 1993; Parlak et al., 1996a; Parlak et al., 2002; Parlak et al., 2000; Pearce et al., 1984; Robertson, 2002; Yaliniz et al., 1996).

The Hatay, Baer Bassit , Troodos, Cilo, Güleman, Zagros, and Oman ophiolites form the peri-Arabic belt (Ricou, 1971), and have been extensively studied because almost all of the ophiolitic units crop out clearly. Bağcı et al. (2005) stated that Kızıldağ ophiolite is one of the best example to observe the seafloor spreading mechanics, structures and related processes, i.e. magmatic and hydrothermal activities as the area did not experience large scale deformation (Dilek and Eddy, 1992). These ophiolites are believed to have formed in a supra-subduction zone system during the Late Cretaceous, and this ophiolitic belt was emplaced onto the Arabian platform during the Campanian-Maastrichtian (Yilmaz, 1993). Late Cretaceous ophiolites also occur along the Tauride tectonic belt in Lycian nappes, Ali Hoca complex, Beyşehir-Hoyran nappes, Pozanti-Karsantı and the Mersin ophiolite, and are primarily made of tectonized mantle rocks, mafic-ultramafic cumulates and gabbros and lack sheeted dyke complexes and volcanic rocks of the complete sequence. Furthermore, mafic dykes intruded into the metamorphic sole rocks associated with these ophiolites (Dilek et al., 1999; Parlak, 1996), demonstrating that the soles were emplaced beneath the ophiolites while SSZ magmatism was on-going. Pontide ophiolites trending in E-W direction along Northern belt are the remnants of the İzmir-Ankara Ocean, and formed after the closure of the Northern branch of Neo-Tethys Ocean. The Orhaneli, Harmancık (Bursa), Tavşanlı (Kütahya) and Dağküplü-Mihalicik (Eskişehir) ophiolites are the best examples of Pontide ophiolites (Sarıfakıoğlu et al., 2017).

2.3 Geological Setting of the Mersin ophiolite

2.3.1 General overview to Mersin ophiolite

The Mersin ophiolite in the southern part of Turkey covers 1500 square kilometers. It formed in a SSZ environment after the closure of Neo-Tethyan Ocean during the Late Cretaceous and was then uplifted and exposed above sea level. The approximate thickness of the ophiolite complex is 6 km (Parlak et al., 1996). The complex is separated from the Eastern Tauride Belt by the Ecemiş Fault to the east (Parlak, 1996; Parlak and Delaloye, 1999; Parlak et al., 2000), the Bolkardağ metamorphic rocks to the north and the Miocene carbonates to the west (Parlak et al., 1996a). Ophiolitic melange, metamorphic sole rocks, and ophiolitic units are observed from the bottom of the sequence upwards (Fig. 2.3). Although the Mersin ophiolite is one of the best preserved and exposed Neo-Tethyan ophiolites, the sequence does not present a complete Penrose sequence, and it lacks a sheeted dyke complex and deep marine sediments.

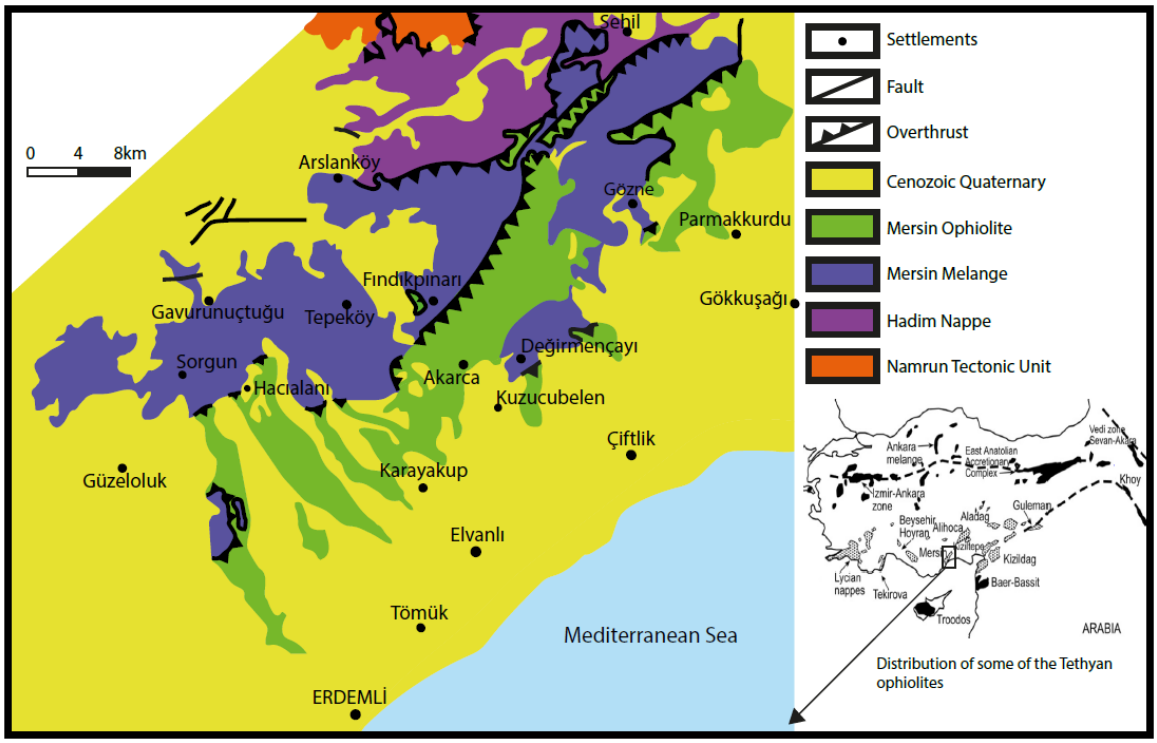

Figure 2.3. Simplified geological map of Mersin ophiolite, its related units and main ophiolites around the Eastern Mediterranean (Modified from Tekin et al., 2016)

2.3.2 Emplacement of the ophiolite

The Mersin ophiolite formed during the Late Cretaceous. Radiometric dating of the metamorphic sole rocks yielded ages ranging from 93 to 91 Ma (Çelik, 2008; Çelik et al., 2006; Dilek et al.,

1999; Parlak and Delaloye, 1999; Parlak et al., 1995). After formation, Robertson (2002) argued that Mersin ophiolite was thrust over the Bolkar carbonate platforms (Fig. 2.4). Koç et al. (2013) showed that post-Danian is the period for the ophiolite emplacement based on ages of planktonic foraminifera found in the ophiolitic melange. Emplacement took place from the southern part of the platform in NW direction, and thrust-related fold structures in the melange and sole rocks also support a top to the NNW emplacement direction over the platform (Parlak et al., 1996a). Furthermore, non-metamorphosed dykes cutting the metamorphic sole rocks intruded after the end of metamorphism, but before the emplacement (Çelik, 2008; Dilek and Eddy, 1992; Dilek and Whitney, 1997).

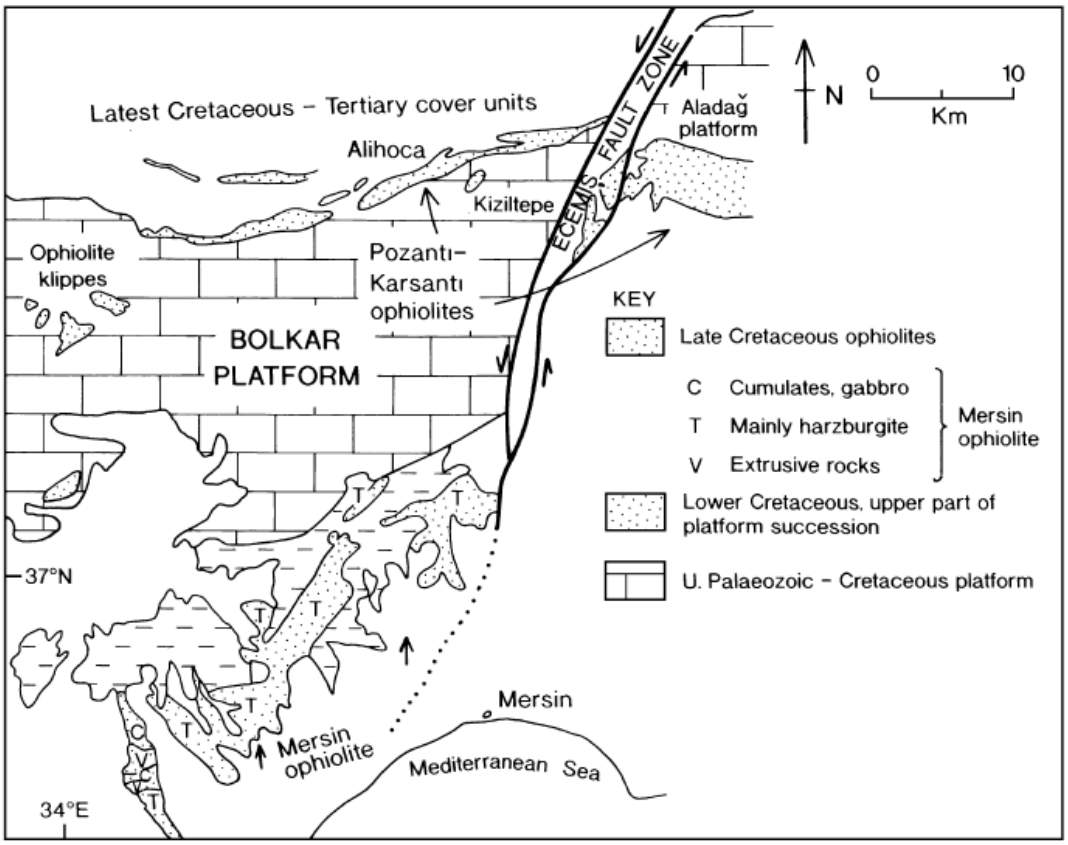

Figure 2.4. The sketch map showing the relationship of the Mersin ophiolite to the Bolkar Platform (from Robertson, 2002)

Robertson (2000) suggested collection of more data to test the emplacement direction onto the carbonate platform that Parlak (1996) proposed. Parlak and Robertson (2004) argued that kinematic evidence in the metamorphic sole rocks (before dyke intrusions) and the ophiolite showed transportation in an E-W or W-E direction in an intraoceanic setting. However, it has

been noted that this direction might be affected by possible rotations (Parlak and Robertson, 2004).

2.3.3 Units in the Mersin Ophiolite

From top to bottom, the Mersin ophiolite consists of ophiolitic units, metamorphic sole rocks and underlying ophiolitic melange (Fig. 2.5).

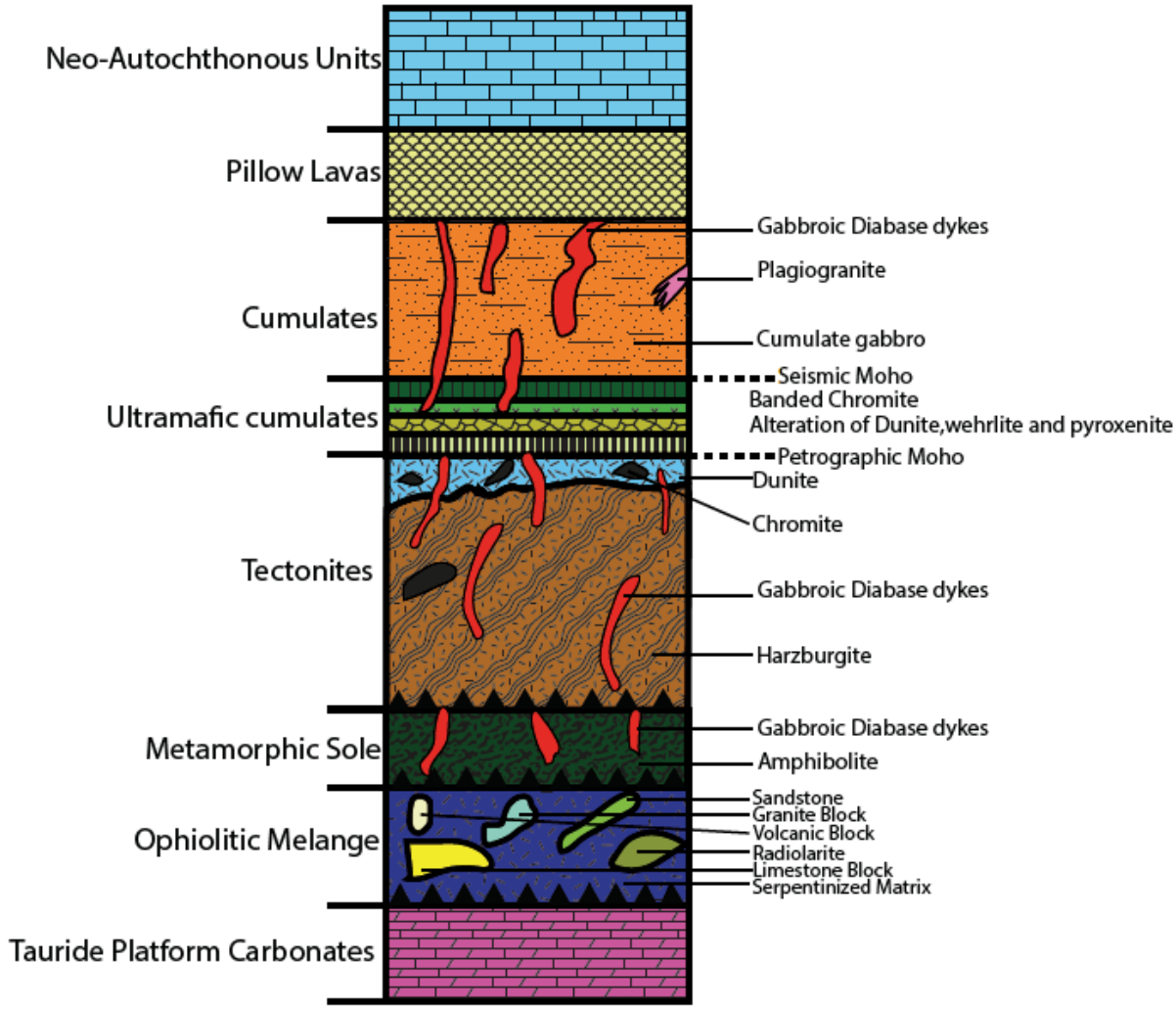

Figure 2.5. Columnar section of Mersin ophiolite (modified from Parlak, 1996)

2.3.3.1 Basaltic units

There are two basaltic sections showing different geochemical characteristics in this part of the ophiolite. One of them indicates tholeiitic basalts features whereas other suggests alkaline basalts (Parlak, 1996). The diabase dykes with dolerite texture beneath these basaltic units have same mineralogical compositions with tholeiitic basalts. All of these volcanic rocks were exposed to low-grade metamorphism, and some of the primary minerals altered (Parlak, 1996). Some of these

secondary minerals were also observed in pillow lavas which were overturned in the field (Omer, 2014).

2.3.3.2 Cumulates

The majority of the ophiolite consists of cumulate gabbroic rocks observed between basaltic units and tectonized harzburgites cut by diabase dykes, with a total thickness of 3 km (Parlak et al., 1996). Ultrabasic cumulates form the bottom part of the section whereas gabbroic rocks (two-third of the cumulates) form the top of the section (Parlak et al., 1996). The U-Pb age of gabbroic cumulates was determined as 82.8 ± 4.0 Ma (Parlak et al., 2013).

The ultramafic portion is composed of dunite with stratiform chromite, clinopyroxenite and wehrlite. Crystallization order of the minerals was determined as olivine, clinopyroxene, plagioclase, orthopyroxene, respectively. In the mafic portion, olivine gabbro forms the bottom part of this section. Gabbro, leucogabbro and anorthosite composes the upper part from bottom to up, respectively. There are some small-scale plagiogranite intrusions observed in the upper parts of cumulates. Some gravity controlled structures were also observed in the cumulates (Parlak et al., 1996).

2.3.3.3 Dykes cutting cross mantle section and soles

The metamorphic sole rocks, mantle sequence and cumulates are cut by non-metamorphosed dykes. Some of the dyke thickness are up to five meters (Omer, 2014). Ar^{39}-Ar^{40} dating indicates that these dykes range from 91 Ma to 86 Ma (Dilek et al., 1999; Parlak and Delaloye, 1996). K-Ar ages of 88.8 ± 2 Ma to 84.4 ± 3 Ma were determined by (Çelik, 2008). The dykes show island arc basaltic characteristics based on cooling age technique (Çelik, 2008; Parlak and Delaloye, 1996). Since there is no metamorphism in the dykes, it is suggested that dykes intruded into the sole after metamorphic activity and before the emplacement of the ophiolite onto the Bolkar carbonate platforms (Çelik and Delaloye, 2004; Dilek et al., 1999; Parlak and Delaloye, 1996). Dolerite dykes cutting cross the sole rocks are composed of amphiboles, pyroxene, plagioclase and some secondary minerals with sub-ophitic or microgranular texture. Some dykes were exposed to hydrothermal alteration, with plagioclase, epidote, and kaolinite observed as alteration

minerals. Also, some of the dykes have chilled margins. It is broadly accepted that dyke emplacement in the mantle section and sole rocks was generated by either roll-back of the subducting plate or delamination of the subducting plate resulting in asthenospheric inflow (Çelik et al., 2006; Morris et al., 2017; Parlak et al., 2006; van Hinsbergen et al., 2015).

2.3.3.4 Metamorphic sole rocks

The Mersin ophiolite is underlain by metamorphic sole rocks which are mainly composed of amphibolites in the upper parts, and mica schists, calcschists, marble and quartzite in the lower parts (Fig. 2.6). Mica-schist lenses are observed in the amphibolites. Foliation is common through the amphibolites and granoblastic, nematoblastic and granonematoblastic textures are frequent in the rocks (Çelik, 2008). Amphiboles are defined as calcic amphiboles based on geochemistry data and the amphibolites most probably originated by metamorphism of mafic igneous rocks (basalts or gabbro) (Çelik, 2008). On the other hand, the origin of the mica schists is probably sedimentary (Çelik, 2008). Geochemical analysis of the sole rocks indicate that they are the metamorphosed equivalents of island arc tholeiites, ocean island basalts, and enriched mid-oceanic ridge basalts, and that the protoliths were formed in a SSZ environment like the other Tauride belt ophiolites (Çelik, 2008). There are some different studies to determine the pressure and temperature conditions. Parlak and Delaloye (1999) suggested that sole rocks cooled below 510°C±25°C. Çelik (2008) determined that the average metamorphic temperature was 522°C±15°C and the pressure less than 5 kbar during the metamorphism, which is more precise than previous studies.

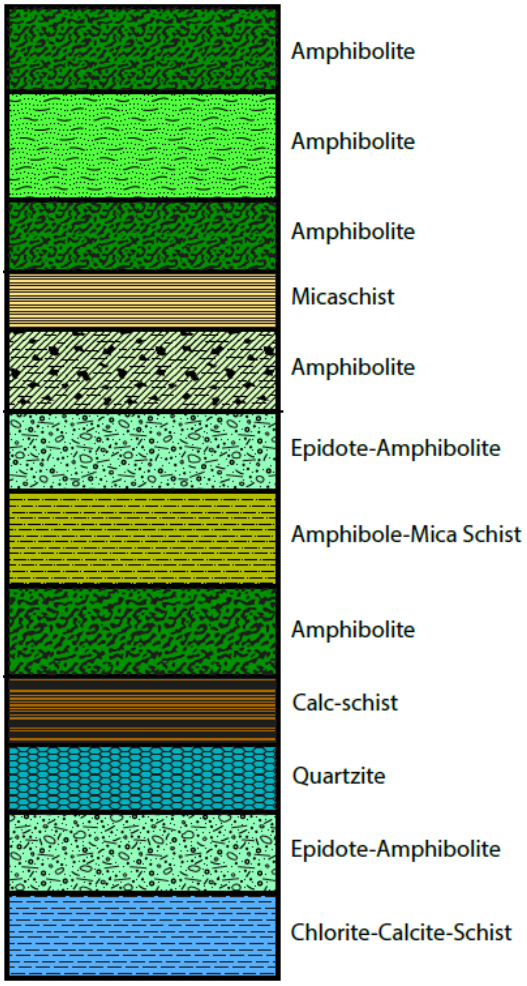

Figure 2.6. Synthetic log of the metamorphic sole rocks of the Mersin Ophiolite from tectonites (top) to ophiolitic melange (bottom) (modified from Çelik, 2008). Note that it is not in scale.

The age of the metamorphic sole rocks ranges between 96 ± 0.7 Ma and 91.6 ± 0.3 Ma (Parlak and Delaloye, 1999), based on $^{40}Ar/^{39}Ar$ results. Dilek et al. (1999) determined an age of 91.3±0.4 Ma. The most recent study in terms of dating the generation of the soles, Çelik (2008) suggested a range from 91 to 93 Ma, which is consistent with all other previous studies. Also, according to the ages of Tauride ophiolites and their metamorphic sole rocks, spreading and sole rock exhumation were almost coincident events (Morris et al., 2017).

Dilek et al. (1999) suggested that the dykes cutting cross the metamorphic sole rocks have geochemical affinities (from basalts to andesites) showing origins from the depleted mantle wedge and the dyke intrustions are simultaneous with, or just after, the initiation of an intraoceanic subduction zone. Therefore, sole rocks should have been above the generated melt at the time of the dyke intrusions, which implies that there must have been a mechanism to exhume the sole rocks from deeper sections to the top of the mantle wedge (Morris et al., 2017; Parlak, 2016).

Çelik (2008) suggested two different models to explain the generation of the metamorphic sole rocks for the Tauride Belt ophiolites. The first one implies that protoliths of the alkaline basaltic rocks formed at the overriding plate and oceanic island basalts over the subducting plate experienced amphibolite facies metamorphism while the plate was subducting. The other model suggests the existence of a second subduction zone or thrusting of another hot and young oceanic lithosphere that triggered the metamorphic activity. Parlak (2016) proposed another model (Fig. 2.7) involving N-dipping subduction inititation along a fracture zone, not at an active spreading ridge, based on the different protoliths of the sole rocks which formed due to the metamorphism of basaltic rocks (OIB-like alkaline and MORB-type) accreted to the bottom part of the overriding

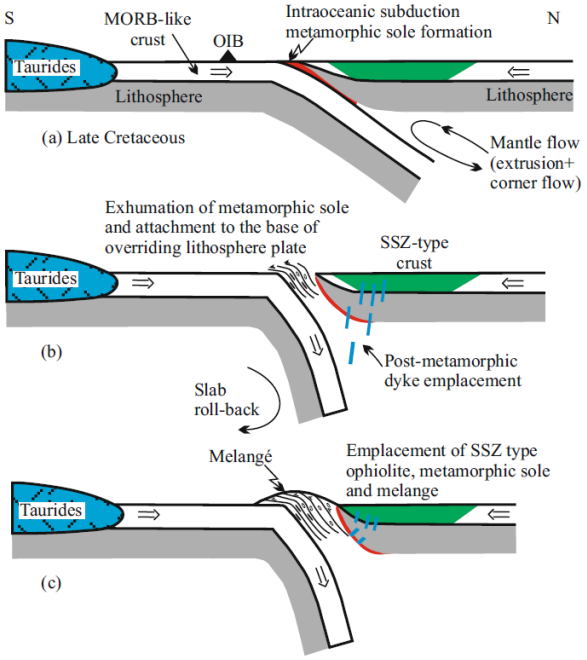

Figure 2.7. Tectonic model for the Tauride ophiolites, generation of the sole rocks and dyke intrusions (from Parlak, 2016)

plate. The old dense lithosphere rolled back, which caused the exhumation of the sole rocks and the welding to the base of the overriding plate. The most recent model for metamorphic sole formation and exhumation (in general) is that of van Hinsbergen et al. (2015) (Fig. 2.8). In this model, metamorphic sole rocks (predominantly amphibolites) are inferred to form at the top of the down-going plate during subduction initiation. The exhumation of these rocks from peak metamorphic depths involves slab flattening caused by the removal of material from the mantle wedge during fore-arc spreading. After sole rocks were welded to beneath SSZ lithosphere, the slab started steepening because of eclogitization resulting in negative buoyancy effect.

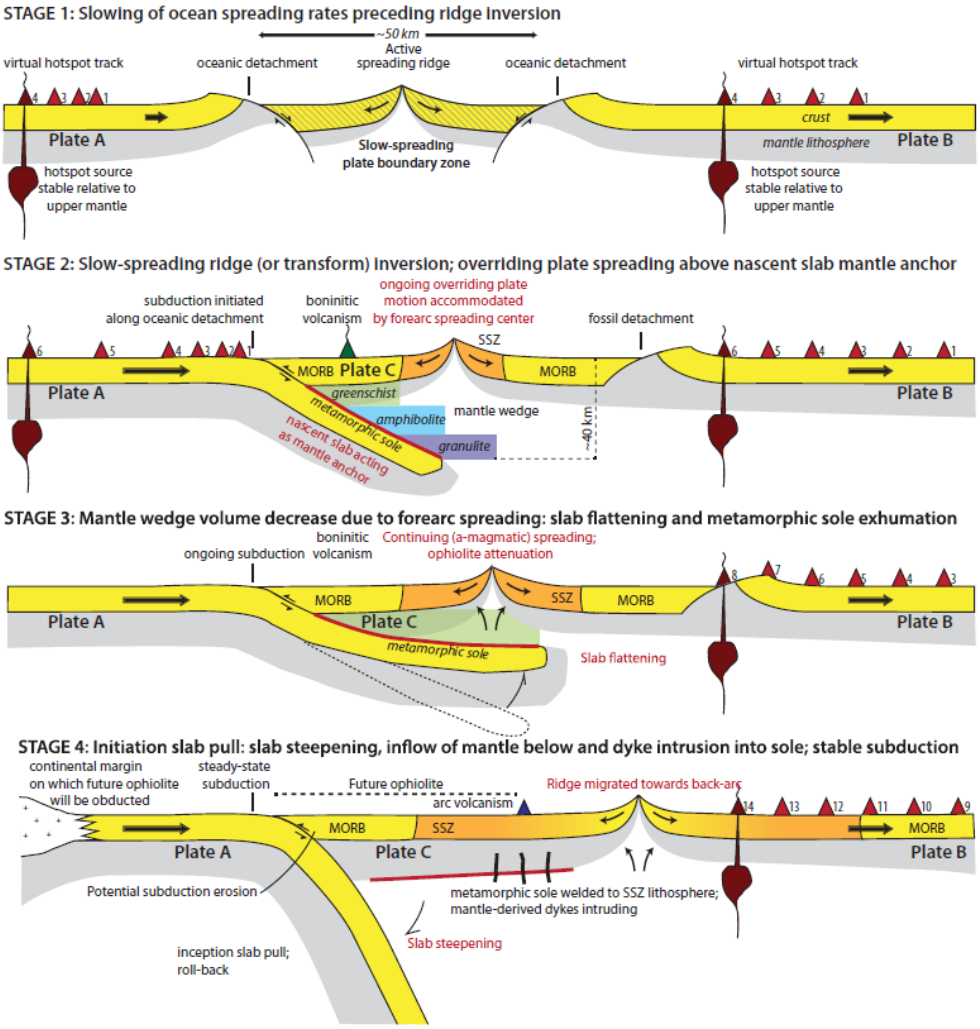

Figure 2.8. Intraoceanic subduction initiation and formation of the ophiolite with its related metamorphic sole rocks (from van Hinsbergen et al., 2015)

For each model, it is accepted by all authors that the dolerite dykes intruded into the metamorphic sole rocks after the metamorphism is finished (e.g. Dilek et al., 1999; Parlak and Delaloye, 1996; Çelik, 2008; Morris et al., 2017; van Hinsbergen et al., 2015; Parlak, 2016).

2.3.3.5 Ophiolitic mélange

The Mersin ophiolitic mélange strikes SW-NE and dips southwards at a steep angle. The mélange is located between the metamorphic sole rocks and continental margin units. The outcrop of the unit is 600 km^2 (40 km length and 15 km wide) and overlies pelagic carbonates (Parlak and Robertson, 2004). Four different assemblages have been observed in the mélange by Parlak and Robertson (2004): shallow-water carbonate association, volcanogenic-terrigenous-pelagic association, basalt-radiolarite-pelagic limestone association, and ophiolite-derived association. The units in different locations consist of shales, sandstones, conglomerates, mudstones, radiolarites, limestone blocks, gabbro, basalts, serpentinized harzburgite, fragments of sole rocks and granitic blocks (Fig. 2.9) (Parlak, 1996; Parlak and Delaloye, 1999; Parlak and Robertson, 2004). The matrix of the mélange formed during Late Cretaceous because of the sedimentary activities and tectonic developments (Parlak and Robertson, 2004).

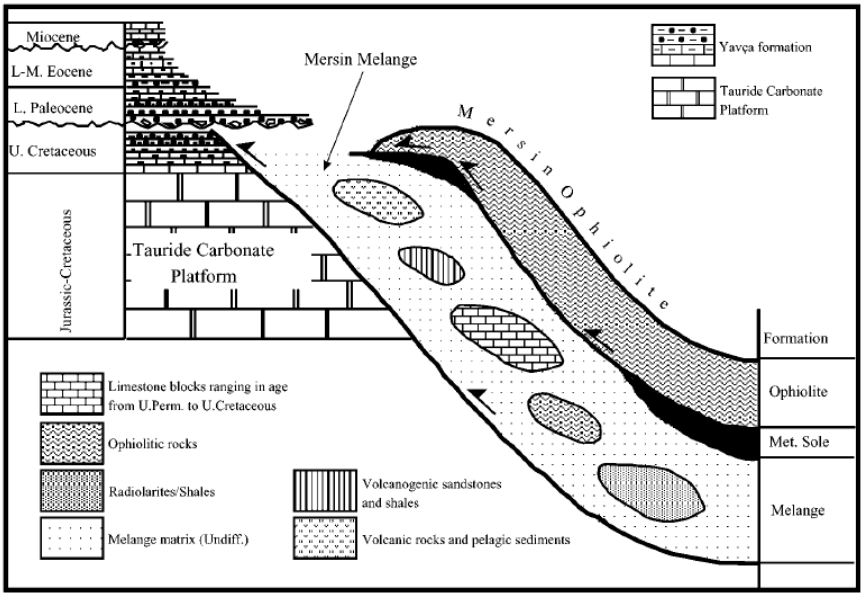

Figure 2.9. Tectonostratigraphic setting of the Mersin melange (from Parlak and Robertson, 2004)

2.4 Previous palaeomagnetic analysis of the Mersin ophiolite

Omer (2014) and Morris et al. (2017) presented the results of a palaeomagnetic study of the Mersin ophiolite, that focussed on sampling of the lower crustal gabbroic cumulates and the doleritic dykes that cut the mantle sequence and the metamorphic sole. The palaeomagnetic data were analysed using a net tectonic rotation approach (Allerton and Vine, 1987; Morris et al., 1998) that yielded estimates of the inclined axes and angles of tectonic rotation of each sampled unit. Results from the non-metamorphosed dykes cutting the sole rocks indicated a 45° clockwise rotation of the sole and dykes around an NE-trending, shallowly plunging, ridge-parallel axis. Also, palaeomagnetic analyses of the cumulate section and mantle-hosted dykes indicate larger rotations around similar shallowly plunging NE-SW directed axes (Fig. 2.10) (Morris et al., 2017).

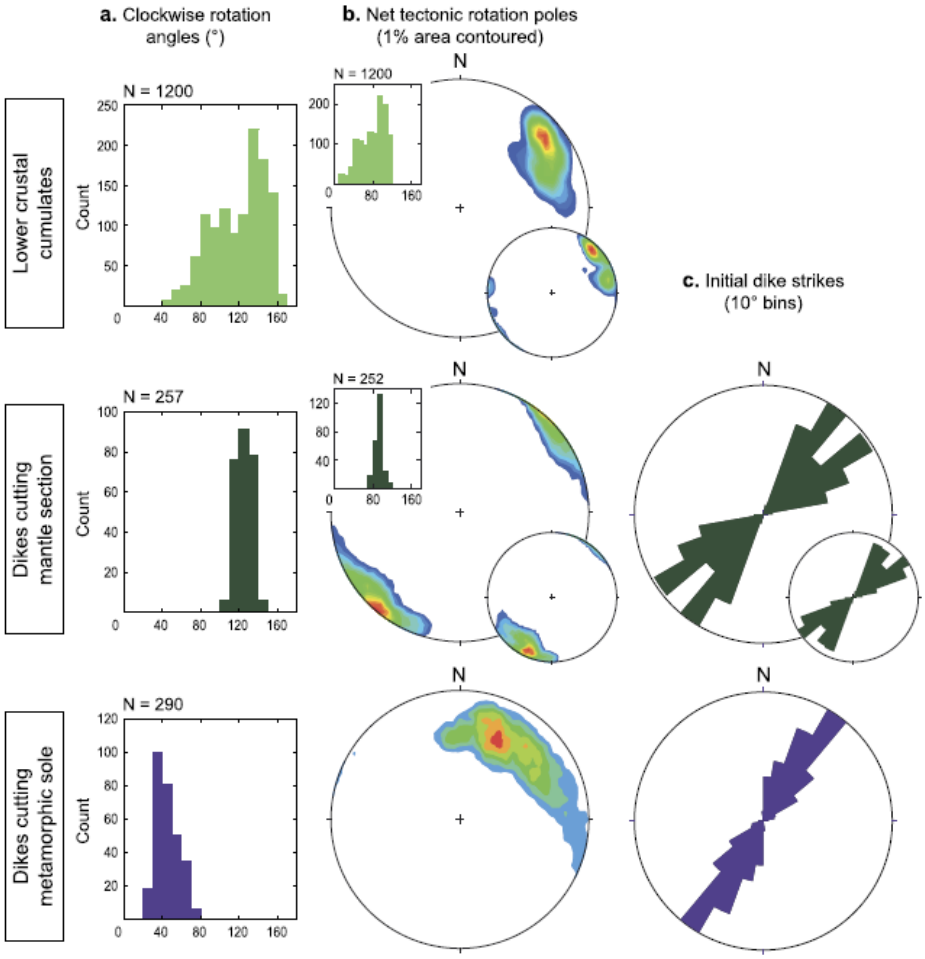

Figure 2.10. Net tectonic rotation results from the Mersin ophiolite, combining site-level preferred solutions from each lithostratigraphic unit. (a) Histograms of rotation angles; (b) contoured equal area stereographic projections of rotation axes; and (c) rose diagrams of restored initial dyke strikes (from Morris et al., 2017)

These palaeomagnetic results and net rotation analyses showing rotation around ridge-parallel, shallowly-plunging axes were interpreted as evidence for rotation of the cumulates and mantle section in the footwall of an oceanic detachment fault during detachment-mode SSZ seafloor spreading. Sole rocks were then separated from the subducting plate and welded to the bottom part of the overriding lithospheric plate because of depletion of the mantle wedge (van Hinsbergen et al., 2015). Later dykes cutting the metamorphic sole rocks experienced rotation around the same axis but with lower magnitude than cumulate rocks (Morris et al., 2017). These rotations occurred via a common mechanism in a pre-obduction, fore-arc setting, and are best explained by combining (hyper)extension resulting from detachment-mode, amagmatic supra-subduction zone spreading in a fore-arc environment with a recently proposed mechanism for the exhumation of metamorphic soles driven by upper plate extension (Morris et al., 2017).

2.5 Fundamentals of magnetism, magnetic terms and parameters

2.5.1 Earth's magnetic field

The Earth's magnetic field is generated by the motion of the electrically conducting liquid iron of the outer core via a self-exciting dynamo process (McElhinny and McFadden, 1999). This produces a simple external field geometry that approximates that of an axial geocentric dipole, when averaged over time periods > 10^5 years (Fig. 2.11).

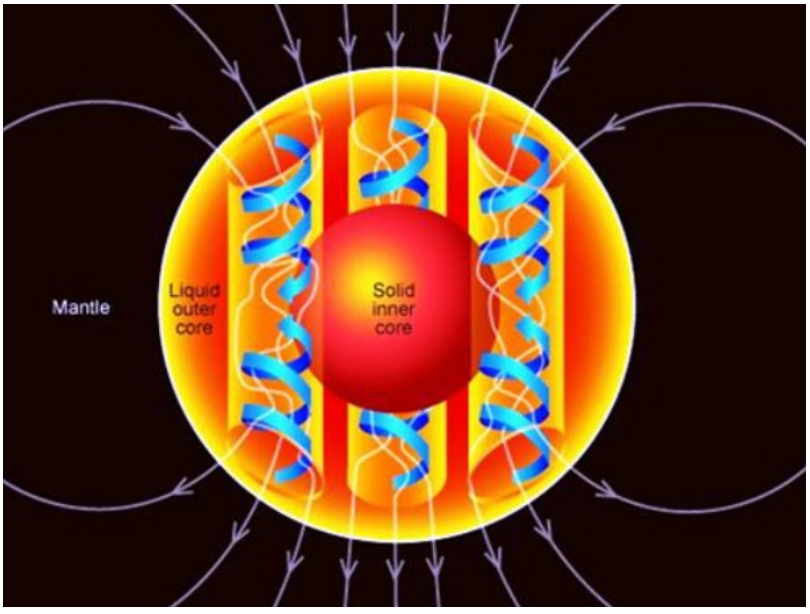

Figure 2.11. Convection currents in the Earth's outer core generate a dipolar geomagnetic field (from Reeve, 2010)

At the Earth's surface, the geometry of the geomagnetic field is described by the declination which is the angle from geographic north to the horizontal field component (ranging from 0° to 360°) and the inclination that is the angle between the horizontal and the geomagnetic field lines (ranging from -90° to 90°) (Butler, 1992). These angles are also used to specify the direction of the palaeomagnetic record of past field directions preserved in studied rocks (Fig. 2.12).

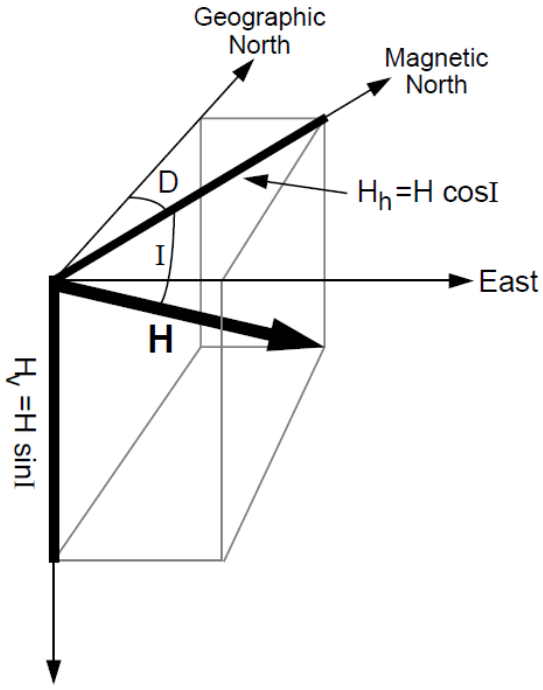

Figure 2.12. Diagram illustrating the geometry of the geomagnetic field (from Butler, 1992)

On shorter timescales, the geomagnetic field varies from that of a simple dipole as a result of palaeosecular variation (PSV) related to the presence of non-dipole field components. Palaeomagnetic studies need to average out PSV in order to determine magnetization directions that can be interpreted using the longer-term geocentric axial dipole (GAD) model (Fig. 2.13). According to this model, the inclination (I) of the field is related to the latitude (λ) by the equation: tan (I) = 2tan (λ) (Butler, 1992).

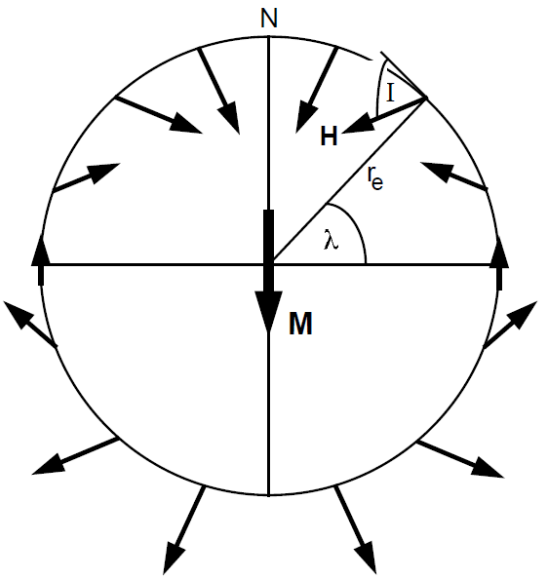

Figure 2.13. Diagram showing the geocentric axial dipole model (from Butler, 1992)

Studies at the beginning of the 20th century showed that the natural remanent magnetization (NRM) of some samples from lava flows had inclinations of the opposite sign to that expected from their hemisphere of formation, indicating that the geomagnetic field had reversed its polarity periodically in the geological past (McElhinny and McFadden, 1999). Normal polarity is defined as the field geometry that we see during the present day with the north/south geomagnetic poles near to the north/south geographical poles (rotation axis of the Earth), whereas reversed polarity periods are marked by an inversion of the geomagnetic poles relative to the geographical ones (Fig. 2.14).

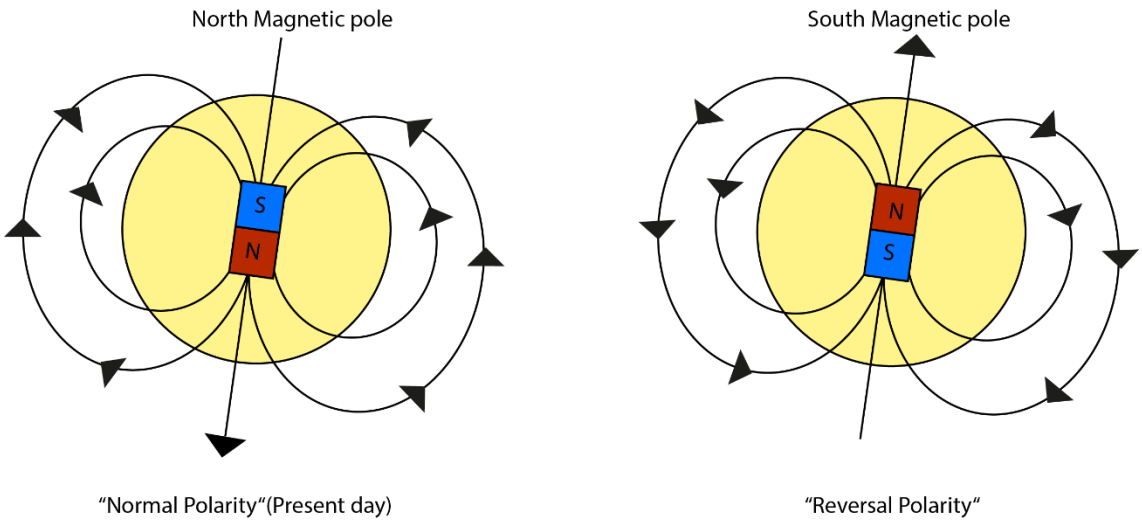

Figure 2.14. Normal and reversed magnetic polarity

2.5.2 Magnetic Behaviours

The origin of magnetism is based on orbital and spin movements of the electrons and their interactions. The best way to distinguish the different types of magnetism is understanding the reactions of materials to applied magnetic fields. All materials show magnetic behaviour at the atomic level but some materials respond more than the others to applied fields due to stronger interactions between atomic magnetic moments. These responses are classified into three main different categories (Butler, 1992):

1. Diamagnetism
2. Paramagnetism
3. Ferromagnetism

Magnetic susceptibility, χ or k, is the constant that relates the induced magnetization (J) in a substance to intensity of the applied inducing field (H), such that $J = \chi H$. Diamagnetic materials (such as quartz and calcite) acquire a very weak induced magnetization in the presence of an applied field in the opposite direction to the field. They therefore have a negative magnetic susceptibility (χ) (i.e. a negative gradient in Fig. 2.15). This magnetization is not permanent and disappears in the absence of an inducing field (Butler, 1992).

Paramagnetic materials have a positive magnetic susceptibility and respond to an applied field by acquiring an induced magnetization parallel to the field direction, that again disappears in the absence of an inducing field (Fig. 2.15) (Butler, 1992). Hornblende, biotite, pyroxene and fayalite are some examples of paramagnetic minerals (Tarling and Hrouda, 1993).

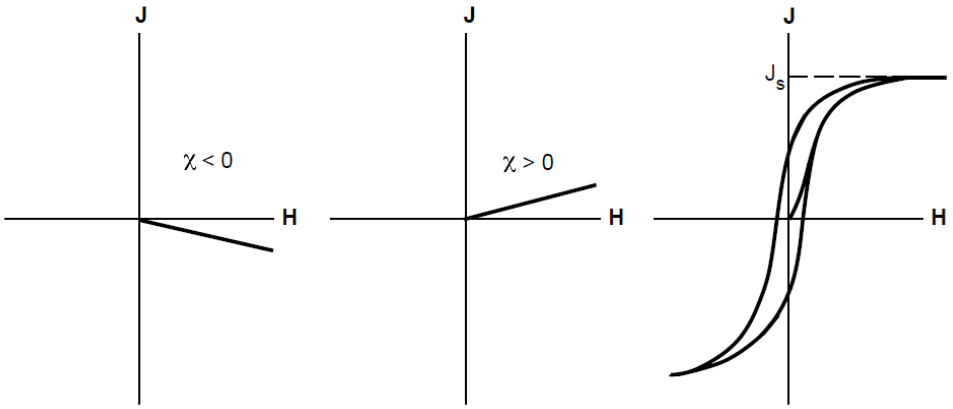

Figure 2.15. Magnetization (J) vs. magnetizing field (H); (left) negative susceptibility (diamagnetic materials), (middle) positive susceptibility (paramagnetic materials), (right) magnetic susceptibility is not constant (ferromagnetic minerals) (from Butler, 1992).

Unlike paramagnetic substances, ferromagnetic materials produce strong interactions between the atomic moments of adjacent atoms. These interactions are produced by powerful electron exchange interaction forces. Even in the absence of a magnetic field, these substances produce large net magnetizations, which means that magnetization does not return to zero after removal of the magnetic field. Fe, Ni and Co elements and their alloys are typical ferromagnetic elements. Of these, the iron oxides magnetite and hematite are the two most important minerals in palaeomagnetism, recording the direction of the geomagnetic field at the time of their formation.

If ferromagnetic grains are abundant enough in the volume of the whole rock, they become dominant and control the magnetic characteristics, including the anisotropy of magnetic susceptibility.

2.5.3 Magnetic Domains

In grains of ferromagnetic materials, the internal magnetization organizes itself into regions of uniform magnetization known as domains, in order to minimize the magnetic energy of each grain. The domain state is principally controlled by grain size but also by shape (Butler, 1992). Single domain (SD) grains have a uniform internal saturation magnetization, that is aligned along the long axes of non-equant grains as a result of shape anisotropy. In larger grains a critical level is reached that causes internal magnetization to reorganise into two domains via the nucleation of a domain wall (McElhinny and McFadden, 1998). If the domains are aligned oppositely after

division, the magnetostatic energy (the self-energy of the grain produced by its magnetization) decreases and the grain obtains a minimum energy state.

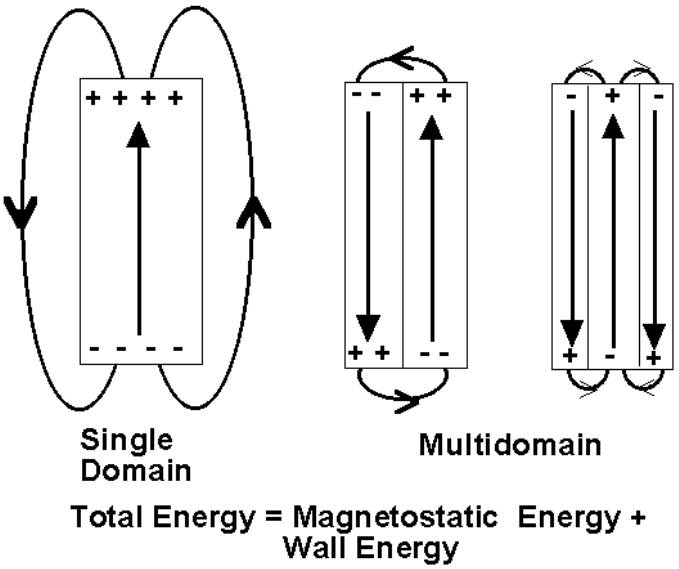

Figure 2.16. Schematic diagram illustrating formation of domains. Arrow shows the direction of magnetization (from Moskowitz, 1991)

This subdivision may continue as long as the energy required to form a new wall is lower than the consequent reduction in magnetostatic energy. SD magnetite particles of cubic shape have diameters < 0.1μm, and the elongated ones might be 1 μm in length (Butler, 1992). Multi-domain (MD) magnetite grains have diameters > 10 μm (Butler, 1992). Between these size limits, grains have more complex pseudo single domain (PSD) structures (Butler, 1992).

2.5.4 Curie temperature

Temperature is one a key factor that affects most characteristics of matter, including a loss of magnetization. If the temperature of a solid matter is increased, the magnitude of thermal vibration of atoms increases, reducing their ability to interact magnetically to produce stable magnetizations. Eventually, magnetic moments are no longer able to interact and all magnetization is lost at a critical temperature known as the Curie temperature. Above the Curie temperature, materials behave paramagnetically (Butler, 1992). All ferromagnetic minerals and elements have characteristic Curie temperature values greater than 0 K (Table 2.1).

Table 2.1. Curie temperature values of some of the magnetic minerals that occur in rocks together with their magnetic state (modified from McElhinny and McFadden, 1999)

Mineral	Composition	Magnetic state	Curie temperature T_C (°C)
Magnetite	Fe_3O_4	Ferrimagnetic	580
Titanomagnetite	$Fe_{2.4}Ti_{0.6}O_4$	Ferrimagnetic	150
Hematite	αFe_2O_3	Canted antiferromagnetic	675
Ilmenite	$FeTiO_3$	Antiferromagnetic	-233
Maghemite	γFe_2O_3	Ferrimagnetic	590-675
Pyrrhotite	$Fe_{1-x}S$ $(0<x\leq 1/8)$	Ferrimagnetic	320
Goethite	αFeOOH	Antiferromagnetic with defect ferromagnetism	120
Iron	Fe	Ferromagnetic	765
Cobalt	Co	Ferromagnetic	1131
Nickel	Ni	Ferromagnetic	358

2.5.5 Relaxation time and blocking temperature

Magnetic relaxation is the decay of remanent magnetization of grains within time. SD grains with short relaxation time are called superparamagnetic and are magnetically unstable. Every material has different critical relaxation time (τ_s). For magnetite, a grain with a width:length ratio is 0.2, length is 0.04 μm, and relaxation time is 100 seconds, is at the superparamagnetic threshold (Butler, 1992).

When magnetite grains reach at 575°C, the relaxation time is less than 1 microsecond. If τ_s.=100 s is considered as critical time, grains begin to behave as stable single domain rather than superparamagnetic at 550°C (Butler, 1992). Between the Curie point and this blocking

temperature, the material behaves superparamagnetic. The material is considered as stable single domain if $T<T_B$ (Fig. 2.17).

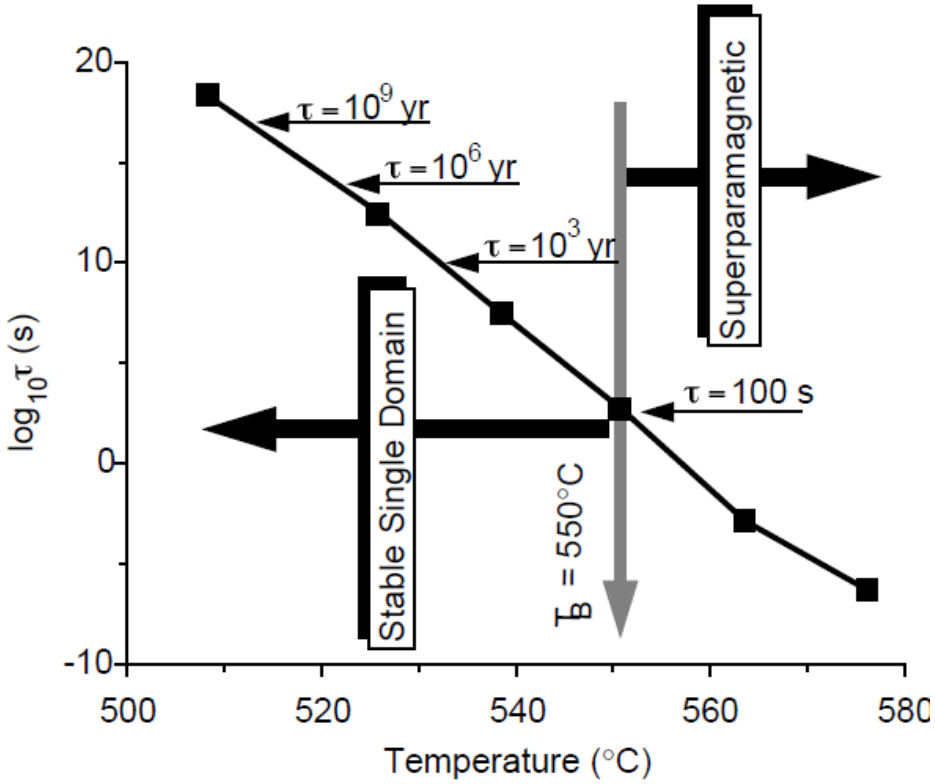

Figure 2.17. log10 τ(s) vs Temperature(C°) plot of single domain magnetite grain ; Superparamagnetic behaviour when T>550°C and stable τ>100s while $T<T_B$ (from Butler, 1992)

2.6 Magnetic minerals

Magnetic minerals are accessory minerals in rocks. Magnetite and hematite form members of solid solution series that may be represented on a ternary diagram displaying proportions of iron oxides and titanium oxides with apexes of FeO (Wüstite), TiO_2 (Rutile), and Fe_2O_3 (Hematite) (Fig. 2.18).

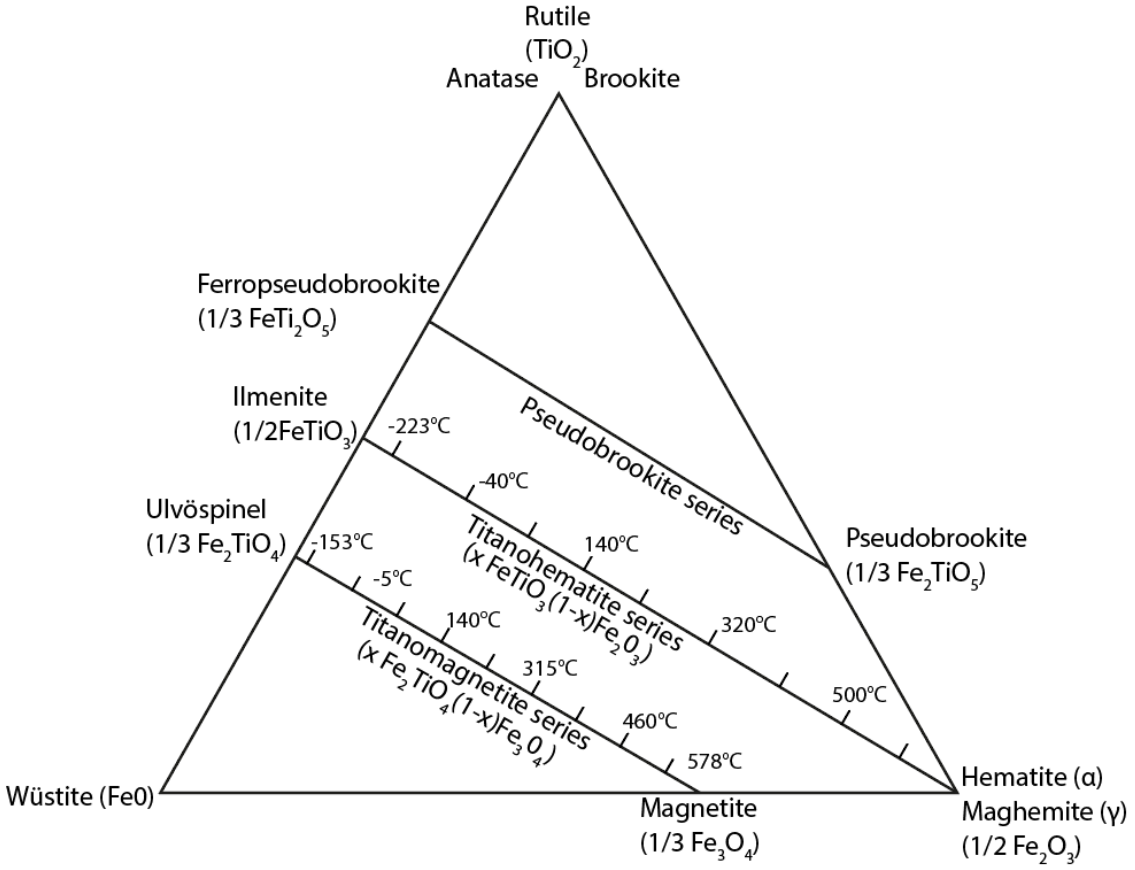

Figure 2.18. Ternary diagram displaying the series between FeTi Oxides, also showing the Curie temperatures for different compositions (modified from McElhinny and McFadden, 1999)

The most common magnetic mineral in rocks is magnetite (1/3 Fe_3O_4). Increase or decrease in the Fe and Ti proportions causes variations in the solid solution series. There are two important series in the system, which are titanomagnetite and titanohematite series. Curie points of intermediate members of these solid solution series decrease as the titanium content increases (Butler, 1992). Both titanohematites and titanomagnetites form solid solution series at high-temperature levels, but exsolve into intergrowths of different phases low temperatures (Merrill and McFadden, 1999). If magnetite is oxidized at low-temperature grades (less than 200°C; Merrill and McFadden, 1999), maghemite formation can be observed (Tarling, 1971).

Titanomagnetite and titanohematite series form in the early crystallization of igneous rocks at 1300°C and cooling rate plays a fundamental role for grain size distribution of Fe-Ti oxides. For example, grain sizes are less than 1 μm in pillow lavas (usually the ones with titanomagnetites)

due to rapid cooling after the lava comes across to water (Butler, 1992). 100 μm grains can be observed in the rocks which formed with slow cooling rates.

2.7 Acquisition of magnetization

Rocks usually acquire a magnetization parallel to the ancient geomagnetic field at the time of formation and this is called a primary magnetization. The conditions during the formation of the rock and acquisition of magnetization determine the kind of remanence. Igneous rocks acquire a thermoremanent magnetization (TRM) during cooling through the Curie and blocking temperatures. Metamorphic rocks may acquire a TRM during cooling from peak metamorphic temperatures, but may also acquire a chemical remanence (CRM) during growth of new ferromagnetic grains. Sedimentary rocks acquire a depositional remanent magnetization (DRM) during or shortly after initial deposition. In addition, rocks may also acquire secondary components of magnetization during their subsequent history, e.g. because of the alteration affecting the ferromagnetic minerals, lighting strikes or long-term exposure to the geomagnetic field (Butler, 1992). Hence, the natural remanent magnetization (NRM) of a rock is the vector sum of the primary and secondary components.

TRM is the natural remanent magnetism formed after cooling from above the Curie temperature. It is observed in most igneous rocks. Spontaneous magnetization is acquired during the cooling at the Curie point, however, individual ferromagnetic grains behave superparamagnetically until they cool below their blocking temperatures, when they experience a drastic increase in relaxation time and their magnetization is locked in (Butler, 1992; McElhinny and McFadden, 1999). Distributions of ferromagnetic grain sizes in the cooling rock result in distributions of grain blocking temperatures, which means that not all of the thermoremanent magnetization is acquired at the Curie temperature. This acquired magnetization stays stable over the million years as long as the acquisition is due to primary cooling (Butler, 1992). Below Curie temperature, magnetization is acquired within cooling intervals. Every interval is called partial thermoremanent magnetization (PTRM). Because the PTRM acquired in each interval is not affected by the field applied at the following intervals on cooling, the total net thermoremanent magnetization is equal to the sum of partial thermoremanent magnetizations. Thellier (1938)

called this the law of additivity (McElhinny and McFadden, 1999). This process is of fundamental importance for palaeomagnetism. During the conditions of $T<T_c$, heating a rock to a temperature T in a zero field environment in the laboratory results in unblocking of grains with blocking temperature < T and these grains become effectively demagnetized. This allows the progressive thermal demagnetization of samples to remove secondary magnetizations that typically have unblocking temperatures less than the primary TRM.

Chemical remanent magnetism (CRM) is acquired when new ferromagnetic minerals form in a rock in the presence of a magnetic field because of alteration, metamorphism or precipitation of ferromagnetic minerals from solution (Butler, 1992; Tauxe et al., 2013). Each individual grain starts growing from zero volume at constant temperature. Grains with smaller volume have lower relaxation times, with relaxation time significantly increasing during grain growth. In this way, superparamagnetic grains become stable single domain grains and acquire stable magnetizations as a CRM when they reach a blocking volume (Butler, 1992). Also, almost all of the CRM formation is related to applied field (McElhinny and McFadden, 1999). The main problem could be faced with CRM is that coercivities generally overlap with the unblocking temperatures.

Finally, isothermal remanent magnetization (IRM) is acquired when rocks are exposed to applied fields higher than the coercive force of their ferromagnetic grains. This can occur naturally if lightning strikes close to a rock formation, causing partial or entirely remagnetization of the rock (Tauxe et al., 2013). In the laboratory, IRMs may be imparted to specimens by exposing them to a pulsed direct magnetic field, providing information on the nature of remanence carrying minerals in the rocks.

2.8 Anisotropy of magnetic susceptibility

Anisotropy of magnetic susceptibility (AMS) is a measure of the directional dependency of magnetic susceptibility (Morris, 2003). There are two factors affecting the magnetic anisotropy of rocks. These are: (1) lattice preferred alignment of crystals with magneto-crystalline anisotropy; and (2) shape anisotropy of ferromagnetic grains. Hence AMS reflects the preferred alignment of grains in a rock and can provide information about the geological processes

operating during their formation and deformation. This can be the direction of emplacement in lavas, the palaeocurrent direction in sediments or ductile deformation patterns in metamorphic rocks (Morris, 2003; Tarling and Hrouda, 1993). The rocks are called anisotropic if the susceptibility differs in the separate directions. These differences are described by a second order tensor that may be represented by an anisotropy ellipsoid with three orthogonal principal axes as maximum, intermediate and minimum. If $K_{max}=K_{int}=K_{min}$, the magnetic susceptibility is isotropic and no fabric is present. If $K_{max}\geq K_{int}>K_{min}$, the ellipsoid is oblate (disc-shaped). If $K_{max}>K_{int}\geq K_{min}$, the ellipsoid is prolate (cigar-shaped). The magnetic foliation is represented by the plane containing K_{max} and K_{int}, with K_{min} representing the pole to the magnetic foliation plane. Furthermore, K_{max} represents the magnetic lineation (Mamtani et al., 2017). For example, oblate shaped susceptibility ellipsoids are generally found in sedimentary rocks and highly foliated metamorphic rocks, which implies K_{min} is perpendicular to the foliation or bedding plane. Also, prolate shaped susceptibility ellipsoids are commonly observed in lava flows and sedimentary current deposits, where K_{max} alignment is parallel to palaeo-flow direction (Morris, 2003). When $K_{max}>K_{int}>K_{min}$ this represents a triaxial ellipsoid shape (Fig. 2.19).

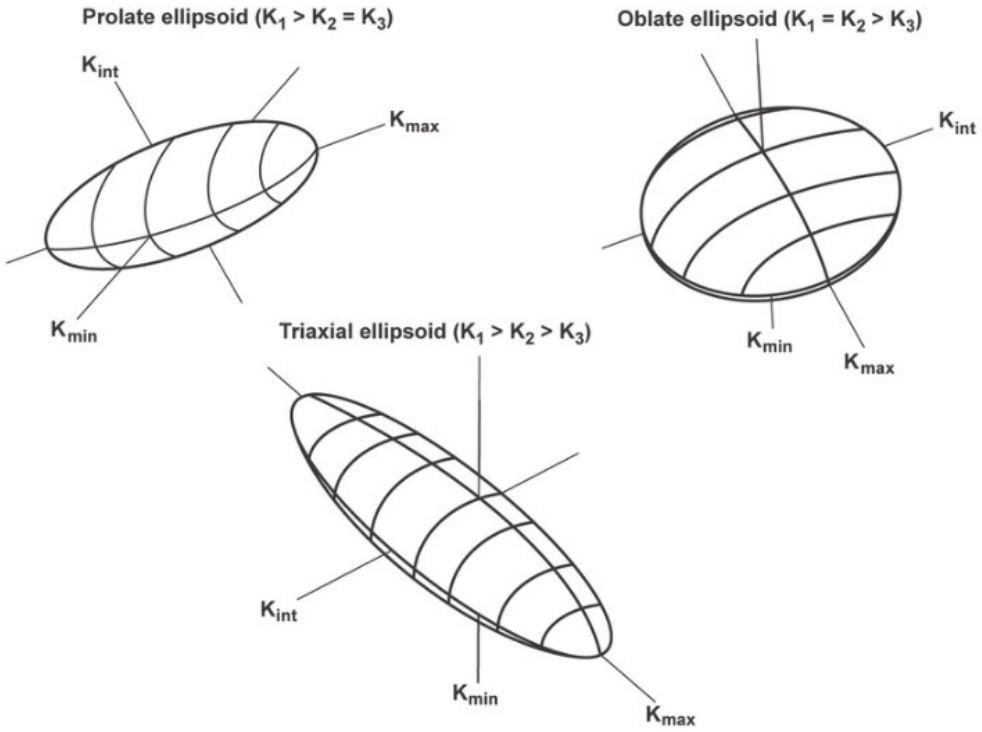

Figure 2.19. Schematic figures illustrating the prolate shape ($K_{max}>K_{int}=K_{min}$), oblate shape ($K_{max}=K_{int}>K_{min}$) and triaxial shape ($K_{max}>K_{int}>K_{min}$) ellipsoids (from O driscoll, 2006)

Chapter 3- Methodologies

3.1 Magnetic methodologies

3.1.1 Sampling and palaeomagnetic sampling

For this study, the Fındıkpınarı road section where the metamorphic sole rocks of the Mersin ophiolite are well-exposed was chosen for sampling. Instead of collecting samples using a portable drill with a water-cooled diamond bit (requiring transportation of bulky field equipment to Turkey), oriented block hand samples were collected that were later drilled and cut using equipment in the laboratory. Two samples from metamorphic sole hosted dykes and 30 samples from metamorphic sole rocks were collected at a series of sites distributed along the exposed section (Fig 3.1). The dip and dip direction data were also collected for each sample during the fieldwork. Strike and lineation lines (if observed) were drawn on the top surface in the field (Fig. 3.2a). During the laboratory preparation, lines perpendicular to the strike lines were drawn on the field oriented surface, with tick marks pointing in the up-dip direction (Fig. 3.2b). The block samples were drilled (Fig. 3.2c) perpendicular to the surface. Fiducial lines were then drawn along the length of the cores by extending the parallel lines. The hade (angle from the vertical) of the core fiducial line is then the same as the dip of the top surface and the core azimuth is the specimen's dip direction ± 180°. Cores were then finally cut by using a dual blade rock saw to produce standard specimens ~22 mm in length (Fig. 3.2d, f). Off-cuts of cores were retained for use in rock magnetic experiments (Fig. 3.2e). Eventually, 111 core specimens (14 from dykes and 97 from the metamorphic sole rocks) were obtained (Fig. 3.2f). The orientation system for specimens is shown in figure 3.3.

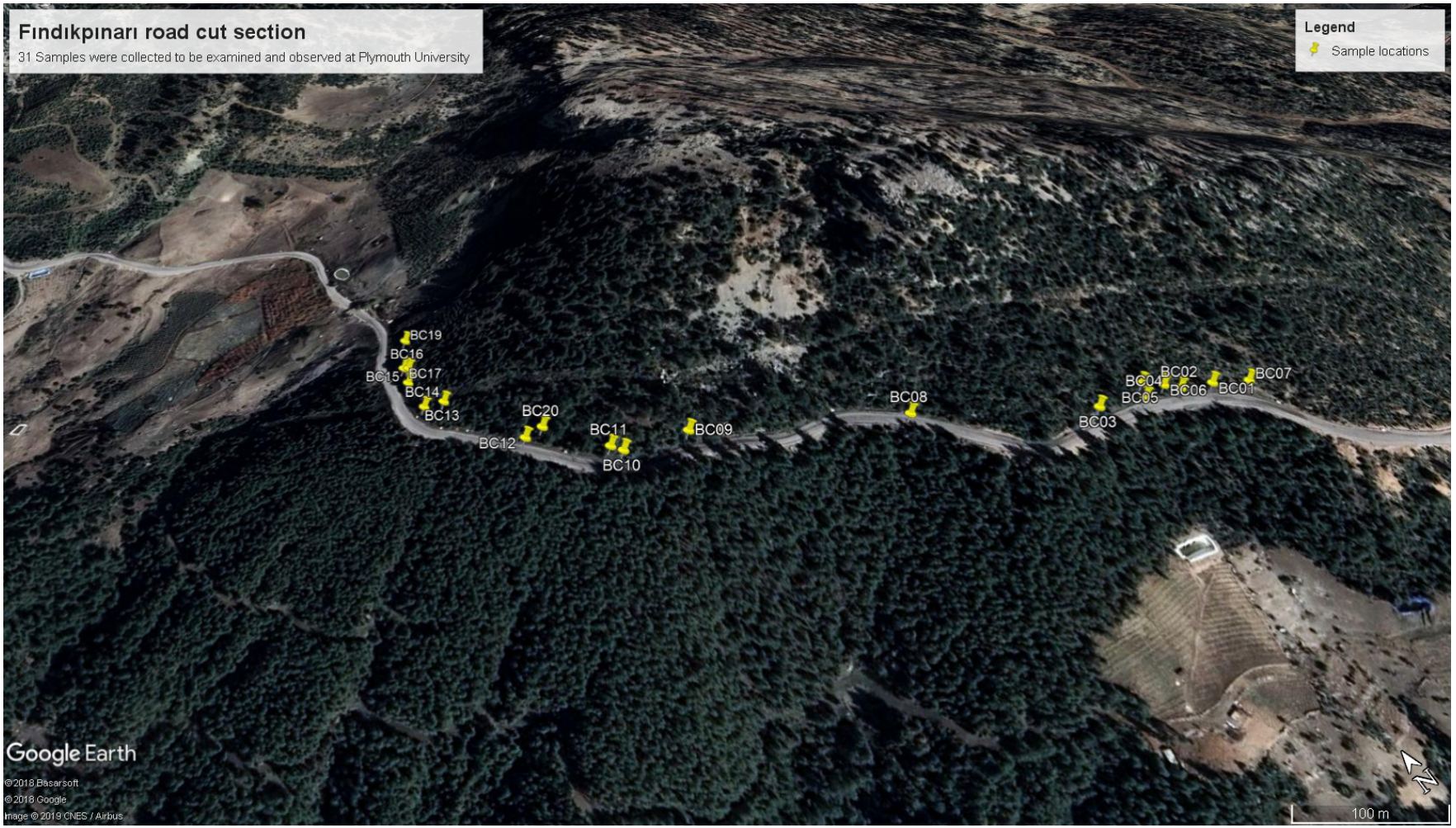

Figure 3.1. Google Earth image indicating the sampling locations at the Fındıkpınarı road cut section

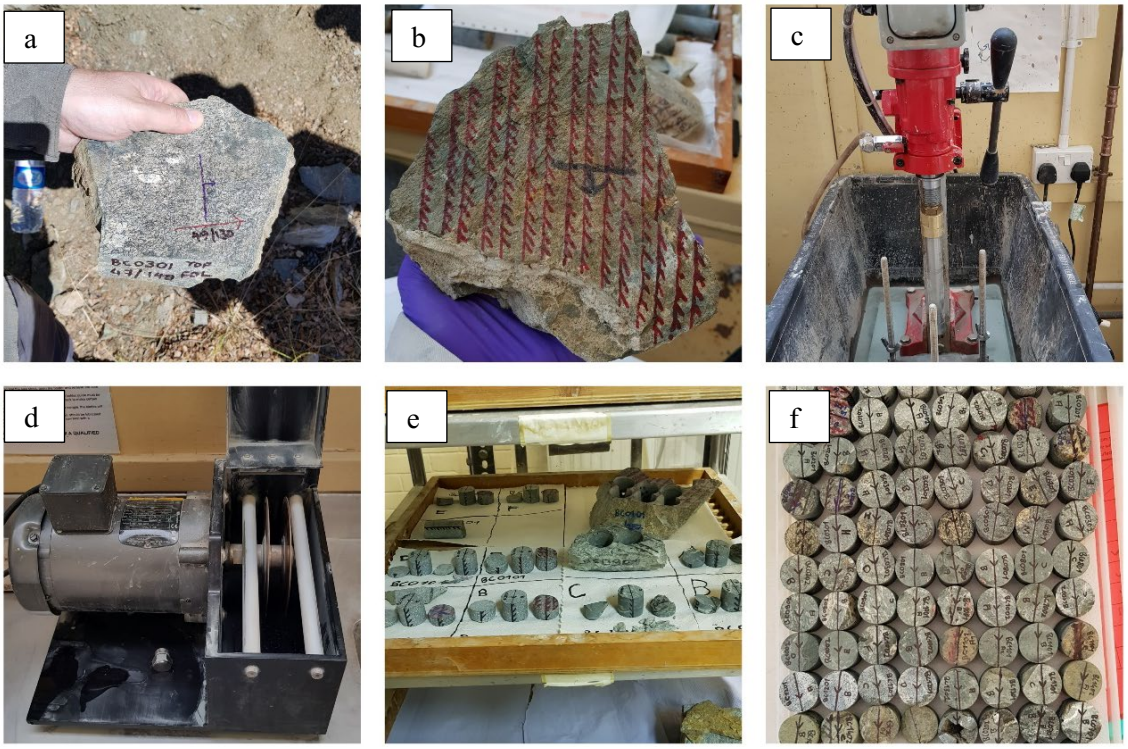

Figure 3.2. (a) Hand sampling from Fındıkpınarı road cut section, (b) Lines perpendicular to the strike and arrows showing the up-dip direction, (c) Used drilling equipment, (d) Dual blade rock saw, (e) Weathered surfaces removed, (f) Core specimens after necessary practises

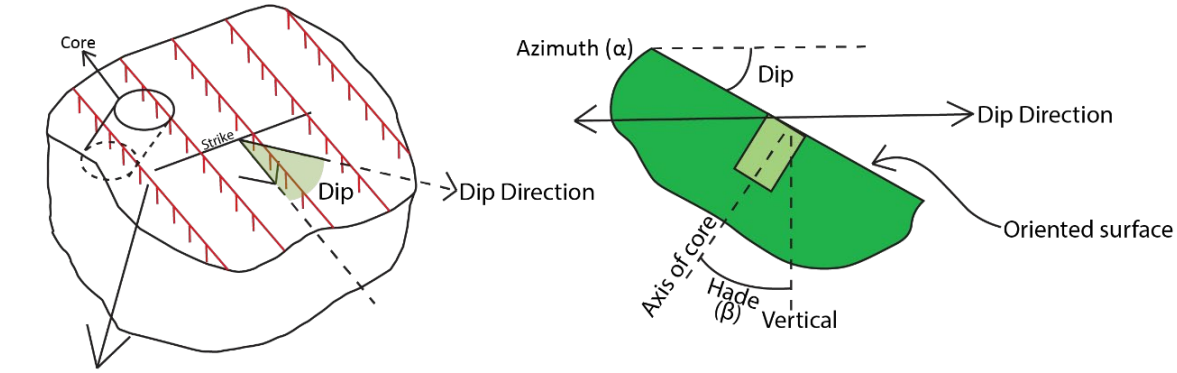

Figure 3.3. Illustration of the orientation of cores drilled from hand samples. First drawing illustrates the red lines drawn parallel to dip direction with arrows pointing up-dip. Second drawing shows the relationship between core azimuth and hade angles

3.1.2 Natural remanent magnetization (NRM) measurements

NRM is the vector summation of magnetization components acquired during different times because of various geological processes. After acquiring a primary NRM during the formation of a rock, secondary NRM components might be subsequently acquired because of processes such as metamorphism, hydrothermal alteration, and long-exposure to the geomagnetic field.

Figure 3.4. JR-6 Dual speed spinner magnetometer

NRM measurements were performed by using an AGICO JR-6 dual speed spinner magnetometer in the University of Plymouth Palaeomagnetic Laboratory (Fig. 3.4) that can measure in the range of 10^{-6}-10^{4} A/m.

3.1.3 Anisotropy of magnetic susceptibility (AMS) measurements

AMS measurements were conducted by using an AGICO KLY-3 Kappabridge (Fig. 3.5) in the University of Plymouth Palaeomagnetic Laboratory, before the demagnetization process. The SUSAR program was used to collect and process the data. The azimuth and hade of each specimen was inputted into the SUSAR software before initializing the measurement. Each specimen was measured in three different positions in order to collect data to define the complete anisotropy ellipsoid (Fig. 3.6). The bridge is automatically zeroed after putting the specimen into the measuring coil. Then, susceptibility variations are measured by spinning the specimen in each position, which provides sensitive determination of each anisotropic component of the susceptibility tensor. The complete AMS tensor was found by the combination of three

measurements in different directions and one bulk susceptibility measurement. The SUSAR software then combined the results and calculated the AMS ellipsoid for each core specimen. The results gave the principal directions (maximum, intermediate, and minimum) of the AMS ellipsoid in both specimen and geographic reference frames. The software also calculated anisotropy factors and parameters for each specimen. These are lineation ($L=K_{max}/K_{int}$), foliation ($F=K_{int}/K_{min}$), P_j (anisotropy degree) and T (shape parameter).

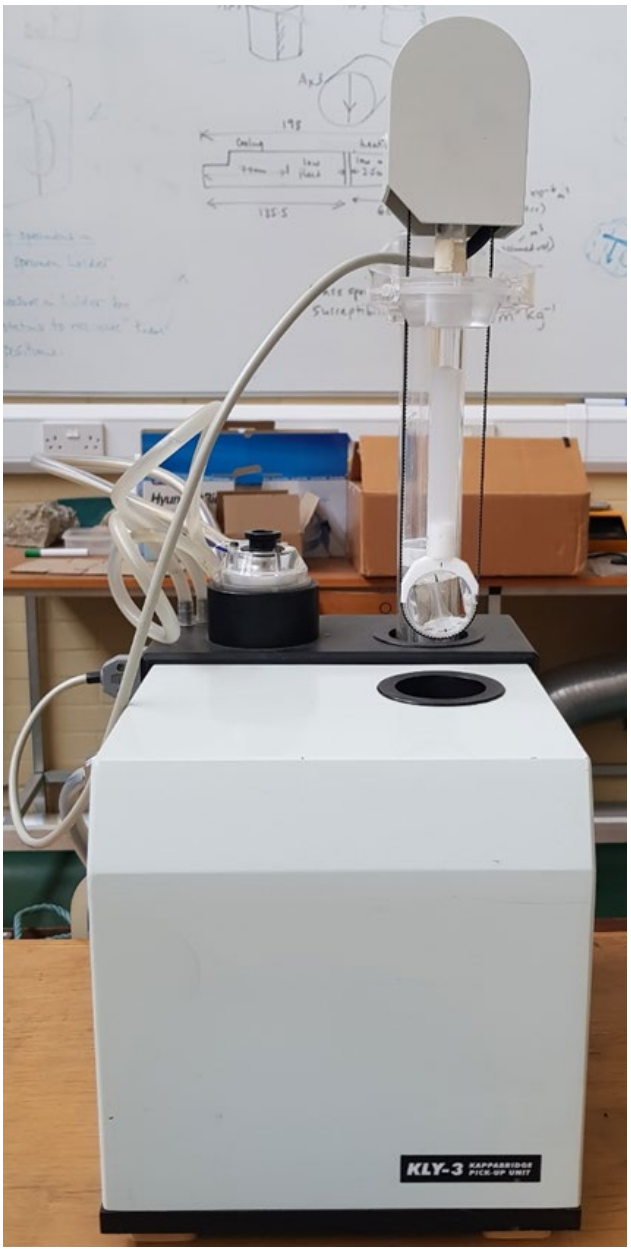

Figure 3.5. AGICO KLY-3 Kappabridge

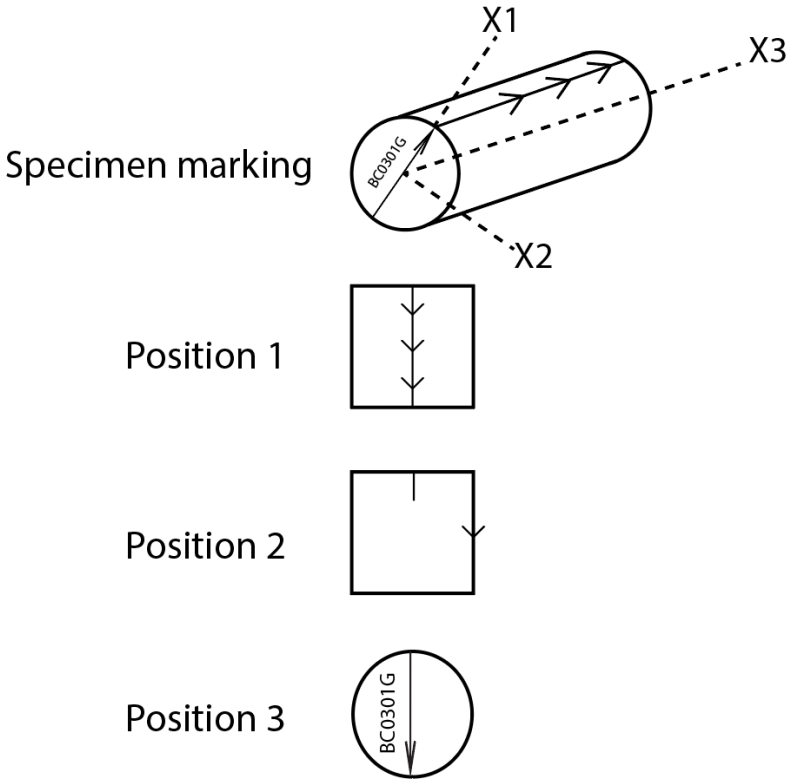

Figure 3.6. Three different positions for the AMS measurement of each specimen

The corrected anisotropy degree (P_j) (Jelinek, 1981) indicates the strength of the anisotropy. P_j = 1.0 represents an isotropic susceptibility. P_j values greater than 1.0 indicate presence of anisotropy, with, for instance, P_j = 1.14 indicating 14% anisotropy. For the P_j calculation, the equation used by the program is;

$$\ln(P_j) = \sqrt{2[\left(\ln\left(\frac{K_{max}}{K}\right)\right)^2 + \left(\ln\left(\frac{K_{int}}{K}\right)\right)^2 + \left(\ln\left(\frac{K_{min}}{K}\right)\right)^2}$$

The shape parameter (T) describes the shape of the ellipsoid, which is oblate (disc-shaped) when $0 < T \leq 1$ and prolate (cigar-shaped) when $-1 \leq T < 0$. If T is close to zero, the shape is a neutral ellipsoid (plane-strain). For the T calculation, this equation used by the program is;

$$T = \frac{\ln(L) - \ln(F)}{\ln(L) + \ln(F)}, where\ F = \frac{K_{int}}{K_{min}}\ and\ L = \frac{K_{max}}{K_{int}}$$

Both of the equations show that all of the principal directions are used to calculate the parameters, which makes results reliable. AGICO-ANISOFT v. 4.2 and 5.0 softwares were used to plot all the measurements obtained from the Kappabridge device i.e. principal directions, T and P_j plots .

The Jelinek plot (Fig. 3.7) indicating the relationship between the corrected anisotropy degree and shape parameter is given below with an example from the metamorphic sole-hosted dykes of the Mersin ophiolite.

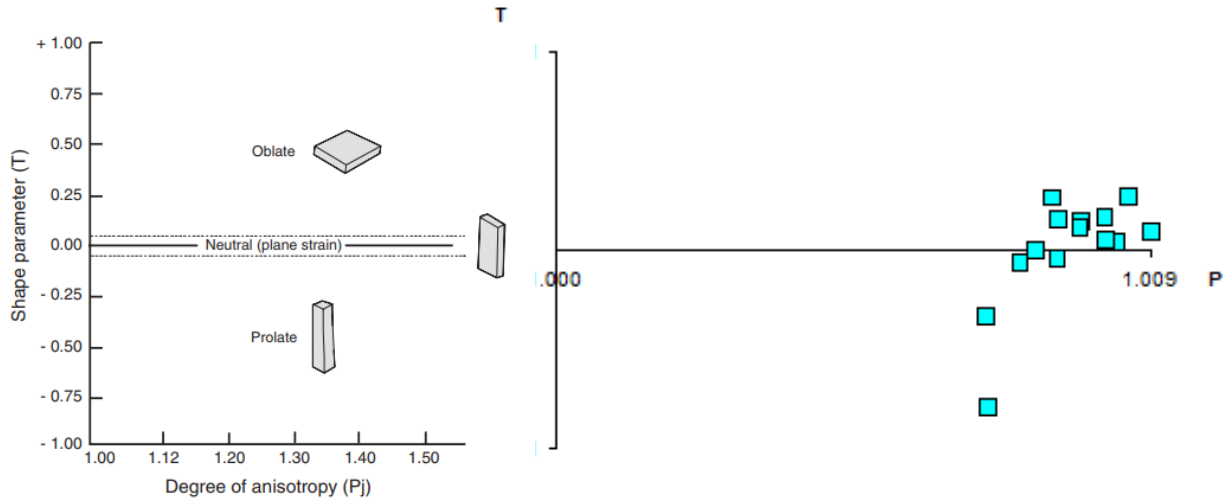

Figure 3.7. Degree of anisotropy (P_j) vs. Shape parameter (T) and an example from Mersin ophiolite sole-hosted dykes indicating mostly oblate shape for the magnetic carriers

3.1.4 Demagnetization techniques and procedures

As described above, the natural remanent magnetization (NRM) of a rock represents the sum of all magnetic components during a rock's history. However, the main aim of palaeomagnetic analyses is to find the earliest component, defined as the characteristic remanent magnetization (ChRM), for geological interpretation. That direction represents the geomagnetic field at the time of acquisition of the magnetization. Therefore, low stability secondary magnetizations (usually carried by the lowest coercivity or blocking temperature grains) needed to be removed. For this purpose, there are two different techniques. One of them is alternating field (AF) demagnetization and the other one is thermal demagnetization. It is quite important to choose the best one for the demagnetization process. Mineralogy and magnetic history are the most important controlling factors to decide the technique (Butler, 1992). For example, the average coercivity values of magnetite and titanomagnetite minerals are less than hematite. Magnetite has a maximum coercivity of 0.3 T whereas hematite grains have coercivities of 1.5 – 5.0 T and goethite grains have coercivities in excess of 5.0 T (McElhinny and McFadden, 1999). For that reason, AF demagnetization is most useful for analysing rocks that have mainly magnetite and

titanomagnetite as ferromagnetic carriers (Morris, 2003). In contrast, rocks with remanences carried by hematite cannot be fully demagnetized using the AF method and are best treated thermally.

3.1.4.1 Thermal demagnetization

Thermal demagnetization is conducted by heating samples in an oven that is magnetically shielded to produce a zero-field environment in the heating chamber, and then cooling them to room temperature. This removes the magnetization carried by ferromagnetic grains with unblocking temperatures less than the oven temperature. Demagnetization experiments are conducted by repeatedly treating samples at progressively higher temperatures, measuring the magnetization remaining after each step.

This study used a Magnetic Measurements Ltd Thermal Demagnetizer –MMTD oven (Fig. 3.8). Since the NRM intensities presented in metamorphic sole rocks are low, only 12 specimens were thermally demagnetized initially to test whether this method gave good results. The temperature steps used were 100, 150, 200, 250, 300, 350, 400, 425, 450, 475, 500, 520, 540, 560 and 580°C. Before cooling to room temperature, specimens were held in the oven for 40 minutes at each step. After cooling, the remanent magnetizations were measured using the AGICO-JR6 spinner magnetometer. Bulk susceptibilities were also measured after each temperature step to monitor if heating had affected the mineral composition and caused alteration, for example, pyrite may alter to magnetite at 350°C-500°C (Morris, 2003).

Figure 3.8.Magnetic Measurements Ltd Thermal Demagnetizer – MMTD ovens

3.1.4.2 Alternating field (AF) demagnetization

In AF demagnetization, specimens are tumbled in an alternating field within a zero direct magnetic field environment produced by magnetic shielding. Grains having smaller coercivity values than the applied field track the alternating field direction as the specimen is tumbled, and as the field is gradually reduced to zero the magnetization of these grains becomes randomized and cancel each other out. This effectively removes secondary magnetization components carried by grains with coercivities less than the peak applied field. In this study, an AGICO LDA-3 AF-demagnetizer (Fig. 3.9) that can reach at maximum peak field of 100 mT was used. Each specimen was put individually within the specimen holder. Alternating fields were applied in 5 mT steps from 5 mT to 100 mT. After each step, remanent magnetizations were measured using an AGICO JR6 spinner magnetometer. Initially, 24 specimens from both sole rocks and sole-hosted dykes (at least one specimen per site) were chosen to see if the results would be reliable since the metamorphic sole rocks have low NRM intensity values. Because the results were somewhat better than the ones demagnetized thermally, nine more specimens were AF demagnetized. However, many of the results were considered as noisy and not usable data since the magnetometer could not measure the remanent magnetizations accurately enough.

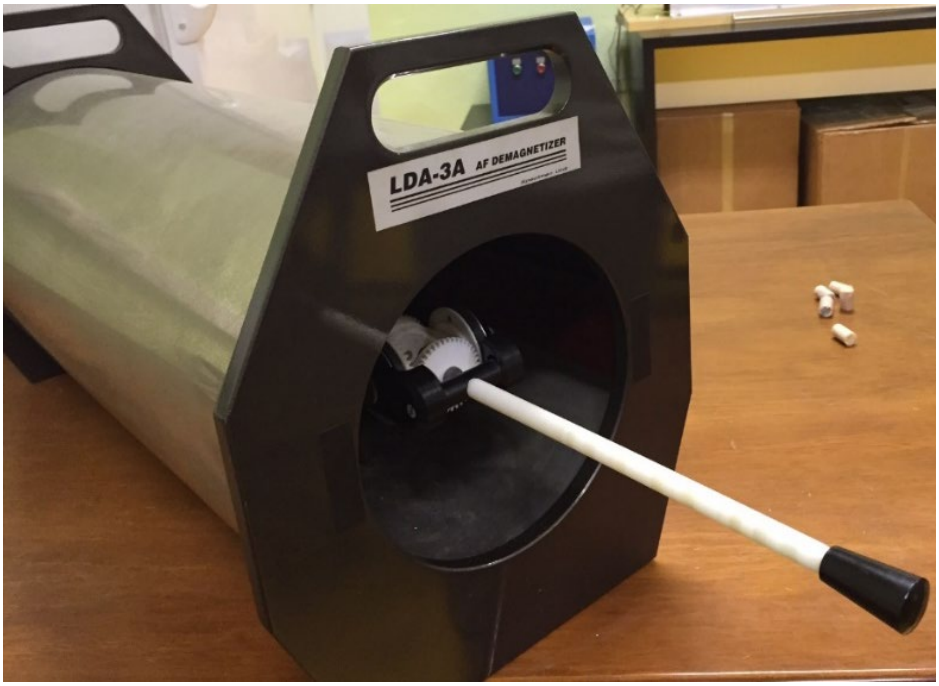

Figure 3.9. AGICO LDA-3 Alternating field demagnetizer

Because of this, the remaining 66 specimens were demagnetized and measured using a 2G-Enterprises DC Cryogenic SQUID (Superconducting Quantum Interference Device) Magnetometer (Fig. 3.10) housed in a magnetically shielded room at the University of Southampton. This equipment (noise level= 5 x 10^{-6} A/m) is more sensitive than the AGICO spinner magnetometer in terms of measuring low-intensity magnetizations. Also, the other advantage is that the measurement takes only about three minutes per each demagnetization step. Unlike the AGICO demagnetizer, it was possible to put eight different specimens in the equipment during each step. The applied field was increased 5 mT at each step up to 110 mT (the maximum field that the 2G system can reach). After each measurement following the different cleaning steps, Long core software automatically calculated the remanent magnetization. One of the samples (BC0701C3) could not be demagnetized since it was slightly too large to enter the demagnetizer.

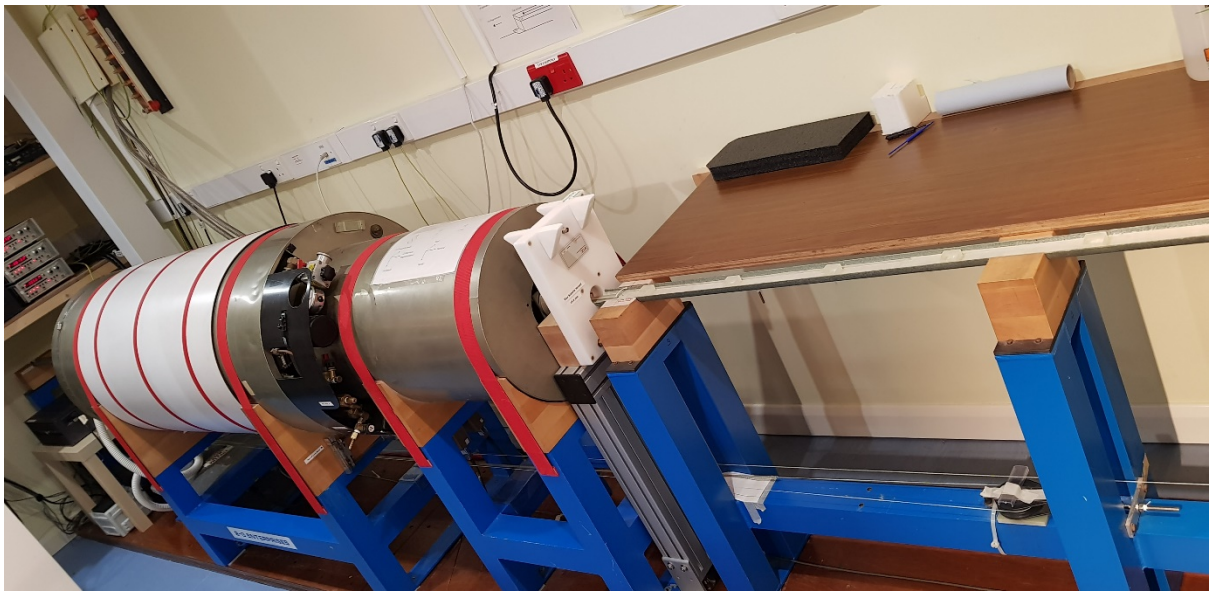

Figure 3.10. 2G-Enterprises DC Cryogenic SQUID (Superconducting Quantum Interference Device) Magnetometer, at the University of Southampton.

3.1.4.3 Displaying the stepwise demagnetization data

There are two different ways to represent the stepwise demagnetization data. The first and most common one is to use an orthogonal projection known as a Zijderveld diagram (Zijderveld, 1967) to show both the direction of remanent magnetization and intensity values after each step by projecting the data onto a two dimensional view (Fig. 3.11).

N–S vertical plane

$$\tan(I) = \tan\left(I_{app}\right)|\cos(D)|$$

E–W vertical plane

$$\tan(I) = \tan\left(I_{app}\right)|\sin(D)|$$

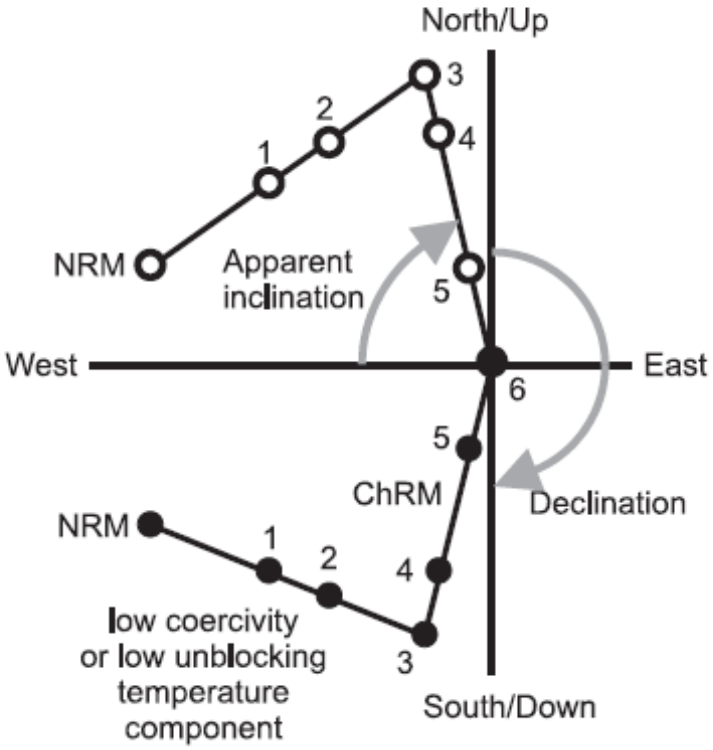

Figure 3.11. Zijderveld plot displaying the demagnetization of specimen with two remanent components, also showing the declination and inclination. Steps NRM-3 yield the secondary magnetization whereas steps 3-6 represent the primary magnetization of the specimen (from Morris, 2003).

The second method is to use equal area projections to show directional changes combined with plots of intensity against demagnetization step (Fig. 3.12). In either case, principal component analysis (PCA; Kirschvink, 1980) is used to statistically determine the direction of the components of magnetization isolated by demagnetization experiments, by least squares best fit lines through the data.

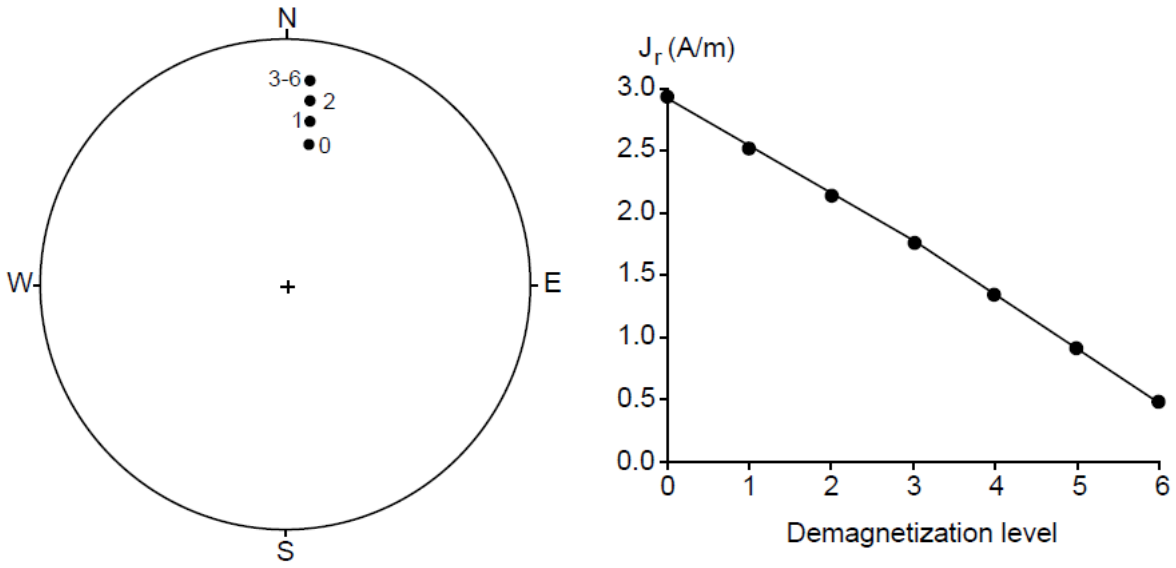

Figure 3.12. The equal area projection indicates the demagnetization results, 3-6 direction indicates constant direction and the direction keeps changing between 0-3 interval. The graphic at the right shows the intensity of the remanent magnetization after each step demagnetization step (from Butler, 1992)

The decrease in the magnetization towards origin does not always follow a straight line as in the step 3-6 interval in Figure 3.11. Instead, magnetization may follow a path within a plane (represented by a great circle in an equal area projection) because of overlapping of the unblocking temperature or coercivity spectra of two or more components (McFadden and McElhinny, 1988). When the NRM consists of more than one component, there are three different scenarios. In the first and most optimistic scenario (Fig. 3.13), there is no overlap of the coercivities/unblocking temperatures of the components and they are demagnetized in different intervals. Thus, the primary magnetization will be revealed after erasing the low stability secondary magnetization.

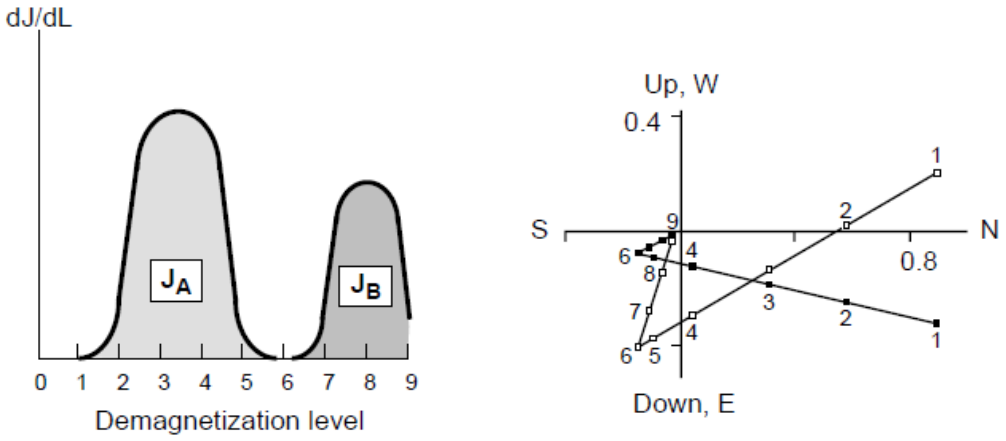

Figure 3.13. JA component is erased between 1-6 intervals whereas JB component (more stable) is erased between 6-9 intervals. This figure indicates that there is no overlapping between two components of natural remanent magnetization (from Butler, 1992).

In the second scenario (Fig. 3.14), there is an overlap in stability at some point in both components. When the less stable one is not totally demagnetized, the removal of the magnetization of the more stable one starts. Therefore, the transition between two components might be observed along a great circle. Nonetheless, it is still possible to get the final magnetization i.e. in interval 7-9 in figure 3.14.

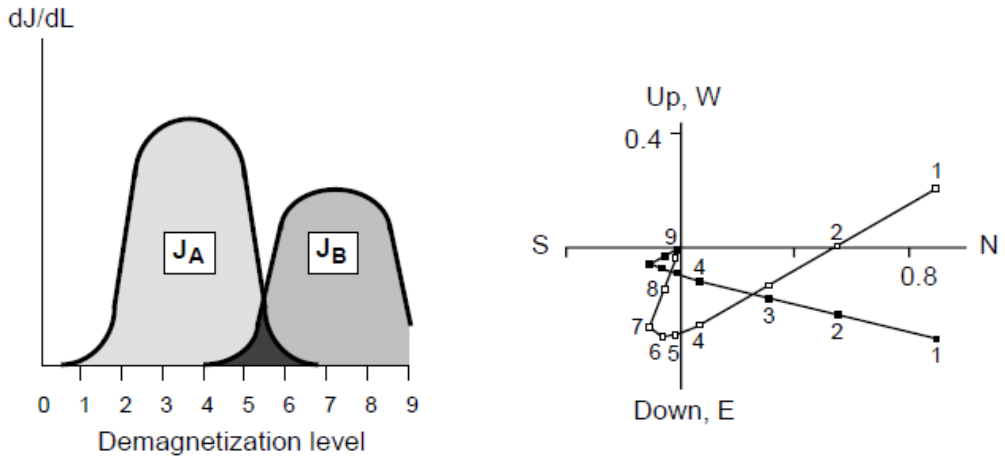

Figure 3.14. J_A component is erased between 1-6 intervals whereas J_B component (more stable) is erased between 4-9 intervals. This figure indicates a small interval of overlap between 4-7 demagnetization intervals. The curve shape between 4-7 intervals is clearly seen in the Zijderveld plot (from Butler, 1992).

The most difficult scenario (Fig. 3.15) is where there is almost complete overlapping of the stability of both components, which means that they might start being demagnetized at the same

temperature levels or AF steps. Thus, both components might be totally erased at the same levels and so there is no way to separate the vector components.

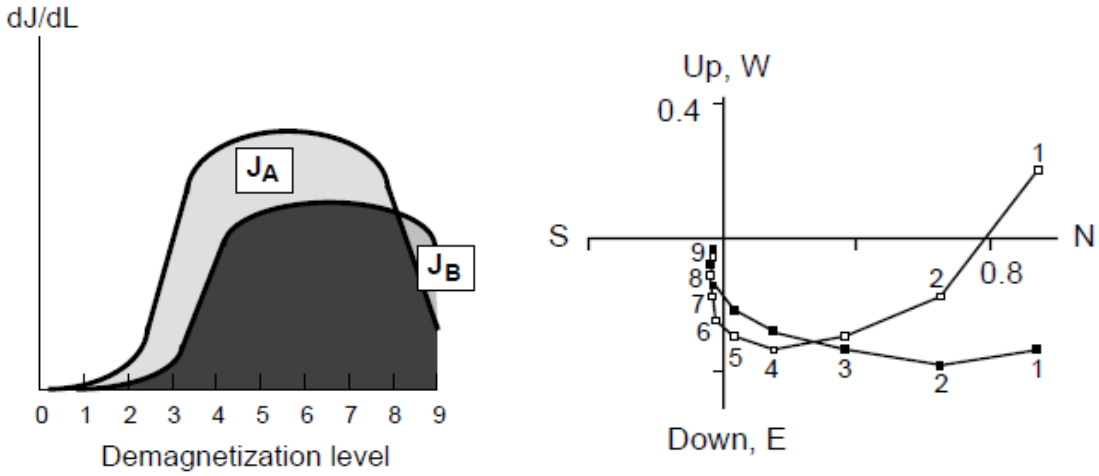

Figure 3.15. J_A and J_B components of NRM are almost completely overlapping because of the similar blocking temperature or coercivity values. The resulting vector component diagram does not indicate linear relations and two components cannot be separated from each other (from Butler, 1992).

When demagnetization data follow a path along a great circle with no stable end point (i.e. no straight line towards the origin in a Zijderveld diagram), the direction of the ChRM is hidden. To overcome this, a great circle analysis method was suggested by McFadden and McElhinny (1988) to be able to find the final palaeomagnetic direction. The method can combine data from great circle demagnetization paths from different samples at a site with any end point directions found by PCA. An initial estimate of the final direction is made (using the end point directions if available) and the nearest point along each great circle to this estimate are calculated. These points are then combined with the end point directions to calculate a new, revised estimate of the final direction, and this process is repeated iteratively to establish the maximum likelihood estimate of the final direction (McFadden and McElhinny, 1988).

3.1.5 Rock magnetic experiments

3.1.5.1 Isothermal remanent magnetization (IRM) and back field IRM analyses

After alternating field demagnetization of the specimens, it is common to perform isothermal remanent magnetization (IRM) acquisition experiments to aid identification of the ferromagnetic minerals in samples. These experiments are performed by applying increasing direct magnetic fields along Z-axis of specimens, measuring the resulting IRM after each field step. In this study, the direct fields were applied using a Molspin pulse magnetizer (Fig. 3.16).

Figure 3.16. Molspin pulse magnetizer

Remanences were then measured with the JR6 magnetometer. The applied fields were 0, 10, 20, 30, 40, 50, 80, 100, 200, 300, 500 and 800 mT. Data were represented by plotting IRM intensities against applied field (after normalising intensities by dividing by the maximum intensity of each sample) Back field IRM experiments were then performed by applying the same fields along the minus Z-direction (Fig. 3.17) to find the coercivity of remanence (B_{Cr}), i.e. the backfield that reduced the forward IRM to zero.

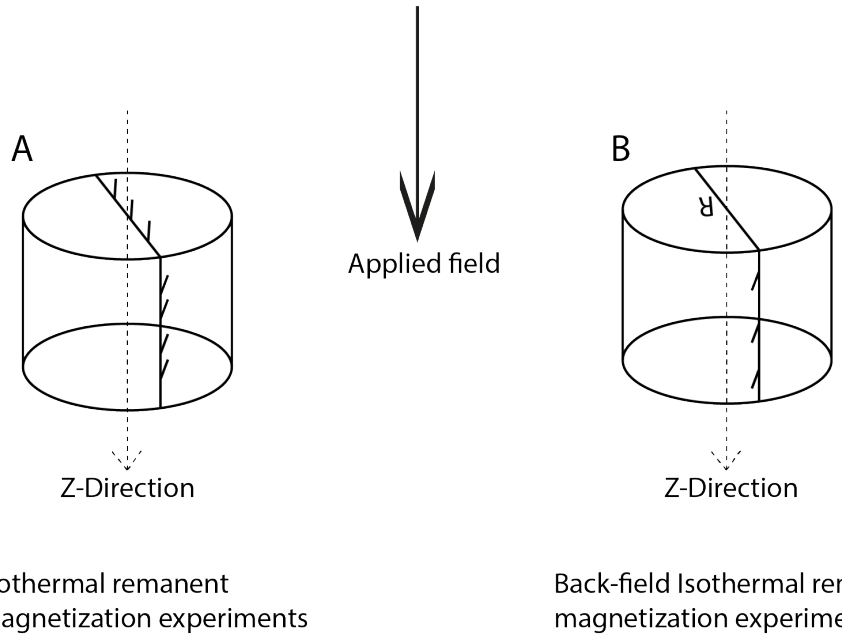

Figure 3.17. Diagram illustrating orientation of specimens relative to the applied field direction during IRM and back field IRM experiments.

IRM acquisition in specimens containing magnetite reach saturation at maximum applied fields around 0.3 T. However, hematite and goethite rich samples do not saturate until very high applied field values because of their higher coercivities (Table 3.1).

Table 3.1.Maximum coercivities and unblocking temperatures for some common magnetic minerals (from Lowrie, 1990)

Magnetic Mineral	Maximum coercivity (T)	Maximum blocking temperature °C
Magnetite	0.3	580
Maghemite	0.3	~350
Titanomagnetite x=0.3	0.2	~350
Titanomagnetite x=0.6	0.1	150
Pyrrhotite	0.5-1	325
Hematite	1.5-5	675
Goethite	>5	80-120

3.1.5.2 Thermal demagnetization of three-component IRMs

IRM acquisition data are not always unequivocal. For example, magnetite, maghemite and titanomagnetite have similar coercivity values, so they become saturated around same values. In addition to IRM results, therefore, the same specimens were subject to thermal demagnetization of three-component IRMs, following the method of (Lowrie, 1990). An IRM was first imparted by applying an 800 mT field along the specimen Z-direction. This was followed by a 300 mT IRM along the Y-direction and by a 50 mT IRM along the X-direction (Fig. 3.18). This allows the unblocking temperature characteristics of each coercivity window (0-50, 50-300 and 300-800 mT) for each sample to be determined using thermal demagnetization (in steps of 50°C from 100-400°C, 25°C from 400-500°C, and 20°C from 500-680°C). Each component's IRM intensity was measured after each demagnetization step by using the JR6 spinner magnetometer and the analyses were performed by using the Remasoft30 software. Eventually, the data obtained from IRM experiments and thermal demagnetization of three component IRMs were combined to make ferromagnetic mineral identifications (Lowrie, 1990).

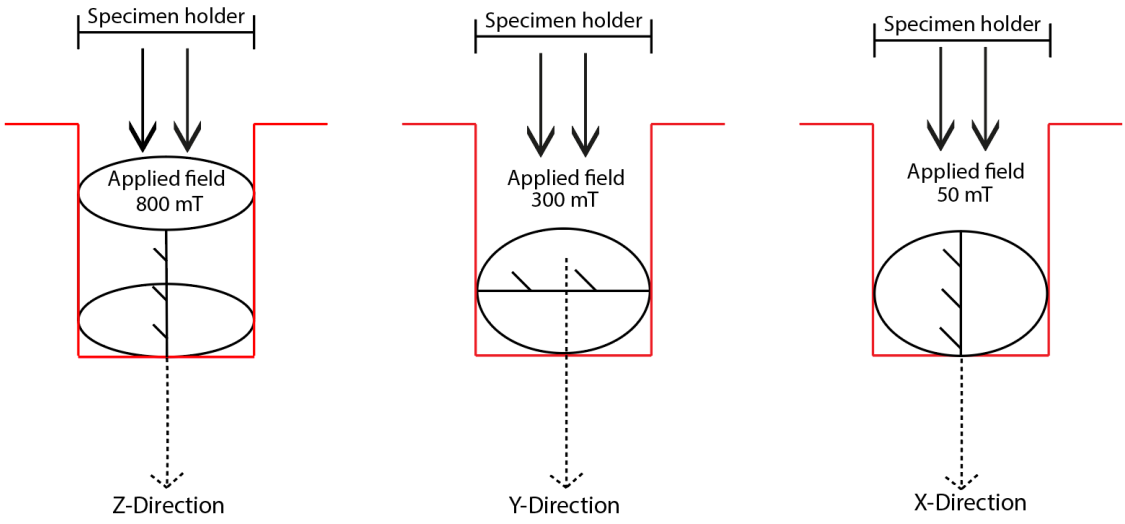

Figure 3.18. Applied fields along X (50 mT), Y (300 mT) and Z (800 mT) directions to find thermal elements of three components of isothermal remanent magnetization. These fields were applied after AF demagnetization at 100 mT and before thermal demagnetization.

3.1.5.3 Anisotropy of isothermal remanent magnetization (AIRM)

Anisotropy of isothermal remanent magnetization (AIRM) measurements were performed on seven specimens that had already been demagnetized to determine if any inverse magnetic fabrics

exists. These can result from the presence of SD magnetite grains that have a maximum susceptibility along their short axes because of shape anisotropy. In a normal magnetic fabric, K_{max} is parallel to X and K_{min} is parallel Z whereas K_{max} is parallel to Z and K_{min} is parallel X in an inverse magnetic fabric (Ferré, 2002) (Fig. 3.19). AIRM experiments were performed by applying a 50 mT field was applied along each specimen axis and measuring IRM intensities.

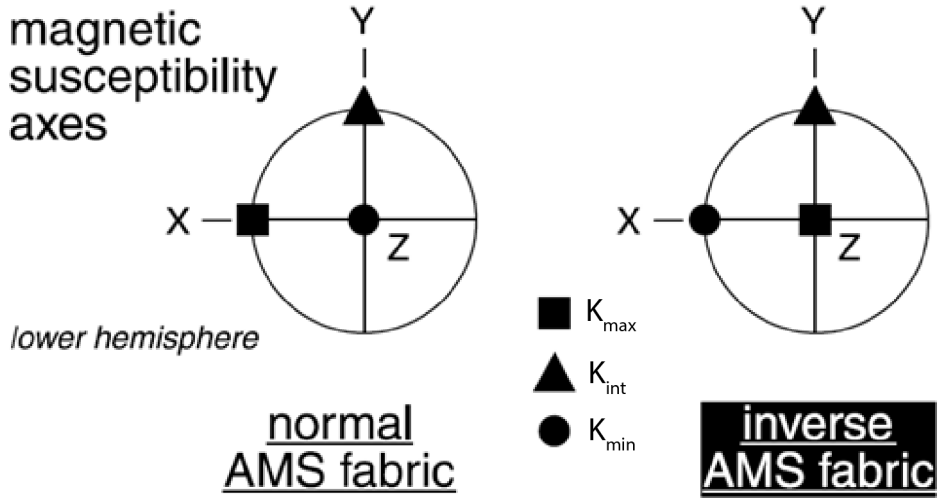

Figure 3.19. Illustration of normal and reverse AMS fabric on lower hemisphere (from Ferré, 2002)

Between field applications the specimens were AF demagnetized in a 100 mT field and measured to determine the residual remanence in the demagnetized state, and these values were subtracted from the IRM values and these data were used to calculate AIRM ellipsoids for each direction ($AIRM_{max}$, $AIRM_{int}$ and $AIRM_{min}$) using a Basic program written by A. Stephenson. Specimen principal axes for AMS and AIRM were compared on stereonets to detect the possible existence of inverse fabrics.

3.1.5.4 Thermomagnetic analyses for Curie temperature

Curie point is the temperature that ferromagnetic minerals lose their ferromagnetic behaviour and become paramagnetic. Each ferromagnetic mineral has a specific Curie point, at which the increase in interatomic distances due to thermal energy causes a decrease in the strength of the exchange coupling between magnetic moments (Butler, 1992; Morris, 2003). This point is also marked by a drastic reduction in low field magnetic susceptibility.

To be able to determine Curie points, specimens were crushed to powder to perform experiments within a furnace attachment of AGICO KLY-3S Kappabridge. As a first step for the analyses, the empty furnace of the equipment was measured to determine the background signal. Specimens were then heated in argon gas to reduce alteration during the heating process, with susceptibility measured continuously from room temperature to 700°C and followed by cooling back to room temperature. The data were then input into AGICO Cureval8 software to find the Curie points of each specimen by using the method from Petrovský and Kapička (2006), which shows the determination the of the Curie temperature on a graph of 1/k vs. temperature.

3.1.6 Net tectonic rotation (NTR) method

Net tectonic rotation method of analysing palaeomagnetic data was originally developed by Allerton and Vine (1987) in for use in the sheeted dyke complex of the Troodos ophiolite (Cyprus) and it has been used in many studies to understand rotation histories (Inwood et al., 2009b; Maffione et al., 2017; Morris and Anderson, 2002; Morris et al., 2017; Morris et al., 1998; Morris et al., 1990; Morris and Maffione, 2016). This method is applicable for both palaeo-vertical and palaeo-horizontal cases, and restores the observed magnetization vector at a site or locality to a reference magnetization vector and present day pole to the geological structure (bedding or dyke margin) to its initial orientation at the time of formation i.e. to the vertical for initially horizontal sedimentary rocks, or to the horizontal for initially vertical dykes. These restorations are achieved simultaneously by a single net rotation around an inclined axis. Some assumptions of the method are:

1- That angle, β, between the direction of magnetization and the pole to the structure does not change during structural deformation (Allerton and Vine, 1987; Morris et al., 1998) (Fig. 3.20).
2- That a reference magnetization vector for the area can be found that represents the geomagnetic field direction at the time of acquisition of magnetization.

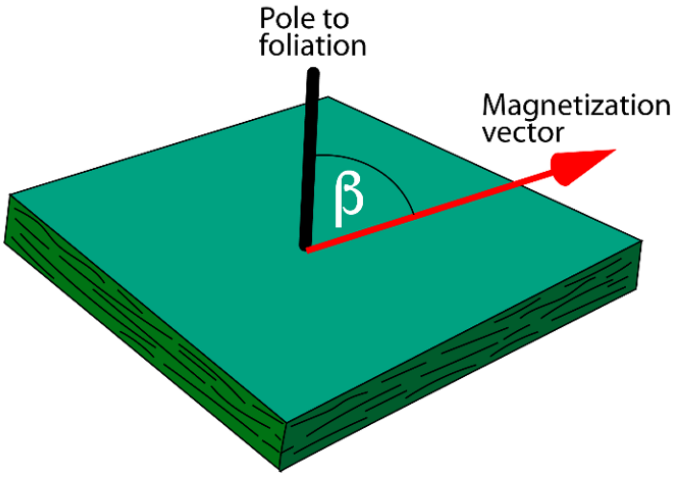

Figure 3.20. Illustration of the angle β between the pole to foliation and the magnetization vector.

In this study, the orientation of the foliation in the metamorphic sole rocks at the time of magnetization acquisition is unknown initially (in contrast to all previous applications of the NTR approach), and so a modification to the method is needed to allow tectonic interpretation of metamorphic sole remanence directions. Three input vectors into the NTR calculation are the observed magnetization direction (in present day geographic coordinates), a reference magnetization direction, and the present-day pole to the metamorphic foliation. Each of these vectors has an associated statistical uncertainty that can be taken into account during the calculation of potential rotation parameters (as documented in Chapter 4). The NTR method is then combined with a Monte Carlo modelling approach and used to determine all potential initial orientations of the pole to the foliation (with no *a priori* conditions on the orientation) that maintain the angle β, and the associated sets of rotation parameters. The full Monte Carlo approach is described in Chapter 4, but figure 3.21 outlines the NTR method for a single estimate of rotation parameters.

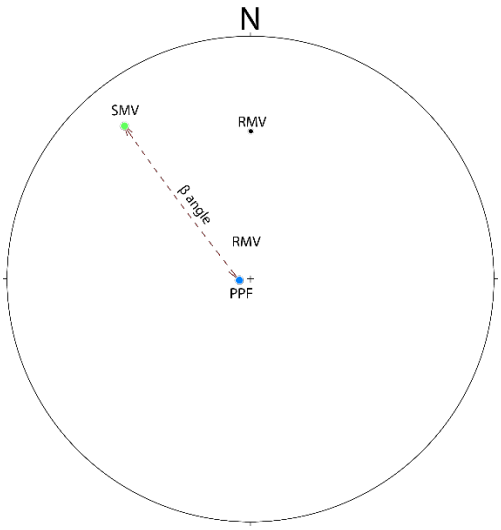

Plotting;

RMV: 000°/039° (Reference magnetization vector)

SMV: 320.6°/19.5° (Site magnetization vector)

PPF: 265.6°/86.2° (Present pole to foliation)

β: Angle between SMV and PPF: 68.4°

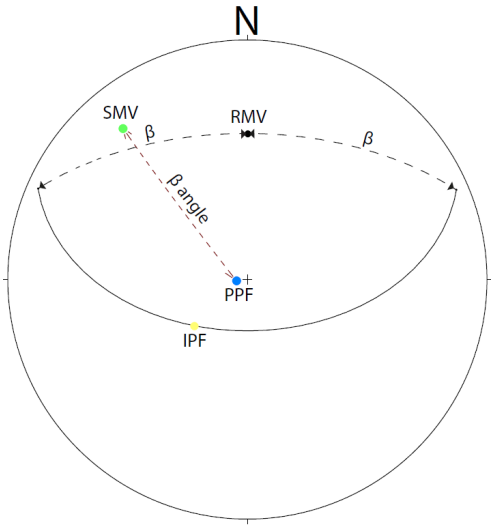

After inputting the data, the circle of radius β centred on the reference magnetization vector (RMV) is drawn. This circle shows the locus of possible poles to foliation at the time of magnetization. A single initial pole to the foliation (IPF) is selected along this locus at random to use in the next step.

IPF=229.2°/66° (For this chosen random point)

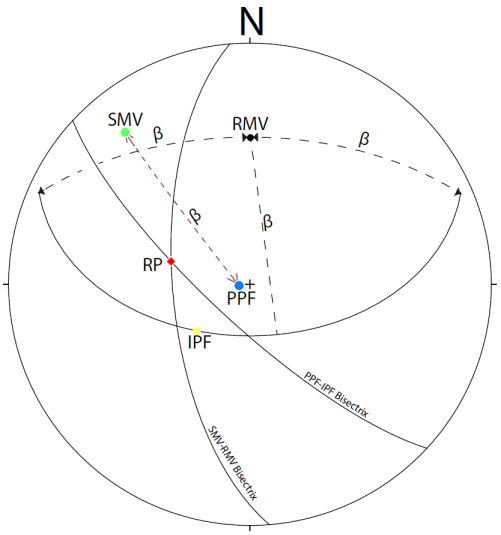

The intersection of the great circles that bisect the vector pairs of the SMV/RMV and PPF/IPF represents the rotation pole (RP). After finding the rotation pole, the sense and angle of rotation around this axis were found.

In this example, rotation 52.7° around a rotation pole (RP) of 286.1°/62.2° in a CCW sense.

Figure 3.21. Example for net tectonic analysis (Allerton and Vine, 1987) by using one of iterations of the Monte Carlo method employed in Chapter 4.

3.2 Petrographic and structural methodologies

3.2.1 Thin section analyses

Thin section analyses using a polarizing light microscope were performed on 10 samples from nine different sites chosen to be representative of the whole road cut section of metamorphic sole rocks. Samples were chosen from rocks that exhibited a clear lineation, foliation or other structural feature i.e. the ones with stretching lineation to be able to perform kinematic analyses. Samples were cut parallel to lineation and perpendicular to foliation, which is the most appropriate method to be able to understand the kinematics and microstructures. The markings were done "U" for upside and "D" for down of the sample, depending on the facing of the surface on which the sample orientation had been marked.

3.2.2 Scanning electron microscope (SEM) analysis preparations

For SEM analyses, polished thin sections from two samples that were thought to be the most representative ones from the field were observed in the Plymouth Electron Microscopy Centre using a calibrated JEOL 7001 FE SEM model. A third prepared section was not observed under SEM due to lack of kinematic and structural indicators under polarizing light microscope. Sections were coated with carbon, and mineral imaging, mineral and kinematic analyses were performed during the SEM sessions. Many spot analyses were done within the minerals as much as possible. The variations in the amphibole minerals were observed. Furthermore, textural analyses were carried out. P-T conditions at the time of formation of the metamorphic sole rocks were estimated by analysing the plagioclase in contact with the amphibole minerals and what conditions caused zonation in some amphibole minerals. For further P-T estimations, the geothermobarometer using "edenite+albite=richterite+anorthite" equation published by Holland and Blundy (1994), in the absence of quartz, was used for both of the polished thin sections. The plagioclase with highest anorthite concentrations were used to increase the accuracy of the results. The error estimate for temperatures using this method is stated as ±35-40°C by the authors (Holland and Blundy, 1994), however, typical uncertainty values for pressure and temperature (±50C° and ±1 kbar) were assumed in this study. The pressure values are based on Anderson and Smith (1995). In order to understand variations in metamorphism grade, chemical profiles were

made from core to rim of zoned amphiboles with 4 to 8 points. Geochemical mapping was also performed for the images to observe elemental differences within minerals.

Chapter 4- Results

4.1 Petrographic results and structural data

The petrography and mineralogy of the metamorphic sole rocks of the Mersin ophiolite have been already described in detail by Çelik (2008) and Parlak (1996). In this study, the main aim is to understand the shear sense direction by using kinematic indicators observed under the microscope, to combine this with the palaeomagnetic studies and the pressure and temperature estimates. During the thin section analyses, the petrography and mineralogy of the rocks were also studied. Additionally, it should be noted that the geochemical data from SEM the analyses are semi-quantitative.

4.1.1 Mineralogy and petrography

The sole rocks are observed between ophiolitic melange to the NW and the Mersin ophiolite to the SE as a thrust slice. The upper part of the sole rocks (towards SE) is mainly composed of amphibolites whereas mainly phyllitic rocks and foliated metabasalts form the lower regions. However, amphibolites are also clearly observed in the lower sections as slices, or lenses. Foliation is typical in the amphibolites, and it is well defined by amphiboles which mostly show ~60° and ~120° cleavage angles. The size range of the amphiboles is fine to medium grained. SEM observations show that the change in mineral size are not accompanied by any geochemical variations. Furthermore, the data indicate the amphiboles are calcic based on the Leake et al. (1997) classification (Fig. 4.1). The amphiboles are classified as mostly edenite, and ferro-edenite in site BC12 and magnesihornblende in site BC07.

The plagioclases are albitic in composition (3-7% anorthite) and altered. Therefore, polysynthetic twinning is not common. Epidote minerals are abundant and chlorite minerals are also observed as a secondary phase. Calcite minerals are observed with thick and straight twins. Pyroxene minerals are observed in sample BC0701 as boudinage. Lineations in the sections are largely defined with parallel alignment of the hornblende, mica and chlorite minerals. Some of the veins are filled with feldspars with potassium. Additionally, some opaque minerals observed in site BC05 are probably ilmenite indicating high temperature values.

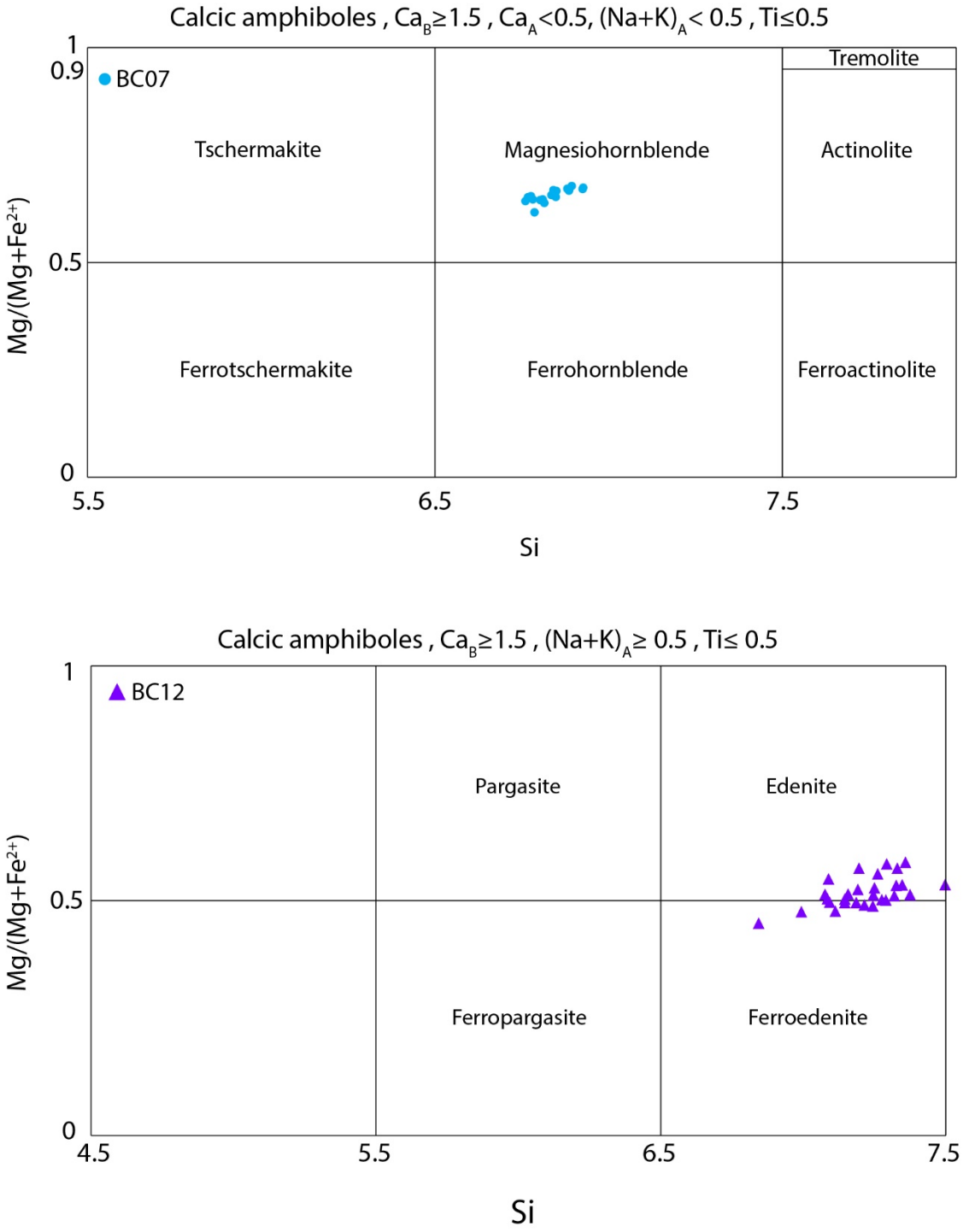

Figure 4.1. Diagrams showing the classification of the amphiboles with calcic characteristic for BC07 and BC12, according to Leake et al. (1997). Note that every point indicates the average chemical composition of an individual grain.

4.1.2 Pressure and temperature estimations

Zonation within the amphibole may be observed because of variations in crystallizing setting during metamorphism. These zonations may be the key to understand the pressure and temperature changes which are recorded in the minerals. Many researches have indicated that decreasing Ti, Al, Na, K concentrations and increasing Si content within the Ca rich amphiboles are associated with a decrease in metamorphism grade (e.g. Holland and Blundy, 1994; Miri et al., 2016). Zones were particularly observed within two of the amphibole minerals in BC1201 thin section as two different zonations i.e. core and rim (Fig. 4.2). In order to understand the variations in the metamorphic grade through the zones, chemical profiles were made from core to rim of zoned amphiboles with 4 to 8 points. Even if the boundaries between the zones are not clear to identify (no optical zonation), the SEM data showed the variations through the key elements. According to these data, the core to rim increase in Si, Mg and decrease of Na-K (A site), Fe, and Al in zoned amphiboles is consistent with a decrease in metamorphic grade (Fig. 4.3). The results used for the analyses of the zonations are given in Table 4.1.

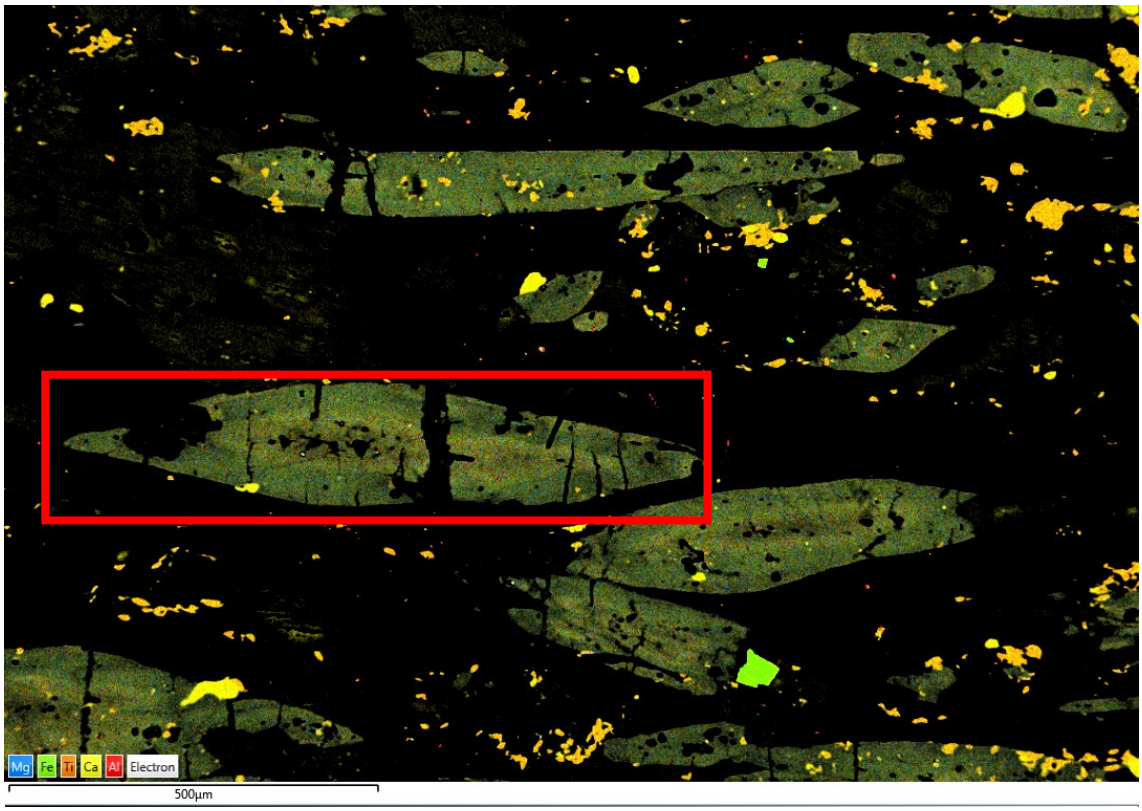

Figure 4.2. SEM image highlighting one of the amphibole minerals showing zonation from core to rim in BC1201 thin section

Table 4.1. Chemical compositions of two amphibole grains to study zonation. The calculations are based on 23 oxygen. Note that Ed=Edenite , Fe-Ed= Ferroedenite).

	Amphibole 1							Amphibole 1							Amphibole 2							Amphibole 2						
	Rim							Core							Rim							Core						
SiO_2	51.54	52.84	51.90	51.67	52.68	53.23	52.68	46.89	48.38	48.29	51.85	47.43	47.86	49.94	48.49	51.63	53.16	53.99	52.25	46.63	47.29	47.92	48.45					
TiO_2	0.00	0.00	0.00	0.00	0.00	0.00	0.00	0.25	0.00	0.00	0.00	0.00	0.33	0.28	0.00	0.00	0.00	0.00	0.00	0.35	0.00	0.34	0.00					
Al_2O_3	4.56	3.76	4.21	4.16	3.57	3.60	3.75	9.09	8.27	8.34	7.84	8.84	7.76	5.83	7.17	4.57	3.35	2.93	3.92	8.59	8.79	7.40	7.07					
FeO*	19.60	19.48	20.90	20.54	19.56	17.07	17.98	20.81	19.75	19.49	15.97	20.29	20.33	21.02	21.77	17.74	17.58	17.34	19.11	21.25	19.71	19.99	21.23					
MnO	0.00	0.00	0.00	0.25	0.00	0.00	0.29	0.00	0.00	0.00	0.24	0.23	0.00	0.00	0.00	0.00	0.00	0.00	0.00	0.00	0.24	0.00	0.28					
MgO	11.79	11.80	10.89	11.30	12.17	13.16	12.93	10.11	10.73	10.82	11.27	10.27	10.23	10.59	9.70	12.79	13.30	13.32	12.30	9.66	10.64	10.65	9.93					
CaO	10.11	9.82	9.66	9.60	9.80	10.87	10.04	9.24	9.49	9.47	8.77	9.53	9.93	9.60	9.65	11.20	10.92	10.62	10.19	10.36	9.88	10.98	10.17					
Na_2O	2.16	2.13	2.27	2.33	2.03	1.86	2.10	3.02	2.77	2.96	3.72	2.83	3.06	2.44	2.79	1.84	1.49	1.65	1.96	2.57	2.85	2.19	2.42					
K_2O	0.23	0.17	0.17	0.15	0.19	0.20	0.23	0.58	0.62	0.62	0.34	0.57	0.50	0.31	0.44	0.24	0.20	0.14	0.27	0.59	0.59	0.53	0.44					
SUM	99.99	100.00	100.00	100.00	100.00	99.99	100.00	99.99	100.01	99.99	100.00	99.99	100.00	100.01	100.01	100.01	100.00	99.99	100.00	100.00	99.99	100.00	99.99					
T *site*																												
Si	7.49	7.65	7.57	7.54	7.63	7.64	7.60	6.92	7.08	7.07	7.40	6.98	7.05	7.32	7.17	7.46	7.64	7.73	7.57	6.91	6.95	7.05	7.16					
Al (iv)	0.51	0.35	0.43	0.46	0.37	0.36	0.40	1.08	0.92	0.93	0.60	1.02	0.95	0.68	0.83	0.54	0.36	0.27	0.43	1.09	1.05	0.95	0.84					
Total T	8.00	8.00	8.00	8.00	8.00	8.00	8.00	8.00	8.00	8.00	8.00	8.00	8.00	8.00	8.00	8.00	8.00	8.00	8.00	8.00	8.00	8.00	8.00					
B+C *site*																												
Al (vi)	0.28	0.29	0.30	0.26	0.24	0.25	0.23	0.50	0.51	0.51	0.72	0.51	0.40	0.33	0.41	0.24	0.21	0.23	0.24	0.42	0.48	0.34	0.39					
Ti	0.00	0.00	0.00	0.00	0.00	0.00	0.00	0.03	0.00	0.00	0.00	0.00	0.04	0.03	0.00	0.00	0.00	0.00	0.00	0.04	0.00	0.04	0.00					
Fe^{2+}	2.38	2.36	2.55	2.51	2.37	2.05	2.17	2.57	2.42	2.39	1.91	2.50	2.50	2.58	2.69	2.14	2.11	2.08	2.32	2.63	2.42	2.46	2.62					
Mg	2.56	2.55	2.37	2.46	2.63	2.82	2.78	2.22	2.34	2.36	2.40	2.25	2.25	2.32	2.14	2.76	2.85	2.84	2.66	2.14	2.33	2.34	2.19					
Mn	0.00	0.00	0.00	0.03	0.00	0.00	0.04	0.00	0.00	0.00	0.03	0.03	0.00	0.00	0.00	0.00	0.00	0.00	0.00	0.00	0.03	0.00	0.04					
Ca	1.57	1.52	1.51	1.50	1.52	1.67	1.55	1.46	1.49	1.48	1.34	1.50	1.57	1.51	1.53	1.73	1.68	1.63	1.58	1.65	1.56	1.73	1.61					
Total B+C	6.79	6.72	6.73	6.76	6.76	6.78	6.77	6.78	6.75	6.74	6.39	6.80	6.75	6.76	6.77	6.87	6.85	6.78	6.79	6.87	6.82	6.90	6.84					
A *site*																												
Na	0.61	0.60	0.64	0.66	0.57	0.52	0.59	0.86	0.79	0.84	1.03	0.81	0.87	0.69	0.80	0.52	0.42	0.46	0.55	0.74	0.81	0.62	0.69					
K	0.04	0.03	0.03	0.03	0.04	0.04	0.04	0.11	0.12	0.12	0.06	0.11	0.09	0.06	0.08	0.04	0.04	0.03	0.05	0.11	0.11	0.10	0.08					
Total A	0.65	0.63	0.67	0.69	0.61	0.55	0.63	0.97	0.90	0.96	1.09	0.91	0.97	0.75	0.88	0.56	0.45	0.48	0.60	0.85	0.92	0.72	0.78					
$Mg/(Mg+Fe^{2+})$	0.52	0.52	0.48	0.50	0.53	0.58	0.56	0.46	0.49	0.50	0.56	0.47	0.47	0.47	0.44	0.56	0.57	0.58	0.53	0.45	0.49	0.49	0.45					
Class	Ed	Ed	Fe-Ed	Ed	Ed	Ed	Ed	Fe-Ed	Fe-Ed	Fe-Ed	Ed	Fe-Ed	Fe-Ed	Fe-Ed	Fe-Ed	Ed	Ed	Ed	Ed	Fe-Ed	Fe-Ed	Fe-Ed	Fe-Ed					

Although more amphibole minerals were analysed to see possible changes towards rim regions during the SEM sessions, they, unfortunately, did not indicate any variations apart from in a few examples. Only for the Fe^{2+} against Si comparison, a few spots in the rim region of the amphibole mineral do not indicate any variations. Apart from this element, all of the others suggest different pressure and temperature conditions for the rim zone during the metamorphism. Furthermore, an increase in the $Mg/(Mg+Fe^{2+})$ ratio from core to rim points to a transition from ferroedenite to edenite composition (Fig. 4.4).

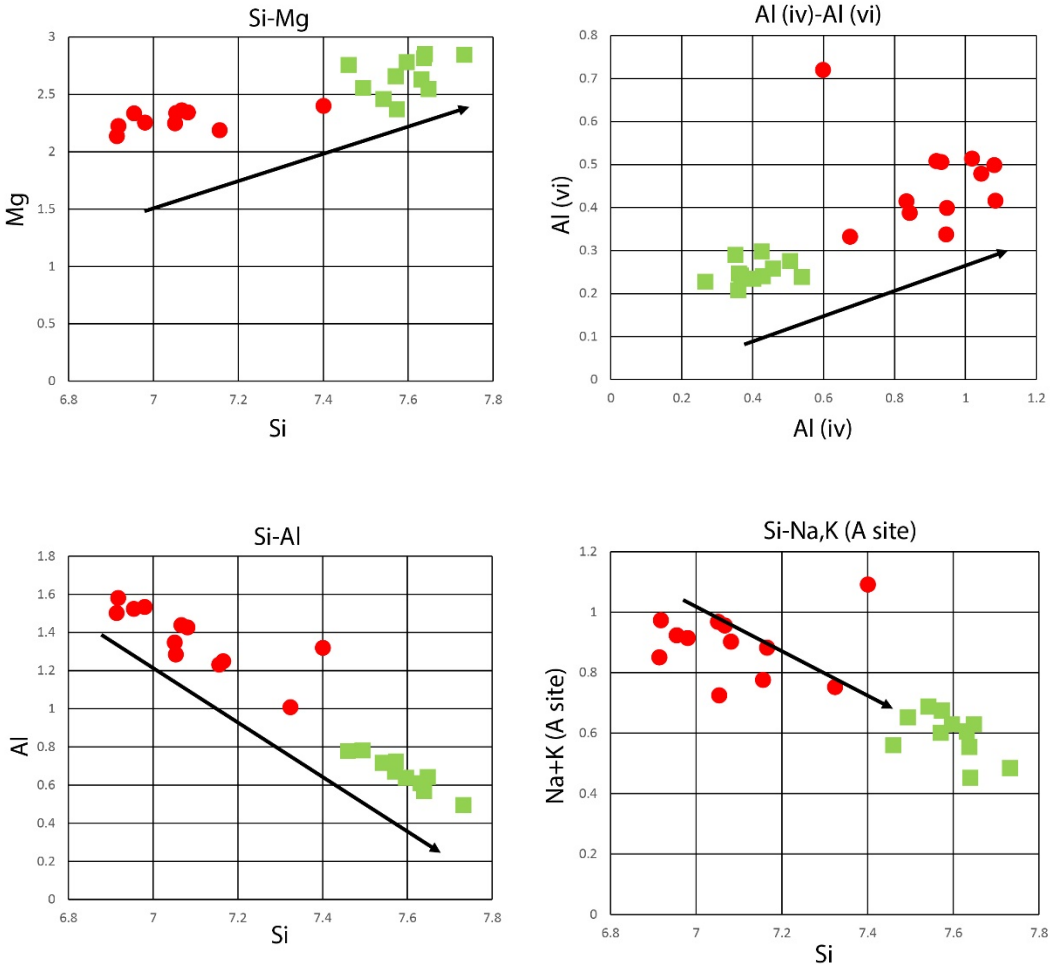

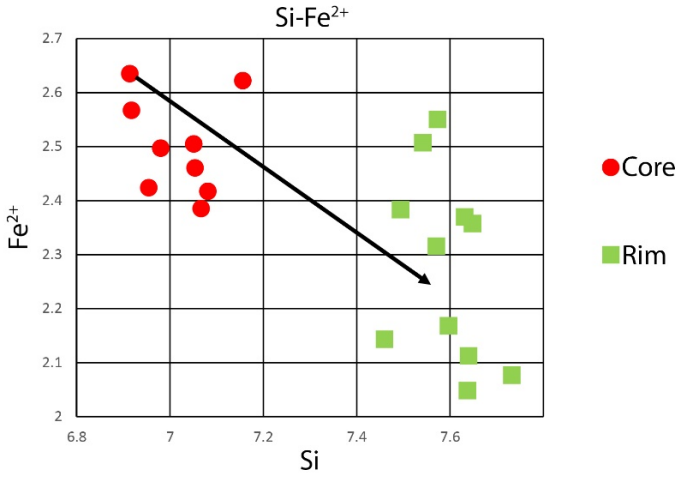

Figure 4.3. Chemical zonation of the samples with regards to Fe, Al Total, Mg, (Na+K) vs. Si and Al (iv) vs. Al (vi) as a function of metamorphism grade decreasing towards rims. Note that each point indicates random point inside the regions of Amphibole-1 and Amphibole-2.

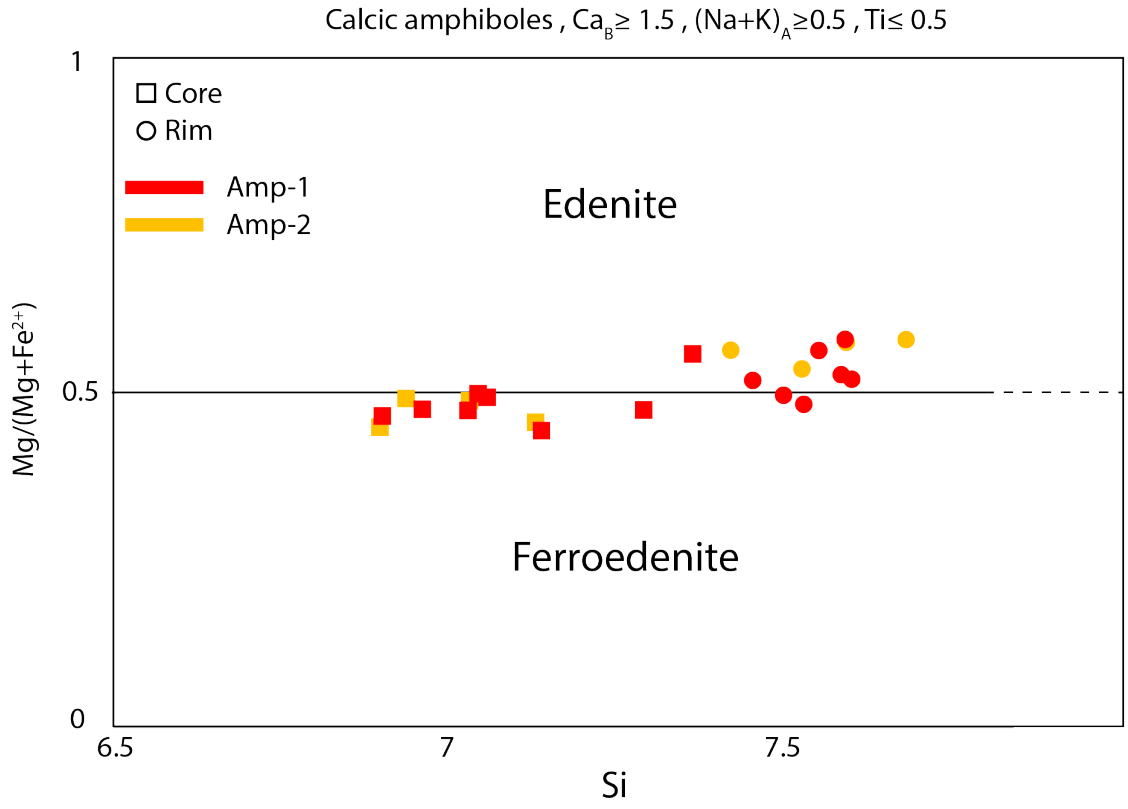

Figure 4.4. The classification of the core and rim regions in two different amphibole minerals according to Leake et al. (1997).

In this study, four amphibole-plagioclase feldspar couples in contact from BC12 and four from BC07 were chosen for pressure and temperature estimations. Since quartz is absent within the amphibolites, it was essential to use the edenite + albite = richterite + anorthite thermometer published by Holland and Blundy (1994), who suggested that this thermometer should be used in the temperature range of 500-900°C, consistent with amphibolite facies conditions. Because of the existence of anorthite in the equation, some plagioclase feldspars with pure albitic composition (0% An) in contact with amphiboles were not included in the calculations to make the equation work. Also, the publishers of the thermometer strictly argued that anorthite should be within the range of $0.1<X_{An}<0.9$. Therefore, examples with the highest anorthite concentrations in the feldspars were chosen. Also, the results giving lower than 2 kbar pressure were excluded because amphibolites are not expected to be formed around very low pressure values. The final results show that the average temperature values obtained from both of the samples are quite close to each other around ~530°C. Unlike the temperature results, the pressure estimates at site BC12 (~3 kbar) are lower than at site BC07 (~5.30 kbar). For the uncertainty of temperature and pressure values, typical uncertainty values (±50°C and ±1 kbar) were used (Fig. 4.5). The thermobarometer results (Table 4.2) and amphibole-plagioclase couples (Tables 4.3 & 4.4) used for the thermobarometer are given below.

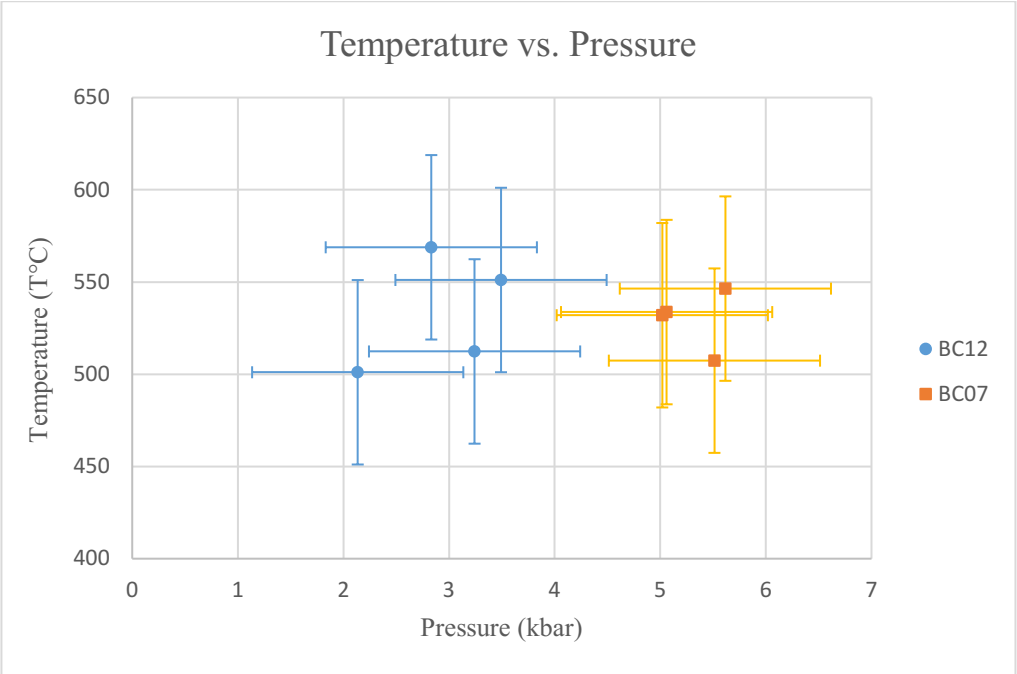

Figure 4.5. Pressure vs. temperature results with the uncertainty limits.

Table 4.2. Thermobarometer results of the studied amphiboles and average results for each sample. T-HB: temperatures based on Holland and Blundy (1994), P: pressures based on Anderson and Smith (1995).

Sample	BC1201				BC0701			
Amphibole	Am-H1	Am-H2	Am-H3	Am-H4	Am-H5	Am-H6	Am-H7	Am-H8
T-HB (±50°C)	551.09	568.81	501.06	512.35	507.36	533.7	531.98	546.42
P (±1 kbar)	3.4921	2.832	2.1352	3.2417	5.513	5.0602	5.0192	5.6165

	BC12	BC07
T (°C)	533.33	529.87
P (kb)	2.93	5.30
σ (T)	27.64	14.14
σ (P)	0.51	0.27

Table 4.3. The chemical compositions of the amphiboles used in the thermobarometer. The formulae based on 23 oxygen and all iron concentration is taken as FeO.

	BC12				BC07			
	Am-H1	Am-H2	Am-H3	Am-H4	Am-H5	Am-H6	Am-H7	Am-H8
SiO_2	48.05	48.67	49.53	48.38	47.64	48.41	47.91	47.08
TiO_2	0.34	0.42	0.00	0.46	0.58	0.74	0.58	1.01
Al_2O_3	7.88	7.10	7.09	8.05	10.65	9.92	9.92	10.43
FeO	20.38	17.91	19.42	19.50	13.50	13.15	13.68	13.86
MgO	10.36	12.10	11.22	10.89	13.76	13.70	14.12	13.81
MnO	0.00	0.00	0.00	0.00	0.00	0.00	0.00	0.00
CaO	9.65	11.36	9.69	9.43	12.10	12.27	12.18	11.99
Na_2O	2.84	2.01	2.58	2.79	1.48	1.48	1.38	1.49
K_2O	0.51	0.42	0.48	0.51	0.29	0.33	0.23	0.33
F	0.00	0.00	0.00	0.00	0.00	0.00	0.00	0.00
Cl	0.00	0.00	0.00	0.00	0.00	0.00	0.00	0.00
Total	100.01	99.99	100.01	100.01	100.00	100.00	100.00	100.00
T site								
Si	7.06	7.09	7.22	7.07	6.89	6.89	6.83	6.73
Al (iv)	0.94	0.91	0.78	0.93	1.11	1.11	1.17	1.27
Total *T site*	8.00	8.00	8.00	8.00	8.00	8.00	8.00	8.00
M1,2,3 sites								
Al (vi)	0.43	0.31	0.44	0.46	0.48	0.55	0.50	0.49
Ti	0.04	0.05	0.00	0.05	0.10	0.08	0.06	0.11
Fe^{3+}	0.00	0.00	0.00	0.00	0.00	0.00	0.00	0.00
Mg	2.27	2.63	2.44	2.37	3.09	2.90	3.00	2.94
Mn	0.00	0.00	0.00	0.00	0.00	0.00	0.00	0.00
Fe^{2+}	2.26	2.02	2.12	2.12	1.33	1.47	1.43	1.45
Ca	0.00	0.00	0.00	0.00	0.00	0.00	0.00	0.00
Total *M1,2,3 sites*	5.00	5.00	5.00	5.00	5.00	5.00	5.00	5.00
M4 site								
Fe	0.24	0.16	0.25	0.26	0.21	0.10	0.20	0.20
Ca	1.52	1.77	1.51	1.48	1.77	1.87	1.80	1.80
Na	0.24	0.07	0.24	0.26	0.02	0.03	0.00	0.00
Total *M4 site*	2.00	2.00	2.00	2.00	2.00	2.00	2.00	2.00
A site								
Ca	0.00	0.00	0.00	0.00	0.00	0.00	0.06	0.04
Na	0.57	0.50	0.49	0.53	0.40	0.38	0.38	0.41
K	0.10	0.08	0.09	0.10	0.06	0.06	0.04	0.06
Total *A site*	0.67	0.58	0.58	0.63	0.46	0.44	0.48	0.51

Table 4.4. The chemical compositions of the plagioclase feldspars used in the thermobarometer and the percentages of anorthite, albite and orthoclase for each plagioclase contact with amphibole grain.

	BC12				BC07			
	Am-H1	Am-H2	Am-H3	Am-H4	Am-H5	Am-H6	Am-H7	Am-H8
SiO_2	67.50	67.55	68.44	68.23	69.19	65.90	67.16	66.88
TiO_2	0.26	0.00	0.00	0.00	0.00	1.01	0.00	0.00
Al_2O_3	19.85	20.68	19.57	19.79	20.70	19.99	21.00	20.73
FeO	0.65	0.00	0.00	0.00	0.00	0.00	0.00	0.00
CaO	0.78	1.08	0.65	0.58	0.61	1.60	0.90	0.90
Na_2O	10.95	10.68	11.34	11.40	8.48	10.48	9.86	10.65
K_2O	0.00	0.00	0.00	0.00	0.75	0.88	0.78	0.58
Total	99.99	99.99	100.00	100.00	99.73	99.86	99.70	99.74
Si	2.96	2.95	2.99	2.98	3.00	2.91	2.94	2.94
Ti	0.01	0.00	0.00	0.00	0.00	0.03	0.00	0.00
Al	1.03	1.06	1.01	1.02	1.06	1.04	1.09	1.07
Fe^{2+}	0.02	0.00	0.00	0.00	0.00	0.00	0.00	0.00
Ca	0.04	0.05	0.03	0.03	0.03	0.08	0.04	0.04
Na	0.93	0.90	0.96	0.97	0.71	0.90	0.84	0.91
K	0.00	0.00	0.00	0.00	0.04	0.05	0.04	0.03
Sum Cat#	4.98	4.97	4.99	4.99	4.85	5.01	4.95	4.99
An	3.79	5.29	3.07	2.73	3.62	7.40	4.58	4.31
Ab	96.21	94.71	96.93	97.27	91.08	87.75	90.70	92.38
Or	0.00	0.00	0.00	0.00	5.30	4.85	4.72	3.31

4.1.3 Structural results

In the field, the metamorphic sole rocks outcrop in different places e.g. Fındıkpınarı, Şahna, and Arslanköy. This research is based only on the sole rocks in the Fındıkpınarı road cut section. According to the observations in wider region, sole rocks are imbricated in five different packages. All of the packages show a southerly dipping foliation that formed during regional metamorphism in a SSZ environment. The foliation is associated with a mostly NW-SE trending lineation within the foliation plane (Fig. 4.7). Only site BC07 shows a NE-SW trending lineation. The plunge and trend of the mean lineation is 49.5°/139.6° (α = 15.8°, kappa = 9.3). It is defined by the parallel alignment of mainly amphibole minerals in the amphibolites whereas mainly biotite defines the lineation in calcschists and chlorite in the metabasalts. A high angle shear zone (dip/dip direction = 84°/251°) is also observed in the amphibolites close to the overlying mantle tectonites.

NW SE

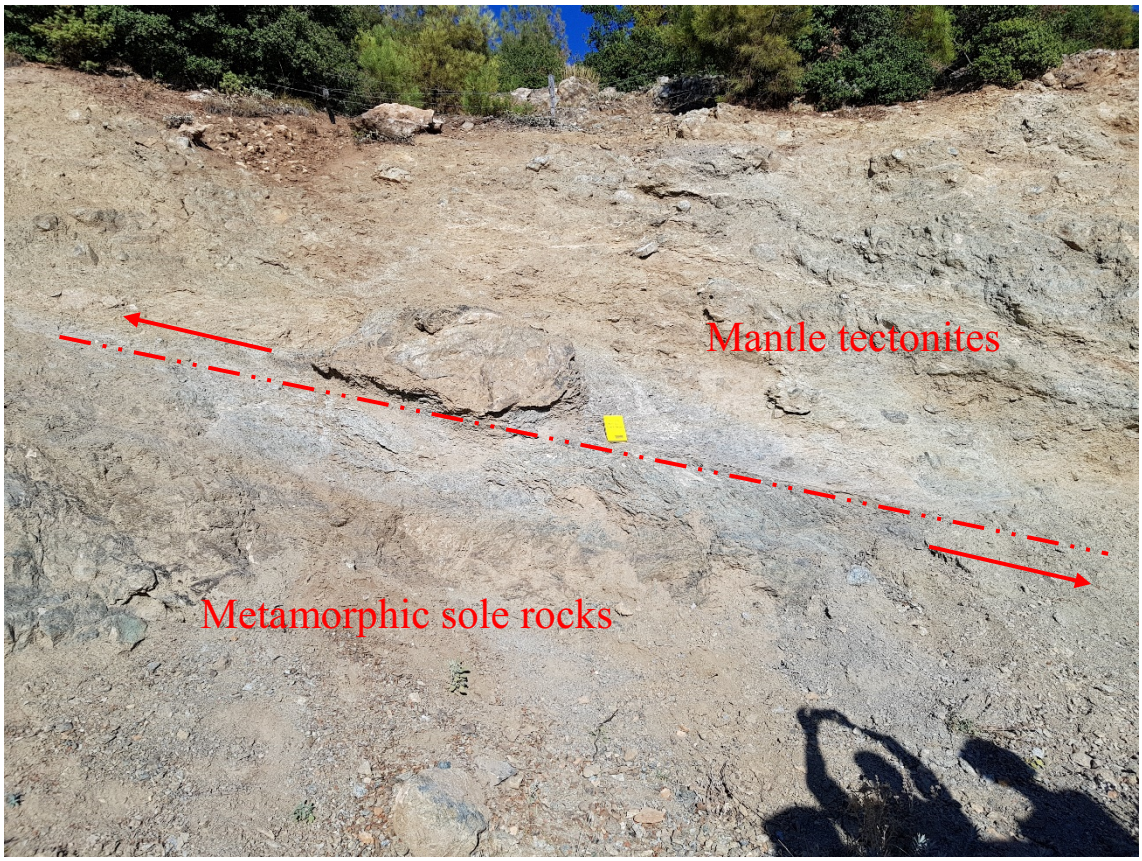

Figure 4.6. The contact between the Mersin metamorphic sole rocks and structurally overlying mantle tectonites of the Mersin ophiolite in the Fındıkpınarı road cut section (field notebook for scale).

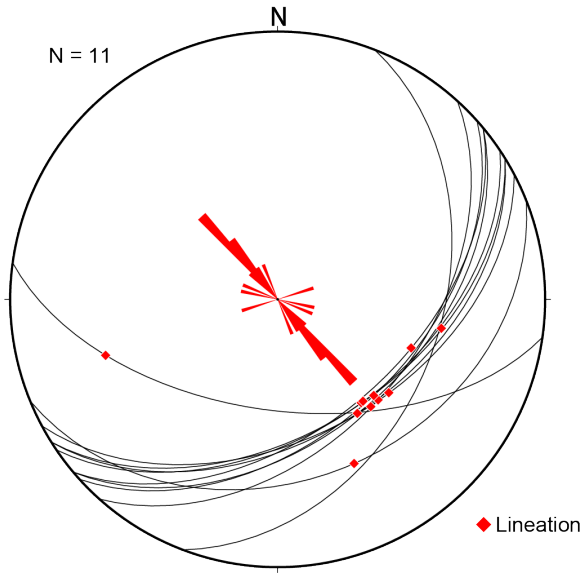

	Foliation		Lineation	
	Dip	Dip Direction	Plunge	Trend
BC0204	46	132	46	135
BC0301	47	148	45	130
BC0302	49	146	49	141
BC0401	48	138	48	135
BC0501	49	148	49	140
BC0701	56	188	35	252
BC1201	50	140	46	110
BC1601	33	158	33	155
BC1902	47	140	47	145
BC2001	39	111	38	100
BC2002	47	152	46	139

Figure 4.7. Equal area stereographic projection illustrating the foliation and lineation data collected in the field

Small-scale asymmetric fold structures have been also observed in some of the units, i.e. phyllite and amphibolites, rather than large-scale and intense folding structures. These can be classified as open and isoclinal folds. One of the fold structures observed in the amphibolite (site BC06) caused an overturning of the unit. The dip and dip direction of the overturned limb on the foliation plane and other limb were measured as 104°/230° and 59°/213°, respectively (Fig 4.8). The direction of the axial plane of the fold is 81°/222°.

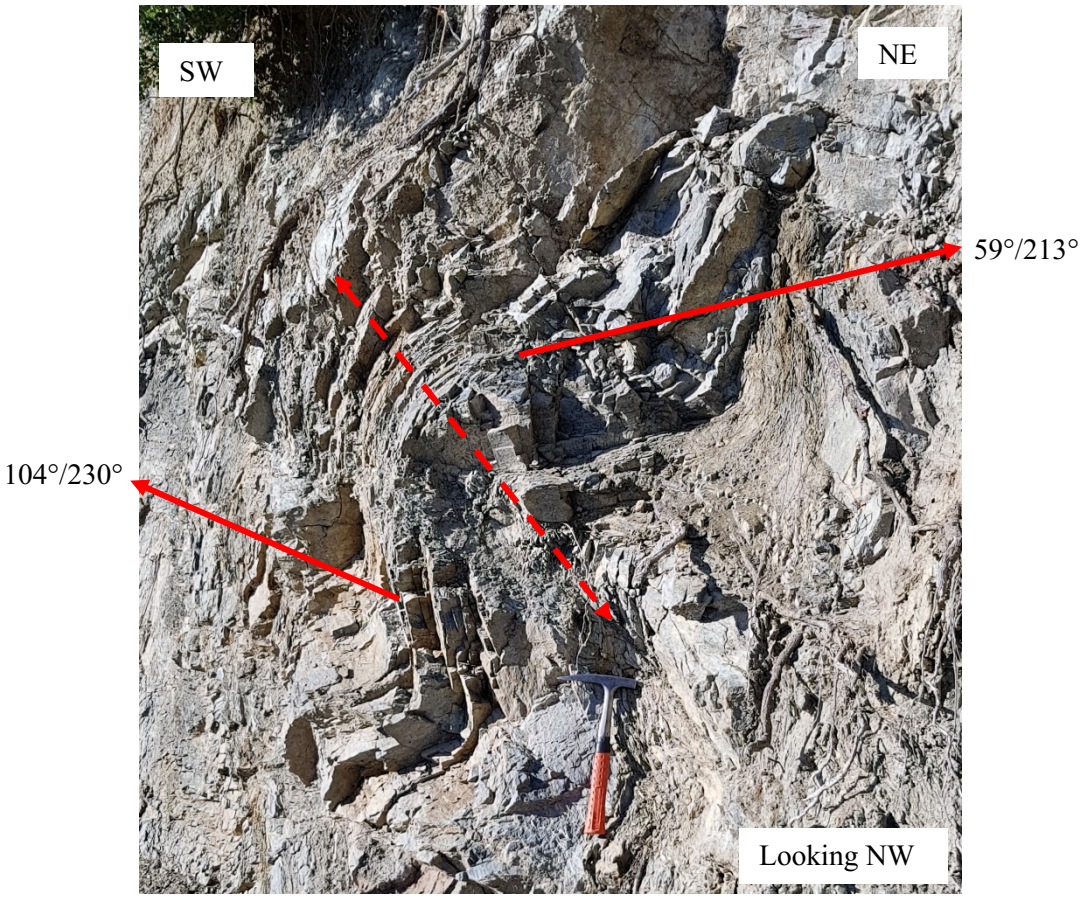

Figure 4.8. Small-scale fold structure at site BC06, where the foliation in the amphibolite is observed as overturned with 104°/230° orientation

More folds were observed towards NW of the section. Two samples were collected from the limbs of one of these folds. According to the fold analysis, the sampled fold is an open asymmetric syncline, with a steeply SE-dipping axial plane (84°/154°) and an inter-limb angle of 95°.

Shear sense indicators were observed at thin section scale. Some ductile structures have been observed during the fieldwork and studied further under the microscope. As a main aim, asymmetric indicators of shearing sense were searched for. Some structures indicate a top-to-the-

SE sense of shear whereas some kinematic indicators imply a top-to-the-NW sense of shear. On the other hand, most of the structures suggest a coaxial deformation, which makes the final shear direction even more unclear. In the site BC05 calcschist thin section, the mica fish structures (group 1 classification) (Fig. 4.9) along with biotites indicate top-to-the-SE, sinistral shearing. However, the opposite direction is represented in site BC16 with chlorite and micas indicating top-to-the-NW, non-coaxial deformation (Fig. 4.10).

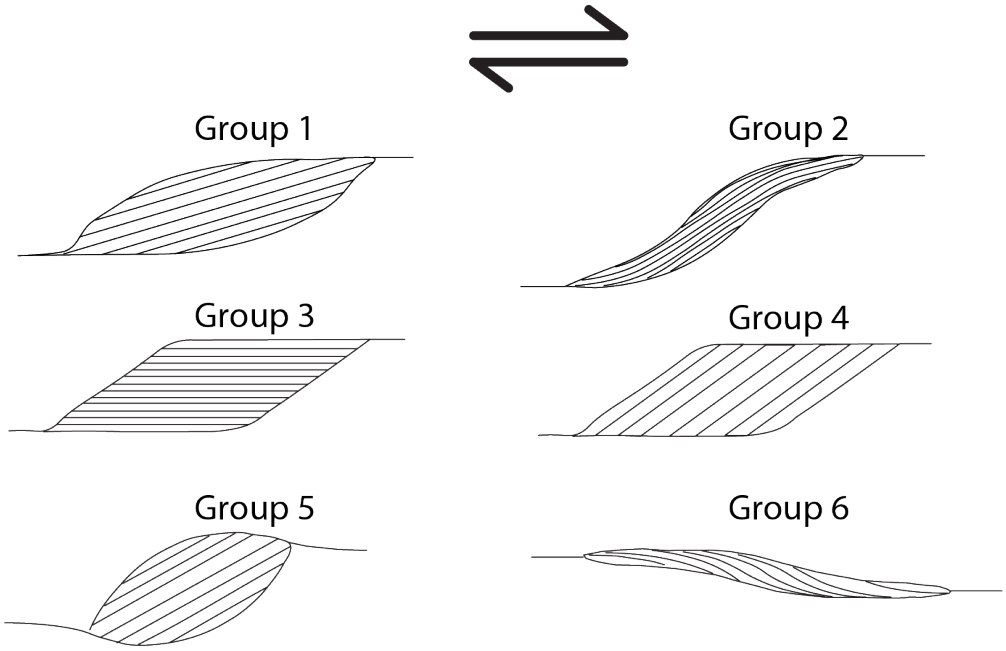

Figure 4.9. Schematic drawings of the different types of mica fish. Group 1, lenticular mica fish; Group 2, lenticular fish with points inclined in the direction of the foliation; Group 3, rhomboidal shaped fish with (001) parallel to longest side of the fish; group 4, rhomboidal shaped fish with (001) parallel to the shortest side of the fish; group 5, fish with small aspect ratio and curved tails; group 6, mica fish with high aspect ratio and inverted stair stepping; if considered out of their context, these structures could lead to an erroneous shear sense determination (from Ten Grotenhuis et al., 2003)

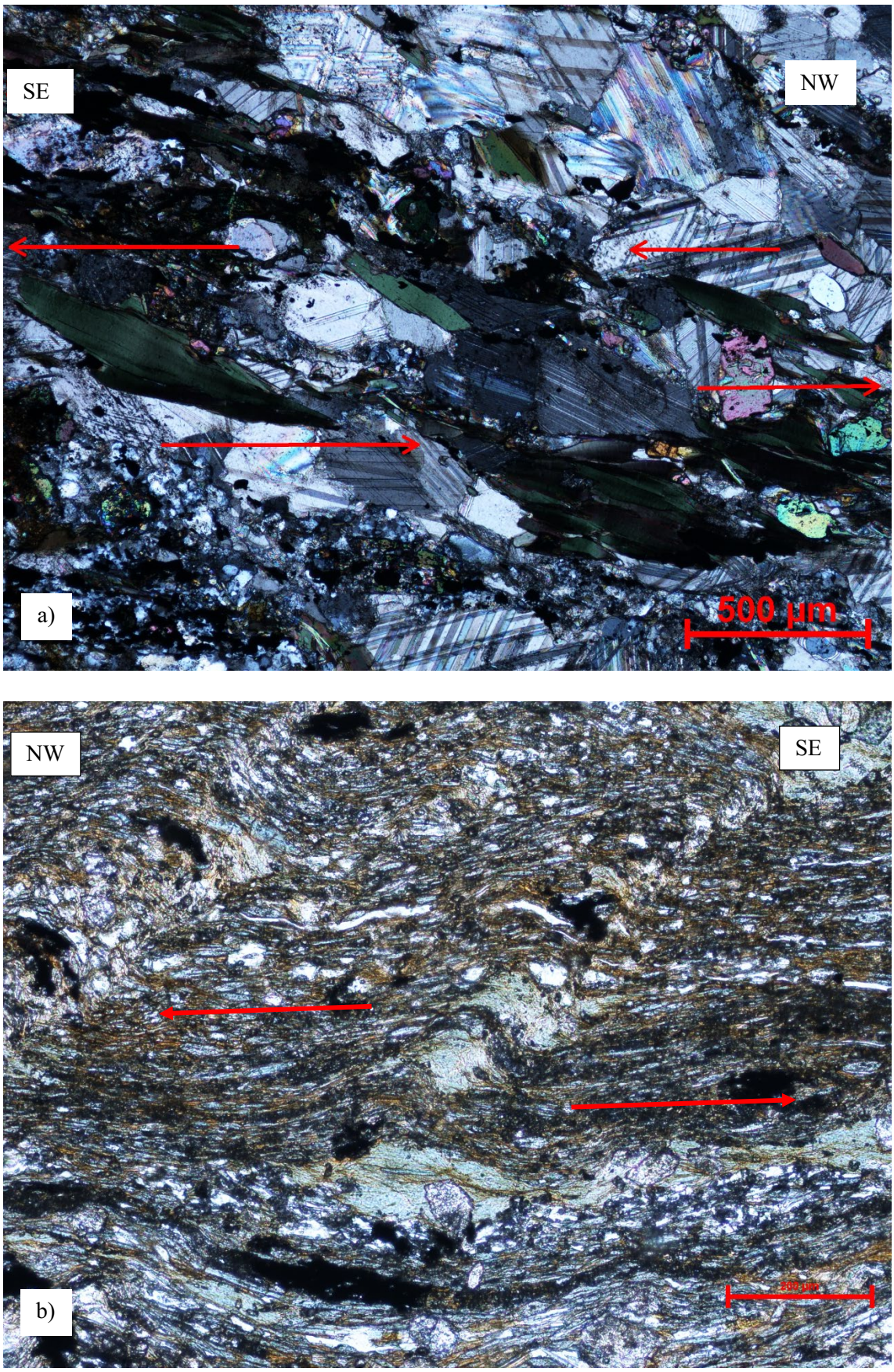

Figure 4.10. Different microstructural shear sense indicators from metamorphic sole rocks of Mersin ophiolite. a) Biotite minerals in calc-schist indicating top-to-the-SE shearing. b) Chlorite and mica minerals in metabasalt showing top-to-the-NW shearing.

4.2 Rock magnetic and palaeomagnetic results

4.2.1 Rock magnetic results

4.2.1.1 Isothermal remanent magnetization (IRM) results

Twenty-four specimens from 12 sites (including the dykes) that had already been AF demagnetized were used in IRM acquisition and backfield IRM experiments. Results are shown in Figure 4.11.

The dyke specimens reached saturation below 300 mT with average coercivities of remanence (defined as the backfield required to reduce the forward IRM to zero) of 70 mT. These data indicate that the magnetic remanence carrier in the dykes is most likely magnetite and/or titanomagnetite with medium coercivity.

Although some metamorphic sole rocks showed IRM increasing up to 500 mT, most samples become saturated around 300 mT with coercivities of remanence between 25-118 mT (with the highest coercivities of ~118 mT seen in two specimens from site BC04). Also, the specimens from sites BC11 and BC13 did not reach saturation by the maximum applied field of 800 mT and had coercivities of remanence >170 mT. This indicates the presence of two different magnetic carriers with high and low coercivity. The high coercivity mineral could be either hematite or goethite. In order to investigate this further, specimens BC1101B, BC1101E, BC1301A and BC1301C were exposed to an 800 mT field along the Z-direction and their IRMs were measured. Then they were thermally demagnetized at 150°C and the magnetizations measured again. A 25-45% decrease in IRM intensity was observed after thermal demagnetization. These values might have indicated that the mineral that becomes demagnetized at 150°C is goethite, which has a Curie temperature of 120°C (Lowrie, 1990). To test this further, the sample was then subjected to a backfield experiment. If the mineral with high coercivity was goethite, its remanence would have been removed by the thermal treatment and coercivities of remanence in the subsequent backfield experiment would reflect only the lower coercivity magnetite and/or titanomagnetite fraction. However, the results were instead more or less same as those obtained before thermal demagnetization. Hence, the phase that thermally demagnetizes at 150°C is considered to be titanomagnetite with the high coercivity signal attributed to minor hematite and/or titanohematite.

There was one more experiment performed to test for viscous remanent magnetization (VRM) in these rocks. To do this, an 800 mT field was again applied along Z-direction again. The remanence of the specimens was then measured repeatedly every 15 minutes for an hour and 30 minutes. However, no significant change in the magnetization was observed, which means VRM is not being acquired by these rocks.

Overall, all of the results from IRM and backfield IRM experiments show that ferromagnetic minerals in the specimens are in most likely pseudo single domain (PSD) or single domain (SD) or elongated single domain (ESD) magnetite and/or titanomagnetites with low to medium coercivity values. The existence of goethite was not observed. However, the presence of a high coercivity phase (not goethite, possibly hematite and/or titanohematite) is noted at two sites (Fig 4.11).

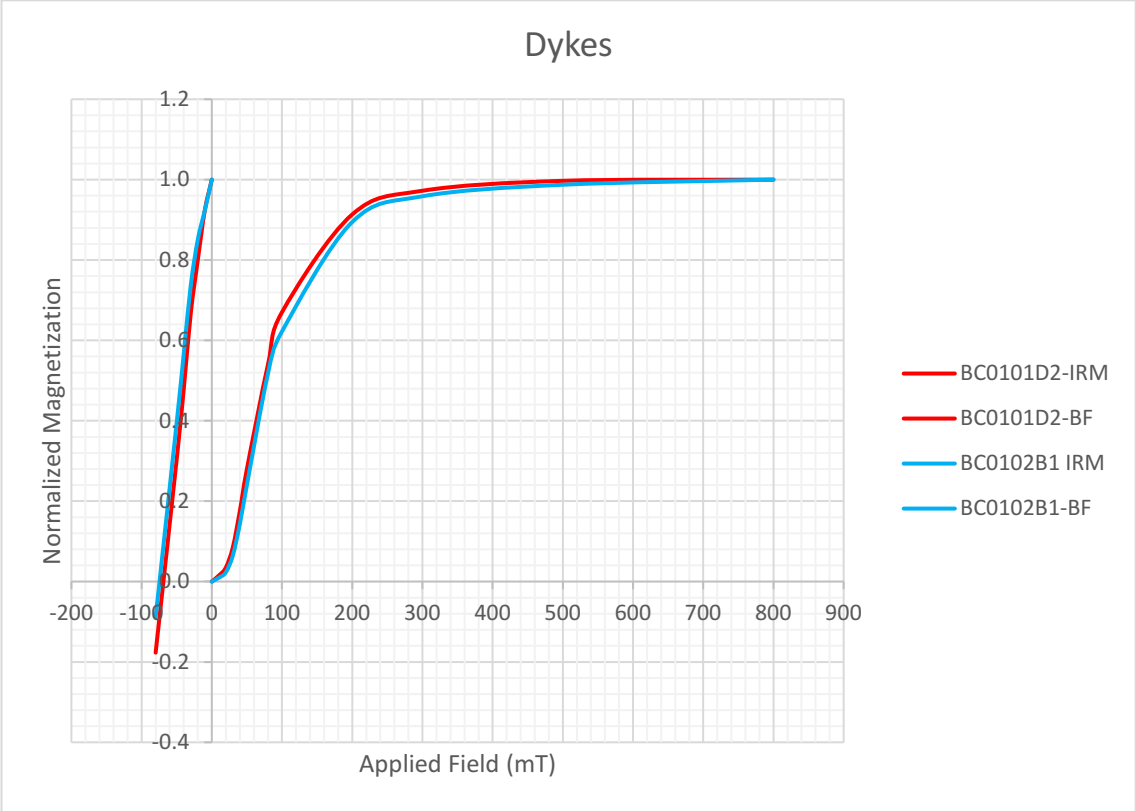

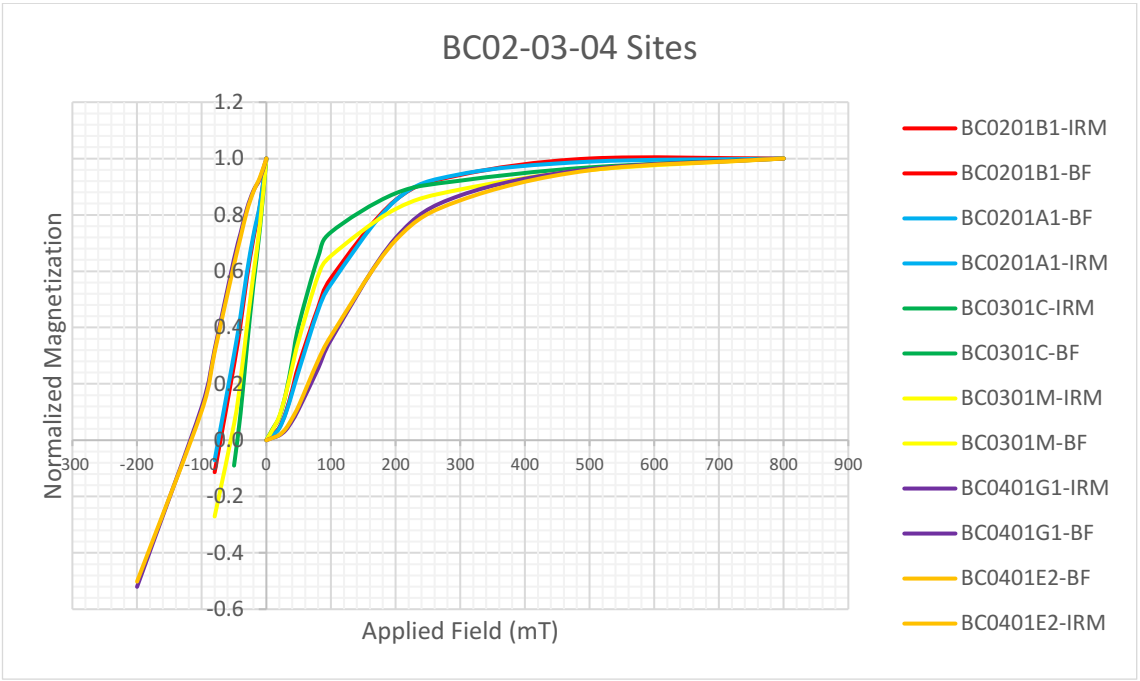
BC02-03-04 Sites
Normalized Magnetization
Applied Field (mT)
1.2
1.0
0.8
0.6
0.4
0.2
0.0
-0.2
-0.4
-0.6
-300
-200
-100
0
100
200
300
400
500
600
700
800
900
BC0201B1-IRM
BC0201B1-BF
BC0201A1-BF
BC0201A1-IRM
BC0301C-IRM
BC0301C-BF
BC0301M-IRM
BC0301M-BF
BC0401G1-IRM
BC0401G1-BF
BC0401E2-BF
BC0401E2-IRM

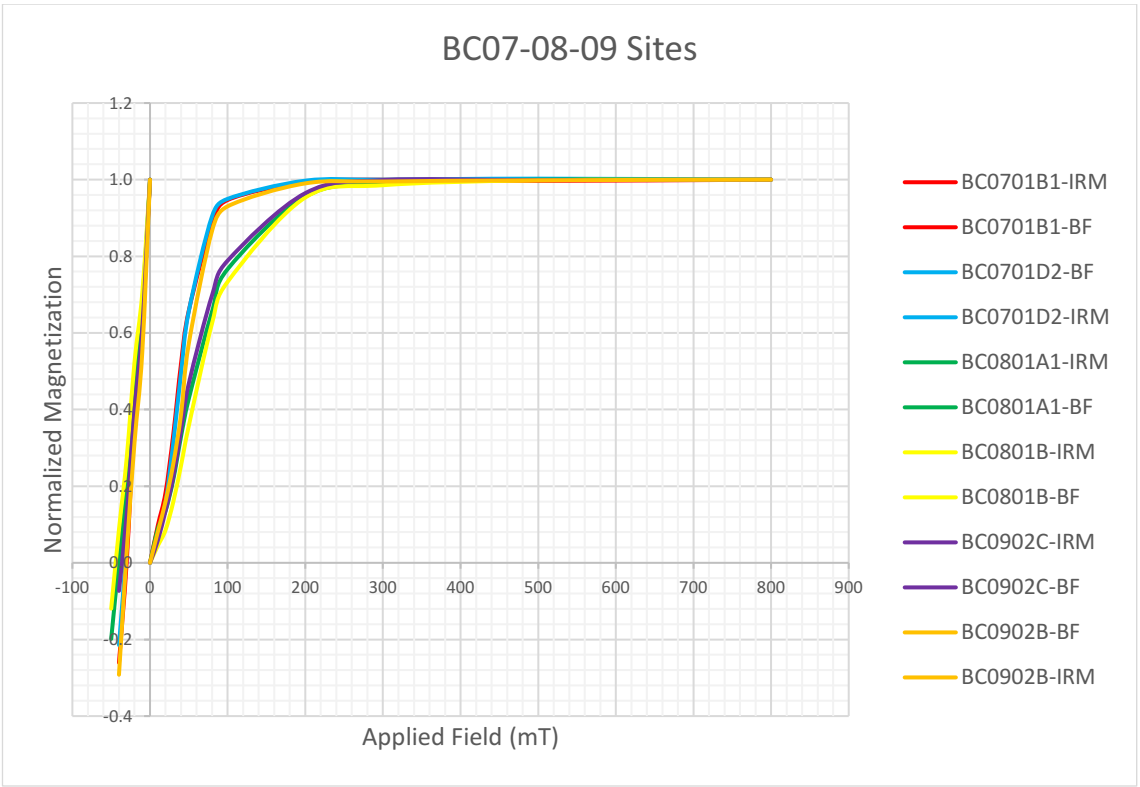
BC07-08-09 Sites
Normalized Magnetization
Applied Field (mT)
1.2
1.0
0.8
0.6
0.4
0.2
0.0
-0.2
-0.4
-100
0
100
200
300
400
500
600
700
800
900
BC0701B1-IRM
BC0701B1-BF
BC0701D2-BF
BC0701D2-IRM
BC0801A1-IRM
BC0801A1-BF
BC0801B-IRM
BC0801B-BF
BC0902C-IRM
BC0902C-BF
BC0902B-BF
BC0902B-IRM

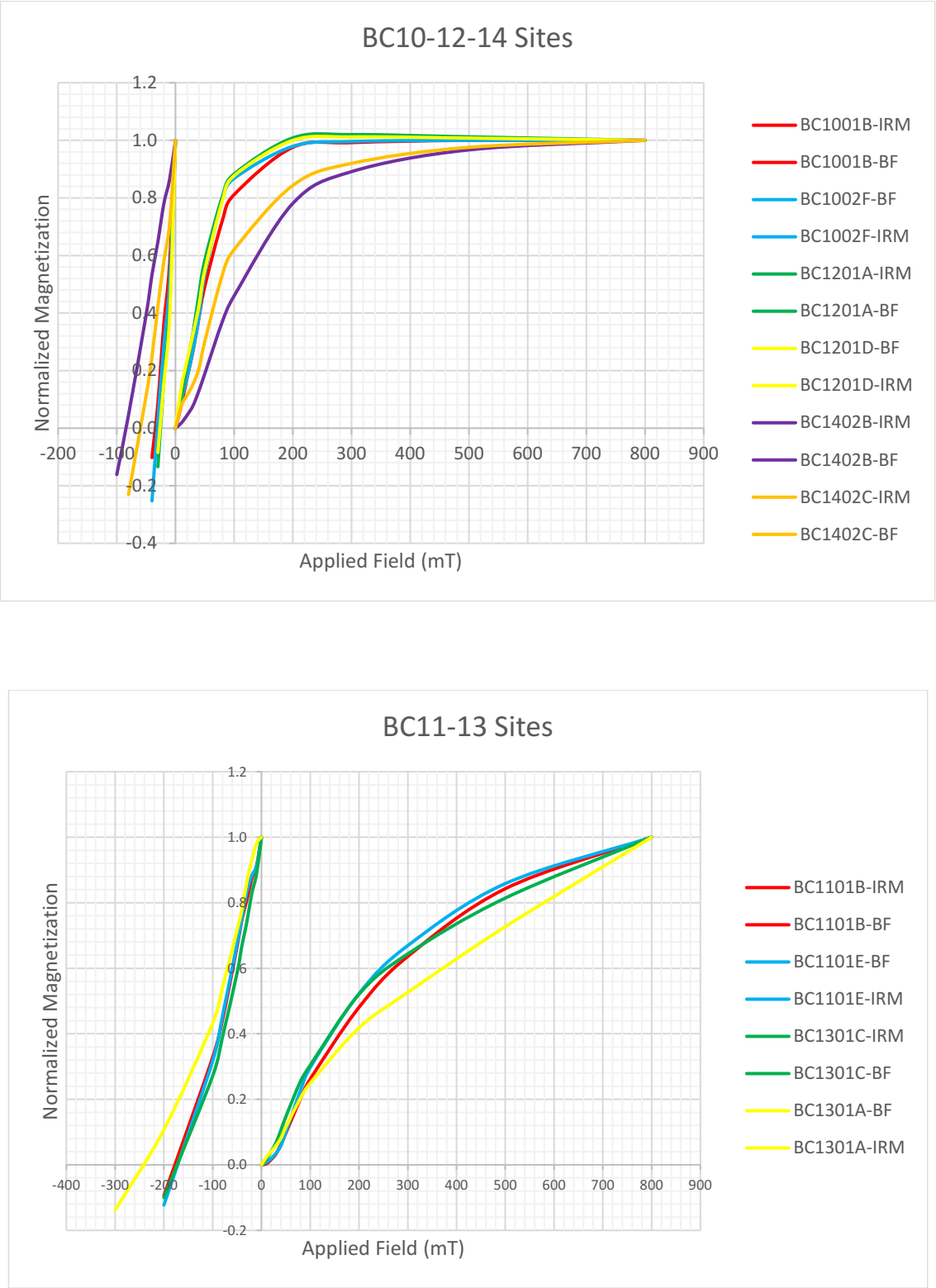

Figure 4.11. Isothermal remanent magnetization curves and back field values for 24 specimens from 12 sites of the Mersin ophiolite metamorphic sole rocks

Additionally, saturation IRM intensity, bulk susceptibility and coercivity of remanence data together were used to determine the domain state of the magnetic carriers, using the variation of the ratio of SIRM/k to coercivity of remanence, $(B_0)_{CR,}$ following the method of Thompson and

Oldfield (1986). These data suggest that ferromagnetic grains in these rocks are mainly in the pseudo-single and elongate single domain grain sizes (Fig. 4.12).

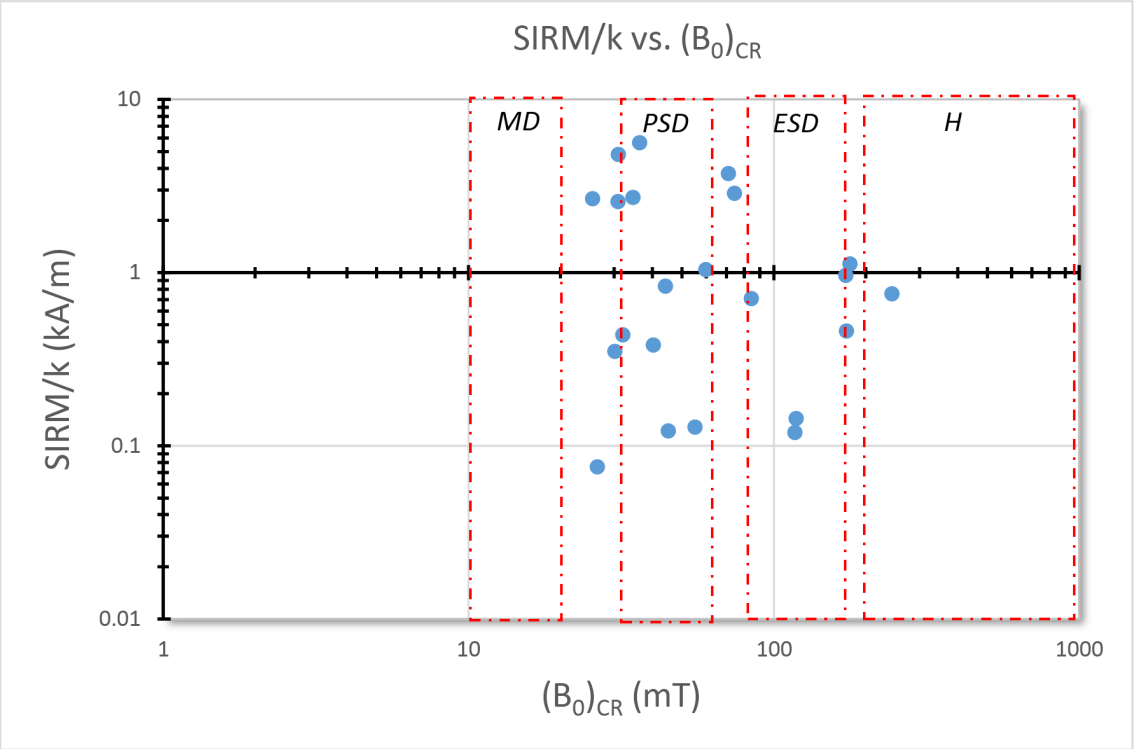

Figure 4.12. SIRM/k (kA/m) vs$(B_0)_{CR}$ graph (modified from Thompson and Oldfield, 1986)

4.2.1.2 Thermal demagnetization of three-component IRMs

This experiment was conducted on 12 AF demagnetized specimens from seven sites (BC01-x2, BC02-x1, BC03-x1, BC04-x2, BC07-x2, BC08-x2 and BC12-x2). After applying an 800 mT pulsed field along the Z direction, 300 mT along the Y direction and 50 mT along the X direction, they were thermally demagnetized until 680°C and measured at each temperature step. The identification of the magnetic carriers was found by the sudden slope changes in the plots obtained from the remanent magnetization results (Lowrie, 1990). Characteristic differences between the coercivity and unblocking temperature of ferromagnetic minerals were utilized to identify remanence carriers.

All three coercivity fractions show a progressive decrease in remanence intensity to 500°C, with magnetization continuing to decrease slightly along all axes between 500°C and 580°C. These results again clearly indicate the presence of magnetite. Only site BC08 (Figure 4.13) shows an additional stepped decrease in intensity between 100°C-150°C steps. In conjunction with

evidence from the IRM and backfield experiments, this probably results from presence of minor titanomagnetite with relatively high titanium content.

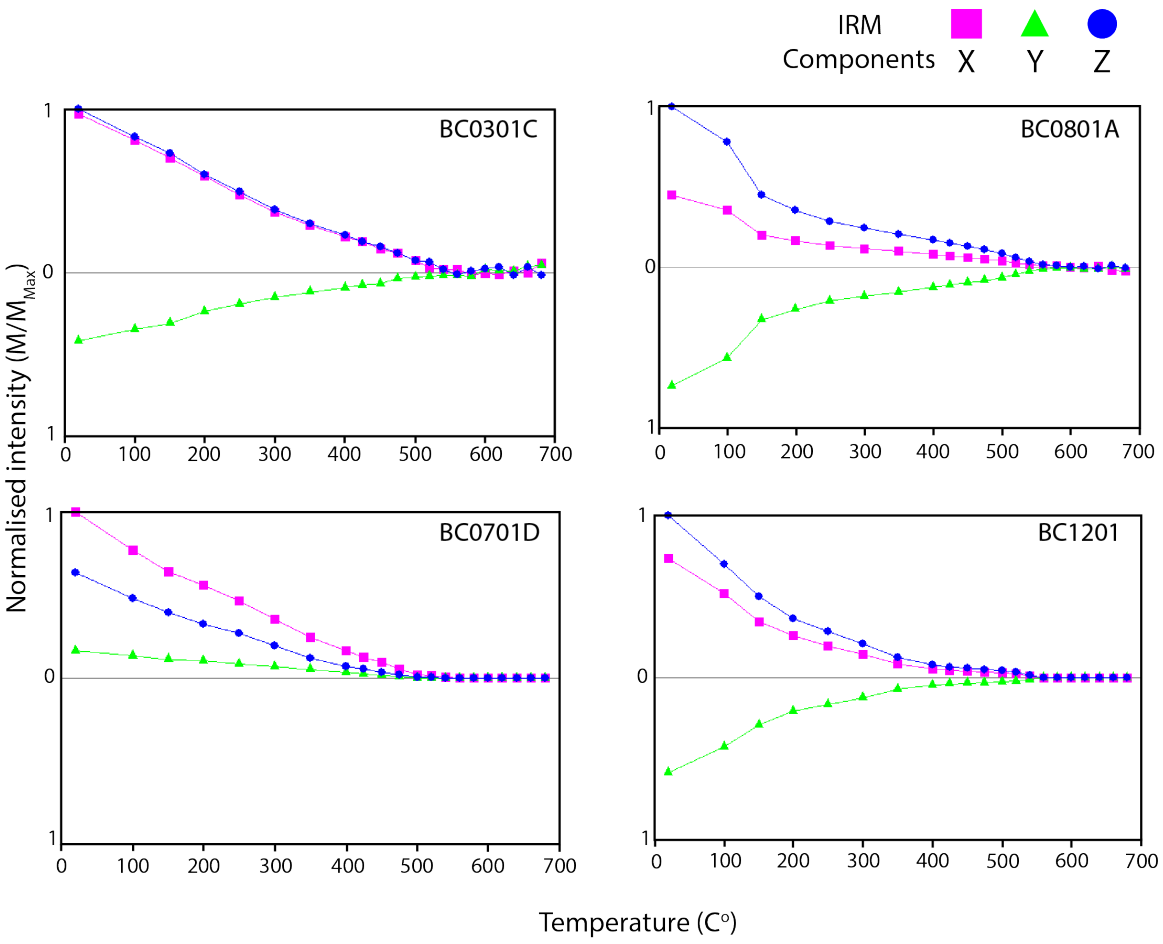

Figure 4.13. Some remanent magnetization results during thermal demagnetization of IRM acquired by applying field along the axes (X-direction:50 mT, Y-direction:300 mT and Z-direction:500 mT)

4.2.1.3 Thermomagnetic analyses for Curie points

High temperature susceptibility experiments were performed on five sole rock specimens to determine the Curie temperatures of the magnetic carriers. Each specimen was heated up to 700°C and then cooled to room temperature in an argon gas environment to minimize the risk of possible alteration or new mineral formation. Data from the metamorphic sole rocks (BC0201B, BC0201B, BC0302A, BC0401B and BC0701E) suggest presence of two different magnetic behaviours. The ferro/para resolution graphics clearly show that one of them is due to a paramagnetic susceptibility signal based on the low field susceptibility variations depending on temperature (Fig. 4.14) whereas the other one is ferromagnetic. Paramagnetic minerals are most likely amphibole (based on the petrography), and the decrease in susceptibility at around 560-

580°C indicates the presence of magnetite. No bumps or abnormal changes during the heating or cooling phases were observed, hence there is no other evidence for any other magnetic carriers within the sole rocks. Plots from Cureval8 software with hyperbola fittings (Fig. 4.15) for a paramagnetic signal on the heating cycle in the sole rocks are given below. An average error margin of 0.3% was obtained while fitting the hyperbolas and the average consistence of hyperbola fitting to the ideal paramagnetic state was 85%.

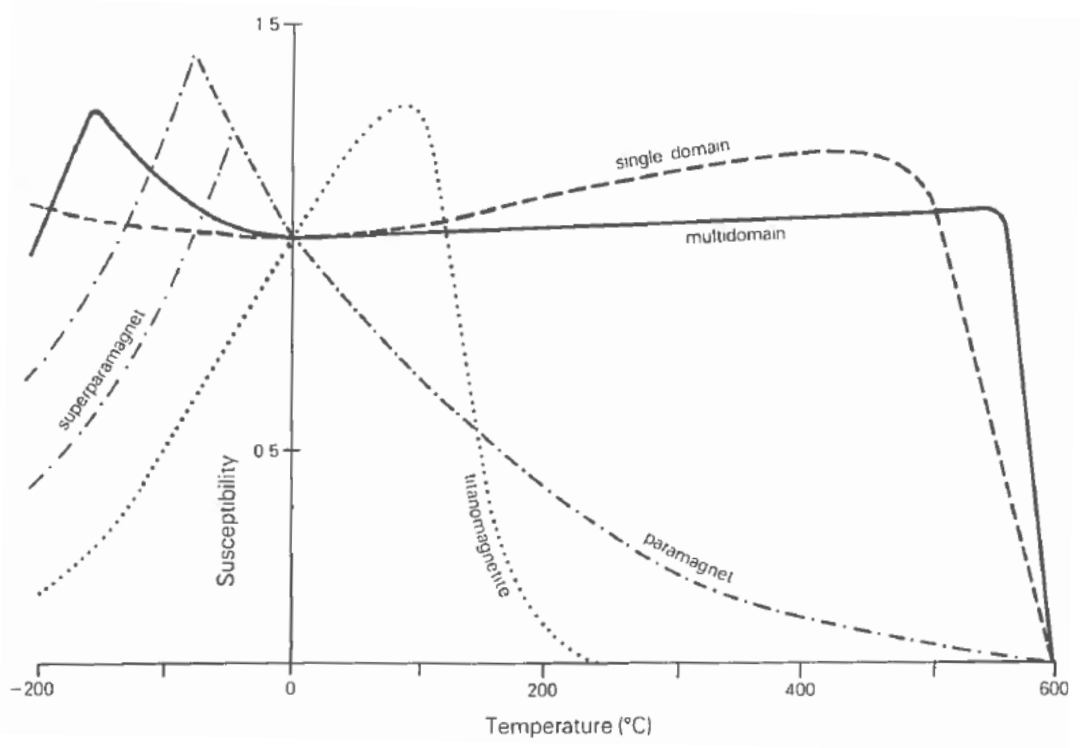

Figure 4.14. Schematic illustration of the variations of low field susceptibility with temperature for different magnetite states and compositions. Results from sole rocks (see Figure 4.15) indicate the same variation as that of paramagnetic phases (from Thompson and Oldfield, 1986)

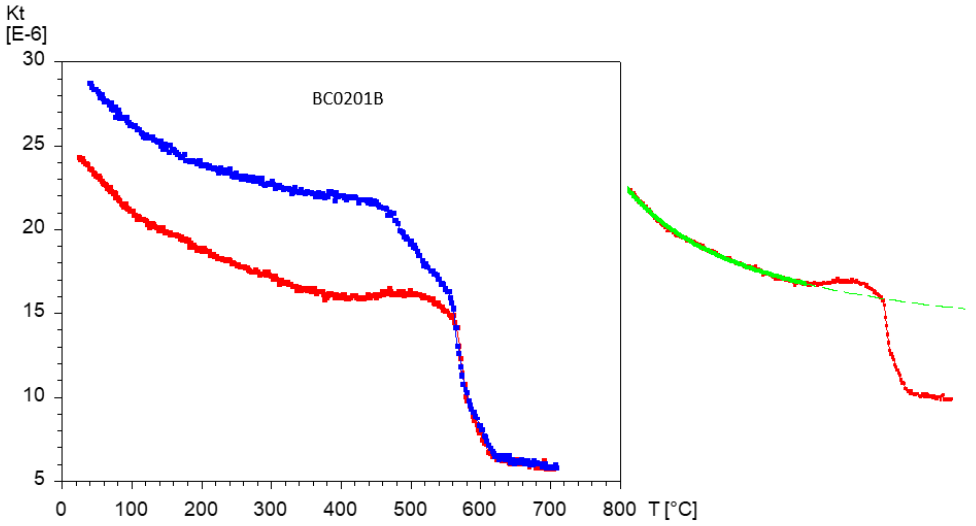
Kt
[E-6]
30
25
20
15
10
5
BC0201B
0
100
200
300
400
500
600
700
800
T [°C]

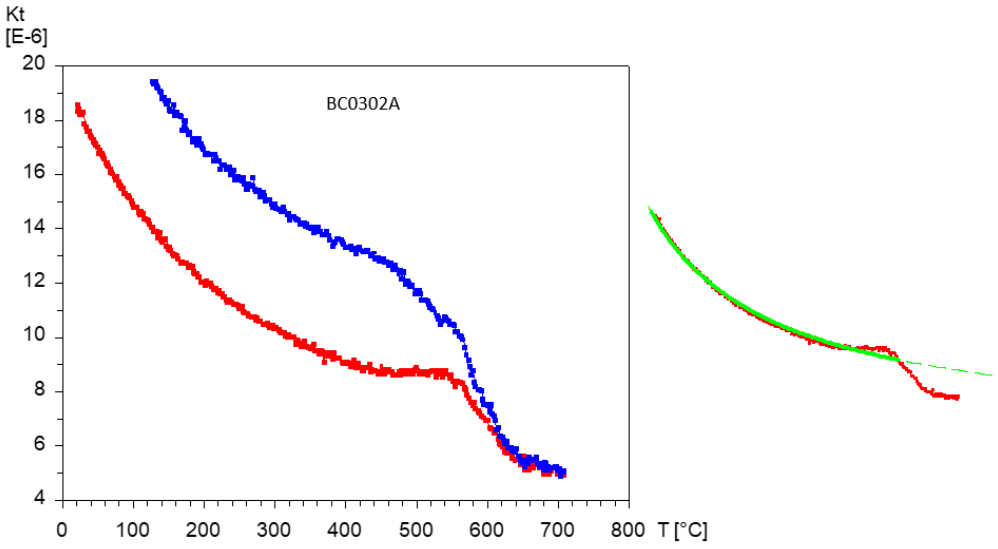
Kt
[E-6]
20
18
16
14
12
10
8
6
4
BC0302A
0
100
200
300
400
500
600
700
800
T [°C]

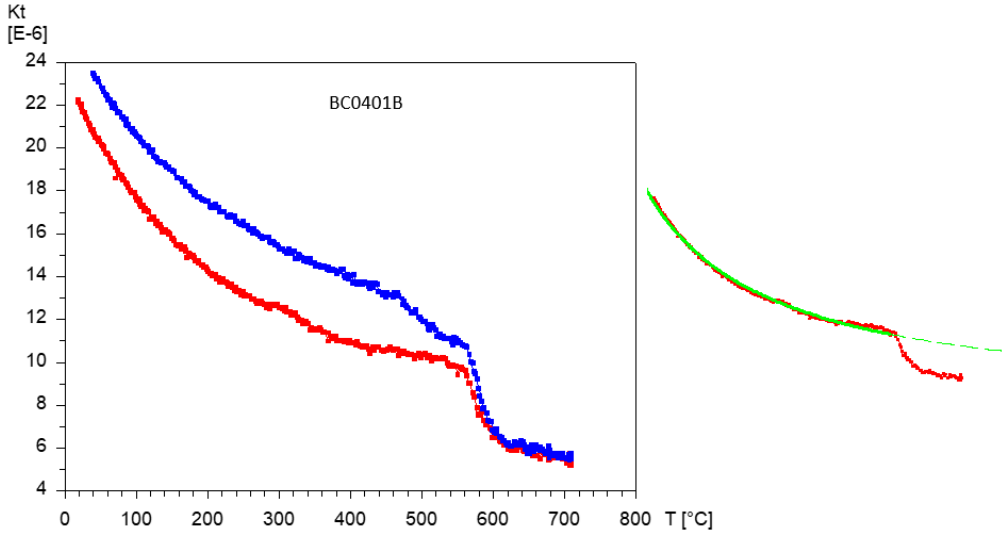
Kt
[E-6]
24
22
20
18
16
14
12
10
8
6
4
BC0401B
0
100
200
300
400
500
600
700
800
T [°C]

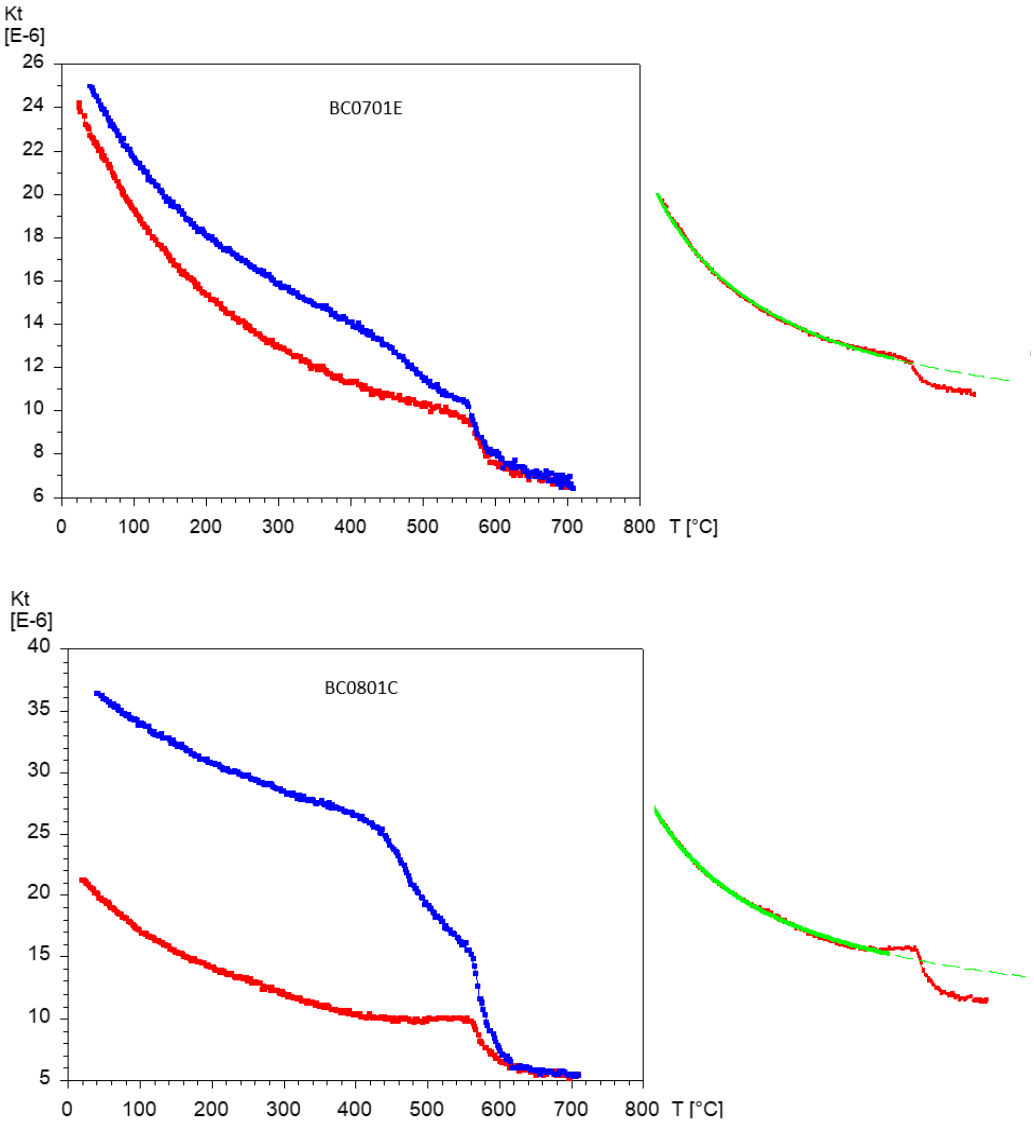

Figure 4.15. High temperature vs. susceptibility results from thermomagnetic experiments of five metamorphic sole rock specimens to determine the Curie points. The red curves indicate the results during the heating, blue curves indicate the results during the cooling and green lines indicate the hyperbola fittings for a paramagnetic state.

4.2.2 Magnetic fabric results

AMS data were determined using an AGICO KLY-3 Kappabridge for 110 specimens (96 from metamorphic sole rocks). Only specimen BC0301B could not be measured because of its small size. Processing yielded determinations of a range of anisotropy factors, the principal axes of the AMS ellipsoids and bulk susceptibility values.

P_j implies strength of anisotropy i.e. P_j=1.03 implies 3% anisotropy and T parameter where T>0; Oblate (disc) shape, T<0; Prolate (cigar) indicates shape parameter (Tarling and Hrouda, 1993).

These parameters were shown in Jelinek plots using the Anisoft42 software and also plotted on Borradaile (1987) plots.

4.2.2.1 Anisotropy parameters and bulk susceptibility results

Bulk susceptibility values range between 0.38 x 10^{-3} SI and 7.85 x 10^{-3} SI for the metamorphic sole rocks whereas dyke specimens range between 4.83 x 10^{-4}SI and 6.54x10^{-4} SI. Hrouda (2010) argued that if the bulk susceptibility is higher than 5x10^{-3} SI (strongly magnetic rocks), paramagnetic and diamagnetic minerals can be neglected and ferromagnetic minerals effectively control the AMS. On the other hand, AMS is controlled by both paramagnetic and ferromagnetic minerals if the bulk susceptibility ranges between 0.5 x 10^{-3} and 5 x 10^{-3} (Hrouda, 2010). Susceptibilities of metamorphic sole rock samples in this study are concentrated in the region around 1 x 10^{-3} SI as seen in the histogram of Figure 4.16. These values suggest that the bulk susceptibilities are dominated by paramagnetic minerals, i.e. amphibole, with a more limited signal from magnetite (Fig. 4.17). In addition to bulk susceptibilities, other experiments i.e. thermomagnetic analyses also indicate the existence of both paramagnetic and ferromagnetic minerals. The bulk susceptibility distribution of the metamorphic sole rocks is also consistent with the range reported for amphibolites by Hrouda (2010) (Fig. 4.18).

The bulk susceptibility range of the dykes hosted by the metamorphic sole rocks was presented by Omer (2014). According to that study, the bulk susceptibility range was 0.70 x 10^{-3} - 4.35 x 10^{-3} (based on analysis of 82 specimens from four different dykes). The bulk susceptibility results in this study are quite similar these values.

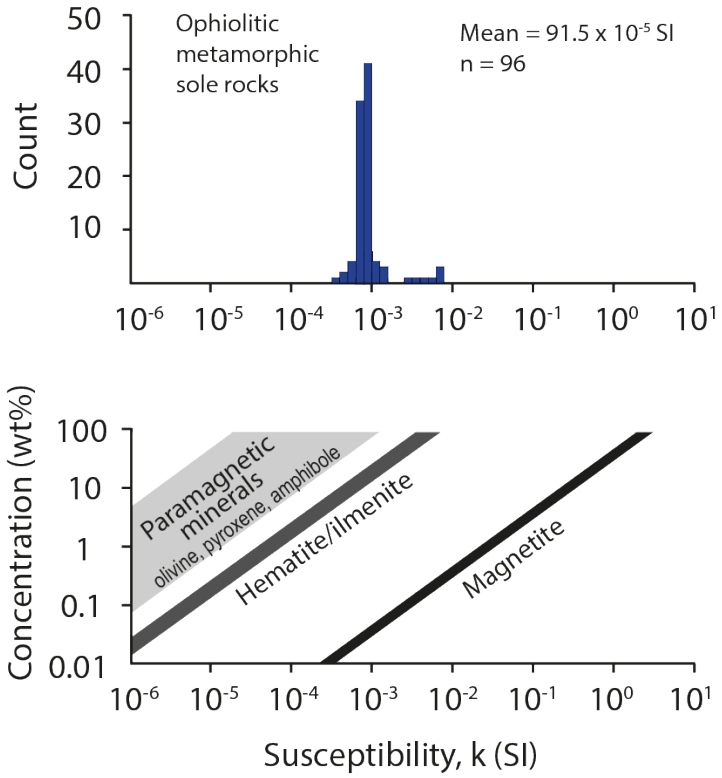

Figure 4.16. Histogram of bulk susceptibilities of metamorphic sole rocks compared to values predicted from different common mineral assemblages (from Tarling and Hrouda, 1993).

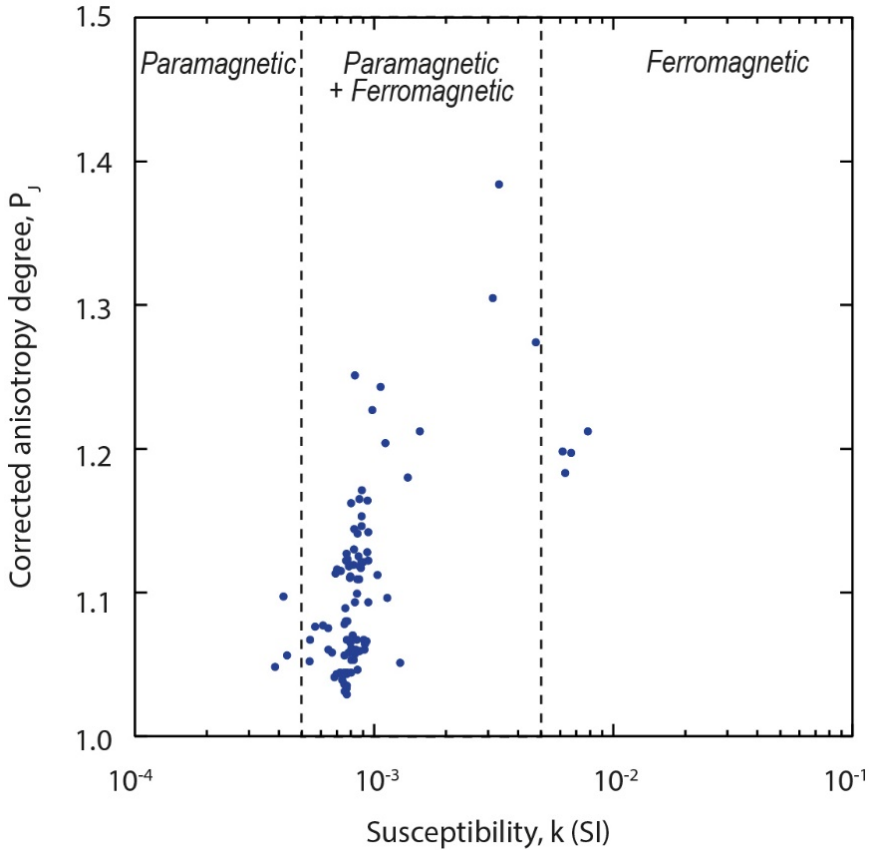

Figure 4.17. Bulk susceptibility against corrected anisotropy degree (P_j) for the Mersin metamorphic sole rocks. Most of the samples indicate that AMS is most likely controlled by both paramagnetic and ferromagnetic minerals.

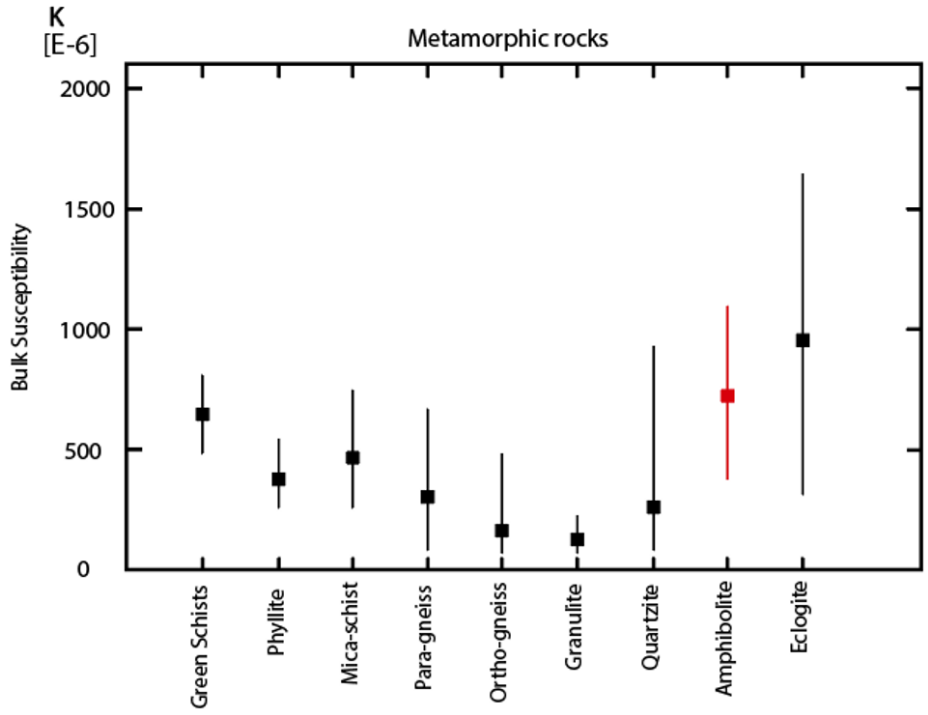

Figure 4.18. Generalized bulk susceptibility values for different metamorphic rocks. The amphibolite is consistent with the samples from this study (modified from Hrouda, 2010).

The measured mean anisotropy parameters and AMS principal axis orientations at all sites are reported in Table 4.5.

Table 4.5. Magnetic fabric results (AMS directions and parameters) of dyke specimens and sole rocks. Note: two specimens from the folded region at site BC10 are not included in mean value.

		Mean										
		K_{Max}			K_{Int}			K_{Min}			Parameters	
Site	n	Dec	Inc	Conf. Angles	Dec	Inc	Conf. Angles	Dec	Inc	Conf. Angles	Pj	T
BC01	14	064.0	27.3	14.0/4.6	184.0	44.1	13.3/6.5	314.0	33.6	6.9/6.2	1.007	0.088
BC02	14	086.6	37.1	32.8/4.2	214.8	39.2	33.0/5.5	331.8	29.0	30.1/5.5	1.084	0.598
BC03	16	119.7	49.0	9.3/3.4	225.7	13.4	09.2/2.7	326.3	37.8	3.9/2.4	1.040	0.596
BC04	17	145.2	47.0	5.8/2.0	238.5	03.1	05.9/2.2	331.4	42.9	2.7/1.9	1.059	0.589
BC07	12	171.3	53.7	20.3/7.2	272.8	08.3	20.4/3.0	008.6	35.0	7.2/3.5	1.125	0.893
BC08	5	098.6	44.7	7.1/1.3	192.5	03.7	07.4/0.9	286.2	45.1	2.1/1.3	1.080	0.712
BC09	7	109.1	44.9	7.3/2.2	212.3	12.9	11.5/3.3	314.3	42.2	11.5/1.9	1.154	0.317
BC10	7	021.4	37.0	12.2/1.1	277.0	18.3	12.2/2.4	166.1	47.3	2.6/1.2	1.108	0.902
BC11	4	032.4	35.2	-	279.4	25.3	-	161.0	41.7	-	1.208	0.793
BC12	4	110.3	46.3	-	213.0	11.2	-	312.2	40.9	-	1.197	0.012
BC13	3	114.3	16.6	-	211.8	26.6	-	357.3	56.6	-	1.114	0.820
BC14	5	281.2	04.6	26.8/4.6	189.1	24.8	26.1/4.0	021.0	64.7	9.4/2.3	1.109	0.814

For the anisotropy parameters, P_j values of dyke specimens ranging between 1.007 and 1.009, which suggests low anisotropy degrees for the dykes cutting cross the sole rocks. Shape parameters (T) show a range between -0.061 and 0.096, indicating both prolate and oblate shapes

of ellipsoids (Fig. 4.19). These results are entirely consistent with the data reported previously from the metamorphic sole hosted dykes of the Mersin ophiolite (Omer, 2014).

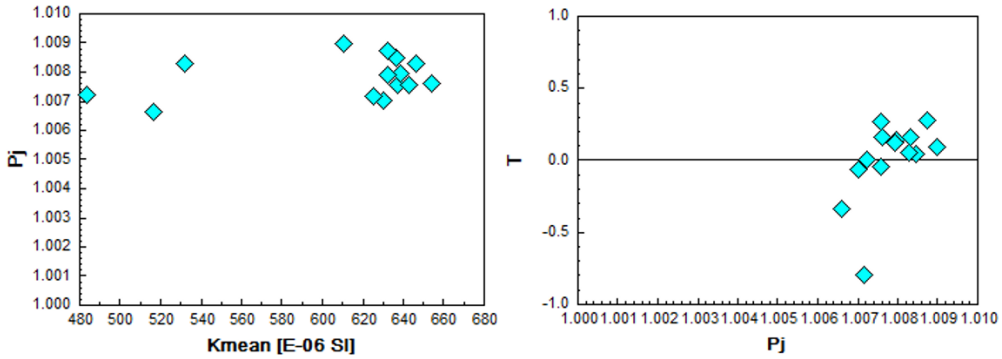

Figure 4.19.K_{mean} vs. P_j and P_j vs. T graphs of the gabbroic dyke from the Mersin ophiolite.

Metamorphic sole rocks show a wider range of magnetic fabrics than the dykes. P_j values are between 1.028 and 1.383 which suggest low to high degrees of anisotropy. All of the shape parameter (T) values are positive in the sole rocks, indicating that AMS ellipsoids are oblate (disc-shaped) (Fig. 4.20).

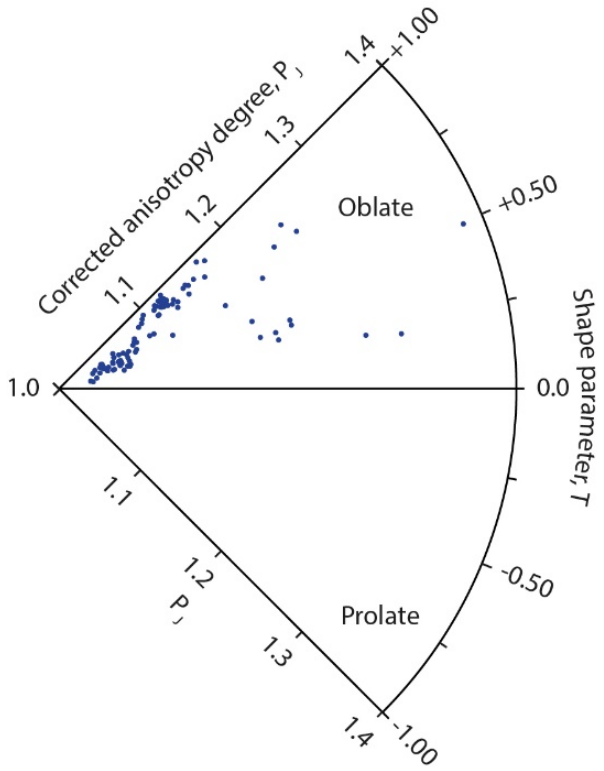

Figure 4.20. Corrected anisotropy (P_j) vs. Shape parameter (T) diagram for the metamorphic sole rocks of the Mersin ophiolite. All specimens indicate oblate (disc shaped) AMS ellipsoids.

Overall, these results from both dyke and sole rocks neither show a correlation between P_j and mean bulk susceptibility nor imply a relationship between T and P_j. Therefore, it can be interpreted that ferrimagnetic concentration does not affect the degree of anisotropy. Moreover, it is suggested that magnetic anisotropy degree and deformation increase as long as metamorphism intensity raises (Hrouda and Janák, 1976). The gradual increase of the magnetic anisotropy degree through the specimens is randomly distributed however, and even at the site level magnetic anisotropy may vary from low to high, i.e. in site BC09. Therefore, excessive variations in metamorphism degree at the time of the formation of sole rocks is not implied.

4.2.2.2 Distribution of AMS principal axes

If all AMS data from the metamorphic rocks are examined, they are consistent across all sites and clearly related to the structure. The eigenvalue method of Woodcock (1977) was used to specify the fabric shape distributions of the different principal axes (K_{max}, K_{int} and K_{min}). After obtaining eigenvalues for each direction [v_1,v_2,v_3] from Stereonet10 (Allmendinger, 2018), normalised values [S_1,S_2,S_3] and the ratios $\ln(S_2/S_3)$ and $\ln(S_1/S_2)$ were determined. Two other parameters (C and K_x) were also used to be able to specify the distributions. The C [= $\ln(S_1/S_3)$] parameter indicates the strength of the preferred orientation and if this value is <1 , the strength is considered as weak. However, if it is greater than three, it indicates strong preferred orientation. On the other hand, K_x [= $\ln(S_1/S_2)/\ln(S_2/S_3)$] describes the girdle/cluster tendency of the data. In order to understand the relationship between the AMS axes and foliation plane, the mean foliation was calculated as 42°/148° (dip/dip direction), α_{95}=6.8°, to represent whole road cut section where sole rocks uniformly dip towards SE. Some local measurements not representing the mean foliation i.e. around small folds, high angle shear zones etc. are not included in this calculation.

	S_1	S_2	S_3	$\ln(S_1/S_2)$	$\ln(S_2/S_3)$	$C=\ln(S_1/S_3)$	$K_x=\ln(S_1/S_2)/\ln(S_2/S_3)$
K_{Max}	1.000	0.256	0.051	1.364	1.602	2.966	0.852
K_{Int}	1.000	0.287	0.098	1.248	1.074	2.322	1.163
K_{Min}	1.000	0.101	0.048	2.296	0.735	3.031	3.124

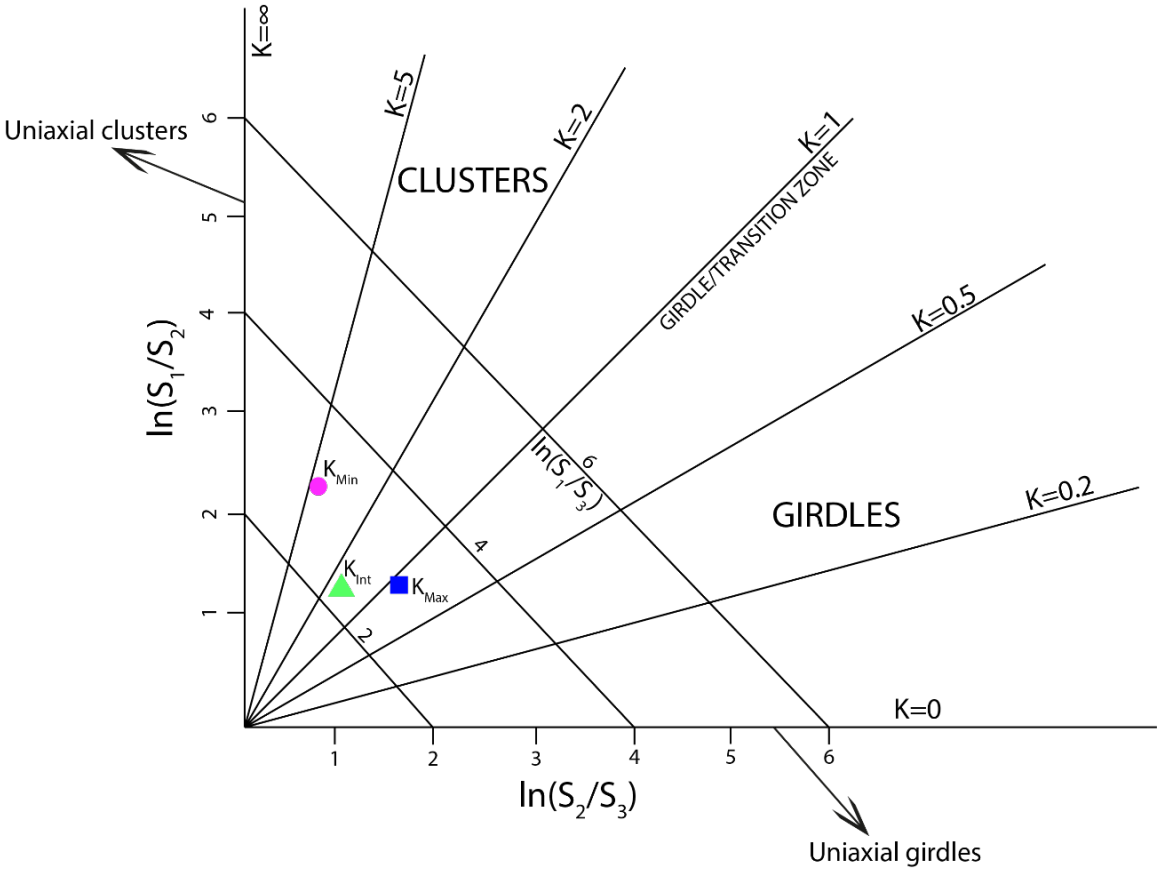

Figure 4.21. Logarithmic plot of the ratios of normalized eigenvalues of each AMS principal direction (after Woodcock, 1977).

K_{max} axes ($K_x \approx 1$ and $C \approx 3$) lie close to the transition from girdle to clustered distributions and are oriented close to the foliation plane and generally dip towards the east (Figs. 4.21 and 4.22). K_{int} axes ($K_x > 1$ and $C > 2$) are also lie close to or in the foliation plane and plunge shallowly to the SW. K_{min} axes have a strongly clustered distribution ($K_x > 3$ and $C > 3$) dipping towards the NW close to the pole to the foliation plane (Fig. 4.22). Overall, for all of the results, K_{max} directions represent a magnetic lineation in the plane of the foliation and K_{min} directions coincide with the pole to the metamorphic foliation in the sole rocks. These results show that the AMS ellipsoids in metamorphic sole amphibolites are coaxial to the main structural elements (Fig. 4.22) and provide an accurate proxy for structural fabrics.

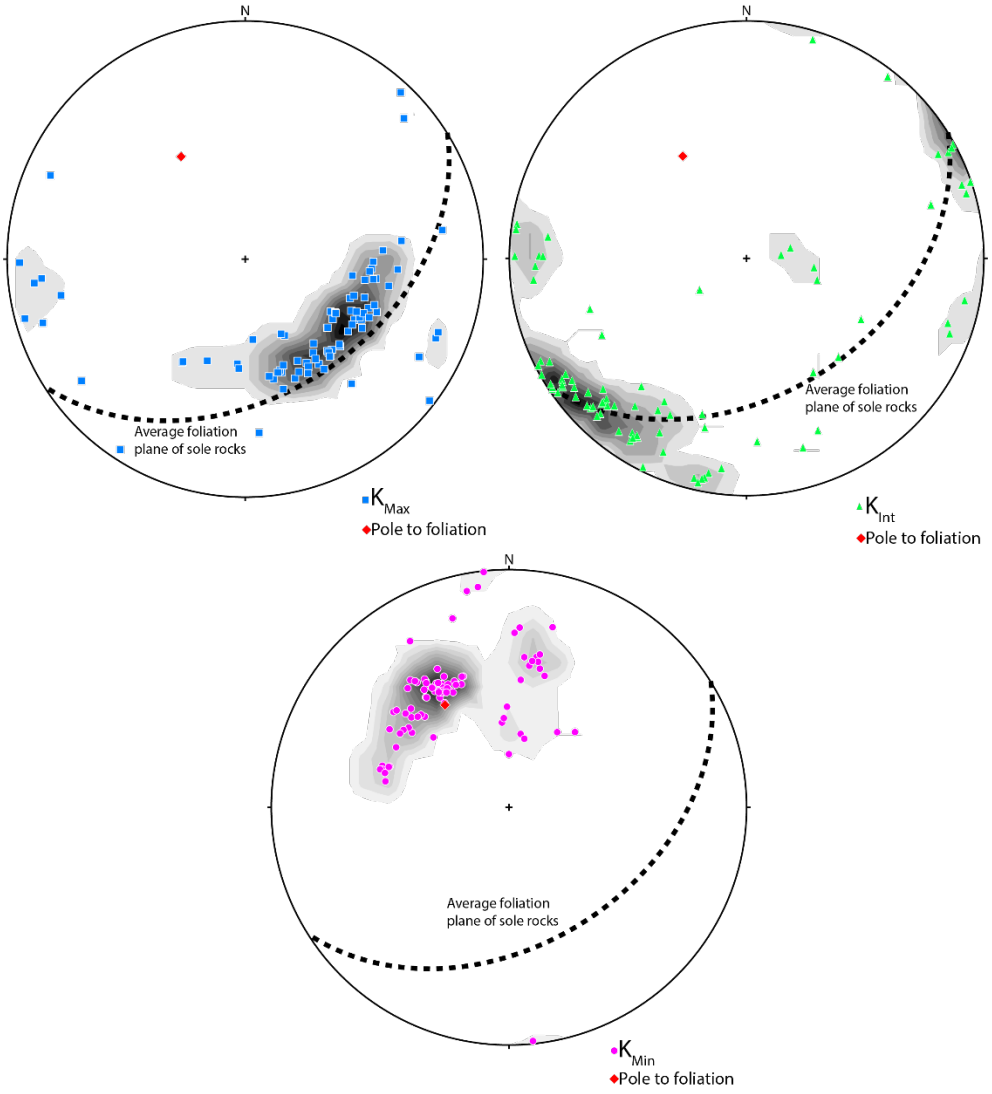

Figure 4.22. The distribution of principal directions of AMS (K_{max}, K_{int} and K_{min}) for metamorphic sole rocks and associated contoured distributions. The average foliation plane of the sole rocks and its pole are also given. K_{max} and K_{int} are generally distributed along the foliation plane, whereas K_{min} axes mostly lie perpendicular to the foliation plane.

There are some inconsistencies between AMS and structural orientations in some hand samples however (Fig. 4.23). In sample BC0201, K_{max} is perpendicular to the foliation unlike at other sites and K_{int} is steeply plunging. Since this hand sample was collected from the high angle shear zone in the amphibolite, localised deformation might have affected the AMS directions. In addition, K_{int} principal directions in hand sample BC0204 lie close to the structural lineation, instead of the K_{max} axes as in most other sites, suggesting swapping of maximum and intermediate axes.

Dyke specimens collected from fracture surfaces at site BC01 show and overall oblate fabric but with a poor correlation with the dyke orientation.

BC0201

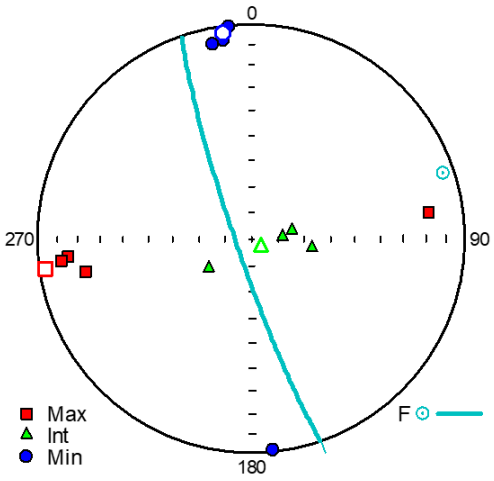

BC0203

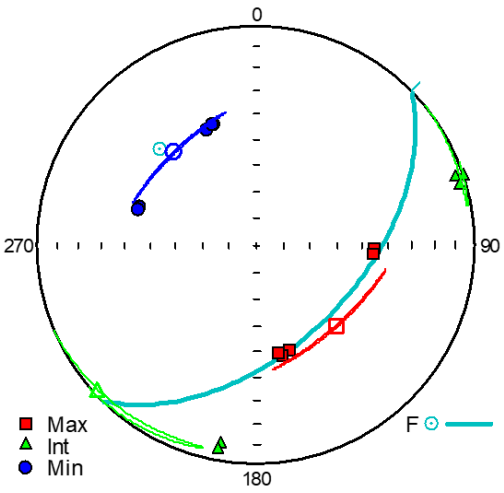

BC0204

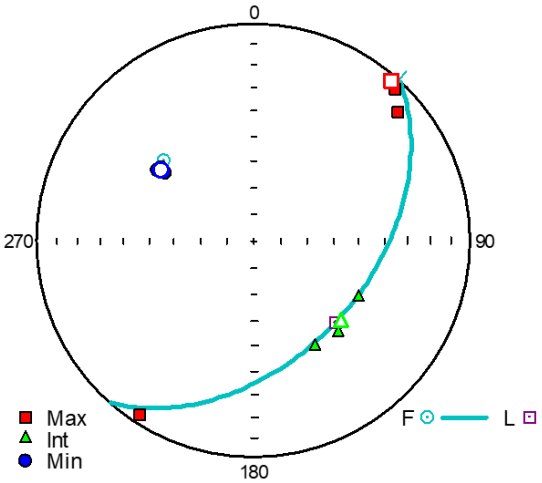

BC03

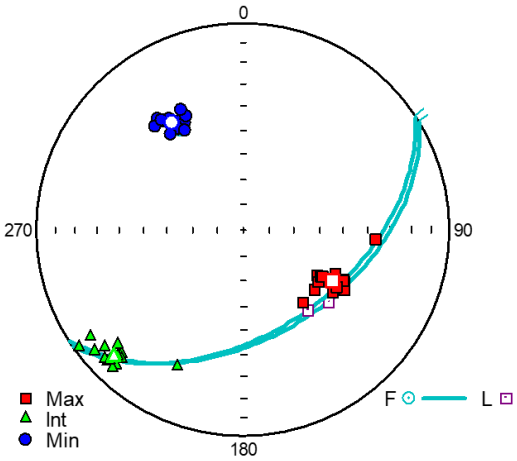

BC04

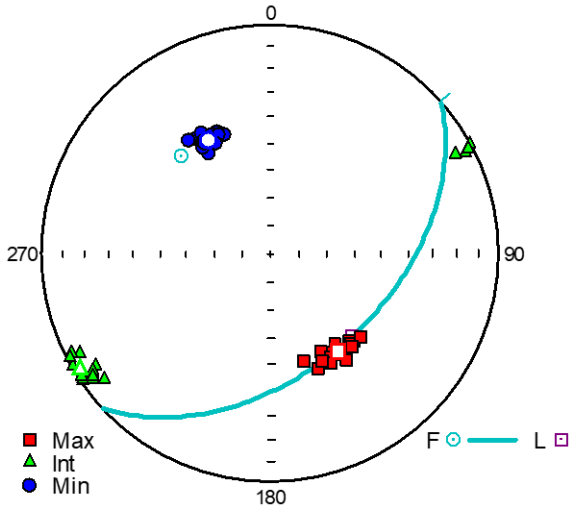

BC07

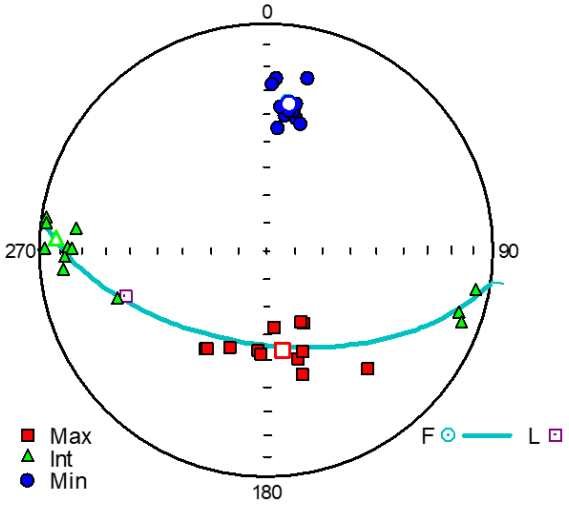

BC08

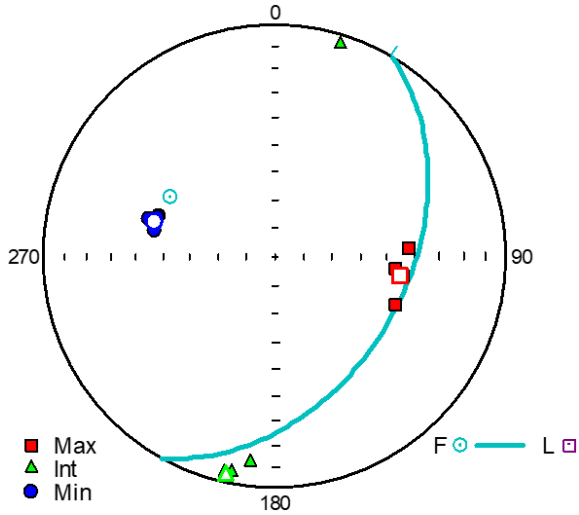

BC09

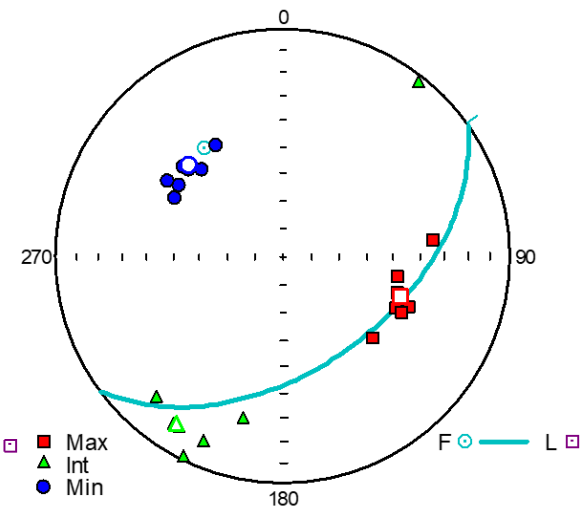

BC1001

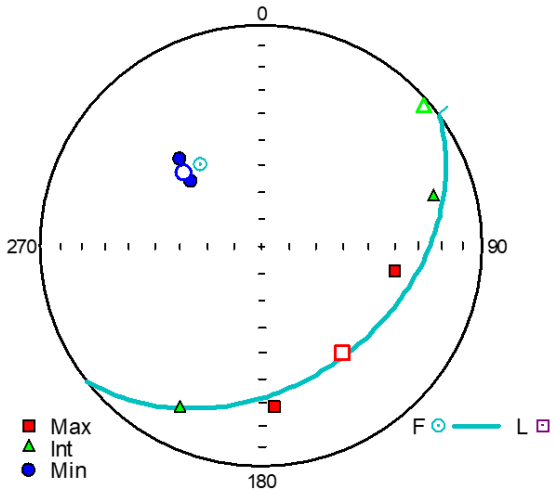

BC1002

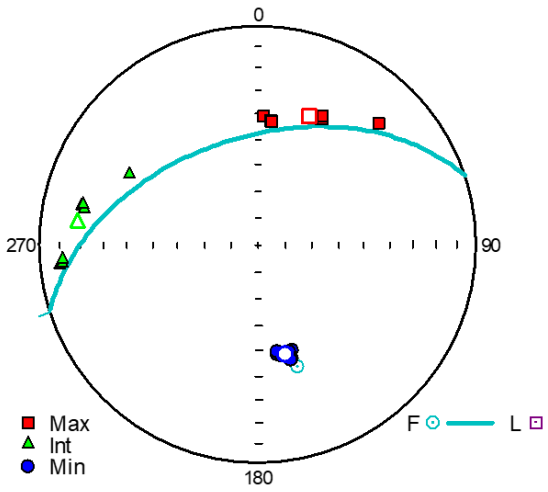

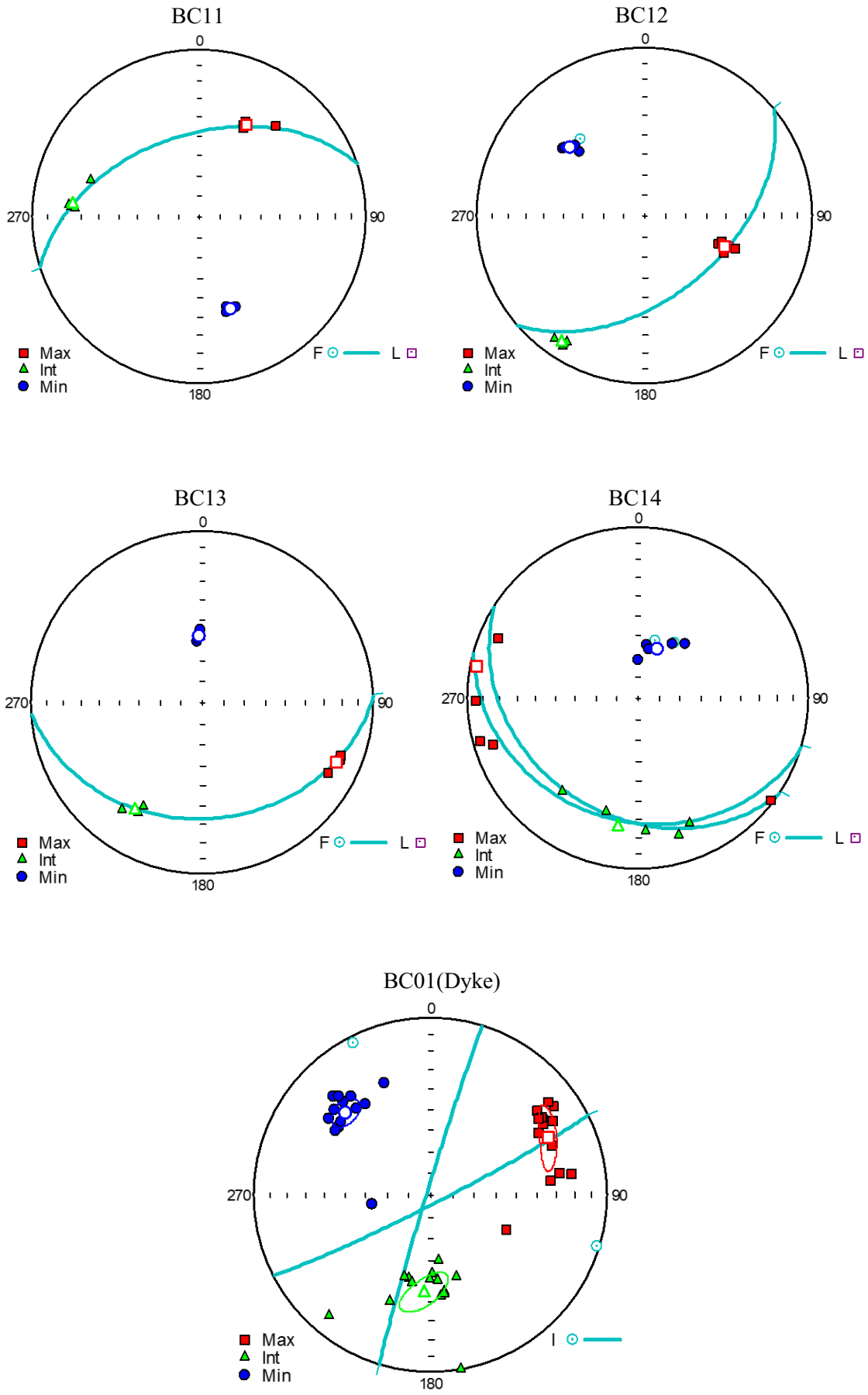

Figure 4.23. Stereoplots of AMS ellipsoid principal axes, together with foliation planes of the metamorphic sole rocks. Note that the hollow symbols indicate the mean values, L=Lineation, F= Foliation, I=Intrusion

4.2.2.3 Anisotropy of isothermal remanent magnetization (AIRM) results

AIRM experiments were performed on seven specimens representing most of the sites to determine if any inverse fabrics exist. According to the results (Fig. 4.24), almost all of them show normal magnetic fabrics where the principal axes of the AMS ellipsoids are close to the orientation of the AIRM principal axes. This indicates that the AMS fabrics are normal and that K_{max} may be interpreted as the magnetic lineation, with no evidence for inverse fabrics. However, one sample (BC0701E3) showed different data to the others. In this case, maximum and intermediate principal directions of the two forms of anisotropy appear to be exchanged, suggesting presence of an intermediate fabric (Fig. 4.24).

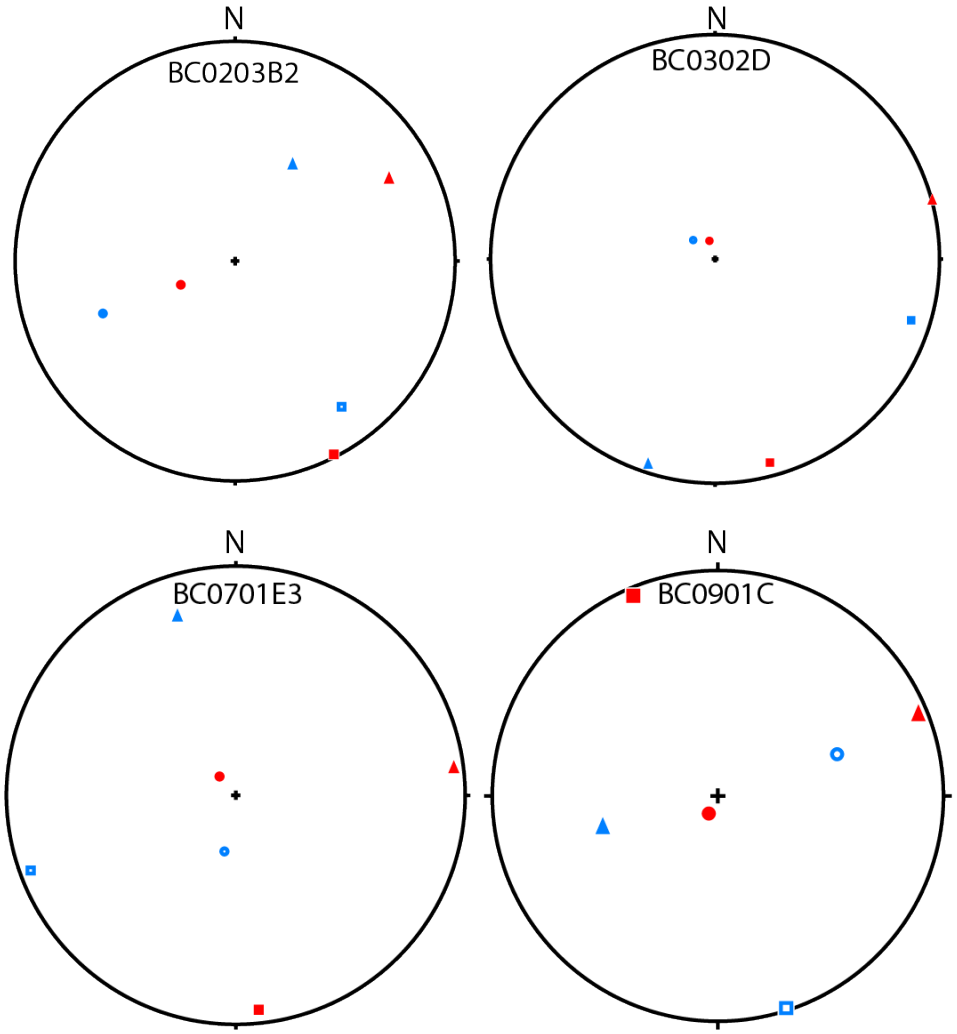

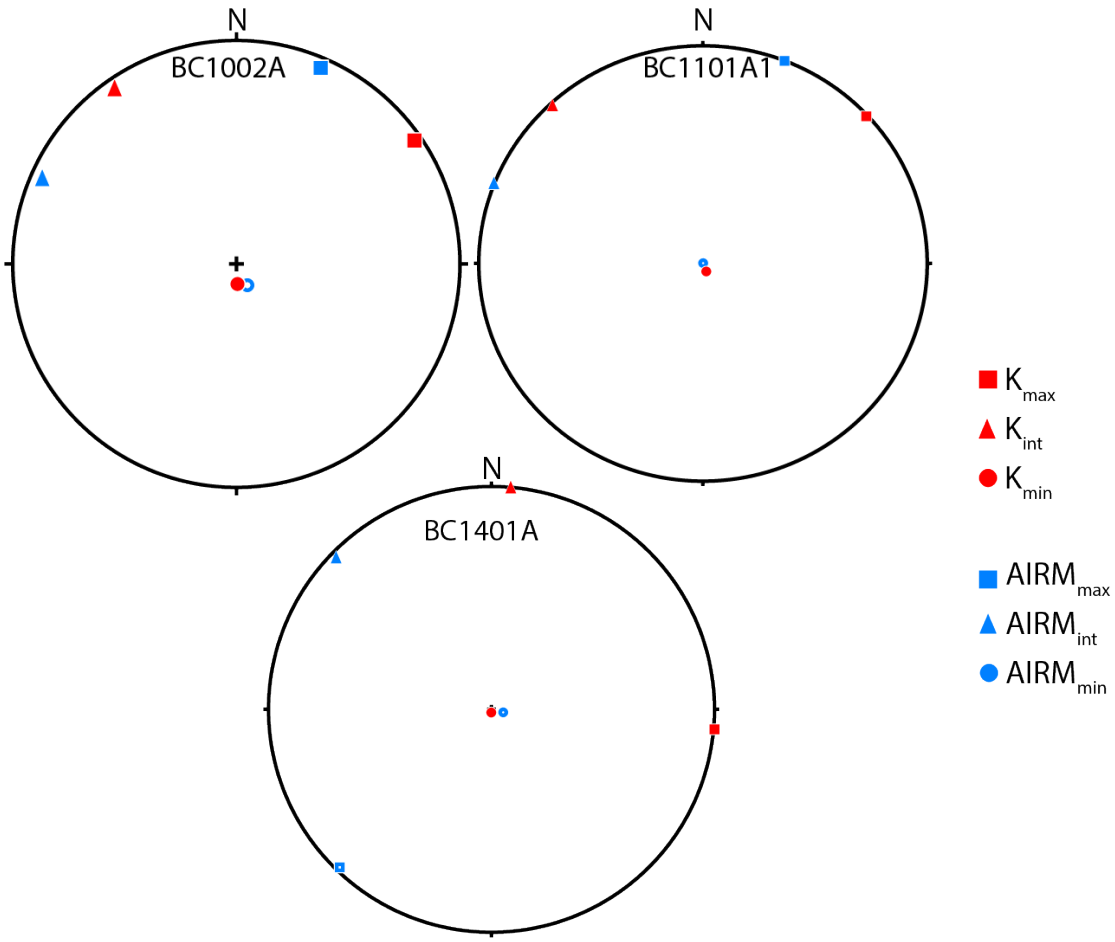

Figure 4.24. Comparison of orientation of principal axes of AMS and AIRM ellipsoids from seven samples from the metamorphic sole rocks of the Mersin ophiolite. Note that the ones with negative plunge are shown in the lower hemisphere.

4.2.3 Palaeomagnetic results

4.2.3.1 NRM results

Natural remanent magnetization intensities and directions for the specimens were measured by JR6 magnetometer before the demagnetization process. All of the dyke specimens were able to be measured but three of the metamorphic sole rocks could not be measured because they were not stable inside the holder of the equipment during spinning due to their small size. NRM intensities for dyke specimens ranging between 7.2–12.7 mA/m. These are similar to values reported previously by Omer (2014). Metamorphic sole rocks have intensities between 0.07 and 69.2 mA/m. This is significantly lower than the other rock units such as cumulates and lavas in the Mersin ophiolite. Low intensities of NRM are not easy to measure and approach the noise level of the magnetometer. Therefore, some of the specimens were measured twice or even three

times till the lowest error values were obtained. Histograms illustrating the NRM intensity data of the dykes and metamorphic sole rocks are given below (Fig. 4.25).

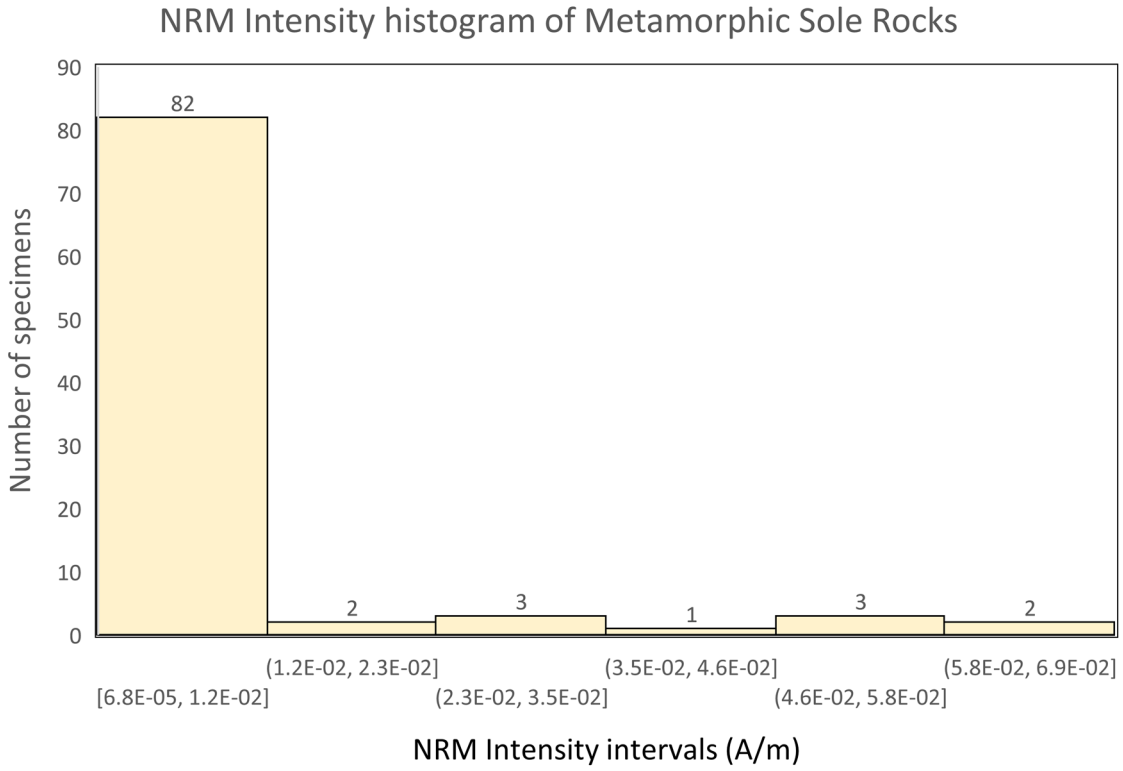

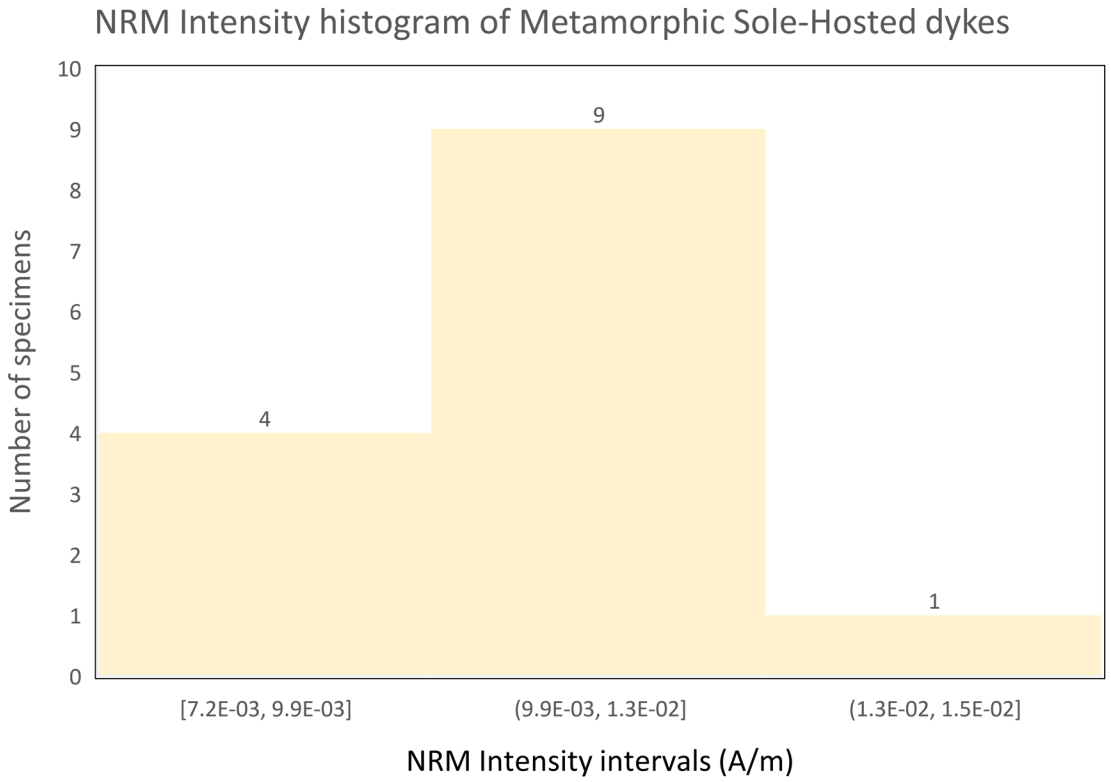

Figure 4.25. Histograms showing the NRM intensities in the Mersin dyke and metamorphic sole rocks.

4.2.3.2 Thermal demagnetization results

Thermal magnetization data might be more useful than AF demagnetization because unblocking temperatures may (under ideal conditions) provide information about the thermal history of the rocks. To test if sole rocks provide usable thermal demagnetization data, 12 specimens (1 dyke, 11 metamorphic sole rocks) were thermally demagnetized with standard steps (100°C-580°C). The specimens having higher NRM values were chosen. Specimens were held within the oven for 40 minutes after reaching the set peak temperatures. Remanent magnetizations were then measured after cooling to room temperature. Most specimens show stable demagnetization behaviour at low treatment levels. However, directions either start to show scattered results at higher temperatures because intensities become close to or lower than the noise level or all demagnetization steps resulted in random directions which cannot be subjected to principal component (PCA) or great circle analysis (Fig. 4.26). As a result, thermal demagnetization was not used for the remaining specimens.

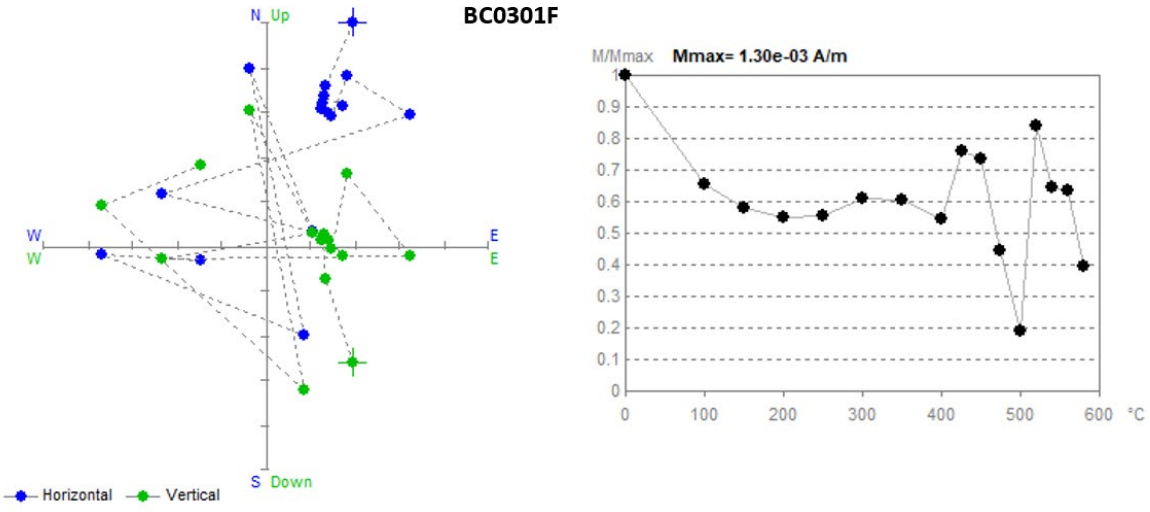

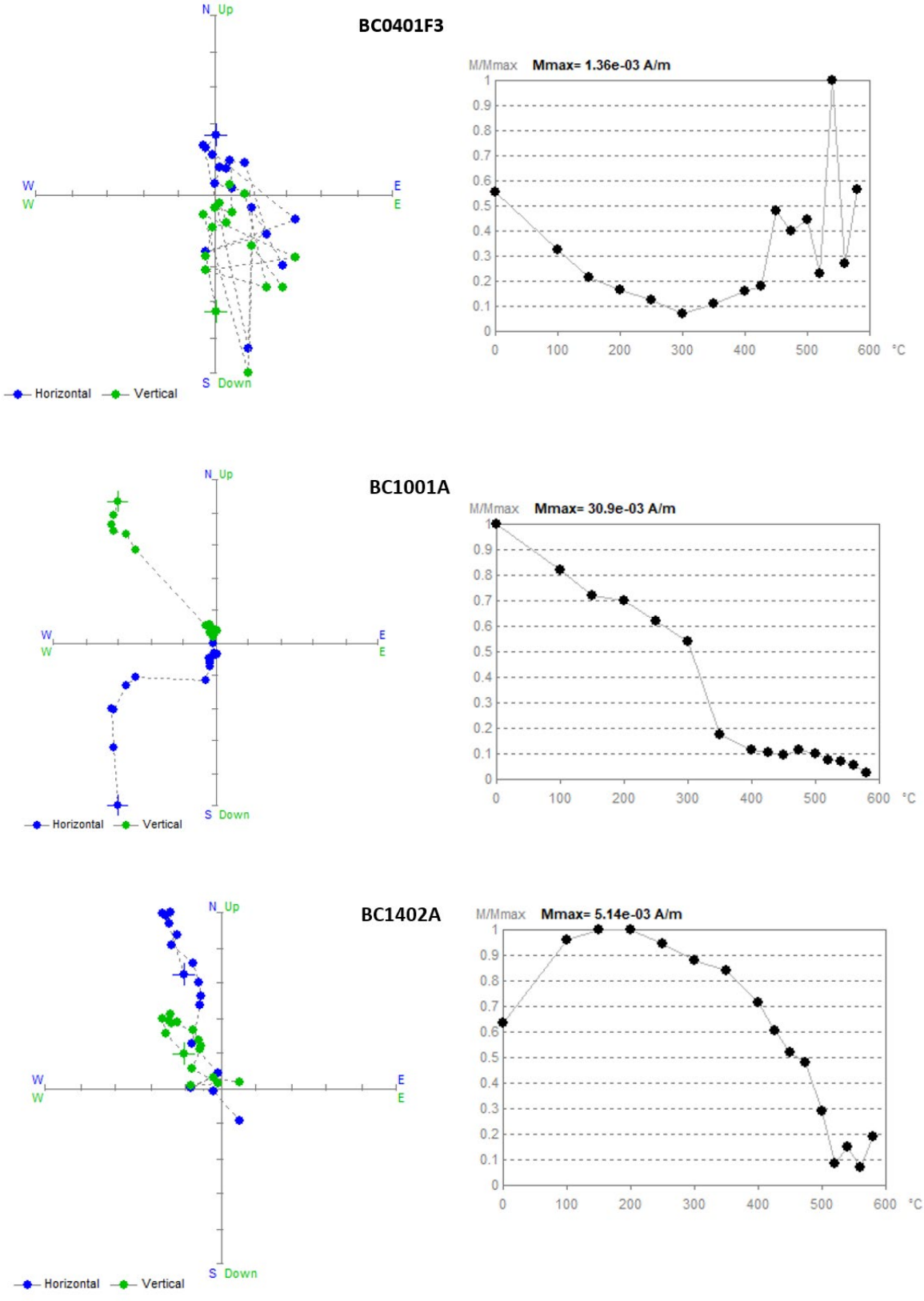

Figure 4.26. Zijderveld diagrams after stepwise thermal demagnetization for some of the specimens (BC0202B, BC0301F, BC0401F3, BC1001A, and BC1402A) with intensity decay plots.

After each thermal demagnetization step, the bulk magnetic susceptibility of each specimen was measured to observe alteration and/or chemical changes within the ferromagnetic minerals that might affect the demagnetization path. The measurements of bulk susceptibilities indicate that most of the specimens did not experience any alteration until the end of the thermal demagnetization process (Fig. 4.27). However, progressive decreases in bulk susceptibility during thermal demagnetization is observed in specimens BC1201B and BC0902A1, whereas specimen BC0202B started experiencing changes susceptibility over 400°C and a sharp increase at 500°C. The bulk susceptibility of specimen BC1301B showed a dramatic increase at 540°C (Fig. 4.27). These results suggest that ferromagnetic minerals in these specimens experienced chemical changes or formation of new minerals a higher temperatures.

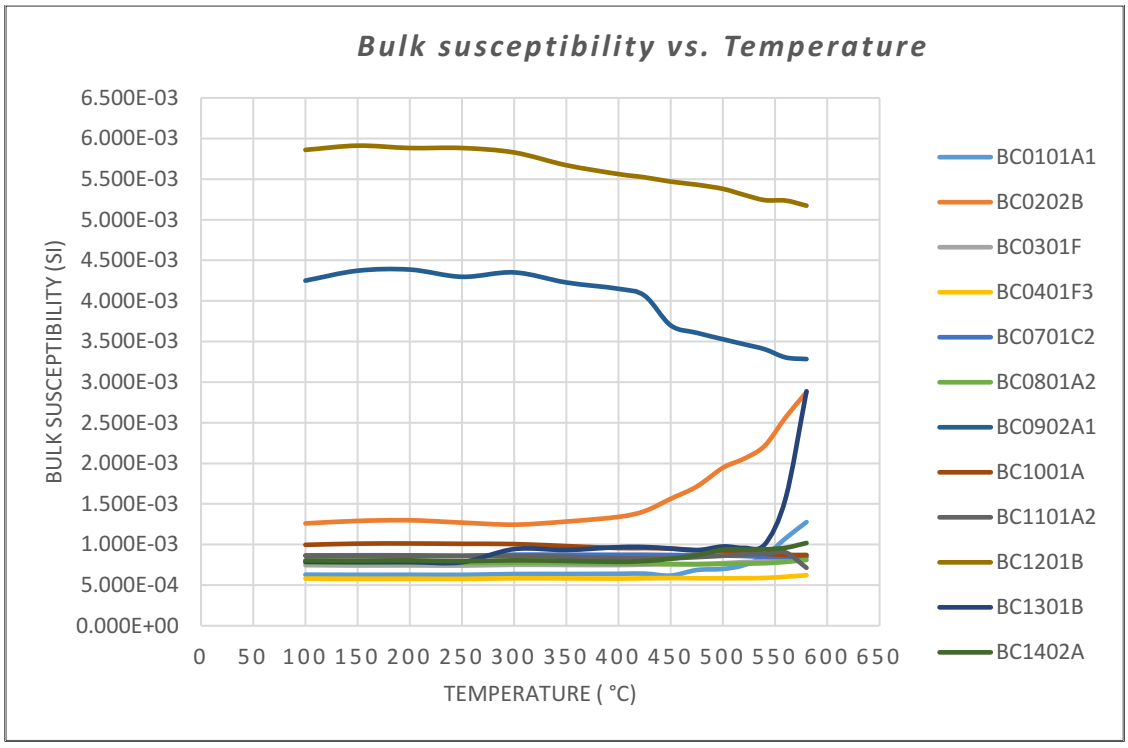

Figure 4.27. Graph illustrating changes in bulk susceptibility with temperature during thermal demagnetization for 12 specimens from 12 different sites.

4.2.3.3 Alternating field (AF) demagnetization results and palaeomagnetic directions

After the unsuccessful results from the thermal demagnetization, AF demagnetization became essential to make progress. A selection of samples were AF treated in the University of Plymouth laboratory, but again almost none of them yielded clear enough data to allow determination of ChRM directions (Fig. 4.28).

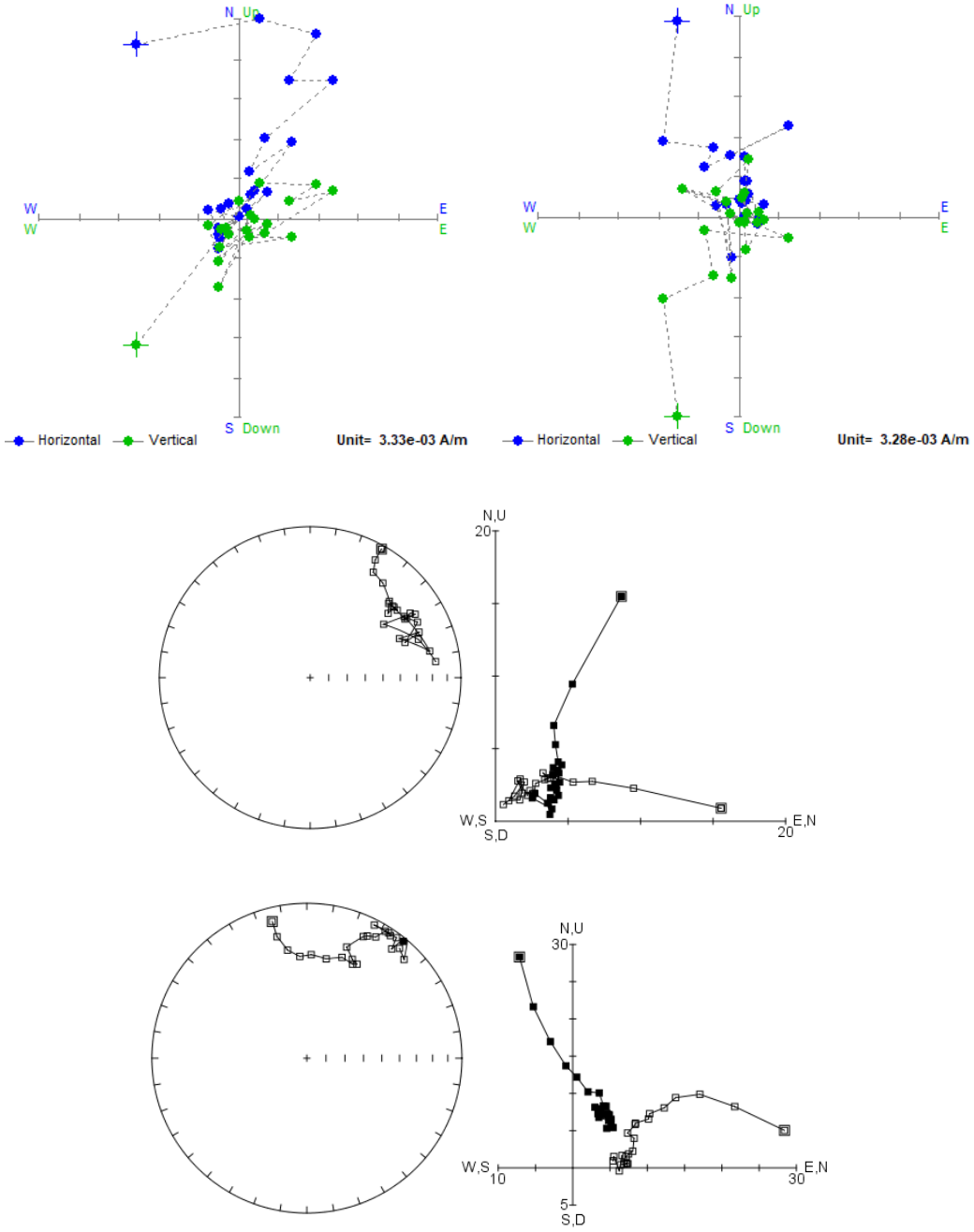

Figure 4.28. Some impracticable results from both of the AF demagnetizers (AGICO and 2G), BC0202A, BC1201C, BC0203C1, BC0204A, respectively. The coloured ones are from Anisoft (JR6) and the other ones are from Puffin Plot (2G)

Therefore, a more sensitive 2G Cryogenic magnetometer (at the University of Southampton) was used to get more reliable and useful data for the remaining specimens (56 from the metamorphic sole, 10 from the dykes). This system allowed a very detailed demagnetization scheme to be used, using applied fields increasing in 5 mT steps up to 110 mT. PuffinPlot (Lurcock and Wilson, 2012) software was used to analyse the resulting data. Stable, NNW-directed ChRMs with shallow positive inclinations (in geographic coordinates) were identified in three specimens (see Fig. 4.29). However, demagnetization of the most specimens yielded great circle paths that converge in the SE quadrant, rather than ending in stable ChRM directions. Such paths occur when two components with overlapping coercivity spectra are present in a rock, and the direction progressively moves away from the least stable component towards the higher coercivity component. In analysing the data, individual specimens having maximum angular deviations (MAD) of the best fitting great circle or stable end point >10° were excluded. The great circle analysis method (McFadden and McElhinny, 1988) was then used to combine the best fit great circles from individual specimens with the stable end point data to identify the final magnetization vector for the metamorphic sole rocks. (n = 42 specimens from 6 sites) (Fig. 4.30). Data from 14 specimens, unfortunately, could not be used because of lack of coherence during demagnetization.

The stable end point data have shallowly inclined, NNW-directed ChRMs and are interpreted as normal polarity magnetizations. The great circle paths for other specimens, however, converge in the SE quadrant in the lower hemisphere, opposite the ChRM components. It is very unlikely that this SE direction results from very large rotation and instead this direction is interpreted as a reversed polarity magnetization, suggesting that the magnetization of the metamorphic sole rocks was acquired across more than one geomagnetic polarity chron. To facilitate joint analysis of the end point and great circle data, the end point directions were first inverted to a reversed polarity SE direction. The combined McFadden and McElhinny (1988) analysis then yielded a mean direction of Dec = 157.3° Inc = 14.3° (α_{95} = 7.5°) (Table 4.6). This was then inverted to a northerly (normal polarity) direction of Dec = 337.3° Inc= -14.3° prior to tectonic analysis to allow comparison with a normal polarity reference direction.

This remanence direction is statistically different to that of the dykes cutting the metamorphic sole, reported by Omer (2014) and Morris et al. (2017), which have a mean direction of Dec = 006.8°, Inc = 17.2°, α_{95} = 10.4°, k = 79.2, N = 4 sites. This indicates significant tectonic rotation between the time of acquisition of magnetization by the metamorphic sole rocks and the intrusion of the dykes. In the net tectonic rotation analysis of data from the metamorphic sole, therefore, the effects of the net rotation of the dykes documented by Morris et al. (2017) will be back-stripped from the palaeomagnetic and structural data from the sole in order to quantify this earlier phase of rotation.

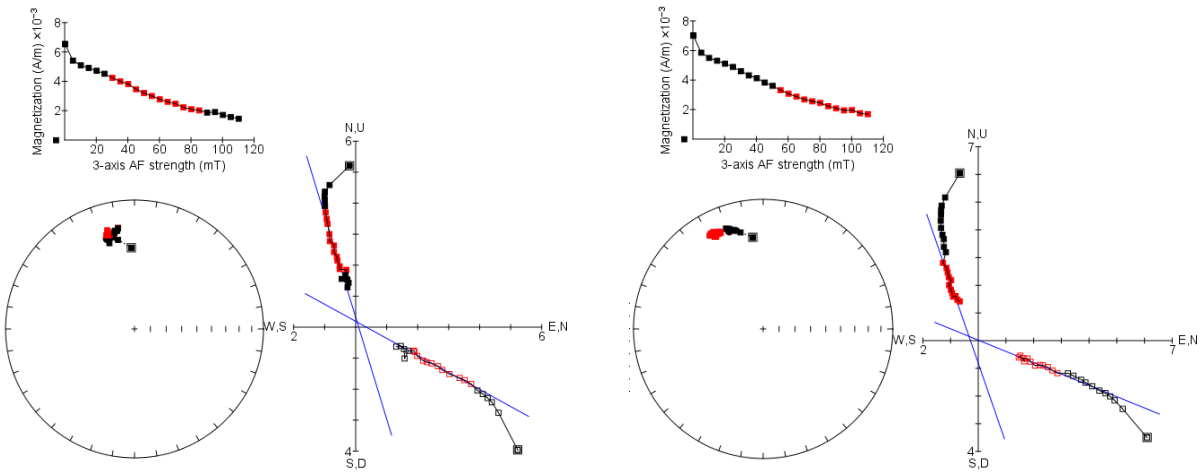

Figure 4.29. The end points obtained by PCA in PuffinPlot for BC0201A2 (left) and BC0201B2 (right). Solid/open symbols represent the projection onto the horizontal/vertical planes, respectively. Axis units on the Zijderveld plots are in mA/m.

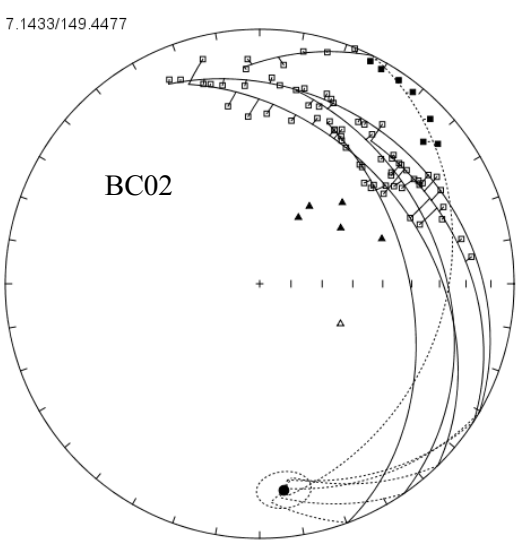
7.1433/149.4477
BC02

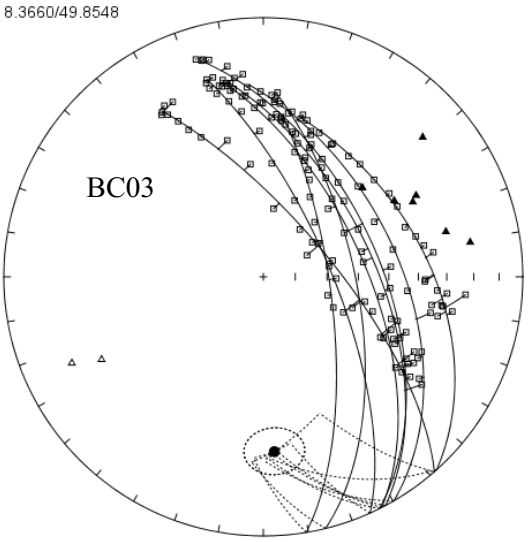
8.3660/49.8548
BC03

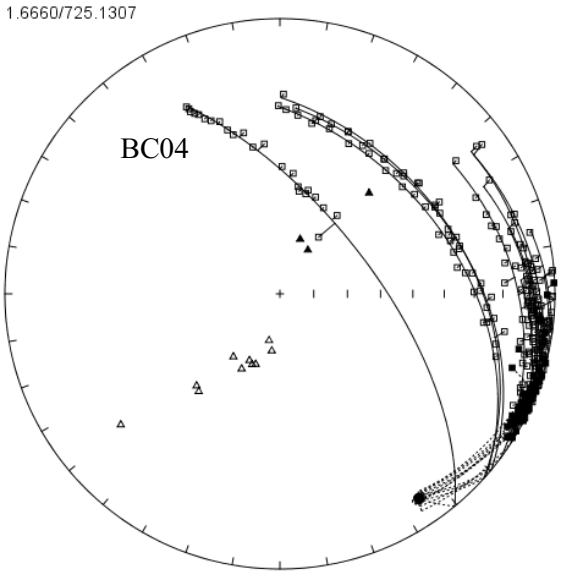
1.6660/725.1307
BC04

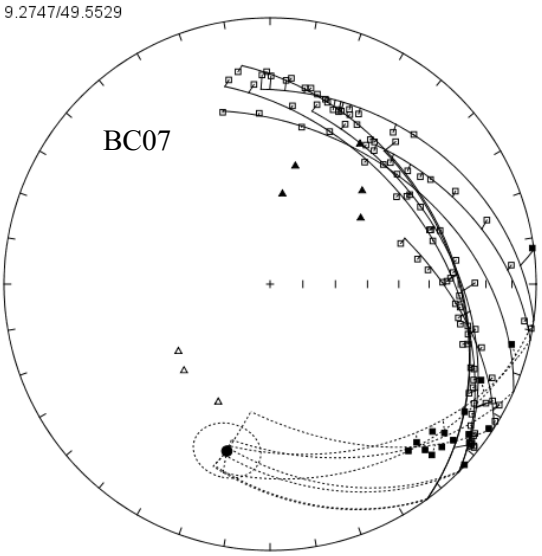
9.2747/49.5529
BC07

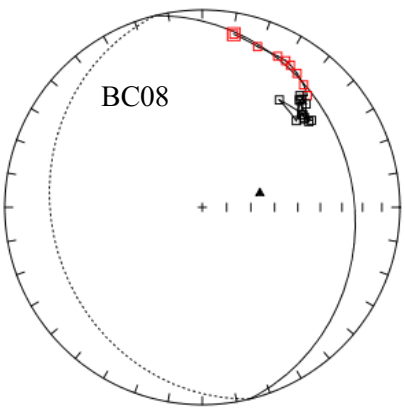
BC08

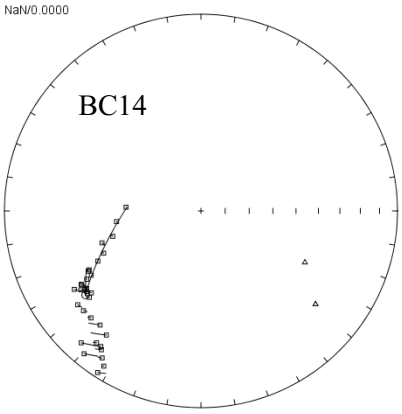
NaN/0.0000
BC14

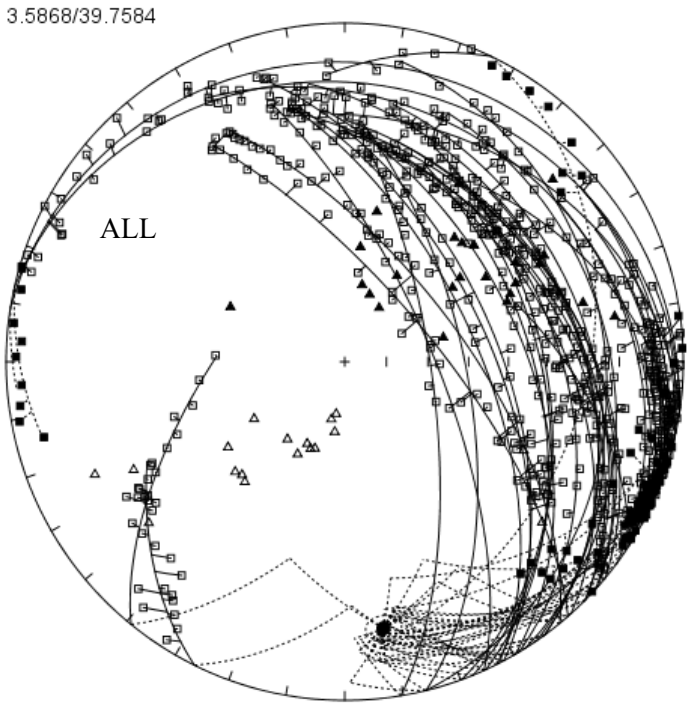

Figure 4.30. Great circle analyses for each site (BC02, 03, 04, 07, 08, and 14, respectively) and all combined within one plot. The given values represent the α_{95} and kappa values respectively. The last plot indicates the result that is the combination of all acceptable great circles paths.

Table 4.6. Palaeomagnetic data from the metamorphic sole rocks of the Mersin ophiolite, combination of great circles and end points.

Great Circle Analysis (McFadden and McElhinny,1988)

Site	Sample	Easting (36S)	Northing (36S)	DD/D	n	GC Declination	GC Inclination	α95	k
BC02	BC0203	619304	4083371	135/52	4	355.46	-16.47	4.87	321.54
	BC0204	619304	4083371	132/46	2				
BC03	BC0301	619238	4083392	148/47	9	160.74	09.61	5.98	56.76
	BC0302	619238	4083392	146/49	4				
BC04	BC0401	619251	4083390	138/48	13	145.33	10.63	1.60	787.22
BC07	BC0701	619330	4083355	188/56	7	188.52	33.56	11.25	43.36
BC08	BC0801	619097	4083484	120/43	1	076.13	65.51	NaN	NaN
BC14	BC1401	618836	4083777	213/32	2	233.98	-28.18	NaN	NaN
ALL	——	——	——	——	42	171.69	21.58	3.59	39.76

PCA (Kirschvink,1980)

Specimen	Easting (36S)	Northing (36S)	DD/D	PCA Dec. (Deg)	PCA Inc. (Deg)	MAD	n
BC0201A2	619298	4083377	251/84	343.07	27.74	5.47	1
BC0201B2				340.91	21.10	7.91	1
BC1001B	618915	4083598	143/38	005.30	15.80	9.80	1

	n	Mean Dec	Mean Inc	Polarity	α95	k
Magnetization vector of metamorphic sole rocks of the Mersin ophiolite after combining the GC and PC data	45	157.3	14.3	Reversed	7.5	8.1
		337.3	-14.3	Normal		

4.2.4 Net tectonic rotation analysis of the palaeomagnetic data

4.2.4.1 Input vectors and potential solutions

The essentials for the net tectonic rotation (NTR) analysis have been already described in Chapter 3. The technique involves finding the poles and angles of permissible net rotations that simultaneously restore the site magnetization vector (SMV) to the reference magnetization vector (RMV) and the present pole to foliation (PPF) to an initial pole to foliation (IPF).

The reference direction was selected from Morris et al. (2017) for analysis of the palaeomagnetic data from the Mersin ophiolite. This has a declination of 000°. The inclination was determined from palaeolatitude estimates based on kinematic reconstructions (van Hinsbergen et al., 2016) placed in the palaeomagnetic reference frame of Torsvik et al. (2012). Uncertainties in the reference inclination relate to the reconstructed width of the Neotethys Ocean and the A_{95} error of the reference global apparent polar wander path. Reconstructions for the Late Cretaceous at 100–90 Ma place the Neotethyan SSZ spreading axis between the southern margin of Eurasia at 33 ± 3°N and the northern margin of Gondwana at 16 ± 3°N. No other constraints on palaeolatitude exist, and therefore a palaeolatitude of 24.5 ± 11.5°N is used to encompass this range. Assuming a geocentric axial dipole field, this converts to a reference inclination of 40.2 ± 15.4° (Morris et al., 2017).

Hence the input data required for the NTR analysis are (Fig. 4.31a):

- Present pole to the foliation, PPF = 328°/48°, α_{95} = 6.8°, k = 20.9
- Site magnetization vector, SMV = 337.3°/-14.3°, α_{95} = 7.5, k = 8.1
- Reference magnetization vector, RMV = 000°/40.2° ± 15.4°

To allow uncertainties in these input vectors to be propagated through the NTR calculation using a Monte Carlo modelling approach, 1000 randomly selected estimates of each input vector were calculated that lie within the confidence limits (Fig. 4.31b). Prior to NTR interpretation, the sets of 1000 PPF and SMV vectors were back stripped by removing the effect of the late rotation of the dykes in metamorphic sole rocks documented by Morris et al. (2017), which was a clockwise rotation of 45° around an inclined axis of 039.8°/31.3°. This gave mean back-stripped input

vectors of PPF = 346.6°/84.7° and SMV = 313.9°/22.7°, retaining the same confidence intervals (Fig. 4.31c). The reference direction input vectors remain the same.

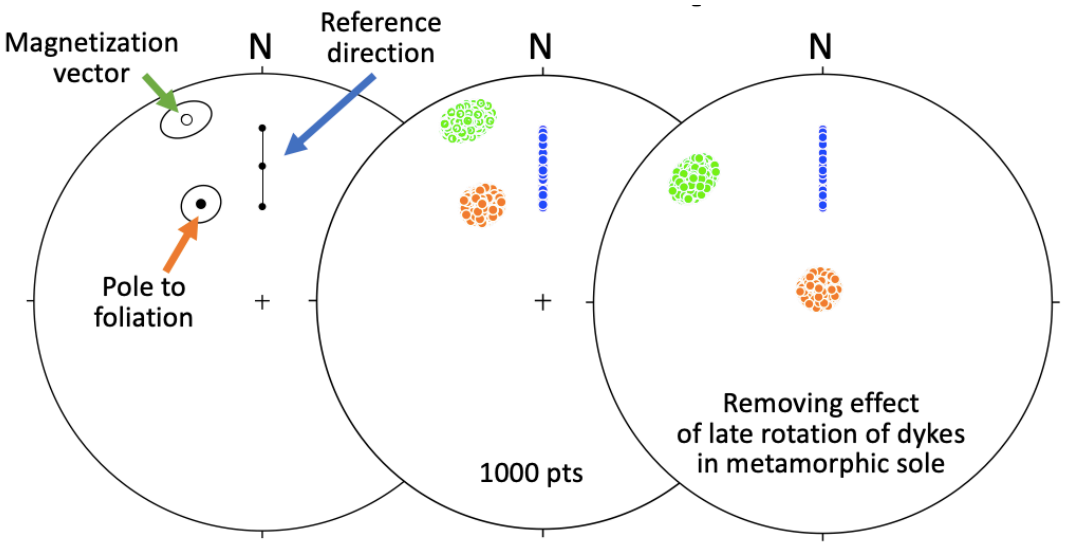

Figure 4.31. (a) Input vectors for the NTR analysis with 95% confidence limits; (b) 1000 points within the confidence intervals of each vector; (c) the directions after removing the effect of late rotation of dykes cutting the sole rocks.

Each of the 1000 pairings of SMV and PPF vectors yields a slightly different estimate of the angle β between the magnetization and the pole to the structure (which is assumed to remain constant in the NTR approach). Each β estimate was then assigned to one of the 1000 RMV vectors, and the pole to the foliation at the time of magnetization acquisition (called the initial pole to foliation, IPF) for that combination of input vectors then must lie β degrees from the selected RMV. To position the IPFs, each was assigned a random azimuth away from its associated RMV, giving a broad distribution of IPFs shown in Figure 4.32.

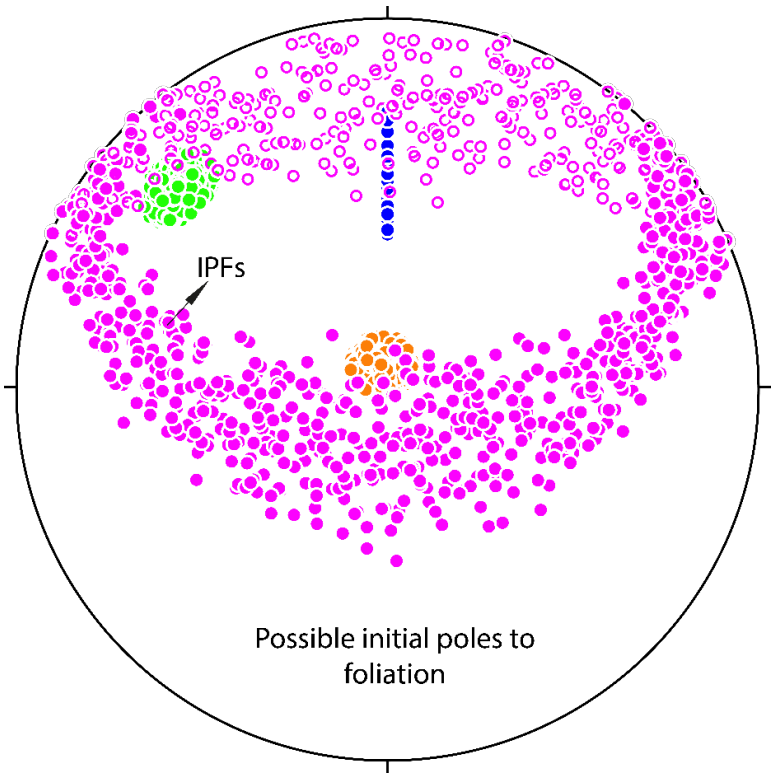

Figure 4.32. Potential initial poles to foliation during acquisition of the magnetization

These steps resulted in a set of 1000 estimates for the four vectors needed to calculate potential rotation angles (i.e. the initial and final directions of the magnetization and the pole to the structure). The great circle bisectrix of each pair of vectors (e.g. the SMV and RMV) represents the locus of all of the infinite number of potential rotation axes capable of rotating the initial to the final vector (e.g. rotating the RMV to the SMV). The intersection of the bisectrixes of the SMV/RMV and PPF/IPF pairs, however, represents the only rotation axis capable of restoring both vectors to their initial positions. Each of the 1000 sets of input vectors generates its own estimate of these inclined axes, and the associated angles of rotation are readily calculated. These are illustrated in the stereonet and histogram of Figure 4.33.

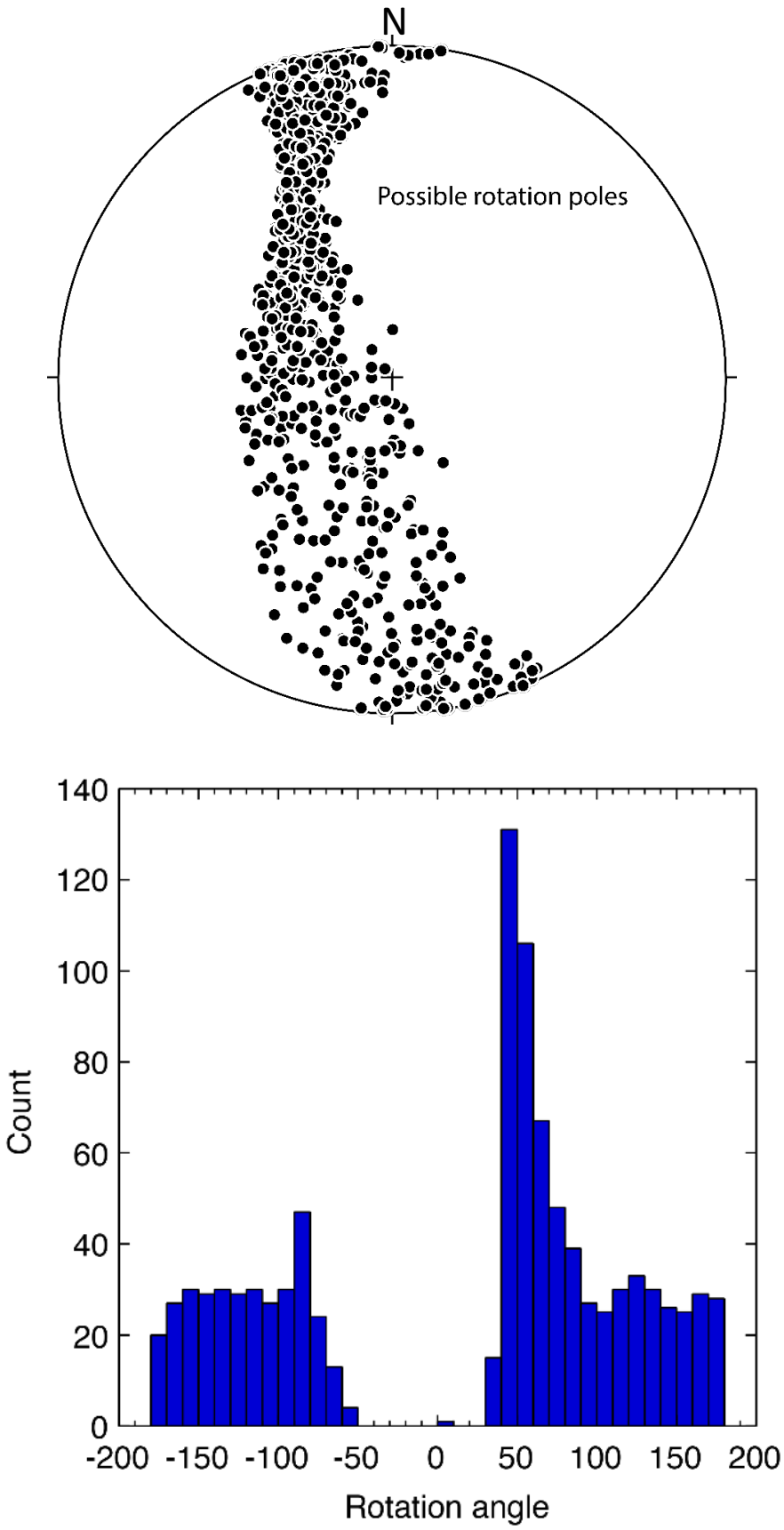

Figure 4.33. Possible rotation poles and angles. Angles with negative values suggest a CW sense of rotation and positive values suggest a CCW sense of rotation.

4.2.4.2 Filtering using geological constraints

Unlike using NTR analysis on dykes and lavas, in the case of the metamorphic sole rocks it is impossible to know in advance what the initial orientation of the foliation in these rocks was at the time when they acquired their magnetization. The analysis so far yields 1000 widely distributed estimates of this orientation (IPF; Fig. 4.32), and hence 1000 widely varying estimates of the rotation parameters (Fig. 4.33). These 1000 estimates represent the range of rotation solutions permissible when the 95% confidence limits on the input vectors are fully taken into account using the Monte Carlo modelling. Not all of these solutions, however, are geologically plausible despite being geometrically possible, and so additional geological constraints need to be used to filter the possible solutions to come up with a set of realistic and acceptable solutions. There are three geological constraints that may be used:

1. The most recent palaeogeographic reconstructions of the eastern Mediterranean region during the formation of the ophiolites in the Late Cretaceous (Maffione et al., 2017) indicates that the Mersin and other ophiolites (e.g. Hatay, Troodos) formed over a suprasubduction zone system dipping towards the east (Fig. 4.34). For metamorphic sole rocks to be formed at the top of a downgoing, easterly-dipping subducted slab and then exhumed from depth requires a counterclockwise rotation. Therefore, the solutions indicating clockwise rotations (negative angles) (n=340) are discarded to be consistent with the regional tectonic framework of a subduction zone dipping to the east.

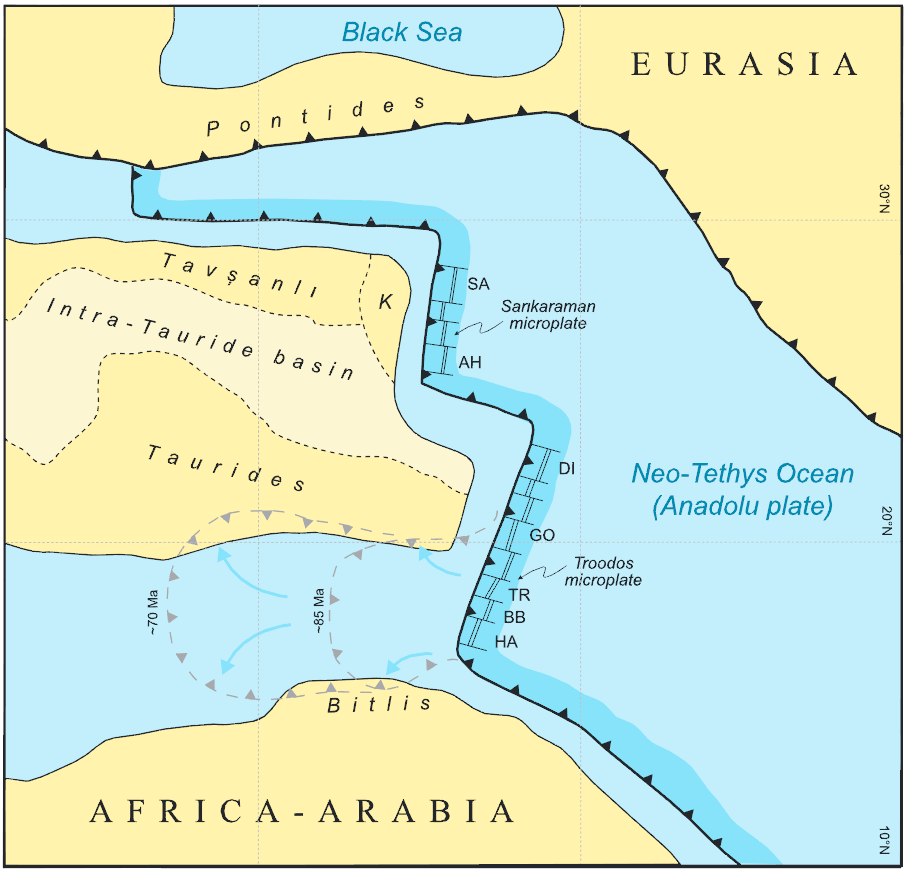

Figure 4.34. Palaeographic reconstruction of the Eastern Mediterranean Neo-Tethys soon after subduction initiation (~95 Ma) showing the main subduction zones (from Maffione et al., 2017).

2. Some of the solutions (n=320) indicate that the sole rocks have been inverted, but there is no reasonable way that this could have happened geologically. Therefore, solutions involving IPF with negative plunges are also discarded to maintain way-up.
3. Solutions suggesting >90° (n=253) rotation are discarded because rotation by more than 90° would imply a reversal of the dip direction of the subduction zone (i.e. to be "bent" back on itself prior to exhumation).

It must be noted that some of the solutions might be rejected because of at least two different constraints i.e. a solution indicating a rotation greater than 90° and having IPF with negative plunge. Omitting the infeasible solutions (846 out of 1000 solutions) leaves 154 geologically plausible NTR solutions for the initial poles to foliation (at the time of acquiring the magnetization) and the rotation axes and angles.

The acceptable IPFs imply that the sole rocks were most likely dipping towards the ENE at a moderate angle at the time of acquiring the magnetization. The associated rotation solutions indicate that sole rocks experienced 70°±12° counterclockwise rotation around a moderately to

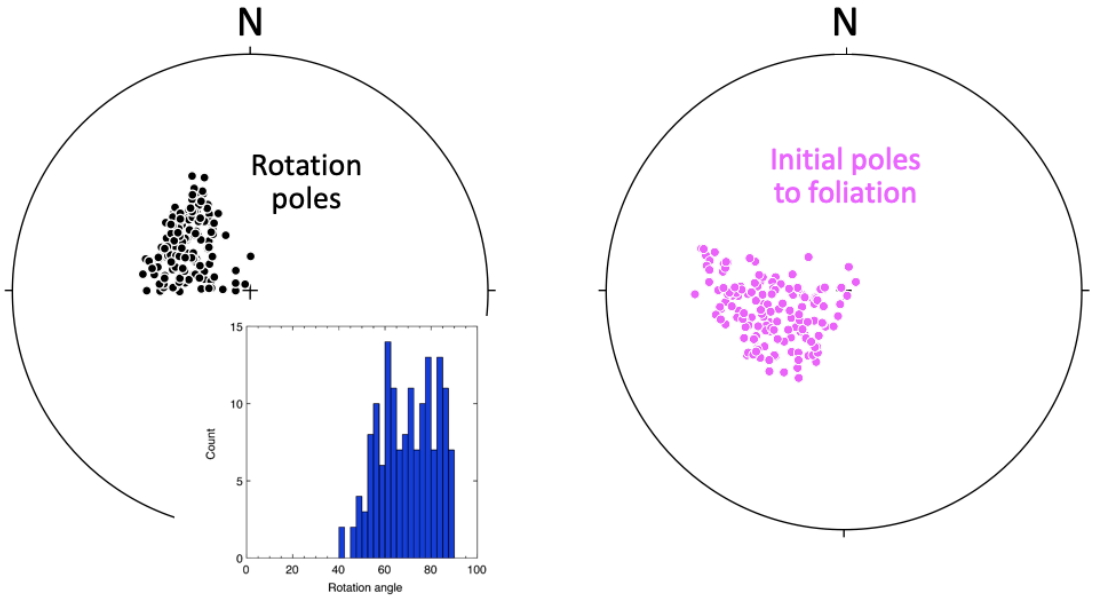

Figure 4.35. Acceptable final solutions of the net tectonic analysis, showing (left) net rotation poles with angles and (right) initial poles to foliation at the time of acquiring the magnetization.

steeply plunging, NW-directed axis (Fig. 4.35). These results are entirely consistent with exhumation of these rocks involving tectonic rotation of the subducted slab, as in the model of van Hinsbergen et al. (2015).

Chapter 5- Discussion

5.1 Pressure & temperature conditions and interpretations

To understand the P-T conditions during the metamorphism, Holland and Blundy (1994) thermometry was used for the amphibolites to estimate the temperature and Anderson & Smith (1995) barometry was used for pressure estimations. The results show that sole rocks were metamorphosed in the interval of 500-570C° and 2.0-5.6 kbar (±50C° and 1 kbar, standard uncertainties), suggesting relatively low pressure and relatively high temperature conditions. The average temperature results of both samples indicate more or less the same values (~530C°). On the other hand, a ~2 kbar difference between the pressure results can be considered as large. The main reasons may be either different oxidation states of Fe in the amphibole minerals during the metamorphism activity (Holland and Blundy, 1994) or very low proportion of the anorthite (~3-7%) which is most likely because of disequilibrium. Also, for this geobarometry method to work it has been stated by the authors that anorthite must be in the range of 10-90%, which is not possible for the amphibolites in this study. Some different P-T results have been also documented from previous studies of other metamorphic sole rocks of Tauride belt ophiolites, i.e. southern Beyşehir ophiolite nappes: 550-600C°/<5 kbar (Çelik and Delaloye, 2006), Lycian nappes (Köyceğiz area): 500-600C°/4.8-5.4 kbar (Çelik and Delaloye, 2004), Beyşehir-Hoyran ophiolite: 630-770C°/6.0 ± 1.5 kbar (Elitok and Drüppel, 2008), Kızıltepe ophiolite: 300-550C°/8.0-12.0 kbar (Dilek and Whitney, 1997), Yeşilova ophiolite: 600-700C°/4.7-5.0 kbar (Çelik and Delaloye, 2004) and Tavşanlı ophiolite: 300-800C°/8.0-10.0 kbar (Plunder et al., 2013) (Fig. 5.1). The results are in a broad range and this can be explained by the P-T conditions depending on the depths where the metamorphism activity takes place. The pressure values of the studied metamorphic sole rocks of the Mersin ophiolite imply depths of ~ 17-18 km, whereas some results from other sole rocks, i.e. the Kızıltepe ophiolite, indicate depths up to 40 km for peak metamorphic conditions.

According to petrographic observations made during this study, there are no signs indicating retrograde P-T paths for the sole rocks, i.e. a transition from amphibolite facies to blueschist facies conditions (Dilek and Whitney, 1997; Plunder et al., 2013). Therefore, three different possible

paths are considered that the metamorphic sole rocks of the Mersin ophiolite might have followed (Fig. 5.1). They all involve a decrease in the temperature and pressure resulting from exhumation from depth during the fore-arc spreading. The first, most probable situation involves a slight decrease in temperature while the pressure progressively decreases as the rocks are exhumed to shallower depths. This path implies a hot subduction zone since the temperature does not change much towards structurally lower sections while the pressure changes. It has been already proposed that temperatures higher than expected at given depths in a mature subduction zone imply that the mantle portion of an ophiolite should have been hot just as its metamorphic sole rocks started forming (van Hinsbergen et al., 2015). The second situation implies a similar decrease in pressure and while the temperature also decreases. The third one suggests a slight decrease in pressure whereas some relatively large decrease in the temperature may also occur during the metamorphism (Fig. 5.1).

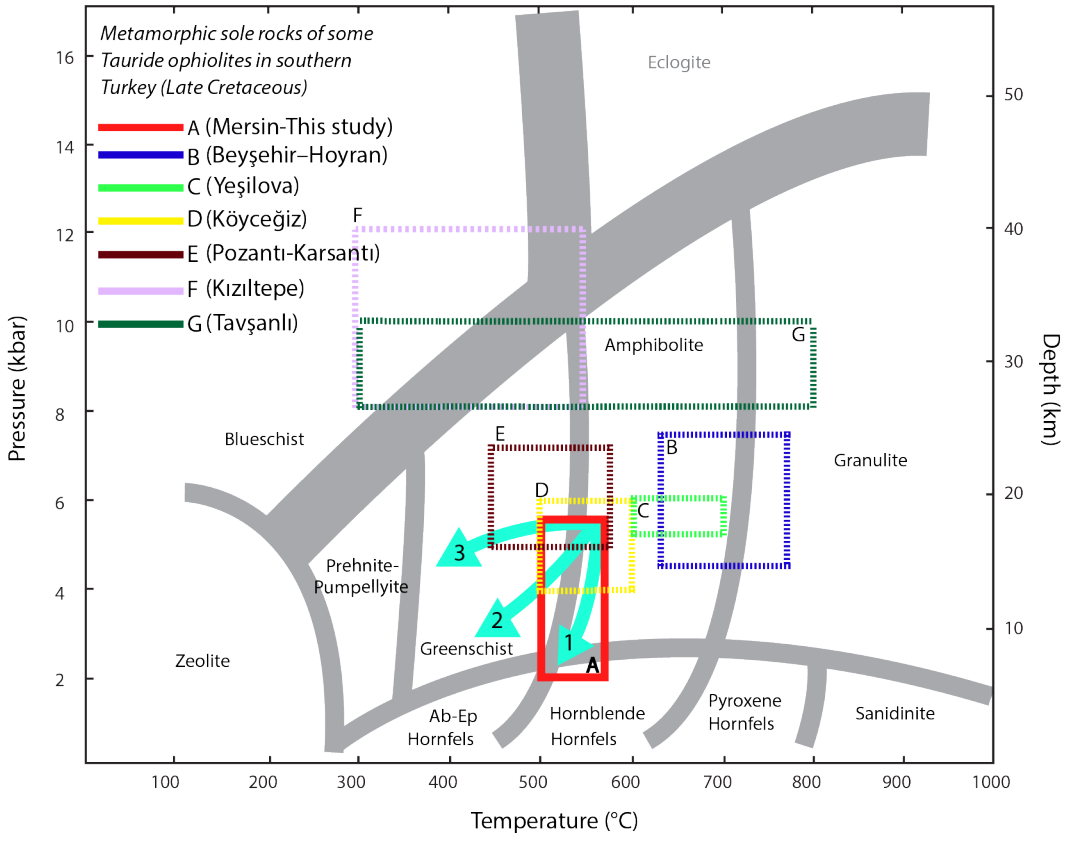

Figure 5.1. P (kbar)-T (C°)-Depth (km) values of some sole systems from Tauride ophiolites located in southern part of Turkey. The possible paths indicating the different levels of the metamorphic sole rocks of the Mersin ophiolite are shown with light green colour. A (with a red rectangle)-In this study-Mersin ophiolite; B = Elitok and Drüppel (2008)-Beyşehir–Hoyran ophiolite; C = Çelik and Delaloye (2004)-Yeşilova ophiolite (Lycian Ophiolites), D = Çelik and Delaloye (2004)- Köyceğiz ophiolite (Lycian Nappes), E = Çelik and Delaloye (2004)-Pozantı-Karsantı ophiolite;,

F=Dilek and Whitney (1997)-Kızıltepe ophiolite; G = Plunder et al. (2013) Tavşanlı ophiolite (modified from van Hinsbergen et al., 2015).

Schistose lenses within the amphibolites and amphibolite layers in the phyllite rocks indicate that greenschist and amphibolite facies conditions characterise the sole rocks. In the absence of rocks formed at granulite and eclogite facies and any sign of an amphibolite-granulite transition, very high P-T (+700C° and +12 kbar) conditions are precluded. The zonation within some minerals may also be an indicator for the P-T regime through the sole rocks. The zonation indicating slight decreases in P-T conditions towards rim regions may result from slight decreases in the P-T conditions during the exhumation of the sole rocks following the formation over the subducting plate at higher P-T conditions.

5.2 Structural interpretations

The aim is to understand the emplacement and transportation direction of the ophiolite by using the structural elements of the metamorphic sole rocks i.e. lineation, folds, shear indicators. However, the existence of asymmetric and symmetric indicators together and fold data are insufficient to find the exact direction of transport. It has been already reported that the emplacement took place in a NW direction onto the passive platform in the central Taurides (Parlak et al., 1996a). However, this direction is not clearly represented in microstructures with shearing indicators. Most of the analyses under the microscope imply a flattening event was the dominant structural style and asymmetric indicators are mostly absent in the samples observed. Therefore, it is difficult to be accurate regarding the emplacement direction.

According to observations during the fieldwork along the Fındıkpınarı road cut section, the units are imbricated and cut by non-metamorphosed diabase dykes. However, there is no evidence of large-scale folding along the road cut section, but small-scale folds are present. The sole rocks are mostly deformed by both normal and reverse brittle and ductile faults. Nevertheless, it must be remembered that the absence of large-scale folds does not indicate that the sole rocks were not pervasively deformed. Thus, three different interpretations were made by considering each structure that has been observed during the field and the results of the laboratory analyses. In all interpretations, there are four foliated packages forming the sole rocks along the road cut and

dipping towards SE. The units at the bottom close to the mélange below are phyllites and may indicate a relatively lower grade of metamorphism than that seen close to the ophiolite contact i.e. amphibolite. Also marble units (relatively HT-HP) occur towards the ophiolite but are not observed at the bottom of the section. This decrease in P-T conditions may be explained by the exhumation of the sole rocks to beneath the SSZ lithosphere due to flattening of the subducting plate resulted from thinning of the mantle wedge in the spreading environment. The three interpretations and their discussions are given below (Figs. 5.2-5.4).

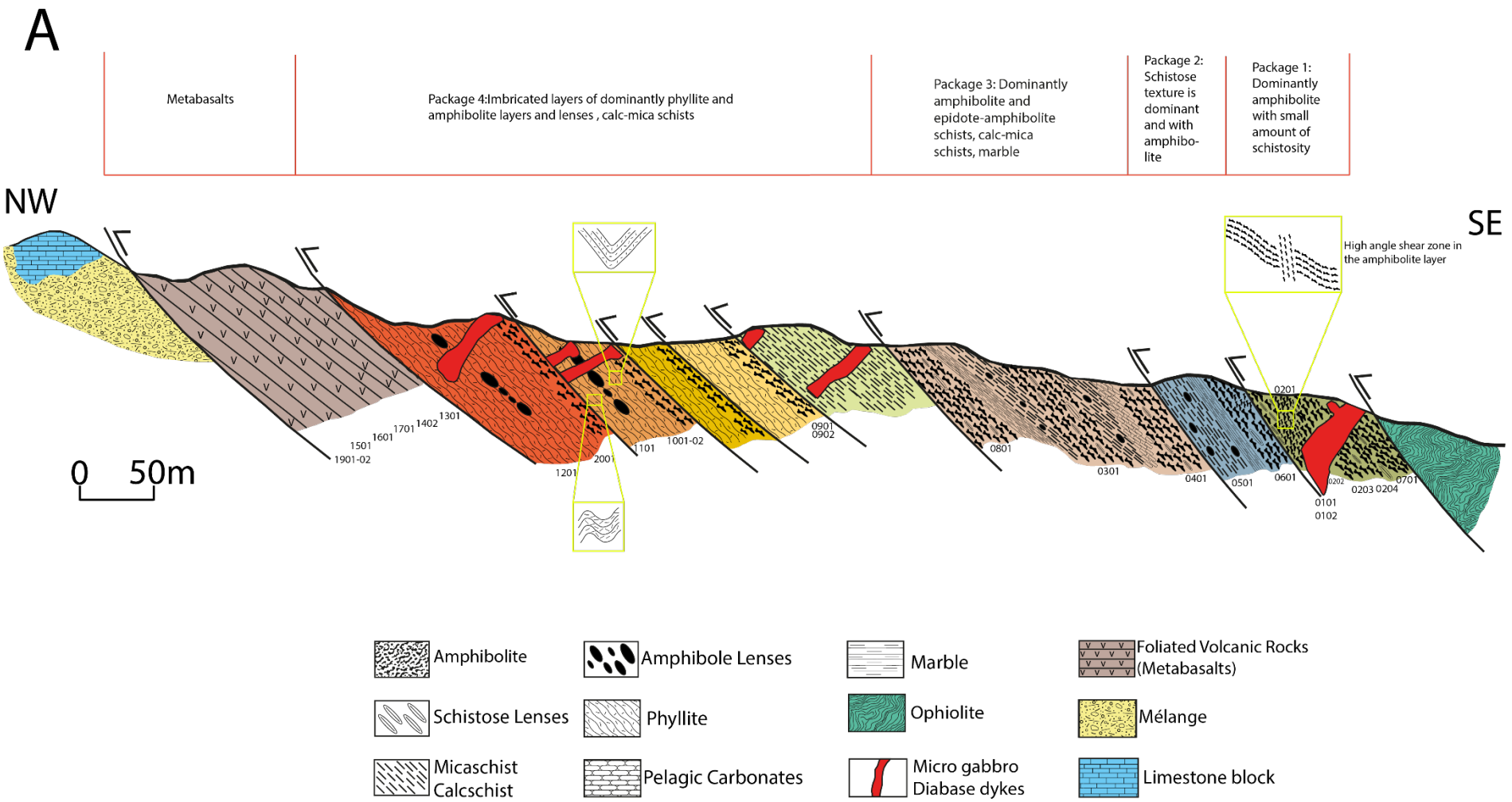

Figure 5.2. Possible cross-section of the ophiolitic metamorphic sole rocks at Fındıkpınarı road cut section as imbricated and successive repetition of the units separated by the faults (modified from Parlak et al., 1996a)

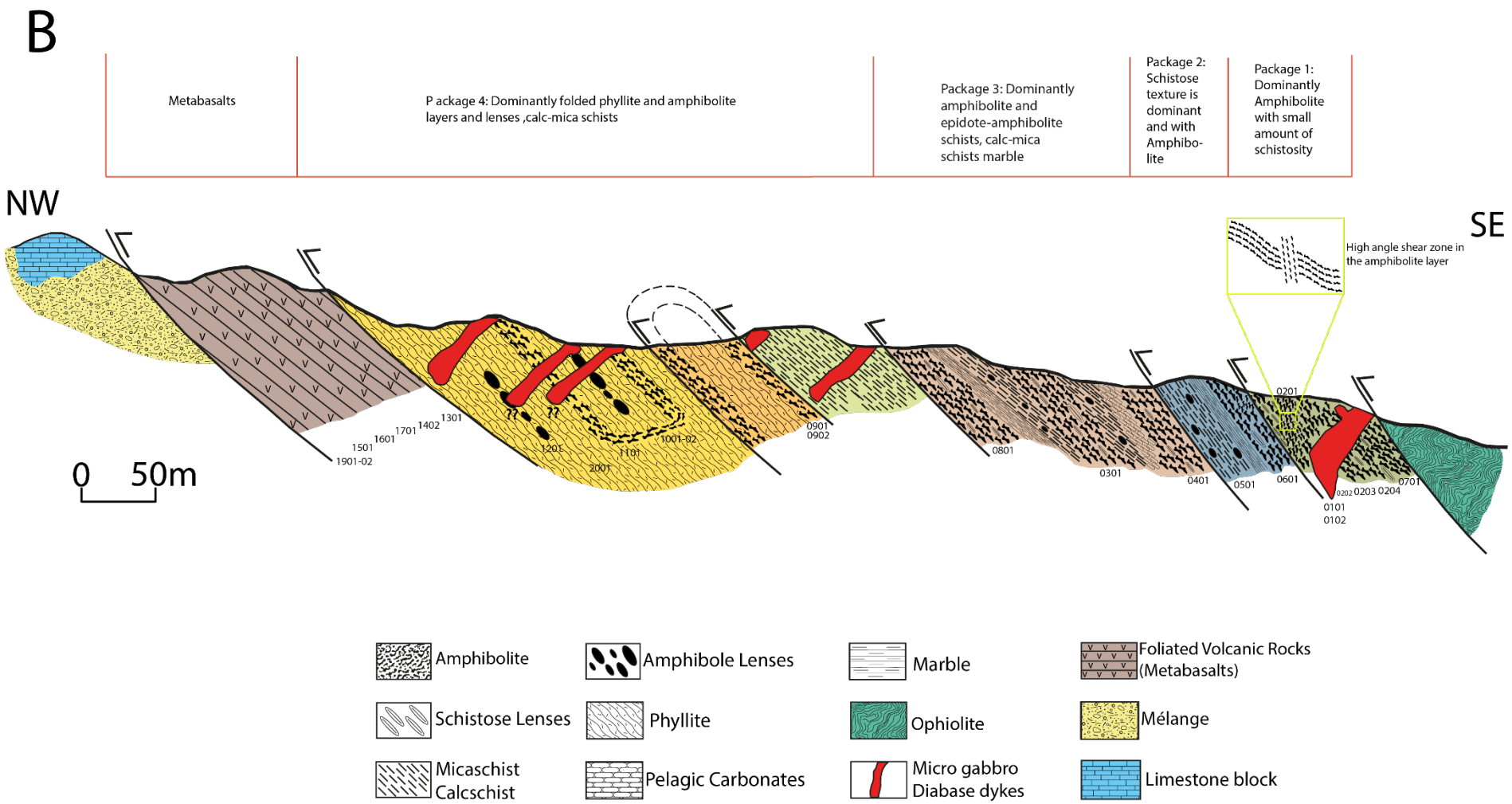

Figure 5.3. Possible cross-section of the ophiolitic metamorphic sole rocks at Fındıkpınarı road cut section as folded in the package 4 because of the shearing during the metamorphism activity (modified from Parlak et al., 1996a)

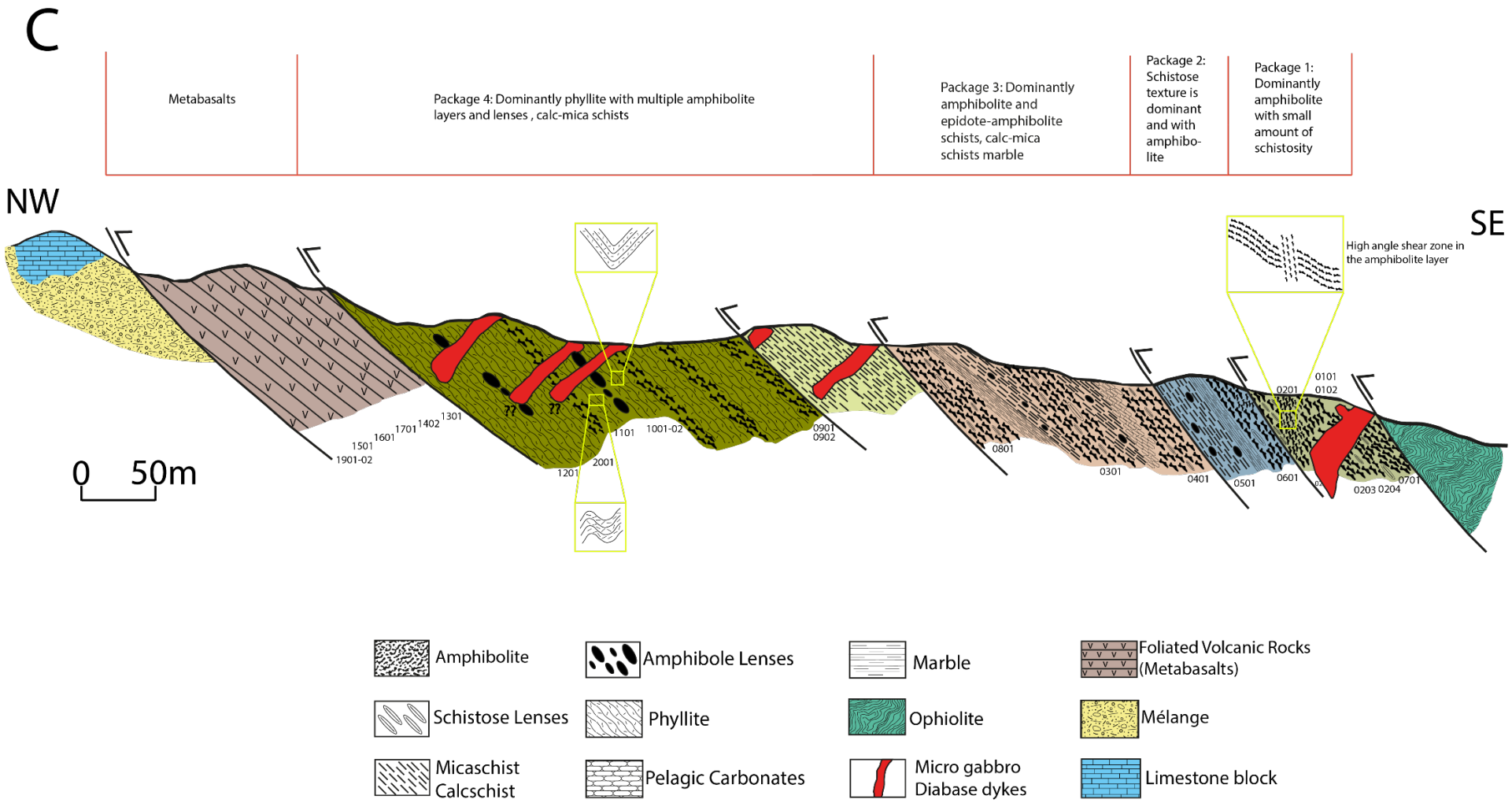

Figure 5.4. Possible cross-section of the ophiolitic metamorphic sole rocks at Fındıkpınarı road cut section indicating that package 4 is mainly imbricated as a whole package rather than existence of the faults separating the units (modified from Parlak et al., 1996a)

The differences in the cross-sections are mainly within the phyllite units that have multiple layers of amphibolite. According to the first interpretation (Fig. 5.2), possible north directed thrust stacking might have formed the repeated layers of amphibolite, probably during the emplacement of the ophiolite to the passive platform. However, it is also possible that the small-scale folds might be an indicator of larger-scale folding that might have formed during the deformation of sole rocks in the SSZ environment (Fig. 5.3). The last interpretation (Fig. 5.4) implies that repetitive layers of amphibolite in the phyllite may be explained by the possible changes in the physiochemical conditions i.e. P-T while the subduction is active, which affects the grade of the metamorphism, and units might have then been thrust as a whole package.

5.3 Rock magnetic and AMS analyses

Results indicate that the magnetic properties of the metamorphic sole rocks of the Mersin ophiolite are effectively controlled by paramagnetic (amphibole) minerals and also low content of ferromagnetic (mostly PSD and ESD magnetite). Furthermore, results from the metamorphic sole-hosted dykes suggest the presence of low to medium coercivity SD or PSD magnetite. These results are consistent with the previous study of the ophiolite (Morris et al., 2017).

All of the specimens display reasonably consistent principal directions and results in terms of AMS data. AMS principal axes are coplanar with the metamorphic foliation observed in the field, and the magnetic lineations (K_{max} axes) also correlate with the stretching lineation seen in the field (Fig. 5.5). This suggests that the AMS fabrics are predominantly controlled by the preferred orientation of paramagnetic amphibole minerals in these rocks. The dominance of oblate (disk-shaped) magnetic fabrics is consistent with the structural evidence for pure shear flattening during formation and exhumation of the amphibolites.

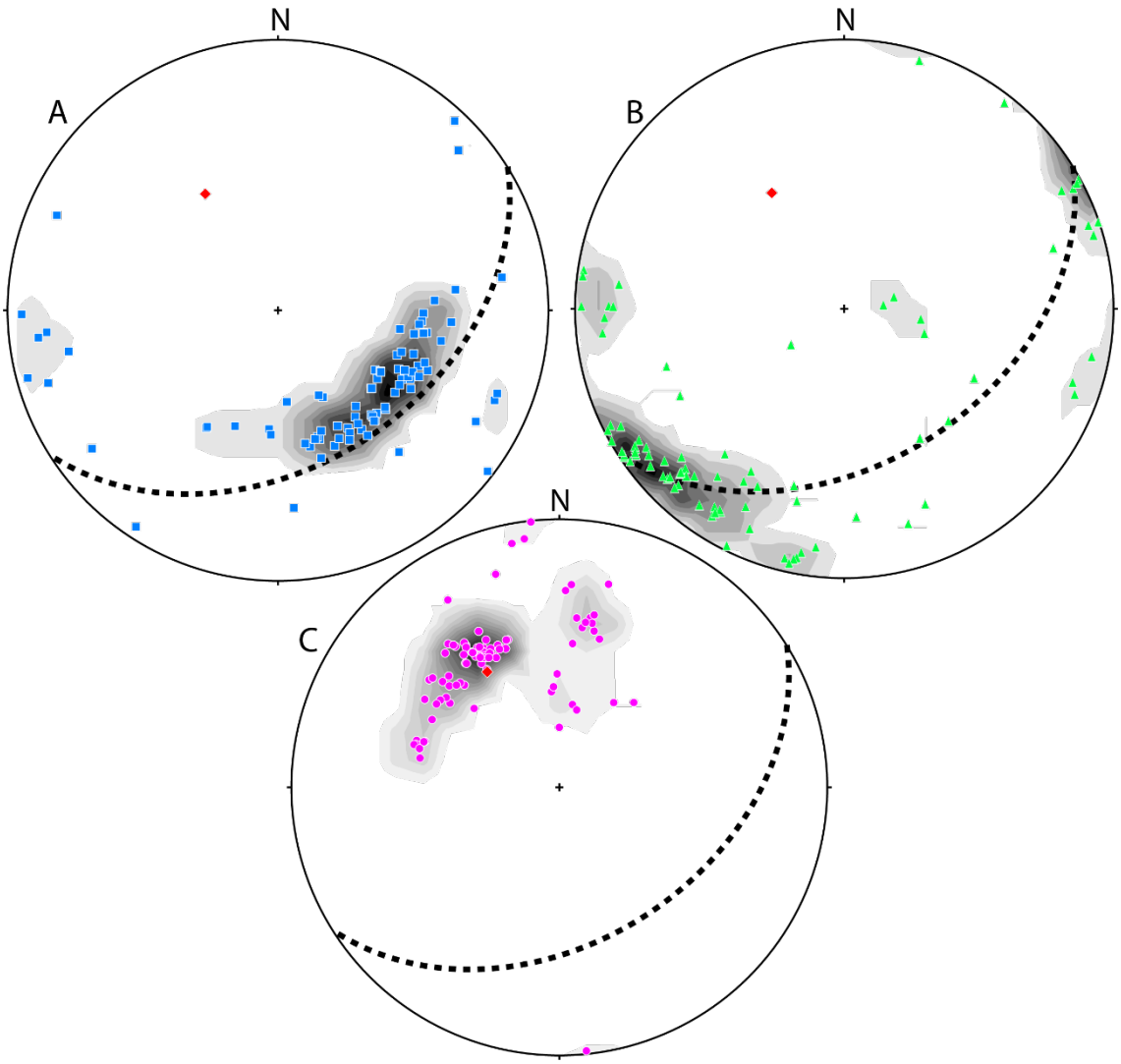

Figure 5.5. Figure illustrating the distributions of AMS principal axes on equal-area stereographic projections. (A): The maximum axes mostly lie on the average foliation of the sole rocks and plunging towards mainly SE, close to the metamorphic lineation observed in the field. (B): intermediate principal directions also mainly lie on the average foliation plane. (C): minimum principal axes dip towards the NW and coincide with the pole to average foliation plane. Note that red point indicates pole to average foliation plane.

5.4 Interpretation of the palaeomagnetic data and rotation analysis

The rotation analyses after removing the late rotation of the dykes cutting the metamorphic sole (reported by Morris et al., 2017) indicate that metamorphic sole rocks of the Mersin ophiolite acquired their weak remanent magnetization when the foliation was moderately dipping towards the ENE and then underwent a rotation around a NW-plunging axis before accretion to the base of the ophiolite. This is consistent with exhumation by slab shallowing during SSZ spreading, as proposed by van Hinsbergen et al. (2015). According to their model, metamorphic sole rocks start forming over a subducting plate in the early stages of initiation of an intra-oceanic subduction

zone and then reach peak metamorphic conditions. However, results of this study show that the sampled metamorphic sole rocks did not reach depths of c. 40 km. This is consistent with the moderate dip of c. 30-40° of the metamorphic foliation at the time of magnetization revealed by the NTR analysis. Metamorphic temperatures of ~530C° obtained in this study imply that most of the rotation experienced by these rocks is recorded by their remanence, as this is carried by magnetite that has a maximum unblocking temperature of 580C°. Hence, the subduction zone probably initiated at dips of 30-40°.

Combined with the results from the Mersin ophiolite reported by Morris et al. (2017), the results of this study indicate that the Mersin metamorphic sole rocks experienced a two-stage rotation history, involving:

1. An early c. 70° counterclockwise rotation around a NW, steeply-inclined axis prior to intrusion of the cross-cutting dykes, as documented here.
2. a c. 45° clockwise rotation around a moderately inclined NE axis after dyke intrusion. Note that restoring the dykes to vertical using this NTR solution restores the metamorphic foliation in the sole rocks to a sub-horizontal orientation at the time of dyke intrusion, indicating that the first phase of rotation occurred entirely prior to the emplacement of the sole to the base of the SSZ lithosphere.

This rotation history is broadly compatible with that inferred by Morris et al. (2017) in the absence of palaeomagnetic data from the sole rocks (Fig. 5.6). This involves: (i) early rotation of the sole due to shallowing of the down-going slab in response to removal of material from the overlying mantle wedge during SSZ spreading; (ii) this rotation is responsible for exhumation of the sole rocks and their emplacement along the base of the SSZ lithosphere by slab flattening; (iii) slab flattening is followed by decoupling and steepening of the slab because of negative buoyancy forces caused by density increase and dehydration activities in the nascent slab (i.e. eclogitization) (van Hinsbergen et al., 2015); (iv) intrusion of dykes that cross-cut the sole rocks; and (v) late rotation of the sole rocks, dykes and overlying SSZ ophiolite as a result of detachment-mode seafloor spreading.

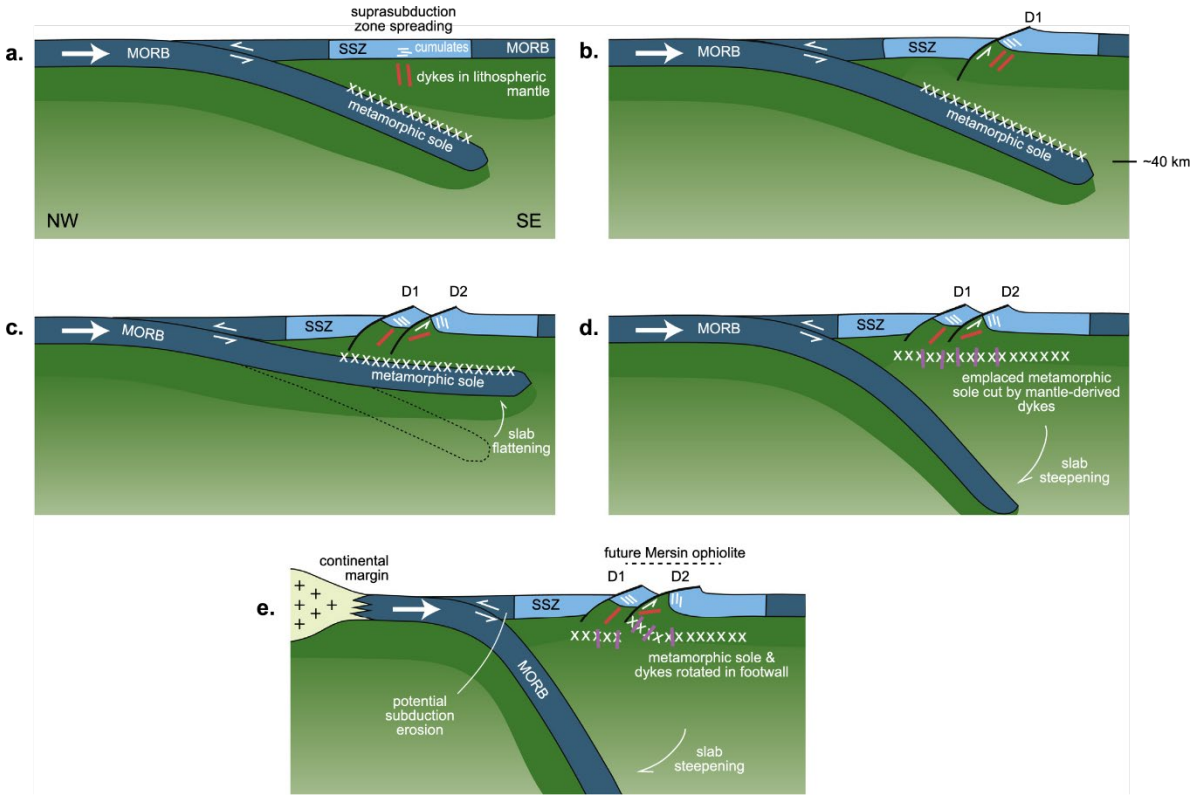

Figure 5.6. Conceptual model for the rapid and extreme rotation of a suprasubduction zone ophiolite and its metamorphic sole in fore-arc environment (from Morris et al., 2017). The details are given in the text.

However, the model illustrated in Figure 5.6 provides only a two-dimensional view of these processes, wherein all rotations are assumed to occur around similar NE trending axes. The results of this study, in contrast, indicate that this is a more complex three-dimensional system. For instance, subduction zones are generally curved in geometry rather than simple planar structures, and NTR results presented here indicate that the early rotation of the sole took place around a very different NW axis than the late, seafloor spreading-related rotation event (around a NE one). These results are best explained by the 3D model shown in Figure. 5.7. Early rotation of the sole around a NW plunging inclined axis is accommodated in this model by a combination of slab flattening and roll-back of the subducting slab. Importantly, this mechanism allows the net 70° of rotation of the metamorphic sole to produce only 30-40° of flattening of the slab during exhumation.

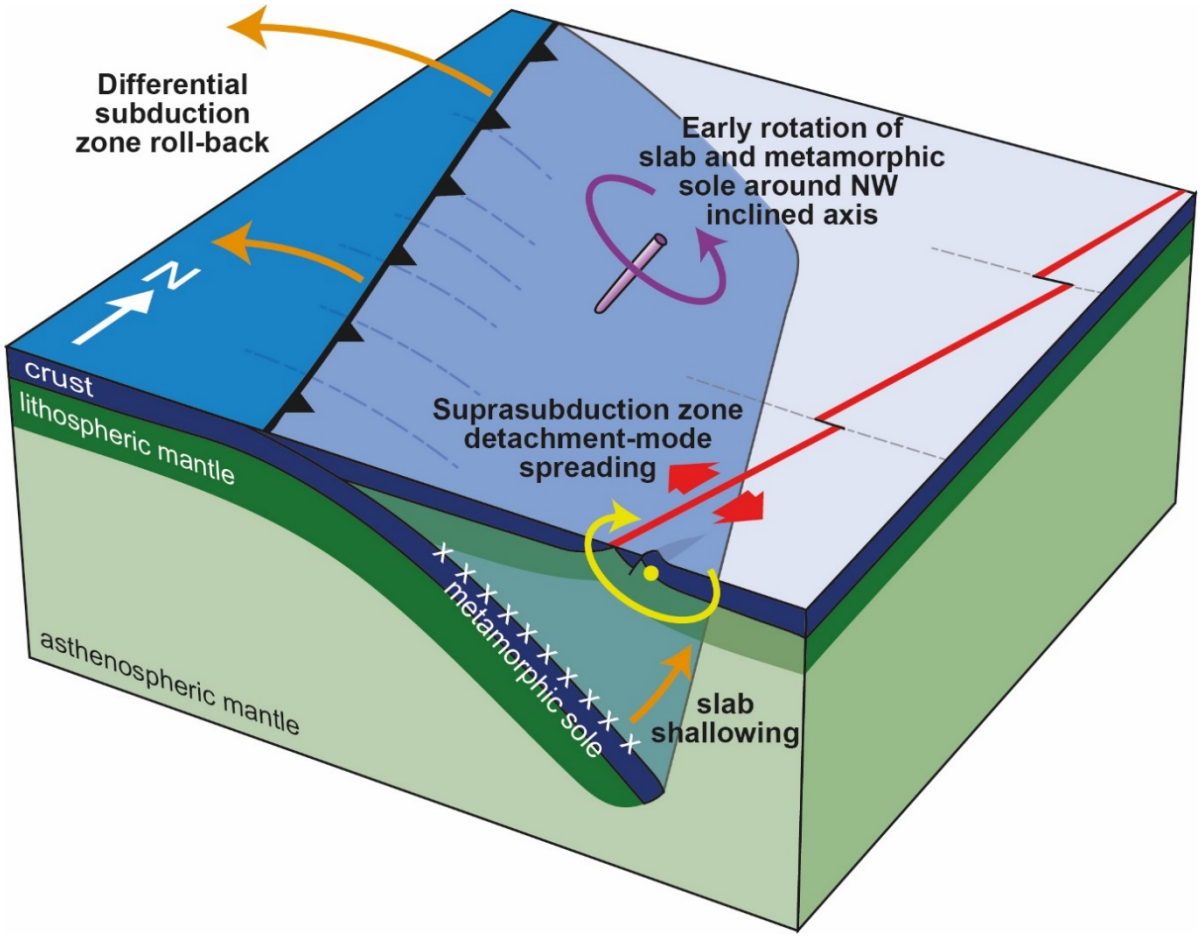

Figure 5.7 3D conceptual model for the rotation history of the Mersin metamorphic sole rocks and ophiolite in a SSZ setting. Differential subduction zone roll back contributes a vertical axis component of rotation that combines with a horizontal axis component due to slab shallowing to produce an early net rotation of the slab and sole rocks around an inclined axis. After rotation and exhumation of the sole rocks to the base of the lithosphere, a late rotation around a ridge parallel axis took place, as documented by Morris et al. (2017).

These rotations around different axes are compatible with a tectonic setting like the modern Andaman Sea subduction zone system (Fig. 5.8), where spreading in the suprasubduction zone environment occurs obliquely to the direction of subduction of the down-going plate.

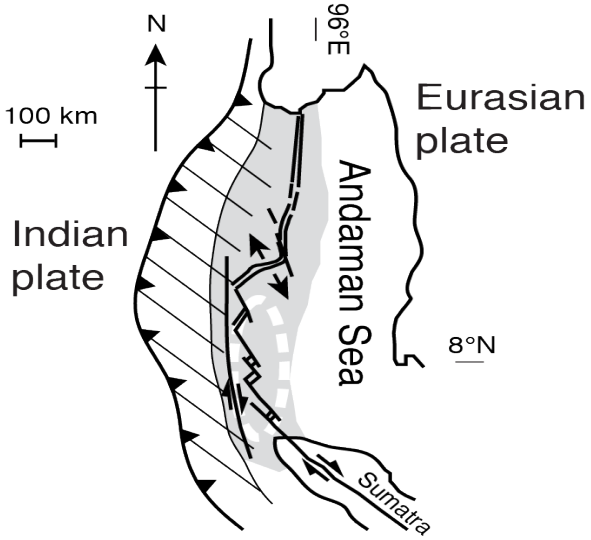

Figure 5.8. Tectonic setting of Andaman Sea region (from Moores et al., 1984).

5.5 Importance of using palaeomagnetism on metamorphic rocks

The processes controlling spreading in SSZ systems have been widely investigated by palaeomagnetic studies of the sheeted dyke complexes, cumulates and sedimentary rocks covering the ophiolite (e.g. Clube and Robertson, 1986; Inwood et al., 2009b; Maffione et al., 2017; Morris and Anderson, 2002; Morris et al., 2017; Morris et al., 1998). The history of metamorphic sole rocks has in contrast been largely investigated using their geochemical and/or petrographic characteristics (e.g. Çelik, 2008; Parlak et al., 1995). However, this study represents the first time that palaeomagnetism has been applied to metamorphic sole rocks. The study clearly demonstrates the potential for net tectonic rotation analysis of remanence data from metamorphic rocks to contribute to understanding their geodynamic evolution. The techniques employed here may also now be applied to some of the other Tauride Belt ophiolites i.e. Göksun ophiolite, Divriği ophiolite, Ali Hoca ophiolite, formed above the same ~N-S to ~NE-SW striking subduction zone system in the Late Cretaceous period (Fig. 4.34).

Chapter 6- Conclusions

The Mersin ophiolite formed in a SSZ environment during the evolution of the Neo-Tethyan Ocean in the Late Cretaceous (Parlak, 1996). Metamorphic sole rocks of the ophiolite formed at the top of the down-going plate (Çelik, 2008; Parlak, 2016) and their magnetization was acquired by magnetite under predominantly amphibolite facies conditions just after subduction initiation.

Amphibolites of the metamorphic sole have a pronounced foliation and well-developed lineation. AMS data reveal oblate shaped ellipsoids and the principal AMS axes of the sole rocks are consistent with the foliation and lineation observed in the field. K_{max} generally lie on the foliation plane forming magnetic lineation and K_{min} coincides to the pole to the foliation plane.

Stepwise AF demagnetization of most metamorphic sole specimens results in great circle demagnetization paths indicating overlap of coercivities of two magnetic components. Combining best fitting great circles with more limited stable end point components results in an overall mean magnetization direction for the sole of 337.3°/-14.3°. This is statistically different from the direction of magnetization of dykes cutting the sole, reported by Morris et al. (2017), suggesting rotation of the sole rocks prior to dyke intrusion.

The palaeomagnetic data may be analysed using a net tectonic rotation approach involving Monte Carlo modelling of uncertainties. After removing the effect of late rotation of the dykes cutting the sole rocks (documented by Morris et al., 2017) and discarding geologically unfeasible solutions, the results show that the sole rocks acquired their magnetization while the foliation dipped towards the ENE and then experienced an early phase of ~70° CCW rotation around an inclined, NW plunging axis.

This rotation can be explained by a combination of slab flattening of the subducting plate because of the decrease in the volume of the mantle wedge during the fore-arc spreading and roll-back of the subduction trench. This led to shallowing and exhumation of the sole rocks formed at the top of the subducting plate.

Zonations in the amphibolite minerals implies a decrease in the metamorphic grade towards rim regions, which is also linked to the shallowing of the sole rocks causing lower P-T conditions. The P-T estimates from geothermobarometric analyses suggest that the temperature was ~530°C during the metamorphism and the pressure was ~4 kbar (±50°C and ±1 kbar, standard uncertainties). These results indicate depths of ~17-18 km for the metamorphism activity prior to exhumation and rotation resulting in decreasing of the P-T conditions.

Chapter 7- Future recommendations

Many previous studies have showed that geometry of the subduction zone systems and seafloor spreading processes can be interpreted with palaeomagnetism tool by using sheeted dyke complexes, cumulates, even sedimentary covers. This study suggests that palaeomagnetic analyses of the metamorphic sole rocks of related ophiolite are also quite useful to estimate the tectonic development in SSZ environment. The Fındıkpınarı road cut section was the region that the samples were collected, however, some samples from other outcrops might have been practical. The further palaeomagnetic studies with the sole rocks from Tauride ophiolites of the eastern Mediterranean region i.e. Alihoca ophiolite, Divriği ophiolite, Beyşehir ophiolite, Lycian ophiolite formed due to closure of the Neo-Tethyan Ocean will definitely contribute to the understanding of the generation of the sole rocks and also formation and generation of the ophiolites in SSZ environment. Also, the vertical and horizontal rotations may be calculated individually to be able to simulate the early rotations in fore-arc environment.

REFERENCES

Aktaş G and Robertson A. (1984) The Maden Complex, SE Turkey: evolution of a Neotethyan active margin. *Geological Society, London, Special Publications* 17: 375-402.

Al-Riyami K, Robertson A, Dixon J, et al. (2002) Origin and emplacement of the Late Cretaceous Baer–Bassit ophiolite and its metamorphic sole in NW Syria. *Lithos* 65: 225-260.

Allerton S and Vine F. (1987) Spreading structure of the Troodos ophiolite, Cyprus: Some paleomagnetic constraints. *Geology* 15: 593-597.

Allmendinger R. (2018) Stereonet, version 10.

Anderson JL and Smith DR. (1995) The effects of temperature and fO_2 on the Al-in-hornblende barometer. *American Mineralogist* 80: 549-559.

Bağci U, Parlak O and Höck V. (2005) Whole-rock and mineral chemistry of cumulates from the Kızıldağ (Hatay) ophiolite (Turkey): clues for multiple magma generation during crustal accretion in the southern Neotethyan ocean. *Mineralogical Magazine* 69: 53-76.

Billor MZ and Gibb F. (2002) The Mineralogy and Chemistry of the Chromite Deposits of Southern (Kızıldağ, Hatay and Islahiye, Antep) and Tauric Ophiolite Belt (Pozantı-Karsantı, Adana), Turkey. *Abstract of 9th international platinum symposium, Billings.* 21-25.

Borradaile G, Keeler W, Alford C, et al. (1987) Anisotropy of magnetic susceptibility of some metamorphic minerals. *Physics of the Earth and Planetary Interiors* 48: 161-166.

Bozkurt E and Mittwede SK. (2001) Introduction to the geology of Turkey—a synthesis. *International Geology Review* 43: 578-594.

Butler RF. (1992) *Paleomagnetism: magnetic domains to geologic terranes*: Blackwell Scientific Publications Boston.

Çelik ÖF. (2008) Detailed geochemistry and K-Ar geochronology of the metamorphic sole rocks and their mafic dykes from the Mersin Ophiolite, Southern Turkey. *Turkish Journal of Earth Sciences* 17: 685-708.

Çelik OF and Delaloye M. (2004) Mineral chemistry and P–T conditions of metamorphic sole rocks from the Lycian and the Antalya ophiolites, western Taurides (SW Turkey). *Proceedings of 5th international Eastern Mediterranean Geology Symposium.* 14-20.

Çelik ÖF, Delaloye M and Feraud G. (2006) Precise 40 Ar–39 Ar ages from the metamorphic sole rocks of the Tauride Belt Ophiolites, southern Turkey: implications for the rapid cooling history. *Geological Magazine* 143: 213-227.

Çelik ÖF and Delaloye MF. (2006) Characteristics of ophiolite-related metamorphic rocks in the Beysehir ophiolitic mélange (Central Taurides, Turkey), deduced from whole rock and mineral chemistry. *Journal of Asian Earth Sciences* 26: 461-476.

Cinku MC, Hisarli ZM, Yılmaz Y, et al. (2016) The tectonic history of the Niğde-Kırşehir Massif and the Taurides since the Late Mesozoic: Paleomagnetic evidence for two-phase orogenic curvature in Central Anatolia. *Tectonics* 35: 772-811.

Clube T and Robertson A. (1986) The palaeorotation of the Troodos Microplate, Cyprus, in the late Mesozoic-early Cenozoic plate tectonic framework of the eastern Mediterranean. *Surveys in Geophysics* 8: 375-437.

Collins AS and Robertson AH. (1998) Processes of Late Cretaceous to Late Miocene episodic thrust-sheet translation in the Lycian Taurides, SW Turkey. *Journal of the Geological Society* 155: 759-772.

Dilek Y and Eddy CA. (1992) The Troodos (Cyprus) and Kizildag (S. Turkey) ophiolites as structural models for slow-spreading ridge segments. *The Journal of Geology* 100: 305-322.

Dilek Y and Furnes H. (2014) Ophiolites and their origins. *Elements* 10: 93-100.

Dilek Y, Thy P, Hacker B, et al. (1999) Structure and petrology of Tauride ophiolites and mafic dike intrusions (Turkey): Implications for the Neotethyan ocean. *Geological Society of America Bulletin* 111: 1192-1216.

Dilek Y and Whitney DL. (1997) Counterclockwise PTt trajectory from the metamorphic sole of a Neo-Tethyan ophiolite (Turkey). *Tectonophysics* 280: 295-310.

Elitok Ö and Drüppel K. (2008) Geochemistry and tectonic significance of metamorphic sole rocks beneath the Beyşehir–Hoyran ophiolite (SW-Turkey). *Lithos* 100: 322-353.

Ferré EC. (2002) Theoretical models of intermediate and inverse AMS fabrics. *Geophysical Research Letters* 29: 31-31-31-34.

Floyd PA, Göncüoğlu MC, Winchester JA, et al. (2000) Geochemical character and tectonic environment of Neotethyan ophiolitic fragments and metabasites in the Central Anatolian Crystalline Complex, Turkey. *Geological Society, London, Special Publications* 173: 183-202.

Göncüoglu MC, Sayit K and Tekin UK. (2010) Oceanization of the northern Neotethys: geochemical evidence from ophiolitic melange basalts within the Izmir–Ankara suture belt, NW Turkey. *Lithos* 116: 175-187.

Holland T and Blundy J. (1994) Non-ideal interactions in calcic amphiboles and their bearing on amphibole-plagioclase thermometry. *Contributions to Mineralogy and Petrology* 116: 433-447.

Hrouda F. (2010) Modelling relationship between bulk susceptibility and AMS in rocks consisting of two magnetic fractions represented by ferromagnetic and paramagnetic minerals—Implications for understanding magnetic fabrics in deformed rocks. *Journal of the Geological Society of India* 75: 254-266.

Hrouda F and Janák F. (1976) The changes in shape of the magnetic susceptibility ellipsoid during progressive metamorphism and deformation. *Tectonophysics* 34: 135-148.

Inwood J, Morris A, Anderson MW, et al. (2009b) Neotethyan intraoceanic microplate rotation and variations in spreading axis orientation: Palaeomagnetic evidence from the Hatay ophiolite (southern Turkey). *Earth and Planetary Science Letters* 280: 105-117.

Jelinek V. (1981) Characterization of the magnetic fabric of rocks. *Tectonophysics* 79: T63-T67.

Kaymakci N, Özçelik Y, White SH, et al. (2009) Tectono-stratigraphy of the Çankırı Basin: late Cretaceous to early Miocene evolution of the Neotethyan suture zone in Turkey. *Geological Society, London, Special Publications* 311: 67-106.
Kirschvink J. (1980) The least-squares line and plane and the analysis of palaeomagnetic data. *Geophysical Journal of the Royal Astronomical Society* 62: 699-718.
Koc H, Tasli K and ÖZER E. (2013) Revised Late Campanian-Danian age of the melange-related turbiditic sequence in the Mersin area (Central Taurides, S. Turkey). *Turkish Journal of Earth Sciences* 22: 239-246.
Leake BE, Woolley AR, Arps CE, et al. (1997) Nomenclature of amphiboles; report of the Subcommittee on Amphiboles of the International Mineralogical Association Commission on new minerals and mineral names. *Mineralogical Magazine* 61: 295-310.
Lowrie W. (1990) Identification of ferromagnetic minerals in a rock by coercivity and unblocking temperature properties. *Geophysical Research Letters* 17: 159-162.
Lurcock PC and Wilson GS. (2012) PuffinPlot: A versatile, user-friendly program for paleomagnetic analysis. *Geochemistry, Geophysics, Geosystems* 13.
Lytwyn J and Casey J. (1993) The geochemistry and petrogenesis of volcanics and sheeted dikes from the Hatay (Kizildag) ophiolite, southern Turkey: possible formation with the Troodos ophiolite, Cyprus, along fore-arc spreading centers. *Tectonophysics* 223: 237-272.
Maffione M, van Hinsbergen DJJ, de Gelder GINO, et al. (2017) Kinematics of Late Cretaceous subduction initiation in the Neo-Tethys Ocean reconstructed from ophiolites of Turkey, Cyprus, and Syria. *Journal of Geophysical Research: Solid Earth* 122: 3953-3976.
Mamtani MA, Abhijith V, Lahiri S, et al. (2017) Determining the reference frame for kinematic analysis in S-tectonites using AMS. *Journal of the Geological Society of India* 90: 5-8.
McElhinny M and McFadden PL. (1998) *The magnetic field of the earth: paleomagnetism, the core, and the deep mantle*: Academic Press.
McElhinny MW and McFadden PL. (1999) *Paleomagnetism: continents and oceans*: Elsevier.
McFadden P and McElhinny M. (1988) The combined analysis of remagnetization circles and direct observations in palaeomagnetism. *Earth and Planetary Science Letters* 87: 161-172.
Merrill RT and McFadden PL. (1999) Geomagnetic polarity transitions. *Reviews of Geophysics* 37: 201-226.
Miri M, asghar Sepahi A, Aliani F, et al. (2016) Chemical zoning of Ca-amphiboles in amphibolites, from the Hamedan area, West Iran. *Arabian Journal of Geosciences* 9: 619.
Moix P, Beccaletto L, Kozur HW, et al. (2008) A new classification of the Turkish terranes and sutures and its implication for the paleotectonic history of the region. *Tectonophysics* 451: 7-39.
Moores E, Robinson PT, Malpas J, et al. (1984) Model for the origin of the Troodos massif, Cyprus, and other mideast ophiolites. *Geology* 12: 500-503.
Morris A. (2003) A palaeomagnetic and rock magnetic glossary. *Tectonophysics* 377: 211-228.
Morris A and Anderson M. (2002) Palaeomagnetic results from the Baër-Bassit ophiolite of northern Syria and their implication for fold tests in sheeted dyke terrains. *Physics and Chemistry of the Earth, Parts A/B/C* 27: 1215-1222.
Morris A, Anderson MW, Omer A, et al. (2017) Rapid fore-arc extension and detachment-mode spreading following subduction initiation. *Earth and Planetary Science Letters* 478: 76-88.
Morris A, Anderson MW and Robertson AH. (1998) Multiple tectonic rotations and transform tectonism in an intraoceanic suture zone, SW Cyprus. *Tectonophysics* 299: 229-253.
Morris A, Creer K and Robertson A. (1990) Palaeomagnetic evidence for clockwise rotations related to dextral shear along the southern Troodos transform fault, Cyprus. *Earth and Planetary Science Letters* 99: 250-262.
Morris A and Maffione M. (2016) Is the Troodos ophiolite (Cyprus) a complete, transform fault–bounded Neotethyan ridge segment? *Geology* 44: 199-202.
Mosier DL, Singer DA, Moring BC, et al. (2012) Podiform chromite depositsdatabase and grade and tonnage models. *US Geological Survey Scientific Investigations Report* 5157: 45.
Moskowitz BM. (1991) Hitchhiker's guide to magnetism. *Environmental Magnetism Workshop (IRM).* Inst. for Rock Magnetism Univ. of Minn., Minneapolis, Minn, 48.
O driscoll B. (2006) Magmatic layering and magnetic fabrics in the Palaeogene Carlingford Later Gabbros, Co. Louth, Ireland. *Irish Journal of Earth Sciences* 24: 37.
Okay A and Kelley S. (1994) Tectonic setting, petrology and geochronology of jadeite+ glaucophane and chloritoid+ glaucophane schists from north-west Turkey. *Journal of Metamorphic Geology* 12: 455-466.
Okay AI. (1989) Alpine-Himalayan blueschists. *Annual Review of Earth and Planetary Sciences* 17: 55-87.
Okay AI and Tüysüz O. (1999) Tethyan sutures of northern Turkey. *Geological Society, London, Special Publications* 156: 475-515.
Okay AI and Whitney DL. (2010) Blueschists, eclogites, ophiolites and suture zones in northwest Turkey: a review and a field excursion guide. *Ofioliti* 35: 131-172.
Omer AF. (2014) Integrated geophysical, geochemical and structural analysis of the Mersin ophiolite, southern Turkey.
Pagé P, Bédard JH and Tremblay A. (2009) Geochemical variations in a depleted fore-arc mantle: the Ordovician Thetford Mines Ophiolite. *Lithos* 113: 21-47.
Parlak O. (1996) Geochemistry and geochronology of the Mersin ophiolite within the eastern Mediterranean tectonic frame (southern Turkey). University of Geneva.
Parlak O. (2016) The tauride ophiolites of Anatolia (Turkey): A review. *Journal of Earth Science* 27: 901-934.
Parlak O, Bozkurt E and Delaloye M. (1996a) The obduction direction of the Mersin Ophiolite: structural evidence from subophiolitic metamorphics in the Central Tauride Belt, Southern Turkey. *International Geology Review* 38: 778-786.

Parlak O and Delaloye M. (1996) Geochemistry and timing of post-metamorphic dyke emplacement in the Mersin Ophiolite (southern Turkey): New age constraints from 40Ar/39Ar geochronology. *Terra Nova* 8: 585-592.
Parlak O and Delaloye M. (1999) Precise 40Ar/39Ar ages from the metamorphic sole of the Mersin ophiolite (southern Turkey). *Tectonophysics* 301: 145-158.
Parlak O, Delaloye M and Bingöl E. (1995) Origin of subophiolitic metamorphic rocks beneath the Mersin ophiolite, southern Turkey. *Ofioliti* 20: 97-110.
Parlak O, Delaloye M and Bíngöl E. (1996) Mineral chemistry of ultramafic and mafic cumulates as an indicator of the arc-related origin of the Mersin ophiolite (southern Turkey). *Geologische Rundschau* 85: 647.
Parlak O, HÖck V and Delaloye M. (2000) Suprasubduction zone origin of the Pozanti-Karsanti ophiolite (southern Turkey) deduced from whole-rock and mineral chemistry of the gabbroic cumulates. *Geological Society, London, Special Publications* 173: 219-234.
Parlak O, Höck V and Delaloye M. (2002) The supra-subduction zone Pozanti–Karsanti ophiolite, southern Turkey: evidence for high-pressure crystal fractionation of ultramafic cumulates. *Lithos* 65: 205-224.
Parlak O, Karaoğlan F, Rızaoğlu T, et al. (2013) U–Pb and 40Ar–39Ar geochronology of the ophiolites and granitoids from the Tauride belt: implications for the evolution of the Inner Tauride suture. *Journal of Geodynamics* 65: 22-37.
Parlak O and Robertson A. (2004) The ophiolite-related Mersin Melange, southern Turkey: its role in the tectonic–sedimentary setting of Tethys in the Eastern Mediterranean region. *Geological Magazine* 141: 257-286.
Parlak O, YILMAZ H and Boztuğ D. (2006) Origin and tectonic significance of the metamorphic sole and isolated dykes of the Divriği ophiolite (Sivas, Turkey): evidence for slab break-off prior to ophiolite emplacement. *Turkish Journal of Earth Sciences* 15: 25-45.
Pearce JA, Lippard S and Roberts S. (1984) Characteristics and tectonic significance of supra-subduction zone ophiolites. *Geological Society, London, Special Publications* 16: 77-94.
Petrovský E and Kapička A. (2006) On determination of the Curie point from thermomagnetic curves. *Journal of Geophysical Research: Solid Earth* 111.
Plunder A, Agard P, Chopin C, et al. (2013) Geodynamics of the Tavşanlı zone, western Turkey: Insights into subduction/obduction processes. *Tectonophysics* 608: 884-903.
Reeve WD. (2010) Geomagnetism Tutorial. *Reeve Observatory Anchorage, Alaska-USA*.
Ricou L-E. (1971) Le croissant ophiolitique pe'ri-arabe, Une ceinture de nappes mises en place au Cre'tace'supe'rieur. *Rev. Géogr. phys. Géol. dynam.*: 327-350.
Rizaoğlu T, Parlak O, Hoeck V, et al. (2006) Nature and significance of Late Cretaceous ophiolitic rocks and their relation to the Baskil granitic intrusions of the Elazığ region, SE Turkey. *Geological Society, London, Special Publications* 260: 327-350.
Robertson A and Grasso M. (1995) Overview of the Late Tertiary–Recent tectonic and palaeo-environmental development of the Mediterranean region. *Terra Nova* 7: 114-127.
Robertson AH. (1998) Formation and destruction of the Eratosthenes Seamount, Eastern Mediterranean Sea, and implications for collisional processes. *Proceedings of the Ocean Drilling Program, Scientific Results, Vol. 160; Chapter 51*.
Robertson AH. (2000) Mesozoic-Tertiary tectonic-sedimentary evolution of a south Tethyan oceanic basin and its margins in southern Turkey. *Geological Society, London, Special Publications* 173: 97-138.
Robertson AH. (2002) Overview of the genesis and emplacement of Mesozoic ophiolites in the Eastern Mediterranean Tethyan region. *Lithos* 65: 1-67.
Robertson AH, Parlak O and Ustaömer T. (2012) Overview of the Palaeozoic–Neogene evolution of neotethys in the Eastern Mediterranean region (southern turkey, cyprus, Syria). *Petroleum Geoscience* 18: 381-404.
Robertson AH, Parlak O and Ustaömer T. (2013) Late Palaeozoic–Early Cenozoic tectonic development of Southern Turkey and the easternmost Mediterranean region: evidence from the inter-relations of continental and oceanic units. *Geological Society, London, Special Publications* 372: SP372. 322.
Robinson AG. (1997) *Regional and Petroleum Geology of the Black Sea and Surrounding Region: AAPG Memoir 68*: AAPG.
Rochette P, Jackson M and Aubourg C. (1992) Rock magnetism and the interpretation of anisotropy of magnetic susceptibility. *Reviews of Geophysics* 30: 209-226.
Sarıfakıoğlu E, Dilek Y and Sevin M. (2017) New synthesis of the Izmir-Ankara-Erzincan suture zone and the Ankara mélange in northern Anatolia based on new geochemical and geochronological constraints.
Searle MP. (2014) Preserving Oman's geological heritage: proposal for establishment of world heritage sites, national geoparks and sites of special scientific interest (SSSI). *Geological Society, London, Special Publications* 392: 9-44.
Şengör A, Görür N and Şaroğlu F. (1985) Strike-slip faulting and related basin formation in zones of tectonic escape: Turkey as a case study.
Şengör A and Yilmaz Y. (1981) Tethyan evolution of Turkey: a plate tectonic approach. *Tectonophysics* 75: 181-241.
Seymen I. (1983) Tectonic features of Kaman group in comparison with those of its neighbouring formations around Tamadag (Kaman-Kırs ehir). *Bulletin of Geological Society of Turkey* 26.
Stern RJ, Reagan M, Ishizuka O, et al. (2012) To understand subduction initiation, study forearc crust: To understand forearc crust, study ophiolites. *Lithosphere* 4: 469-483.
Tarling D. (1971) Gondwanaland, palaeomagnetism and continental drift. *Nature* 229: 17.
Tarling D and Hrouda F. (1993) *Magnetic anisotropy of rocks*: Springer Science & Business Media.
Tauxe L, Banerjee SK, Butler RF, et al. (2013) Essentials of paleomagnetism: second web edition. *Scripps Institution of Oceanography*.

Ten Grotenhuis S, Trouw R and Passchier C. (2003) Evolution of mica fish in mylonitic rocks. *Tectonophysics* 372: 1-21.

Thellier E. (1938) Sur l'aimantation des terres cuites et ses applications géophysique. *Ann. Inst. Phys. Globe Univ. Paris* 16: 157-302.

Thompson R and Oldfield T. (1986) Environmental Magnetism. *London: Allen and Uniwin* 227.

Torsvik TH, Van der Voo R, Preeden U, et al. (2012) Phanerozoic polar wander, palaeogeography and dynamics. *Earth-Science Reviews* 114: 325-368.

Ustaomer T and Robertson A. (1998) Tectonic-sedimentary evolution of the North-Tethyan margin in the Central Pontides of northern Turkey. *MEMOIRS-AMERICAN ASSOCIATION OF PETROLEUM GEOLOGISTS*: 255-290.

van Hinsbergen DJ, Maffione M, Plunder A, et al. (2016) Tectonic evolution and paleogeography of the Kırşehir Block and the Central Anatolian Ophiolites, Turkey. *Tectonics* 35: 983-1014.

van Hinsbergen DJ, Peters K, Maffione M, et al. (2015) Dynamics of intraoceanic subduction initiation: 2. Suprasubduction zone ophiolite formation and metamorphic sole exhumation in context of absolute plate motions. *Geochemistry, Geophysics, Geosystems* 16: 1771-1785.

Woodcock N. (1977) Specification of fabric shapes using an eigenvalue method. *Geological Society of America Bulletin* 88: 1231-1236.

Yaliniz M, Floyd P and Göncüoĝlu M. (1996) Supra-subduction zone ophiolites of Central Anatolia: geochemical evidence from the Sarikaraman ophiolite, Aksaray, Turkey. *Mineralogical Magazine* 60: 697-710.

Yilmaz YC. (1993) New evidence and model on the evolution of the southeast Anatolian orogen. *Geological Society of America Bulletin* 105: 251-271.

Zijderveld J. (1967) AC demagnetization of rocks: Analysis of results, Methods in Paleomagnetism DW Collinson, KM Creer, SK Runcorn, 254–286. Elsevier, New York.

APPENDICES

Table A1. Possible rotation points out of 1000 points after back-stripping the late rotation effect of the dykes and discarding 846 potential rotations based on the geological constraints. SMV=Sole magnetization vector; PF=Present pole to foliation; RMV=Reference magnetization vector; IPF=Initial pole to foliation; RP=Rotation pole; Beta=β angle between the magnetization vector and pole to foliation.

	SMV Dec	SMV Inc	PF Dec	PF Inc	RMV dec	RMV inc	IPF dec	IPF inc	Beta	RP dec	RP inc	Angle	Sense
1	310.00	22.40	326.50	82.60	0.00	54.70	245.20	51.85	60.52	292.51	56.63	88.52	CCW
2	318.20	19.60	327.10	81.70	0.00	37.20	267.80	53.27	62.21	315.85	53.95	75.24	CCW
3	309.50	20.10	330.70	81.00	0.00	32.70	250.59	78.92	61.55	292.94	71.04	60.25	CCW
4	313.60	16.00	325.80	84.60	0.00	44.00	209.15	64.92	68.73	270.51	58.94	61.10	CCW
5	318.80	25.20	320.30	84.60	0.00	26.10	288.76	71.44	59.40	336.66	68.87	53.35	CCW
6	319.60	27.00	2.00	80.40	0.00	41.20	273.00	54.21	56.13	322.92	54.71	82.77	CCW
7	321.40	21.30	342.10	85.30	0.00	39.80	248.09	62.29	64.31	306.26	58.11	62.55	CCW
8	320.60	19.50	265.60	86.20	0.00	39.00	229.18	66.05	68.35	286.10	62.24	52.71	CCW
9	306.50	22.50	358.70	84.40	0.00	53.80	211.39	59.28	64.14	272.95	60.16	75.54	CCW
10	314.90	19.90	329.30	80.00	0.00	32.40	270.91	65.56	60.44	314.01	61.07	66.02	CCW
11	319.30	20.20	358.60	83.70	0.00	26.30	139.58	88.32	64.98	275.25	80.63	42.47	CCW
12	315.30	16.10	312.30	82.50	0.00	53.30	236.95	49.66	66.41	287.47	51.96	79.76	CCW
13	311.80	18.80	335.00	85.50	0.00	47.50	237.60	54.46	67.07	291.97	56.95	77.53	CCW
14	312.90	19.70	320.50	82.30	0.00	37.70	225.76	75.94	62.67	277.91	67.50	56.89	CCW
15	307.60	22.00	28.00	81.80	0.00	51.40	231.80	53.06	66.87	292.60	58.18	86.81	CCW
16	309.60	19.50	351.20	86.10	0.00	54.30	223.22	52.20	67.61	280.22	56.33	79.52	CCW

	SMV Dec	SMV Inc	PF Dec	PF Inc	RMV dec	RMV inc	IPF dec	IPF inc	Beta	RP dec	RP inc	Angle	Sense
17	310.60	22.00	16.90	81.60	0.00	37.20	207.97	76.59	64.85	286.95	69.56	60.30	CCW
18	316.20	18.30	345.50	84.00	0.00	25.40	265.41	76.04	66.50	315.69	69.22	53.75	CCW
19	311.80	16.90	166.90	89.00	0.00	35.20	254.74	47.21	73.92	316.23	51.86	86.56	CCW
20	308.00	21.60	69.00	86.30	0.00	44.20	201.56	64.14	70.34	270.30	65.79	63.95	CCW
21	312.50	21.20	331.10	86.70	0.00	33.40	268.06	51.30	65.68	319.85	56.61	78.63	CCW
22	313.00	22.80	350.00	79.00	0.00	35.20	253.13	79.05	58.61	301.55	68.35	60.43	CCW
23	309.10	24.30	310.50	80.40	0.00	36.40	258.91	80.04	56.10	285.53	73.65	59.08	CCW
24	317.80	23.20	14.90	81.70	0.00	42.60	259.86	52.92	62.49	315.59	54.22	82.62	CCW
25	320.00	20.80	266.50	86.80	0.00	36.50	228.19	70.81	67.32	285.38	66.68	49.75	CCW
26	314.50	22.90	37.50	85.50	0.00	51.80	237.56	50.60	66.63	296.95	56.44	81.77	CCW
27	316.90	19.00	261.10	85.50	0.00	38.20	269.14	37.41	68.51	318.38	50.69	85.80	CCW
28	310.40	28.60	343.30	81.80	0.00	30.60	288.86	57.64	54.62	332.35	59.71	80.25	CCW
29	316.50	21.40	356.80	79.30	0.00	31.90	266.84	72.63	60.63	315.83	63.07	61.89	CCW
30	312.60	20.80	22.10	87.90	0.00	33.60	234.56	71.08	68.48	299.00	68.55	59.53	CCW
31	313.50	29.50	332.80	87.30	0.00	31.60	284.29	48.16	57.96	334.18	56.47	83.76	CCW
32	315.10	19.80	348.10	83.10	0.00	34.00	255.21	66.86	64.46	309.42	61.72	64.78	CCW
33	313.30	22.20	30.30	86.30	0.00	44.20	257.76	45.48	67.01	311.80	54.50	89.10	CCW
34	313.70	20.70	8.90	81.00	0.00	51.50	226.71	57.64	64.36	289.55	56.37	77.28	CCW
35	312.90	27.10	337.30	83.90	0.00	30.60	282.22	65.97	57.38	329.33	64.77	67.65	CCW
36	314.00	23.50	338.40	85.40	0.00	50.50	221.14	62.59	62.33	280.77	60.09	67.12	CCW

	SMV Dec	SMV Inc	PF Dec	PF Inc	RMV dec	RMV inc	IPF dec	IPF inc	Beta	RP dec	RP inc	Angle	Sense
37	311.60	22.00	357.50	81.50	0.00	28.00	273.29	74.46	62.23	320.93	67.54	62.86	CCW
38	311.10	19.70	26.00	85.10	0.00	37.20	251.68	55.54	69.10	310.18	57.96	77.91	CCW
39	313.20	25.30	316.50	87.30	0.00	42.90	265.15	48.57	62.00	314.60	56.95	85.86	CCW
40	312.50	24.10	33.80	81.60	0.00	50.70	227.70	57.54	64.90	293.80	59.03	78.32	CCW
41	313.20	24.50	314.50	84.70	0.00	26.60	287.14	42.56	60.20	334.33	52.33	84.86	CCW
42	314.00	22.70	356.30	79.60	0.00	29.90	277.93	65.22	59.82	325.34	59.54	70.97	CCW
43	314.80	26.10	355.10	83.70	0.00	41.10	257.25	63.29	59.17	311.21	61.46	72.29	CCW
44	313.50	30.10	328.90	83.40	0.00	41.20	248.22	79.11	53.55	294.19	72.81	57.36	CCW
45	313.50	19.20	345.10	84.20	0.00	55.50	207.73	56.37	65.89	270.67	54.17	70.00	CCW
46	318.20	23.30	74.80	86.00	0.00	41.90	243.27	55.95	68.54	308.94	58.17	70.79	CCW
47	311.30	25.40	338.10	81.00	0.00	27.50	289.69	55.40	56.65	332.79	57.56	78.76	CCW
48	312.50	22.50	13.60	88.30	0.00	40.00	262.11	46.71	66.69	315.35	55.45	85.93	CCW
49	311.40	21.10	348.50	82.50	0.00	27.30	277.06	60.99	63.00	325.83	59.63	72.38	CCW
50	318.90	18.30	346.50	84.50	0.00	53.70	216.72	55.35	66.85	279.39	52.27	68.17	CCW
51	315.60	21.50	5.60	79.30	0.00	39.00	213.78	77.24	61.89	288.57	65.67	57.64	CCW
52	314.40	23.30	286.20	83.70	0.00	55.00	236.97	54.24	61.19	285.05	56.97	75.48	CCW
53	312.40	26.30	335.50	84.70	0.00	35.50	279.48	47.23	58.85	325.80	55.30	88.10	CCW
54	312.70	23.70	344.90	83.30	0.00	28.90	283.21	46.92	60.69	330.66	52.99	85.31	CCW
55	314.00	22.70	49.70	86.10	0.00	36.20	231.26	69.70	67.74	301.23	66.96	60.66	CCW
56	315.10	29.70	289.10	82.10	0.00	25.60	314.48	72.99	53.27	0.74	77.85	50.91	CCW

	SMV Dec	SMV Inc	PF Dec	PF Inc	RMV dec	RMV inc	IPF dec	IPF inc	Beta	RP dec	RP inc	Angle	Sense
57	313.90	22.80	300.00	82.80	0.00	32.80	273.67	60.16	60.22	318.37	62.06	68.16	CCW
58	311.80	17.80	34.50	89.30	0.00	40.60	235.46	56.67	72.11	294.96	59.72	70.72	CCW
59	318.70	24.60	337.20	79.30	0.00	51.80	254.65	56.92	55.31	302.70	55.61	80.64	CCW
60	316.20	28.20	330.30	81.30	0.00	46.70	261.42	62.25	53.39	307.31	60.71	74.86	CCW
61	310.50	22.40	339.10	82.10	0.00	29.10	275.10	74.13	60.72	317.21	69.19	62.79	CCW
62	314.40	23.60	306.80	88.20	0.00	45.00	230.30	63.30	64.62	288.38	62.94	64.29	CCW
63	308.50	23.50	300.70	81.60	0.00	42.90	243.67	69.86	58.18	285.45	66.51	67.18	CCW
64	312.80	22.30	336.20	85.70	0.00	28.90	262.12	76.54	63.77	312.88	72.51	56.70	CCW
65	318.00	23.90	37.50	83.70	0.00	32.50	264.35	59.53	65.10	326.74	56.34	72.74	CCW
66	311.90	25.80	336.70	85.40	0.00	31.40	281.42	47.77	60.04	329.40	55.32	85.26	CCW
67	313.70	22.00	331.50	82.60	0.00	37.40	260.68	63.36	60.98	309.43	61.00	70.26	CCW
68	318.20	24.00	283.50	86.80	0.00	49.10	216.89	63.87	63.38	275.33	60.16	57.71	CCW
69	312.10	27.80	349.40	84.80	0.00	31.20	280.29	61.56	58.11	330.25	62.20	73.28	CCW
70	317.60	18.60	51.90	85.40	0.00	32.80	227.61	69.76	71.81	301.57	64.68	56.09	CCW
71	314.50	22.60	261.60	87.40	0.00	36.30	232.17	71.90	65.85	287.76	70.25	54.93	CCW
72	313.90	22.70	2.30	84.60	0.00	26.70	273.28	71.22	63.78	327.30	66.47	61.16	CCW
73	316.00	20.20	346.30	84.70	0.00	41.60	263.06	46.42	65.25	314.08	52.67	85.47	CCW
74	314.50	23.20	74.20	86.20	0.00	40.80	259.86	44.49	68.72	318.37	53.54	89.46	CCW
75	315.30	21.20	59.30	88.60	0.00	34.20	233.69	69.59	69.14	300.24	67.49	57.38	CCW
76	308.40	19.20	345.50	84.30	0.00	39.40	222.30	70.08	66.29	282.84	65.79	65.44	CCW

	SMV Dec	SMV Inc	PF Dec	PF Inc	RMV dec	RMV inc	IPF dec	IPF inc	Beta	RP dec	RP inc	Angle	Sense
77	313.70	23.30	11.80	86.80	0.00	42.20	256.57	51.86	65.04	311.58	57.06	81.61	CCW
78	314.50	25.80	307.00	84.90	0.00	44.70	252.69	61.02	59.15	302.04	61.89	71.08	CCW
79	320.50	27.30	352.00	88.00	0.00	34.30	268.09	62.04	61.00	327.05	61.05	63.83	CCW
80	321.00	26.70	108.30	88.30	0.00	35.10	268.82	49.57	64.73	329.34	55.09	74.75	CCW
81	314.50	24.30	30.20	84.40	0.00	43.00	241.87	61.20	64.44	304.83	60.64	72.42	CCW
82	321.40	20.90	312.00	80.90	0.00	29.10	278.32	83.08	60.13	285.04	76.15	42.34	CCW
83	316.40	24.20	311.60	81.60	0.00	32.00	276.60	82.04	57.43	292.52	76.74	48.83	CCW
84	313.90	22.20	269.60	89.10	0.00	33.70	237.22	71.97	67.16	297.59	70.62	56.29	CCW
85	319.40	25.10	2.70	85.00	0.00	26.80	286.92	37.36	61.31	338.19	47.04	88.71	CCW
86	315.90	17.40	314.50	81.60	0.00	51.80	236.15	54.15	64.20	286.91	53.37	75.48	CCW
87	313.70	23.90	350.60	83.40	0.00	45.40	246.57	60.91	60.89	301.34	59.83	75.03	CCW
88	311.80	18.40	355.80	82.40	0.00	40.00	254.65	54.25	66.22	307.63	55.65	81.26	CCW
89	314.00	23.00	353.90	80.90	0.00	26.50	50.08	84.68	60.17	274.84	85.03	47.01	CCW
90	315.60	17.80	348.60	84.30	0.00	33.40	215.04	77.06	67.45	281.25	68.56	52.56	CCW
91	310.70	19.00	312.10	85.80	0.00	30.10	269.43	52.74	66.80	319.68	57.32	76.67	CCW
92	306.50	21.90	18.80	80.60	0.00	30.50	268.72	56.77	65.54	322.34	57.42	84.87	CCW
93	313.90	24.70	13.60	80.40	0.00	37.50	193.74	81.52	60.76	285.34	72.02	54.54	CCW
94	313.80	21.60	266.30	85.80	0.00	29.50	271.34	54.59	65.60	323.74	59.86	69.87	CCW
95	313.10	15.60	337.20	79.10	0.00	39.50	262.72	50.71	64.51	309.38	52.10	84.42	CCW
96	312.40	22.90	344.30	84.40	0.00	27.10	277.06	68.18	62.38	326.93	65.50	64.33	CCW

	SMV Dec	SMV Inc	PF Dec	PF Inc	RMV dec	RMV inc	IPF dec	IPF inc	Beta	RP dec	RP inc	Angle	Sense
97	314.70	24.80	338.20	85.00	0.00	54.60	213.67	61.79	60.63	274.94	58.59	66.51	CCW
98	313.70	21.50	313.00	89.00	0.00	30.10	269.70	50.25	67.50	325.18	56.18	76.31	CCW
99	313.30	21.50	49.60	89.10	0.00	31.00	254.94	63.94	68.60	317.33	63.49	65.70	CCW
100	317.30	23.80	349.10	82.80	0.00	34.10	197.09	85.57	60.14	275.21	75.42	46.91	CCW
101	313.90	22.50	305.90	84.60	0.00	27.20	284.81	39.76	62.15	332.12	50.84	85.71	CCW
102	316.00	25.40	38.20	85.70	0.00	35.50	274.20	42.60	64.09	327.86	52.07	89.84	CCW
103	308.90	28.60	36.40	82.90	0.00	51.20	206.15	65.76	61.33	279.15	65.60	69.22	CCW
104	315.60	19.00	21.50	81.80	0.00	39.70	250.62	55.05	67.83	310.56	54.65	78.08	CCW
105	311.10	20.70	19.80	84.90	0.00	43.80	203.26	67.28	67.52	274.10	64.04	62.18	CCW
106	314.10	15.20	310.70	85.70	0.00	46.90	227.59	54.99	70.51	283.44	55.12	70.56	CCW
107	313.20	23.00	327.00	87.30	0.00	24.80	283.11	41.58	64.38	334.69	51.28	84.26	CCW
108	317.40	19.80	338.30	84.40	0.00	27.70	256.30	80.31	64.98	304.43	73.15	49.59	CCW
109	312.20	18.90	353.20	84.20	0.00	28.10	272.40	52.10	66.77	324.48	54.54	78.31	CCW
110	313.20	27.30	36.60	83.20	0.00	46.00	243.68	59.87	62.13	306.39	61.00	77.94	CCW
111	310.80	18.00	352.80	83.90	0.00	41.70	206.16	69.10	67.52	273.21	63.42	61.96	CCW
112	312.60	27.50	19.60	84.90	0.00	49.00	207.64	68.61	60.61	277.79	65.38	62.62	CCW
113	310.30	26.10	335.00	80.10	0.00	26.50	10.92	81.32	54.99	326.64	86.86	51.09	CCW
114	311.30	21.80	355.60	80.10	0.00	34.90	250.34	74.84	61.31	304.43	66.33	64.84	CCW
115	318.10	26.30	297.10	82.50	0.00	35.70	272.89	65.65	56.73	316.57	65.37	60.14	CCW
116	312.10	25.70	336.30	84.00	0.00	48.00	243.53	62.10	58.86	296.05	61.59	74.83	CCW

	SMV Dec	SMV Inc	PF Dec	PF Inc	RMV dec	RMV inc	IPF dec	IPF inc	Beta	RP dec	RP inc	Angle	Sense
117	319.20	22.50	339.10	85.10	0.00	30.60	280.82	40.90	62.90	331.57	49.03	84.57	CCW
118	309.50	18.30	11.80	82.00	0.00	40.40	250.39	53.83	68.14	306.43	56.03	84.04	CCW
119	316.00	15.70	335.90	87.30	0.00	32.80	235.84	66.89	71.76	296.58	62.99	58.23	CCW
120	318.80	18.40	346.40	84.80	0.00	28.90	259.27	68.62	67.01	315.65	62.46	57.25	CCW
121	313.40	19.70	344.60	83.50	0.00	37.20	254.96	60.70	64.78	308.17	59.00	72.23	CCW
122	314.90	22.40	28.10	86.60	0.00	24.90	271.63	66.44	66.66	332.28	63.29	62.74	CCW
123	315.00	23.60	331.30	79.80	0.00	45.50	257.80	60.73	56.65	303.90	58.39	76.42	CCW
124	317.70	17.80	35.80	87.20	0.00	33.30	255.01	53.75	71.64	316.25	55.05	70.39	CCW
125	312.40	21.50	26.20	80.50	0.00	52.20	235.27	51.75	66.15	296.72	55.66	86.47	CCW
126	314.60	22.00	14.30	85.30	0.00	46.10	257.37	45.88	65.69	310.43	53.94	89.26	CCW
127	313.80	23.60	344.20	84.70	0.00	43.30	258.04	54.59	61.86	309.33	57.74	80.28	CCW
128	315.00	21.80	340.60	85.40	0.00	29.80	279.27	42.19	64.07	329.29	50.73	85.72	CCW
129	311.80	19.00	322.30	81.00	0.00	39.00	230.39	73.88	62.16	280.94	65.42	60.67	CCW
130	312.80	25.30	343.80	84.30	0.00	50.10	234.57	61.95	59.85	290.80	60.90	73.34	CCW
131	317.90	25.30	306.40	83.50	0.00	31.20	284.30	47.56	58.34	331.58	54.30	77.58	CCW
132	314.30	19.30	12.20	83.60	0.00	25.80	252.39	80.51	67.40	313.12	72.31	53.97	CCW
133	307.80	24.60	116.20	88.90	0.00	38.90	209.91	72.71	66.48	273.55	73.25	59.37	CCW
134	306.80	23.30	331.90	79.40	0.00	35.70	275.68	59.06	57.19	315.64	60.10	82.96	CCW
135	310.30	21.60	300.60	84.80	0.00	31.90	234.69	81.46	63.28	275.78	76.75	54.02	CCW
136	307.20	22.00	28.50	83.80	0.00	27.30	269.79	58.08	67.20	325.97	59.29	79.16	CCW

	SMV Dec	SMV Inc	PF Dec	PF Inc	RMV dec	RMV inc	IPF dec	IPF inc	Beta	RP dec	RP inc	Angle	Sense
137	312.50	24.60	347.40	84.80	0.00	27.40	328.50	88.32	61.17	301.06	84.21	49.66	CCW
138	318.10	24.80	326.20	82.70	0.00	50.50	248.25	58.08	57.98	298.68	57.41	74.50	CCW
139	320.90	26.90	328.40	83.00	0.00	51.00	219.26	69.46	56.16	279.02	60.13	56.36	CCW
140	309.50	22.10	34.80	89.50	0.00	30.80	270.78	46.07	67.86	324.20	55.76	84.15	CCW
141	316.10	20.50	59.80	86.20	0.00	37.20	213.27	69.61	70.44	287.66	66.39	55.58	CCW
142	308.00	18.40	44.50	86.40	0.00	29.80	196.73	77.68	72.04	274.95	75.87	56.52	CCW
143	314.20	22.60	348.40	85.00	0.00	40.70	227.89	70.86	63.30	289.22	65.49	60.55	CCW
144	316.10	26.20	343.40	87.80	0.00	26.30	281.29	60.25	61.85	337.87	60.83	66.56	CCW
145	314.40	23.90	348.70	83.90	0.00	38.00	243.30	72.76	61.11	300.24	66.73	61.02	CCW
146	316.50	22.50	326.00	80.00	0.00	41.00	250.96	70.35	57.65	296.69	62.73	62.28	CCW
147	310.50	20.20	0.00	86.50	0.00	29.20	271.87	48.05	67.55	324.57	54.39	82.77	CCW
148	319.60	17.90	334.30	79.50	0.00	25.00	287.00	38.33	61.97	333.39	44.65	84.25	CCW
149	316.60	28.50	341.50	82.70	0.00	40.10	268.18	65.21	54.93	316.87	62.49	69.73	CCW
150	307.90	26.60	5.10	87.00	0.00	45.00	241.48	62.61	61.80	297.78	64.78	75.74	CCW
151	315.80	25.10	348.50	84.70	0.00	43.10	246.07	64.86	60.48	302.59	62.05	67.83	CCW
152	314.30	21.80	346.30	84.70	0.00	49.10	242.34	54.80	63.74	296.88	56.90	78.49	CCW
153	313.70	26.90	328.40	87.20	0.00	28.30	283.06	83.31	60.39	326.08	81.23	50.67	CCW
154	314.10	22.50	345.70	84.40	0.00	54.60	235.84	53.18	62.76	290.61	56.09	80.83	CCW

Figure A1 Non-metamorphosed diabase dyke cutting cross the metamorphic sole rocks

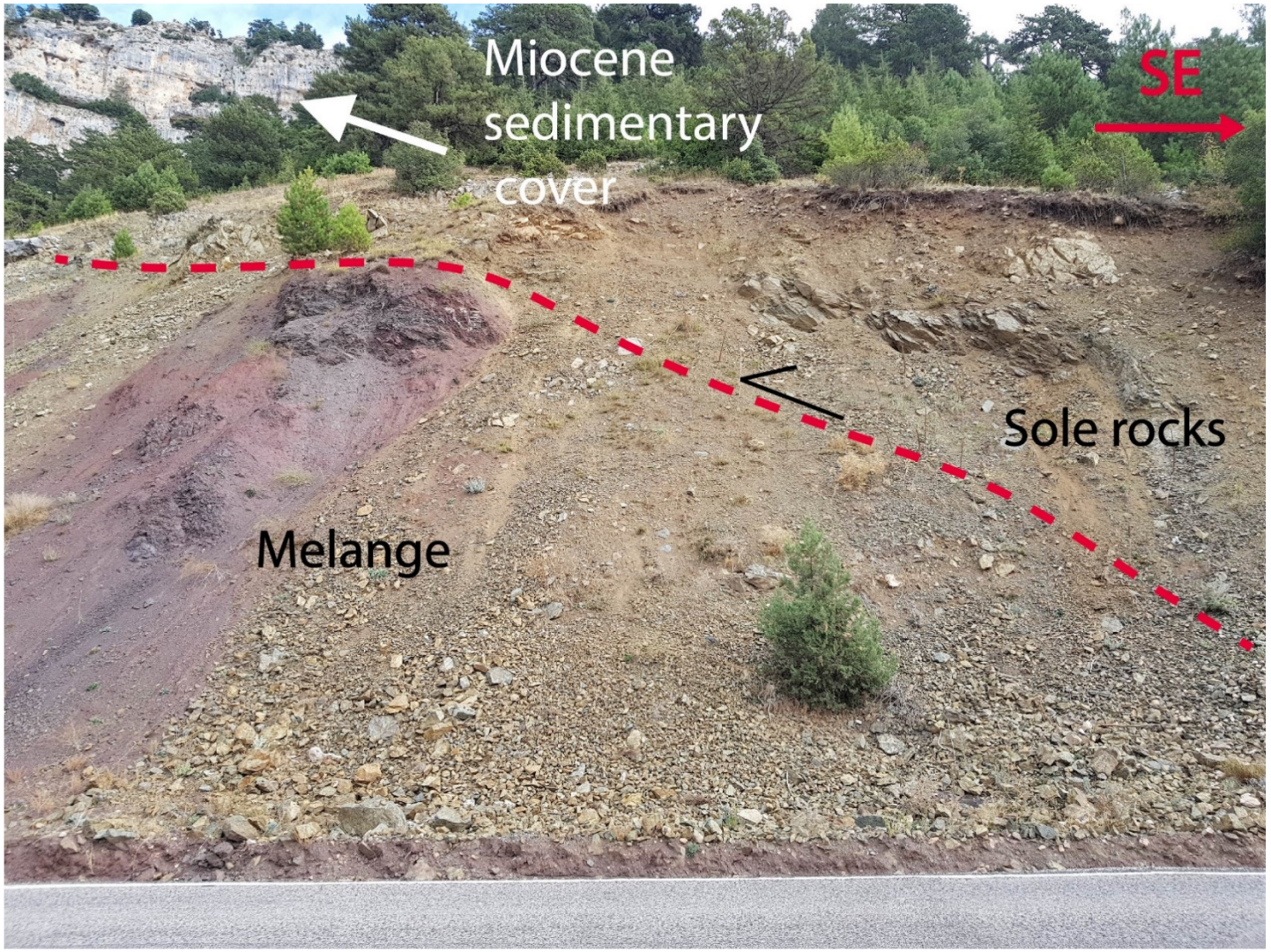

Figure A2.Melange contact with sole rocks at NW portion of the road cut section. The sedimentary cover can also be seen in the upper left.

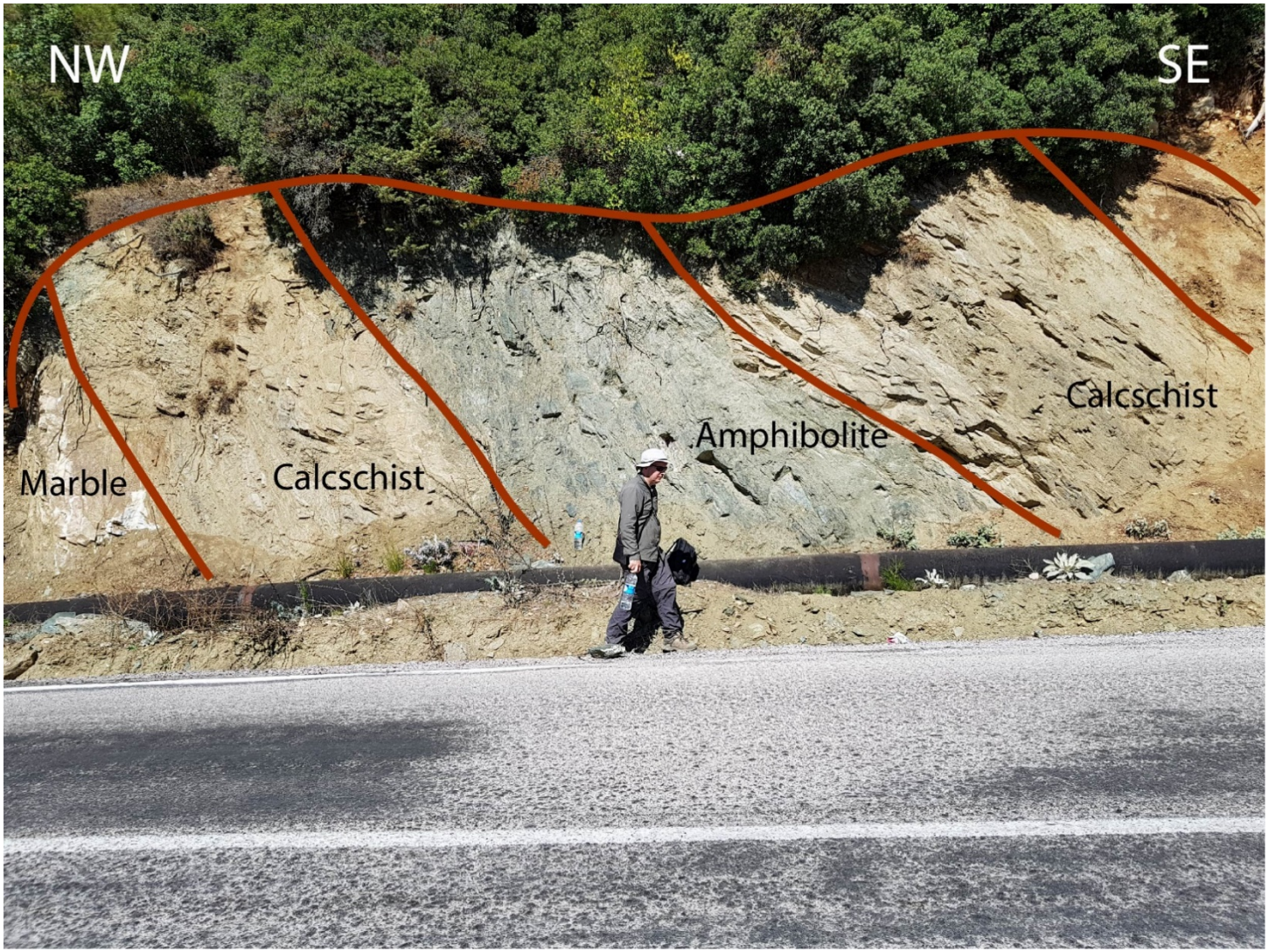

Figure A3. Amphibolite-calcschist-marble intercalation uniformly dipping towards SE

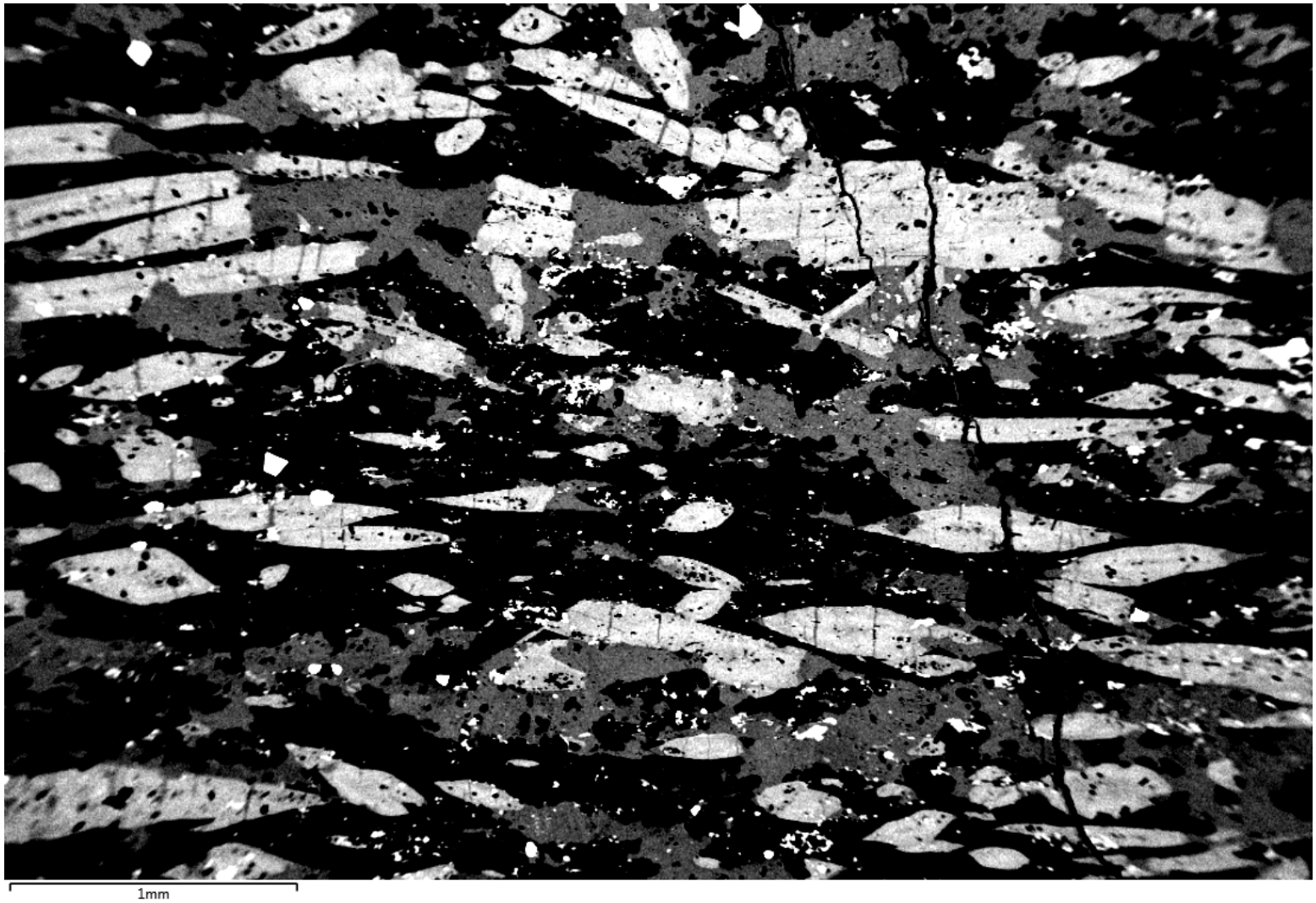

Figure A4. SEM image from BC1201. White ones are amphibole minerals, grey ones are calcite minerals and black region is plagioclase feldspar.

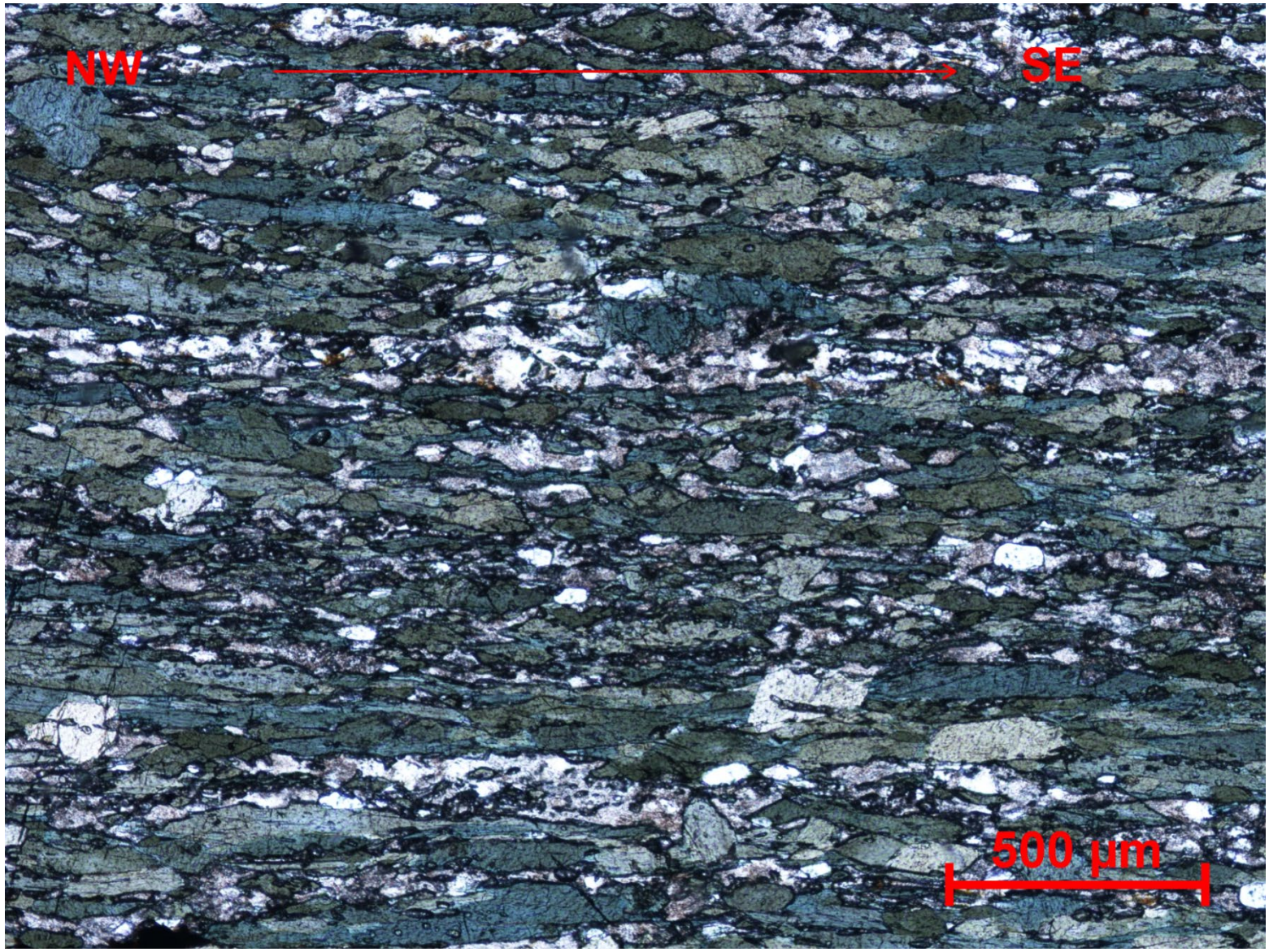

Figure A5. BC0204 illustrating lineation along NW-SE direction. The lineation is represented by amphibole minerals. (DD/D=135°/46°)